FOSSIL ENERGY

DOE/PC/91008-5
(DE98000469)

FRACTURED RESERVOIR DISCRETE FEATURE NETWORK TECHNOLOGIES

Annual Report
March 7, 1996 to February 28, 1997

By
William S. Dershowitz
Paul R. La Pointe
Herbert H. Einstein
Violeta Ivanova

January 1998

Performed Under Contract No. DE-AC22-94PC91008
Subcontract G4S51728

Golder Associates Inc.
Redmond, Washington

National Petroleum Technology Office
U. S. DEPARTMENT OF ENERGY
Tulsa, Oklahoma

DISCLAIMER

This report was prepared as an account of work sponsored by an agency of the United States Government. Neither the United States Government nor any agency thereof, nor any of their employees, makes any warranty, expressed or implied, or assumes any legal liability or responsibility for the accuracy, completeness, or usefulness of any information, apparatus, product, or process disclosed, or represents that its use would not infringe privately owned rights. Reference herein to any specific commercial product, process, or service by trade name, trademark, manufacturer, or otherwise does not necessarily constitute or imply its endorsement, recommendation, or favoring by the United States Government or any agency thereof. The views and opinions of authors expressed herein do not necessarily state or reflect those of the United States Government.

This report has been reproduced directly from the best available copy.

Available to DOE and DOE contractors from the Office of Scientific and Technical Information, P.O. Box 62, Oak Ridge, TN 37831; prices available from (615) 576-8401.

Available to the public from the National Technical Information Service, U.S. Department of Commerce, 5285 Port Royal Rd., Springfield VA 22161

DOE/PC/91008-5
Distribution Category UC-122

Fractured Reservoir Discrete Feature Network Technologies

Annual Report
March 7, 1996 to February 28, 1997

By
William S. Dershowitz
Paul R. La Pointe
Herbert H. Einstein
Violeta Ivanova

January 1998

Work Performed Under Contract No. DE-AC22-94PC91008

Prepared for
BDM-Oklahoma
and
U.S. Department of Energy
Assistant Secretary for Fossil Energy

Robert Lemmon, Project Manager
National Petroleum Technology Office
P.O. Box 3628
Tulsa, OK 74101

Prepared by:
Golder Associates Inc
4104-148th Avenue, NE
Redmond, WA 98052

TABLE OF CONTENTS Page No.

LIST OF TABLES

LIST OF FIGURES

EXECUTIVE SUMMARY

This report describes progress on the project, "Fractured Reservoir Discrete Feature Network Technologies" during the period March 7, 1996 to February 28, 1997. The report presents summaries of technology development for the following research areas: (1) development of hierarchical fracture models, (2) fractured reservoir compartmentalization and tributary volume, (3) fractured reservoir data analysis, and (4) integration of fractured reservoir data and production technologies. In addition, the report provides information on project status, publications submitted, data collection activities, and technology transfer through the world wide web (WWW).

Research on hierarchical fracture models included geological, mathematical, and computer code development. The project built a foundation of quantitative, geological and geometrical information about the regional geology of the Permian Basin, including detailed information on the lithology, stratigraphy, and fracturing of Permian rocks in the project study area (Tracts 17 and 49 in the Yates field). Based on the accumulated knowledge of regional and local geology, project team members started the interpretation of fracture genesis mechanisms and the conceptual modeling of the fracture system in the study area.

Research on fractured reservoir compartmentalization included basic research, technology development, and application of compartmentalized reservoir analyses for the project study site. Procedures were developed to analyze compartmentalization, tributary drainage volume, and reservoir matrix block size. These algorithms were implemented as a Windows 95 compartmentalization code, FraCluster.

Fractured reservoir data analysis research included development of advanced methods for analysis of fracture sets, spatial fracture patterns, and hydraulic parameters. The analysis of fracture sets utilizes neural networks to define sets based on orientations and other attributes. Spatial fracture pattern analysis extended statistical and fractal analyses to include a rule-based approach to consider spatial patterns associated with tectonic processes. Research on derivation of hydraulic parameters for fractured reservoirs extended the concept of fractional dimensional flow to analysis of well tests in fractured reservoirs.

Research on integration of fractured reservoir data and production technologies will be carried out primarily during 1997 and 1998. However, during the current project year, initial research was carried out on definition of interfaces between stratigraphic reservoir models and 3D fracture flow codes, and an application of techniques developed during the year to the project study site.

LIST OF ATTACHMENTS

Attachment A Conference Presentation — Removed for separate processing
La Pointe, P., T. Eiben, W. Dershowitz, and E. Wadleigh (1997)
Compartmentalization Analysis using Discrete Fracture Network Models presented at Fourth International Reservoir Characterization Technical Conference
March 2-4, 1997
Houston, Texas

Attachment B Conference Presentation — Removed for separate processing
Dershowitz, W. and T. Doe (1997)
Analysis of Heterogeneously Connected Rock Masses by Forward Modeling of Fractional Dimensional Flow Behavior
Submitted to be presented at Proceedings, NYROCKS '97, New York

Attachment C Refereed Publication
Chakrabarty, C. and T. Doe (1997)
Analysis of Well Tests in Two Zone Composite Systems with Different Spatial Dimensions
Submitted to Water Resources Research (in review)

Attachment D Refereed Publication
Dershowitz, W., P. La Pointe and T. Foxford
Generating Fractured Reservoirs Through Neural Net Analyses of Geological Data
Submitted to American Association of Petroleum Geologists Bulletin (in review)

1. ANNUAL PROGRESS OVERVIEW

1.1 Overview of Progress

This annual progress report describes activities during the period March 7, 1996 through Feb 29, 1997. Chapters 2 through 6 provide information describing technical progress on the tasks which were active during the year. Table 1-1 presents the active project tasks.

Table 1-1 Active Project Tasks

Chapter	Task	Task Description
2	1.1.1	Initial Data Warehouse
2	1.1.2	Data Updates
3	1.2.1	3D Hierarchical Fracture Model
4	1.3.1	Improved Matrix Block Analysis
4	1.3.2	Drainage Volume Analysis
5	2.1.1	Fracture Set Analysis
5	2.1.2	Spatial Location Analysis
5	2.1.3	Hydraulic Parameter Analysis
5	2.1.4	Compartmentalization Analysis
6	3.1.1	Linkage to Reservoir Model/Software Development
7	3.2.1	MS Windows 95 Fracture Data Analysis System
7	3.2.2	Discrete Fracture Analysis for the TAGS Process
7	3.2.3	Software Linking
8	4.1.1	Fracture Image Data Acquisition
8	4.1.2	Well Testing Data Acquisition
1,2	5.1.1	WWW Server Development
1,2	5.1.2	WWW Site Updates

The major activity in the year was development and implementation of fracture set, fracture hydraulic parameters, and compartmentalization analyses, research related to development of the hierarchical fracture model, and establishment and maintenance of the project WWW site.

Detailed technical information can be found in the research report and quarterly reports provided by the project team, and in the four attached professional publications produced within the scope of the project. See the project web page for access to project reports, databases, and software. The project web page was developed and maintained under the scope of project tasks 5.1.1 and 5.1.2.

http://www.golder.com/niper/niprhome.htm

1.2 Project Deliverables

The following project deliverable documents were scheduled or submitted during the first year of the project. In addition to these, information on the project WWW server was updated regularly throughout the year. Reports, presentations, and papers were prepared under the scope of project Tasks 5.2.1 through 5.2.4.

Deliverable	Scheduled Date	Date Submitted
Work Plan	96.03.30	96.04.24
First Quarter Progress Report	96.06.15	96.06.26
Second Quarter Progress Report	96.09.15	96.10.24
Third Quarter Progress Report	96.12.15	96.12.20
Peer Reviewed Papers (2)	by 96.12.30	97.02.28
Prof. Meeting Papers (2)	by 96.12.30	96.12.05
Research Report, Fractured Reservoir Compartmentalization	96.11.30	97. 02.14

The professional papers produced within the scope of this project during the current year are as follows:

La Pointe, P., T. Eiben, W. Dershowitz, and E. Wadleigh, 1997. Compartmentalization Analysis Using Discrete Fracture Network Methods. Proceedings, Third International Reservoir Characterization Conference, Houston. NIPER, Bartlesville.

Dershowitz, W. and T. Doe, 1997. Analysis of Heterogeneously Connected Rock Masses by Forward Modeling of Fractional Dimensional Flow Behavior. Proceedings, NYROCKS '97, New York. AA Balkema, Rotterdam.

Chakrabarty, C. and T. Doe, 1997. Analysis of Well Tests in Two Zone Composite Systems with Different Spatial Dimensions. Submitted to Water Resources Research (in review).

Dershowitz, W., P. La Pointe and T. Foxford. Generating Fractured Reservoirs Through Neural Net Analyses of Geological Data. Submitted to American Association of Petroleum Geologists Bulletin(in review).

These papers are provided as Appendices A, B, C, and D, and are posted on the project web site.

2. TASK 1.1 FRACTURED RESERVOIR SITE CHARACTERIZATION DATA

2.1.1 Task 1.1.1 Initial Data Warehouse

The locations of the study site tracts 17 and 49 within the Yates fractured reservoir field are illustrated in Figure 2-1. During the first quarter, Marathon Oil Company collected fracture and production data from project study site and provided this data to Golder Associates to provide the basis for the initial data warehouse. The following data was donated to the project:

- core analysis,
- geophysical logs,
- structural analyses,
- well performance histories,
- lineament maps,
- production data related to TAGS, and
- well adjustment and response monitoring).

This data was assembled and processed into an information warehouse within the World-Wide-Web (WWW) server application (Task 5.1.1). Figures 2-2 through 2-8 present examples of the data available to anyone with Internet access and a browser capable of interpreting HTML2.

Marathon Oil Company
Mid-Continent Region

YATES FIELD UNIT
Pecos & Crockett Counties, Texas

▢ Approximate boundary for areas of investigation

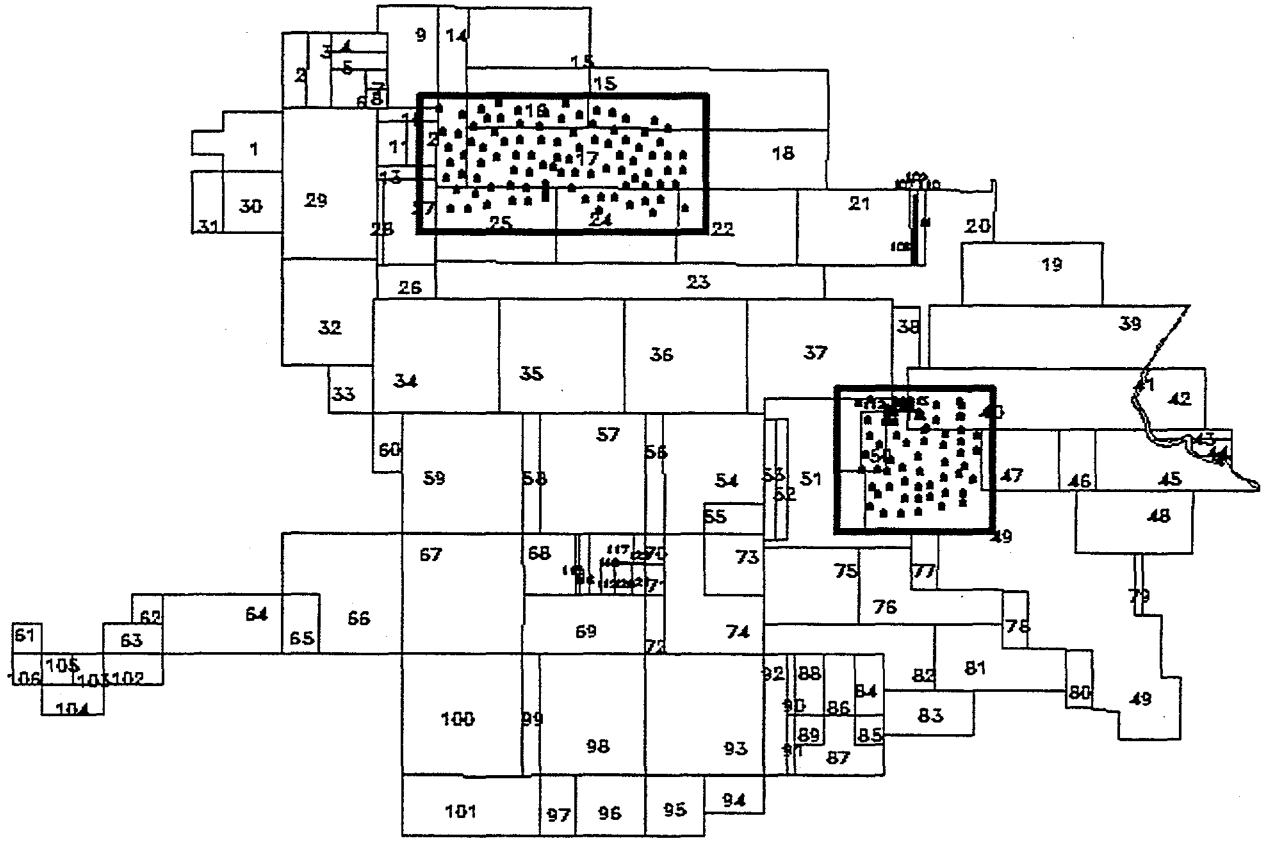

FIGURE 2-1
PROJECT STUDY SITE
BDM-NIPER/FRACMAN

PROJECT NO. 963 1357.521 DRAWING NO. 69405 DATE 4/4/97 DRAWN BY CB

Golder Associates

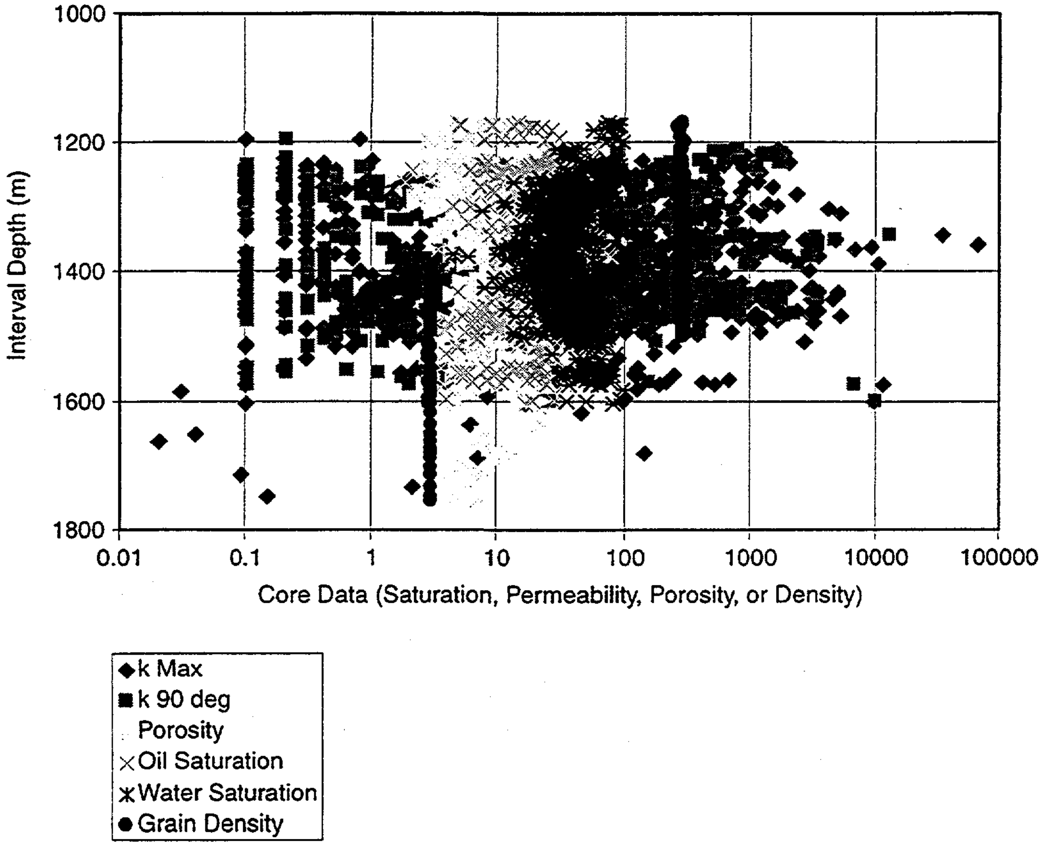

FIGURE **2-2**

CORE LOG ANALYSIS

BH-17, WELL 11

BDM-NIPER/FRACMAN

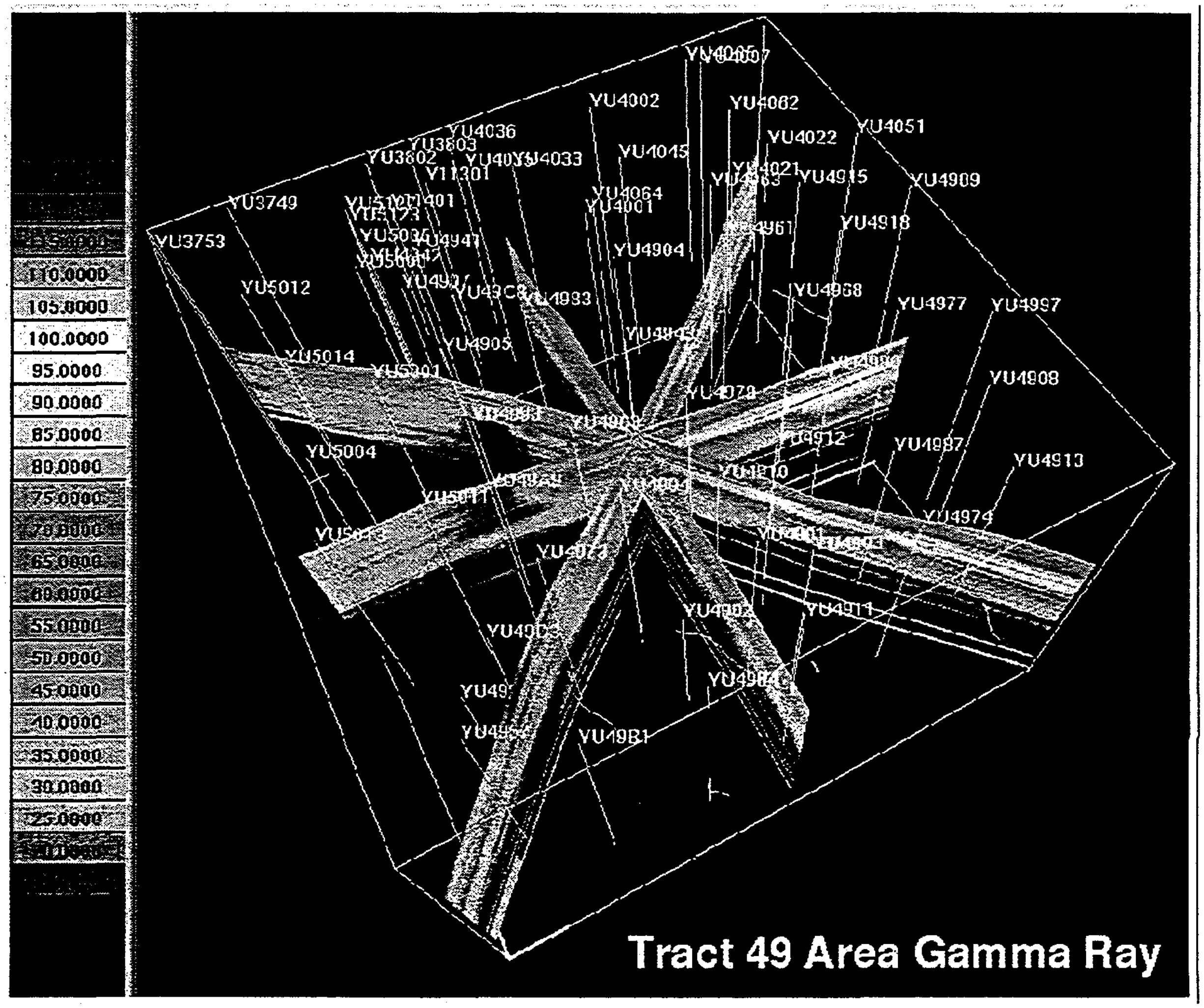

FIGURE **2-3**

FENCE DIAGRAM OF GAMMA RAY LOGS

FOR RESERVOIR TRACT 49

BDM-NIPER/FRACMAN

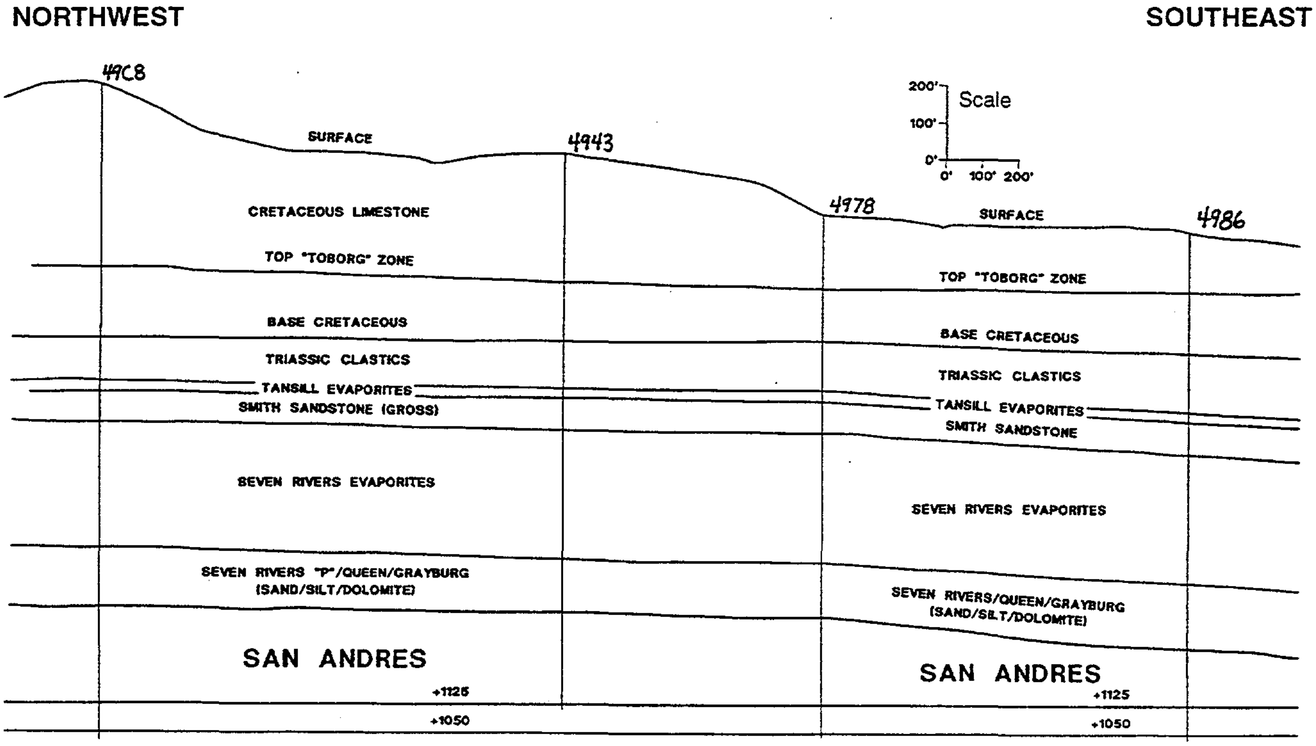

FIGURE **2-4**
CROSS SECTION THROUGH YATES FIELD STUDY SITE
BDM-NIPER/FRACMAN

PROJECT NO. 963 1357.521 DRAWING NO. 69408 DATE 4/4/97 DRAWN BY CB

Golder Associates

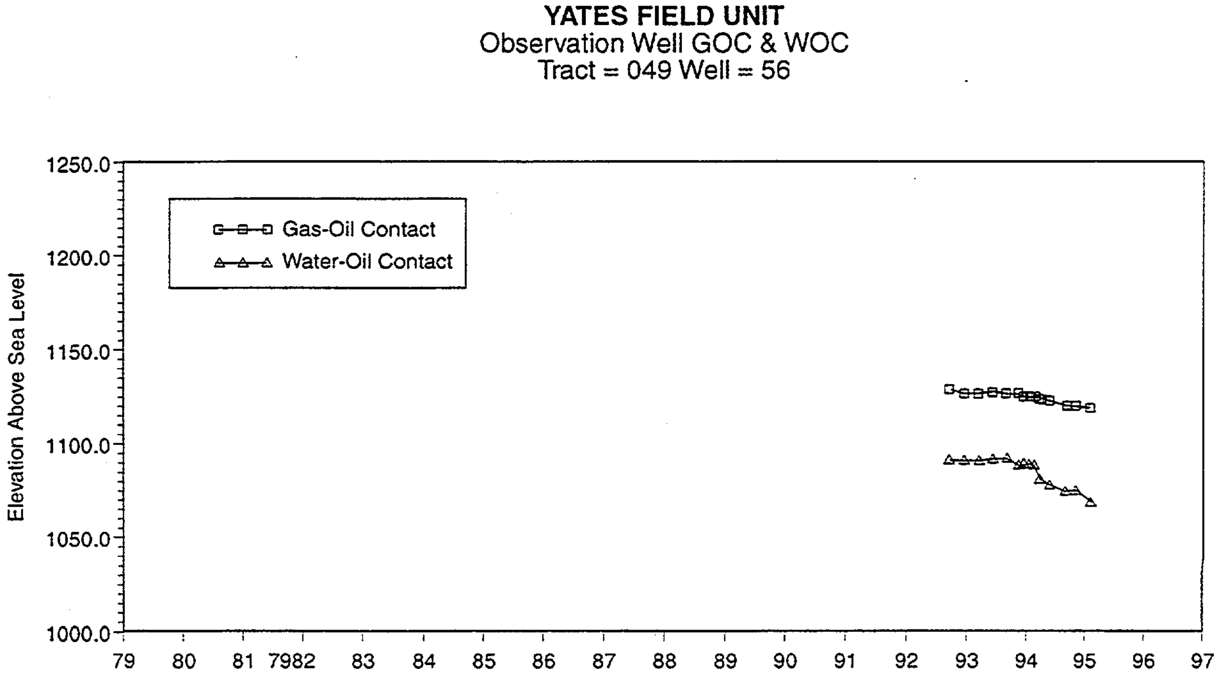

FIGURE **2-5**

FLUID CONTACT HISTORIES

BDM-NIPER/FRACMAN

- Tract 17 area
- Incorporates local large-scale features

FIGURE **2-6**
SYNTHETIC LINEAMENT MAP
FOR TRACT 17 AREA
BDM-NIPER/FRACMAN

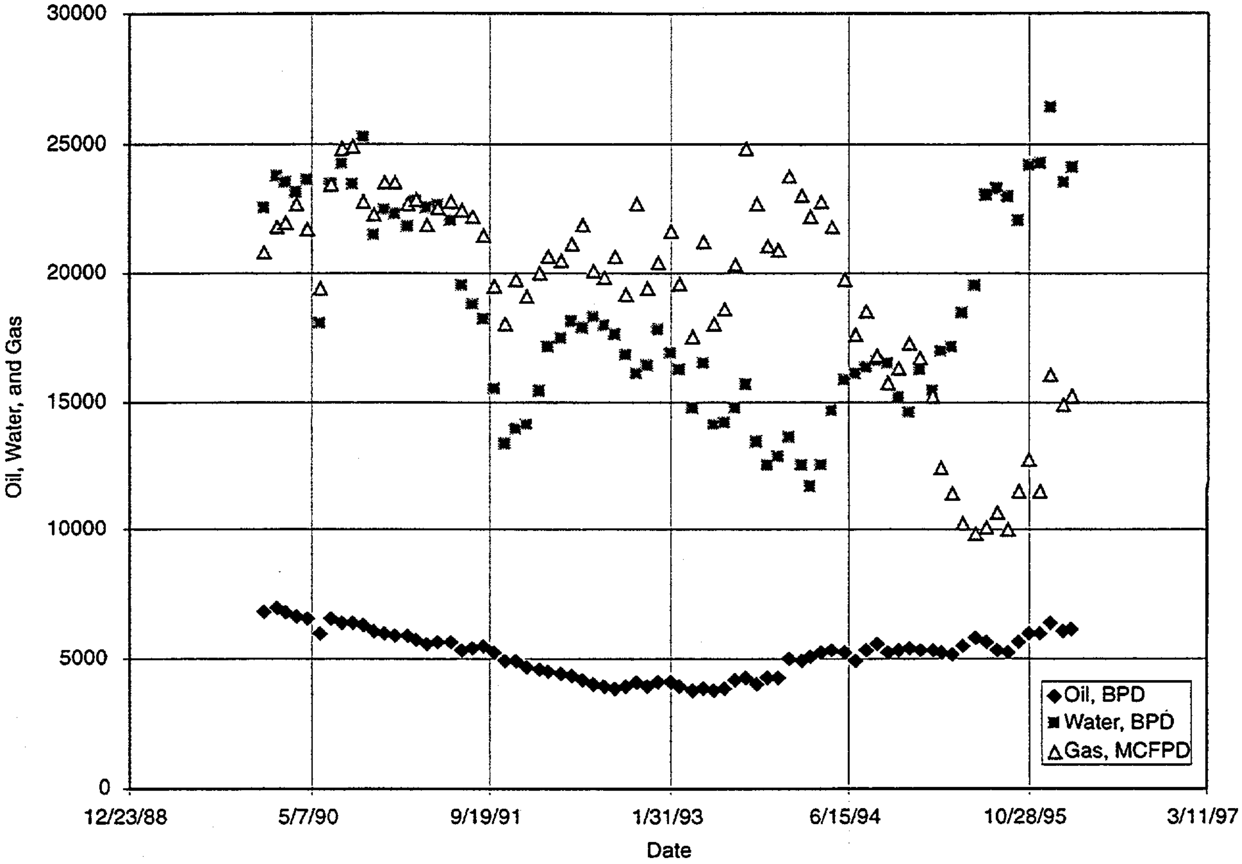

FIGURE **2-7**

YATES AREA 17 PRODUCTION DATA

BDM-NIPER/FRACMAN

PROJECT NO. 963 1357.521 DRAWING NO. 69411 DATE 4/4/97 DRAWN BY CB

Golder Associates

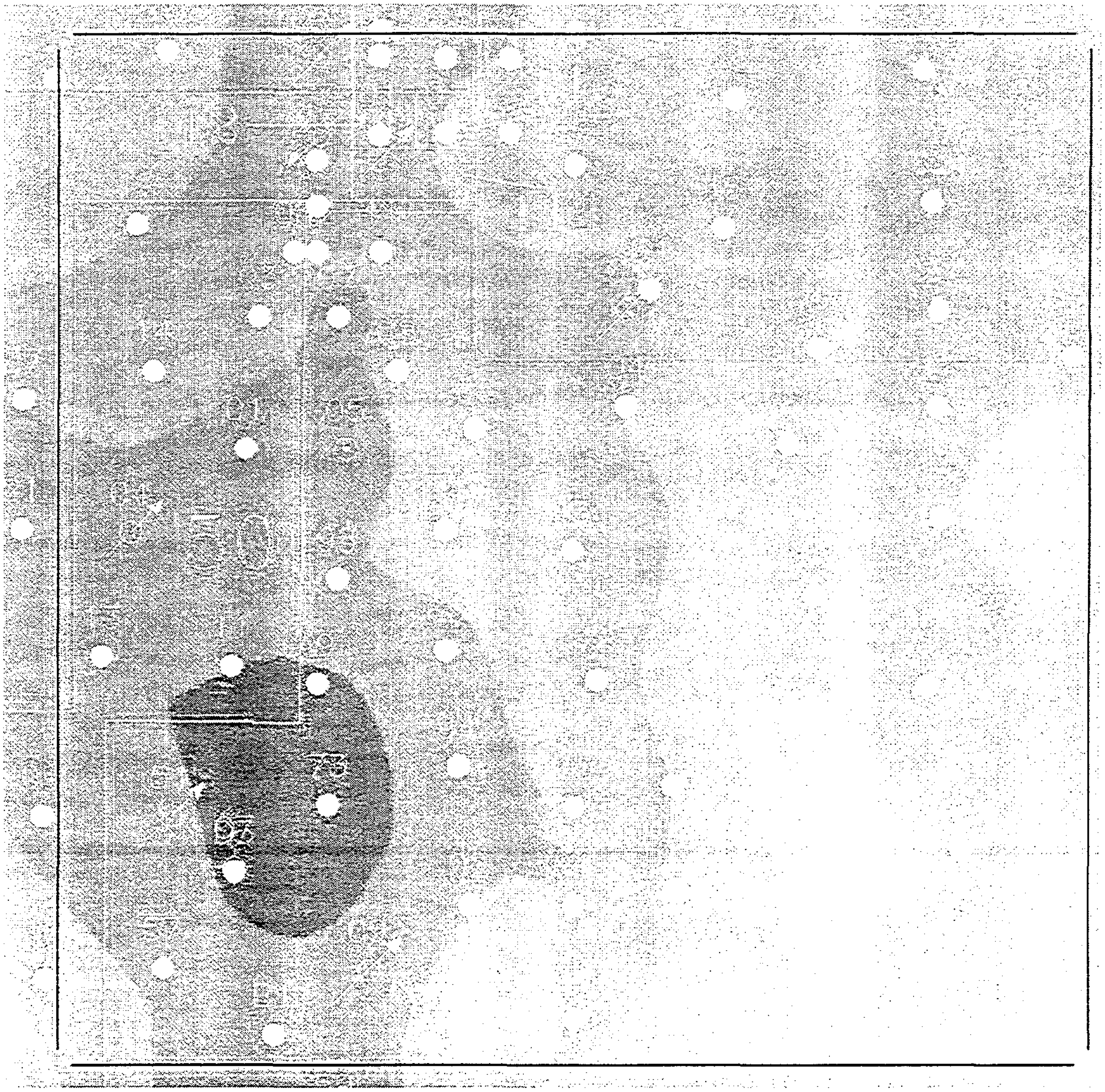

FIGURE **2-8**
TRACT 17 AREA MAP
BDM-NIPER/FRACMAN

The WWW server organizes the Technology Transfer Database into the following categories:

- **Progress Reports:** An annotated list of project progress reports. By selecting a report from the list, you may download the Microsoft Word file from our anonymous FTP site.
- **Peer Reviewed Papers:** An annotated list of peer reviewed papers produced within the project. By selecting a report from the list, you may download the selected file from our anonymous ftp site.
- **Professional Meeting Presentations:** A list of past and future meeting presentations.
- **Site Characterization Data:** An annotated list of site characterization data files. Selecting a file from the list begins downloading.
- **Algorithms and Software:** An annotated list of available free and proprietary software and algorithms. A link to the proper directory in Golder's FTP server allows easy downloading of free software and algorithms.
- **Reservoir Data and Simulations:** An annotated list of reservoir data and simulation files, accompanied by a link to the proper directory in Golder's FTP server.
- **Technology Transfer Workshop Information:** Schedule and registration information for the technology transfer workshop.

2.1.2 Task 1.1.2 Data Updates

During the year, Marathon Oil Company regularly collected fracture and production data from the project study site and provided these data to Golder Associates to update the online data warehouse. The following additional data were donated to the project during the year:

- FMI Geophysical logs
- Geophysical logs from selected wells
- Well performance histories
- Production data related to TAGS
- Well adjustment and response monitoring

In addition to the above, Marathon Oil Company provided geological data requested by MIT, which forms the basis for the interpretation of the fracture system in the Yates Field. Marathon Oil donated the following data to the project:

- Internal Marathon reports on 3D geologic reservoir characterization (StrataModel) of Yates Field

- Extracts from StrataModel with formation sequences and distribution of porosity, shale, calcite, and caves in Tract 17 and 49
- Core data on lithology, fracturing, and rock properties from locations near Tracts 17 and 49
- Additional log interpretations from Tract 17 and 49

These data were assembled and incorporated into the project World-Wide-Web (WWW) site (Task 5.1.2). Figures 3-1 through 3-15 present additional examples of the data provided by Marathon during the year. These figures are related to work carried out under Task 1.2.1, and are therefore located near the appropriate citations in the next chapter.

3. TASK 1.2 3D HIERARCHICAL FRACTURE MODEL

During the year, 3D Hierarchical Fracture Model research focused on four main tasks:

- Hierarchical Model Development
- Regional geology of the Permian Basin
- Detailed information on the lithology, stratigraphy, and fracturing of Permian rocks in the Yates field study area (Tracts 17 and 49)
- Preliminary modeling of fracture formation and geometry.

3.1 Hierarchical Model Development

During the year, the 3D Hierarchical Model (Ivanova 1995; Ivanova et al. 1995), model was enhanced with some new procedures, the most important being the Fractal Line Tessellation. This is expected to be particularly useful for modeling the San Andres formation and similar fractured reservoirs because it reproduces the clustering of fractures into zones.

3.1.1 Basic Concepts of the 3D Hierarchical Model

The 3D Hierarchical model incorporates the following basic models:

- *A geometric-mechanical model* - it uses relatively simple geometric procedures to duplicate the three-dimensional geometry of fracture networks created by complex mechanical processes.
- *A hierarchical model* - fractures are grouped into hierarchically related fracture sets based on the field data and the geologic history of the region.
- *A stochastic model* - fracture sets are generated through a sequence of three stochastic processes based on the statistics of the geologic data.

In the current version of the model, the fractures are convex polygonal planar objects of discontinuous rock, randomly located in three-dimensional space. The pole orientation and the coordinates of the center and the vertices of an individual fracture are determined indirectly when this fracture is generated as a member of a fracture set.

3.1.2 Generation of a Single Fracture Set Using the 3D Hierarchical Model

A collection of fractures with related orientations, sizes, and locations define a fracture set. In the 3D hierarchical model, the following four parameters characterize a fracture set: (1) mean orientation; (2) probability density function (PDF) describing the distribution of fracture orientations around the mean orientation; (3) size variation of the fractures which belong to that particular set; and (4) density of fracturing as it varies in space.

A fracture set is generated by applying a sequence of three stochastic processes to a modeling volume which represents the fractured rock mass. The modeling volumes of independent sets are defined by the boundaries of geologic structures in which the particular primary fractures are created. Dependent sets are usually generated within modeling volumes, determined by the randomly located independent fracture sets. Figure 3-1 illustrates the modeling volumes for secondary and tertiary fractures, enclosed between the primary and secondary fractures, respectively, in strike-slip fault zones.

The primary process consists of a homogeneous, isotropic or anisotropic, Poisson plane network, representing the planes of principal tensile and shear stress. The variation of plane orientations is described with PDF's. Figure 3-2 shows examples of how the stress field determines the fracture orientations, and the choice of appropriate PDF in these cases.

The secondary process, subdivision of each plane into a fractured region and its complementary region of intact rock, is accomplished by a homogeneous line network and a non-homogeneous polygon marking procedure. The secondary process produces sets of fractures which have certain size and shape variation, and are arranged in clusters. The secondary stochastic process represents the intensity of fracturing, which can be defined as the ratio of fractured to intact rock.

The subdivision of every plane is obtained with the Fractal Line Tessellation procedure (Figure 3-3). First, the original plane is divided into large polygons by a small number of Poisson lines and some of the polygons are marked as fracture zones. The probability of marking a polygon as fractured, P, is calculated for every polygon as:

$$P[\text{a polygon is fractured}] = P[\text{location, size, shape, termination, ...}] \tag{3-1}$$

Next, a Poisson line tessellation of small density and a marking process is performed only in the fracture zones. This procedure is repeated in a number of iterations. The parameters of the Fractal Line Tessellation (number of iterations, density of Poisson lines in every iteration, and the probability of marking polygons as fracture zones) can be chosen to represent low or high intensity of fracturing, as well as different fracture persistence. The Fractal Line Tessellation leads to a relatively fast subdivision of a plane into the desired fractured and intact areas.

The tertiary stochastic process involves random shifting and rotation of (a portion of) the fractured polygons in the vicinity of their original positions. The tertiary stochastic process represents possible variations of the stress field, for example, rotation of the principal stress axes, which leads to some specific fracture patterns such as fractures arranged en echelon.

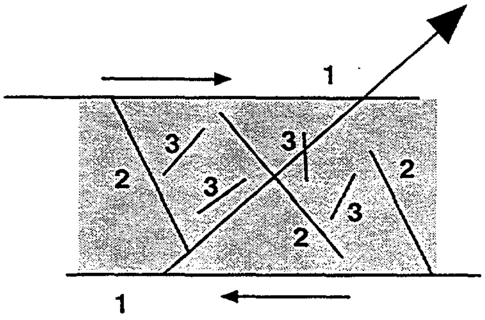

Mean Pole Direction for Secondary (2) Joints

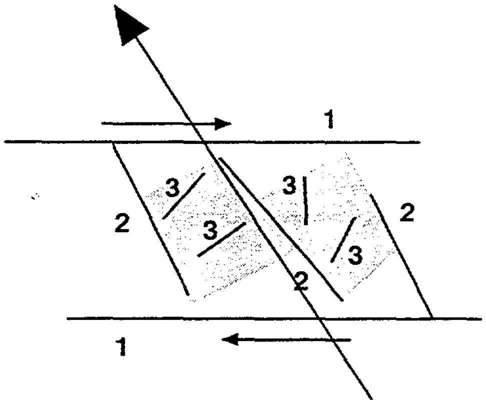

Mean Pole Direction for Tertiary (3) Joints

FIGURE **3-1**

MODELING VOLUMES FOR SECONDARY AND TERTIARY JOINTS

BDM-NIPER/FRACMAN

PROJECT NO. 963 1357.521 DRAWING NO. 72191 DATE 3/28/97 DRAWN BY TK

Golder Associates

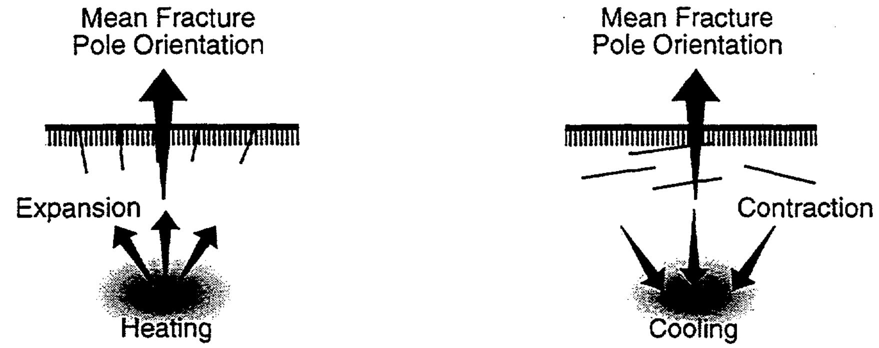

PDF Around Mean: Bingham

PDF Around Mean: Fisher

Thermal Joints

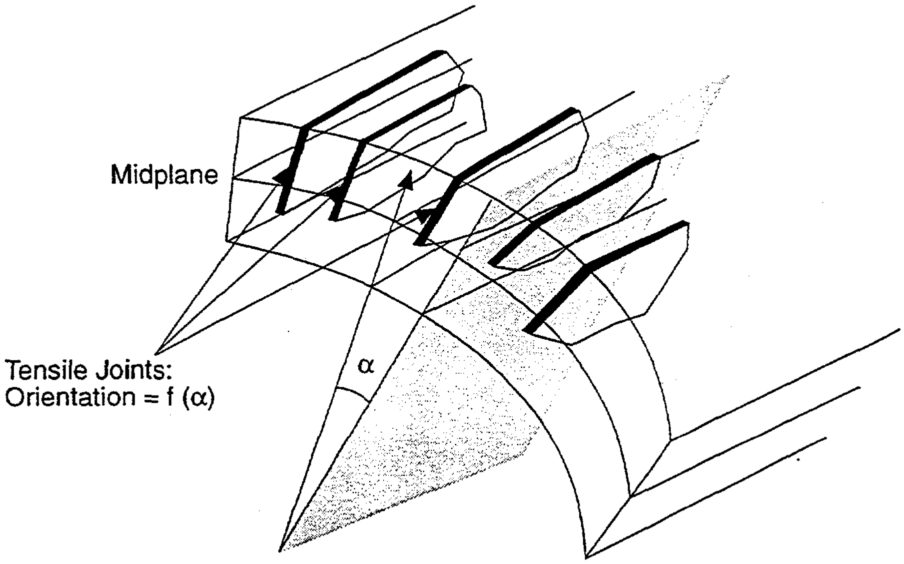

Tensile Joints in the Crest of a Fold

FIGURE **3-2**

FRACTURE PLANE ORIENTATIONS
DEFINED BY THE STRESS FIELD
BDM-NIPER/FRACMAN

PROJECT NO. 963 1357.521 DRAWING NO. 72192 DATE 3/28/97 DRAWN BY TK

Golder Associates

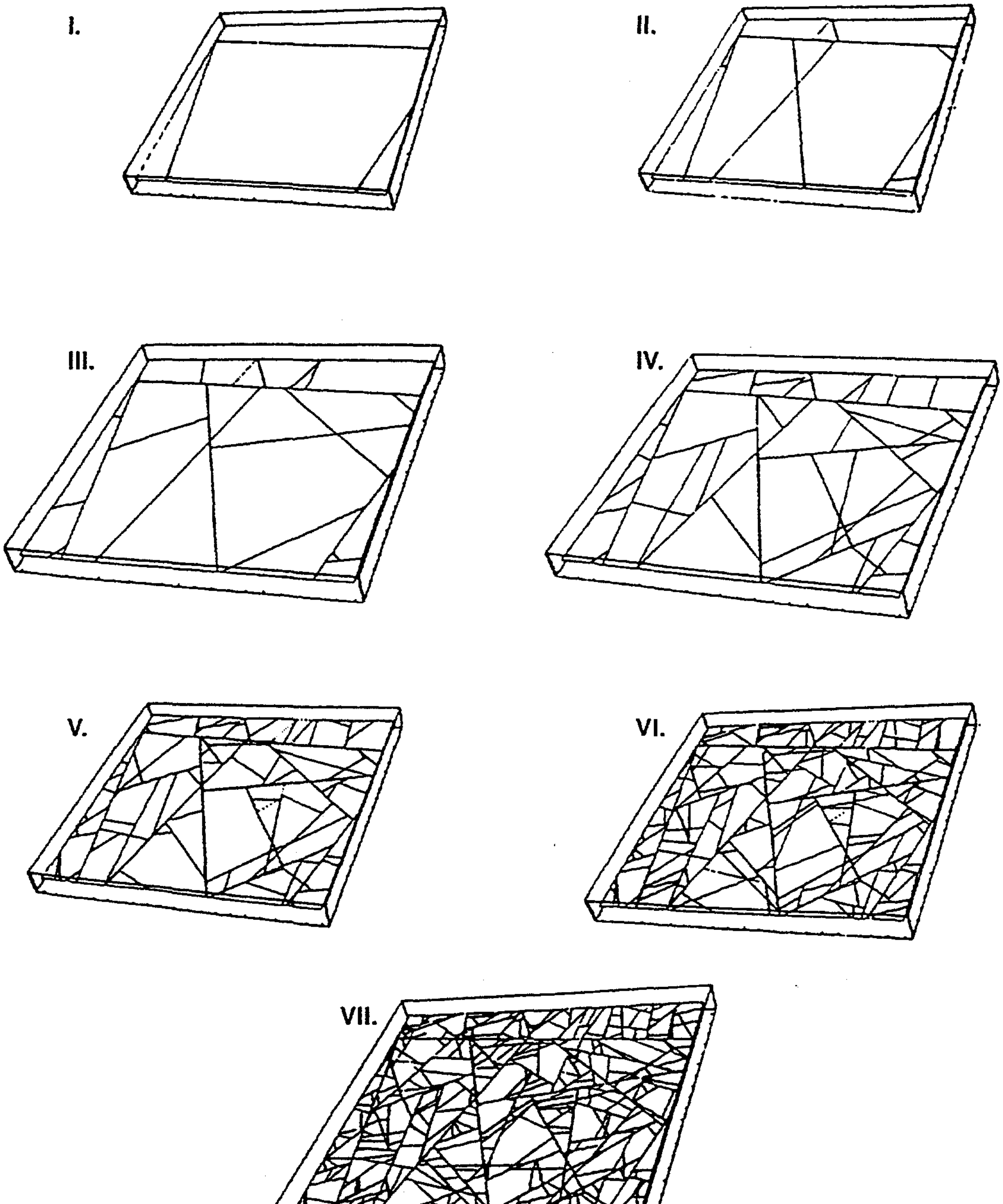

FIGURE **3-3**
FRACTAL LINE TESSELATION
BDM-NIPER/FRACMAN

PROJECT NO. 963 1357.521 DRAWING NO. 72193 DATE 3/28/97 DRAWN BY TK

Golder Associates

3.1.3 Generation of a Fracture System with the 3D Hierarchical Model

A natural rock fracture system is reproduced in three dimensions through a superposition of independent and dependent fracture sets. For example, dependence on previously generated sets can be obtained by (1) specifying the marking probability for a polygon as a function of the distance to the primary fractures, and (2) by defining a function for termination of fractured polygons from a secondary set at the intersections with fractures from a primary set.

3.1.4 Applicability of the 3D Hierarchical Model for Representation of Geologic Fracture Networks

The 3D Hierarchical Model has been chosen to simulate the fracture system in the San Andres formation because of its capability to reproduce hierarchical fracture genesis and clustering. The model combines the advantages of the purely geometric and the purely mechanical models.

The conceptual model duplicates natural fracture systems on the basis of the available geologic information. The implemented stochastic processes are inherently related to the underlying mechanics and geology, which makes the model promising as a tool for simulation of geologic fracture systems.

3.2 3D Reservoir Characterization of Permian Rocks in the Yates Field

In the three-dimensional hierarchical fracture model, fracture system generation is based on the material properties of the host rock and the geologic mechanisms that have acted in the area. Prior to fracture modeling, it is essential to develop a realistic representation of the geologic mechanisms, defined by the deposition sequence and the structural deformation. During the year, MIT researchers became familiar with the three-dimensional reservoir characterization of the Yates field by Marathon Oil geologists and engineers (Tinker 1996; Tinker et al. 1995; Tinker and Mruk 1995; also Tinker, Uland, pers. comm.).

The reservoir characterization of the Yates Field includes a 3D geologic model of the complete reservoir, based on a database that integrates geologic and engineering data from 1800 wells, 118 cores (total of 23,000 ft of quantified core description and analysis), and historical production data. The geologic model was built at Marathon Oil, Littleton by Scott Tinker and other Marathon Oil geologists. The model, containing 6.8 million cells and 40 attributes per cell, was created using StrataModel and other commercial software.

3.2.1 Field Structure

Figure 3-4 shows the location of the Yates Field on the southeastern tip of the Central Basin Platform. This location represents the highest present position of the structure of the Permian strata (San Andres, Grayburg, Queen, and Seven Rivers formations) on the platform.

The maximum dips on top of the San Andres are 3° to 5° to the east and south into the Midland Basin and the Sheffield Channel, respectively, and 0.5° to the west towards the Central Basin Platform axis (Craig 1990; Tinker et al. 1995). The Yates Field anticlinal structure was formed primarily by Late Permian (post-Salado and pre-Rustler) drape folding over buried pre-Permian anticlines and fault scarps (Hills 1970). The main cause for the drape folding is interpreted to be the differential compaction between relatively rigid shoal facies and highly compactible lagoonal and intertidal facies (Craig 1990; Tinker and Mruk 1995).

3.2.2 Depositional Model, Stratigraphy, and Lithology

Figure 3-5a represents a west-to-east stratigraphic section from the 3D geologic model of the Yates Field. The stratigraphic framework of the upper San Andres formation is composed of two major depositional sequences (Figure 3-5b): Sequence 1: a ramp complex, prograding from west to east, overlain by Sequence 2: a group of four major cycles, aggrading and prograding to the east (Tinker 1996; Tinker and Mruk 1995). Paleoelevations of the surface boundaries between major cycles were reconstructed according to depths from a datum in the Seven Rivers horizon which was deposited as a horizontal layer (Craig 1988). In Figure 3-5a, Cycle 4 is not shown because it was almost entirely removed by subaerial erosion following the deposition of San Andres creating the major unconformity at its top.

Figure 3-5b illustrates the west-to-east distribution of the three dominant San Andres lithofacies, superimposed on the major sequence stratigraphy. Each major cycle in the San Andres represents a high-frequency sequence (HFS), composed of three to five minor sequences. On the west side of the Yates field, HFSs consist of vertically stacking shale-carbonate layers, deposited as low-energy mudstones and wackestones (classification by Dunham 1962). Shales (shown in green in Figure 3-5b) are thickest and most extensive at the base of each HFS, and become thinner and laterally discontinuous near the HFS top. Figure 3-6 shows a typical log profile from the west side of the field. The HFS boundaries in the geologic model were correlated between the wells in the west side of the field. The vertical distribution of shale is explained by the deposition of clays (90% illite and 10% chlorite) in lagoons behind the shoal islands during sea level fall, and their later upward grading during subsequent sea level rise into shallow subtidal mudstone/wackestone, and shallow shelf packstone/grainstone.

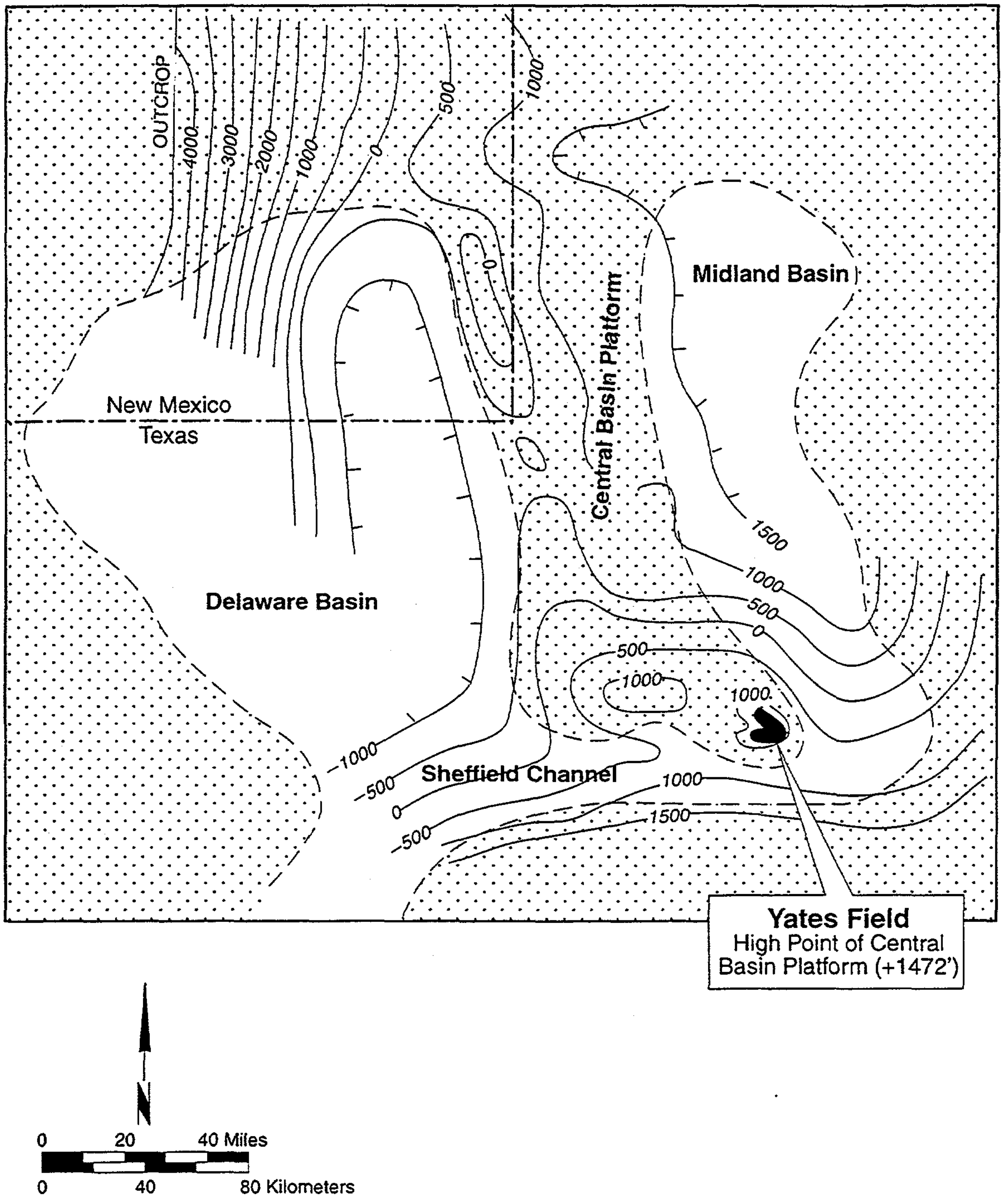

(after Craig 1990)

FIGURE **3-4**

LOCATION OF THE YATES FIELD ON THE CENTRAL BASIN PLATFORM

BDM-NIPER/FRACMAN

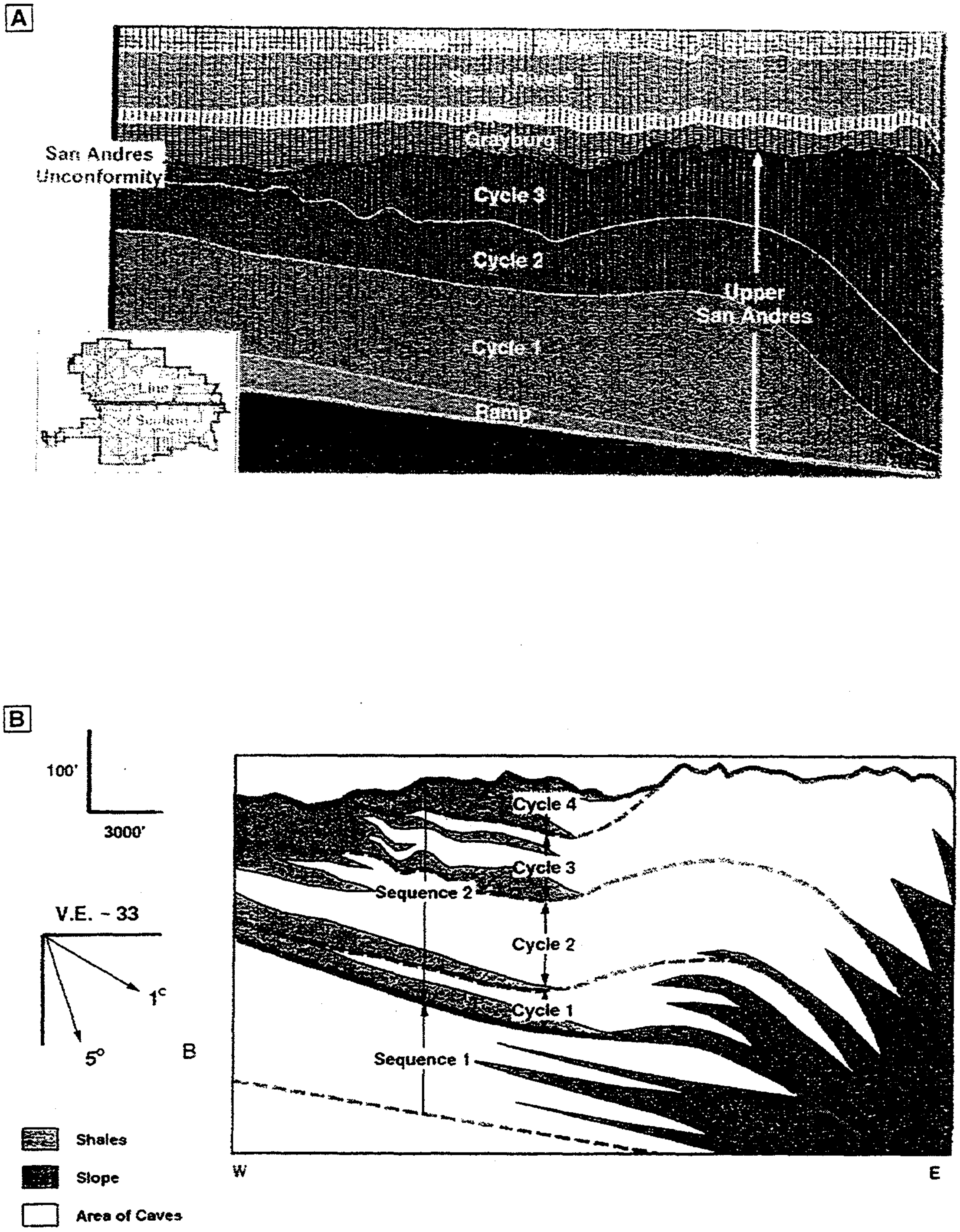

(after Tinker et al. 1995)

FIGURE **3-5**

EAST-TO WEST STRATIGRAPHIC AND LITHOLOGIC SECTION OF THE YATES FIELD

BDM-NIPER/FRACMAN

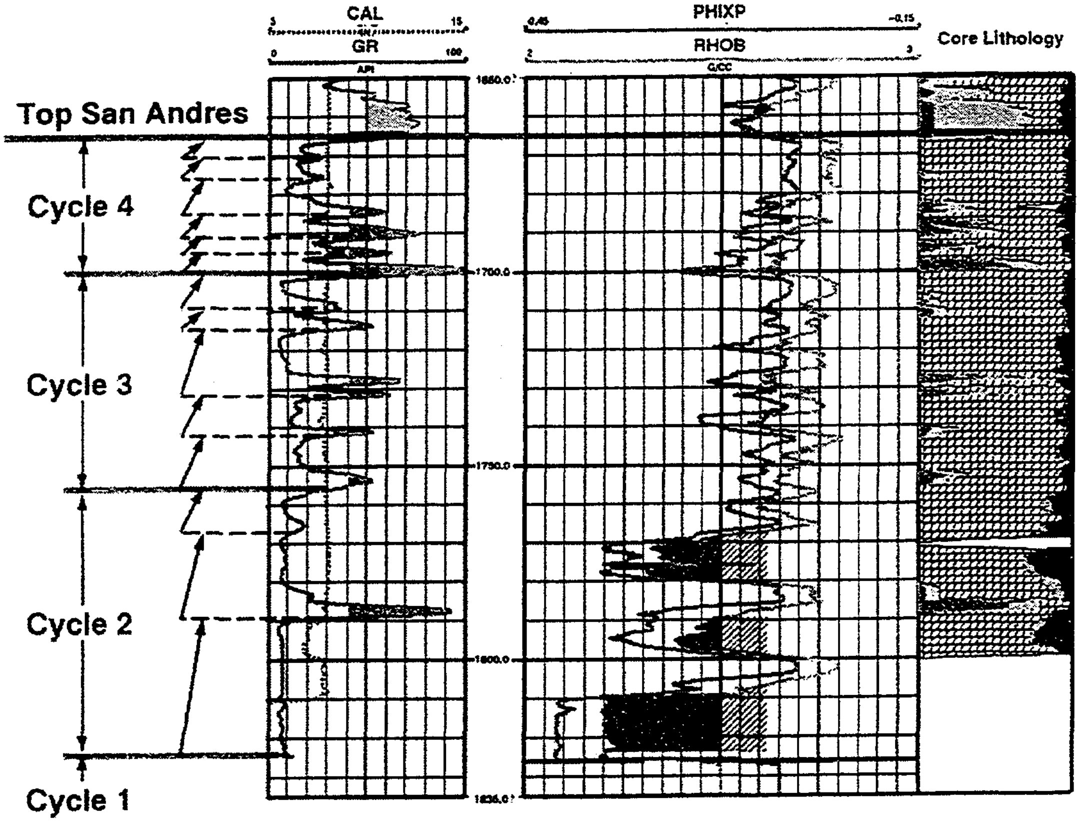

(after Tinker et al. 1995)

FIGURE **3-6**

CYCLE STRATIGRAPHY IN THE YATES FIELD ILLUSTRATED ON A WEST-SIDE LOG

BDM-NIPER/FRACMAN

In the deep west side and on the upper east side of the Yates Field, the HFSs of the San Andres consist of hundreds of vertical feet of clean carbonates (white in Figure 3-5b) with higher porosity and low gamma ray response. The carbonates were deposited as higher-energy, shallow, subtidal shoals of fusulinid packstones and grainstones which were subsequently dolomitized. A third lithofacies, present on the lower east side of the field, is the low porosity, low gamma ray, wackestone of the eastern slope and deep ramp (blue in Figure 3-5b). The major cycles cannot be correlated from log and core data on the east side of the field since the shale layers are missing. The major cycles, correlated in the west, are projected into the clinoformal geometries of the shoals in the east according to the depositional model of eastward carbonate shoal progradation and aggradation.

The Grayburg sediments (Figure 3-5a) onlapped the karst paleosurface of the San Andres during a marine transgression, filling topographic lows and thinning over topographic highs. The Grayburg and Queen sediments were deposited as clastic and carbonate mudstones and wackestones in shallow subtidal to intertidal/supratidal environments. The predominantly evaporite facies of the Seven Rivers were deposited in hypersaline environments. On the east side of the Yates Field, sandstone facies of the Seven Rivers were deposited in the subaerial environment of a low-relief beach and dune complex over the buried San Andres topographic high.

3.2.3 Porosity Distribution Defined by Rock Lithology and Texture

Table 3-1 summarizes the distribution of dominant lithofacies, rock textures, and porosity types within the San Andres formation in the Yates Field (Tinker and Mruk 1995). On the west side of the field (Tract 17), two major lithofacies are present in the San Andres formation: (1) argillaceous dolomites ("shales"), and (2) clean dolomites (95% dolomite per rock volume). On the east side of the field (Tract 49) dolomite is the predominant mineral (96% of the rock volume). Limestone, principally as calcite cement, is the only other significant lithologic/mineralogic component, present both on the west and east side of the field. Rock matrix pores in both areas, the low porosity west side and the higher porosity east side, are dominated by moldic, fusumoldic, and vuggy types (classification by Choquette and Pray 1970), in addition to the crystalline porosity typical for dolomite.

Grayburg sediments (10 to 115 ft thick) consist of approximately equal amounts of clastics (mostly silt) and carbonates (90% dolomite). The Queen formation (about 45 ft thick) also consists of clastics (sand and silt) and carbonates (mostly dolomite). The predominant porosity in both Grayburg and Queen is of micro-intercrystalline type, some vuggy and fenestral pores also being present. The Seven Rivers anhydrite (300 to 400 ft thick) forms the seal of the reservoir. The clastic portion of the Seven Rivers (an up to 100 ft thick arc of sandstone, siltstone, and dolomite cement) has predominantly micro-crystalline and intercrystalline porosity.

Table 3-1 Lithology, Texture, and Porosity of the San Andres in the Yates Field

Formation	San Andres west Tract 17	San Andres east Tract 49
Lithology	"shales" - argillaceous dolomites, silt and shale; clean dolomite; limestone (calcite cement)	96% clean dolomite; limestone (calcite cement)
Texture	mostly mudstone and wackestone; some packstone	packstone and grainstone
Porosity type	intercrystalline and micro-intercrystalline; moldic, fusomoldic, vuggy	intercrystalline and micro-intercrystalline; moldic, fusomoldic, vuggy
Comment	low porosity; high gamma ray	high porosity; low gamma ray (corrected for uranium) best quality reservoir rock

3.2.4 Secondary Calcite

Calcite in the San Andres formation is present primarily as secondary cement, filling the pores of the rock matrix and decreasing its permeability (Tinker and Mruk 1995). Measured percent of calcite in cores and estimated percent of calcite calculated from log analysis are integrated into the StrataModel. The 3D geologic model of the reservoir includes spatial distribution of pore-filling calcite and a model for the calcite origin. The secondary calcite formed by biodegradation of oils at the paleo oil-water contacts. Under this process, a horizontal layer of calcite would be deposited at the oil-water contact elevation during a relatively long period of constant sea level.

3.2.5 Cave System and Other Karst in the San Andres

Paleokarst topography in the San Andres formation is recognized by lithologic features in cores, extremely high flow rates from early wells, bit drops and other log anomalies. Karst topography in the San Andres was formed by carbonate dissolution, including dissolution along joints in porous limestone which later was subjected to dolomitization. Caves were observed in more than 15% of the wells across the Yates field. One thousand fifty caves, ranging in height from 1 to 21 feet, or a total of 4477 cave feet (i.e., vertical feet of cave) were recorded throughout the field (Tinker et al. 1995).

Figure 3-7a shows the position of caves in the San Andres formation, superimposed on the sequence-stratigraphic framework from Figure 3-5. Figure 3-7b summarizes the distribution of normalized cave feet (cave feet per 1000 logged feet) and average cave height in Cycles 1 and 2 (green) and Cycle 3 (blue) as a function of depth below the Seven Rivers M datum. The spatial distribution of caves in the San Andres is best explained by the island hydrologic model, illustrated in Figure 3-7c for Cycle 3. According to this model, karst was formed by the action of dynamic freshwater lenses beneath low-relief limestone islands during relative fall of the level of Permian seas (Craig 1988). Such meteoric processes under subaerially exposed islands occurred several times during the Permian, leading to the present distribution of caves and other karst features within the San Andres: shifting to the east from Cycle 1 to 3, and progressively decreasing in number and size under the paleo sea levels (Tinker et al. 1995).

3.3 3D Geologic Characterization of Permian Rocks in Tracts 17 and 49

During the year, MIT obtained core descriptions from locations in the vicinity of the study area. These data are not available for presentation to the public, being from locations outside of Tract 17 and 49 (there are no cored wells in the study area). However, core data, although very sparse, present the most reliable information on the lithology and the type of fracturing in Permian rocks in the Yates field. Core data will be input in the interpretation and modeling of the fracture system in the study area.

In addition, MIT obtained data from the mini-StrataModels of Tract 17 and Tract 49, extracted from the field model and further enhanced by Marathon Oil engineers (John Whitney for Tract 17 and Mike Uland for Tract 49). Table 3-2 summarizes information on the StrataModels of the study area.

Table 3-2 StrataModels of Tracts 17 and 49 Area

Location	Number of Geocells	Number of Attributes
Tract 17	1.12 million	28
Tract 49	0.78 million	65

From the mini-StrataModels, MIT obtained structure maps of the contact surfaces between major and minor formation sequences, and complete spatial distribution of the following attributes within the study area: gamma ray response (corrected for uranium in Tract 49), porosity, calcite content, and cave locations. In addition, values of structure curvature and slope were obtained for Tract 49 (not available for Tract 17). These attributes were selected for input into the 3D hierarchical fracture model of the study area for the following reasons: (1) they significantly affect fracture intensity, orientation, and permeability in the Yates field; (2) their spatial distribution is extrapolated from data available from all 1800 logged wells and 118 cores in the field. Many other StrataModel attributes, although closely related to fracturing, are extrapolated throughout the reservoir volume from very sparse data in the geologic model.

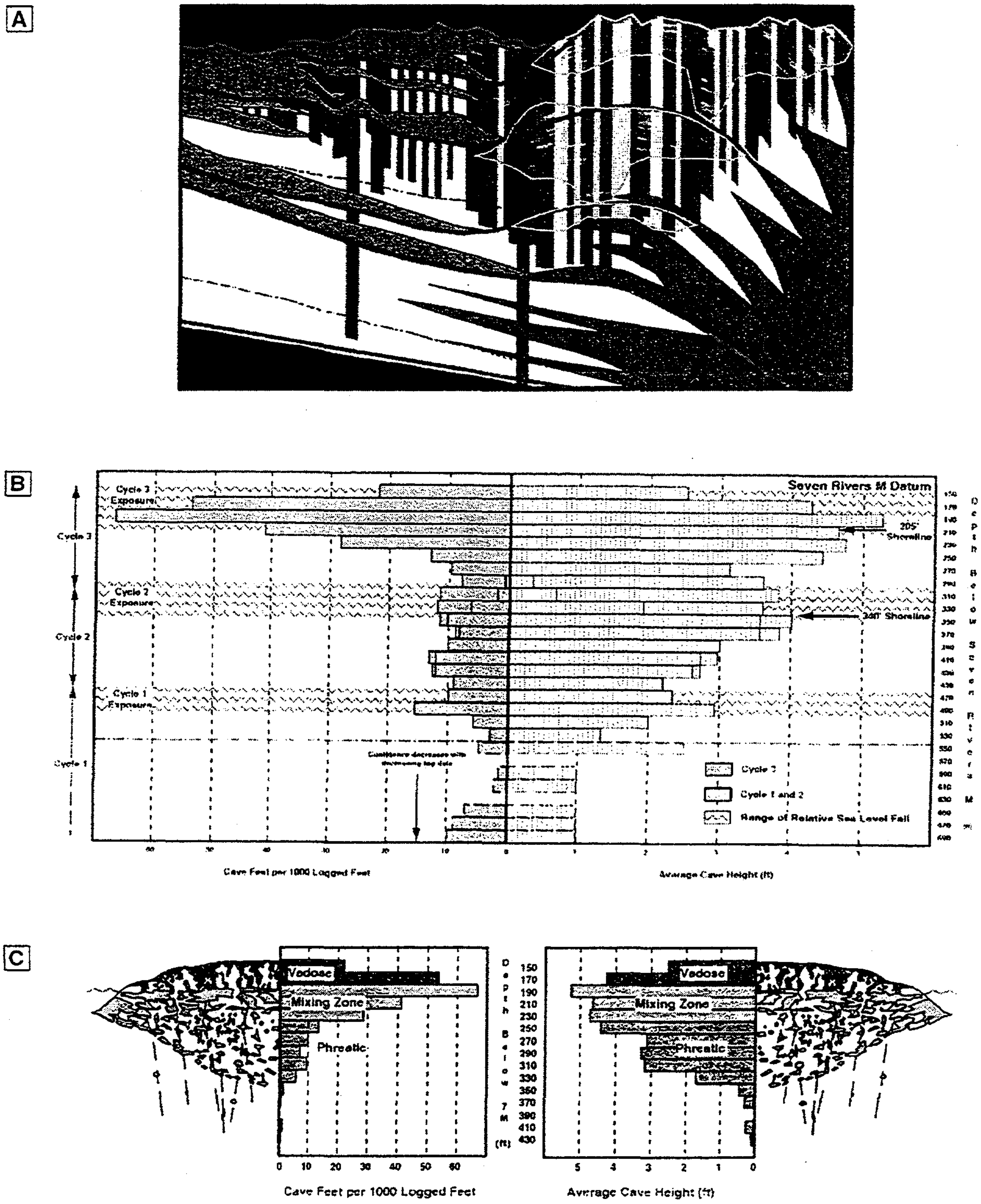

(after Tinker et al. 1995)

FIGURE **3-7**

CAVE DISTRIBUTION IN THE SAN ANDRES FORMATION AND INTERPRETATION BY THE ISLAND HYDROLOGIC MODEL

BDM-NIPER/FRACMAN

3.3.1 Structure and Stratigraphy

Figure 3-8 summarizes how the stratigraphic framework in Tracts 17 and 49 is built. Sequence 1 is the deep ramp. Sequence 18 is the erosional surface of the unconformity, truncating the underlying top San Andres carbonates. Proportionally layered sequences (odd numbers) are carbonate shoals, and onlap sequences (even numbers) are shales.

Figures 3-9 and 3-10 are structural slices along two layers in the San Andres formation in Tract 49: layer 168 is in the top carbonate facies of the San Andres, and layer 15 is within the first carbonate shoal above the ramp, respectively. Color scale in these figures indicates elevation, hot and cold colors representing relative topographic highs and lows, respectively. The holes in Figure 3-9 represent locations where this layer is missing. In these areas Grayburg sediments penetrate deep into the San Andres, filling the topographic karst depressions. The wells which penetrate each layer are indicated in Figure 3-9. Most wells in the Yates field were drilled to relatively shallow depths and do not penetrate the entire San Andres; therefore, properties of the reservoir, extrapolated between wells in the geologic model, are more reliable for the upper San Andres. Only two deep wells penetrate the entire thickness of the San Andres in this version of the full-field StrataModel. Scott Tinker has recently updated the full-field model with data from eight deep wells. Since mini-StrataModels of the study area are not available yet, and because of the time constraints, MIT has started its fracture modeling based on the previous full-field StrataModel.

Sequence No.	Type
1	Independent
2	Onlap
3	Proportional
4	Onlap
5	Proportional
6	Onlap
7	Proportional
8	Onlap
9	Proportional
10	Onlap
11	Proportional
12	Onlap
13	Proportional
14	Onlap
15	Proportional
16	Onlap
17	Proportional
18	Truncated
19	Onlap
20	Proportional
21	Proportional
22	Proportional

Independent

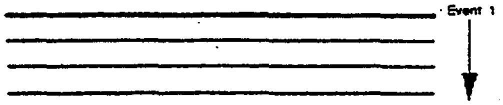

Proportional

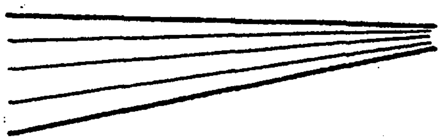

Onlap

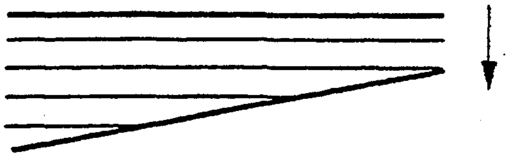

Truncation

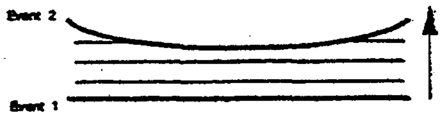

FIGURE **3-8**
YATES FIELD STRATIGRAPHIC FRAMEWORK (TRACTS 17 AND 49)
BDM-NIPER/FRACMAN

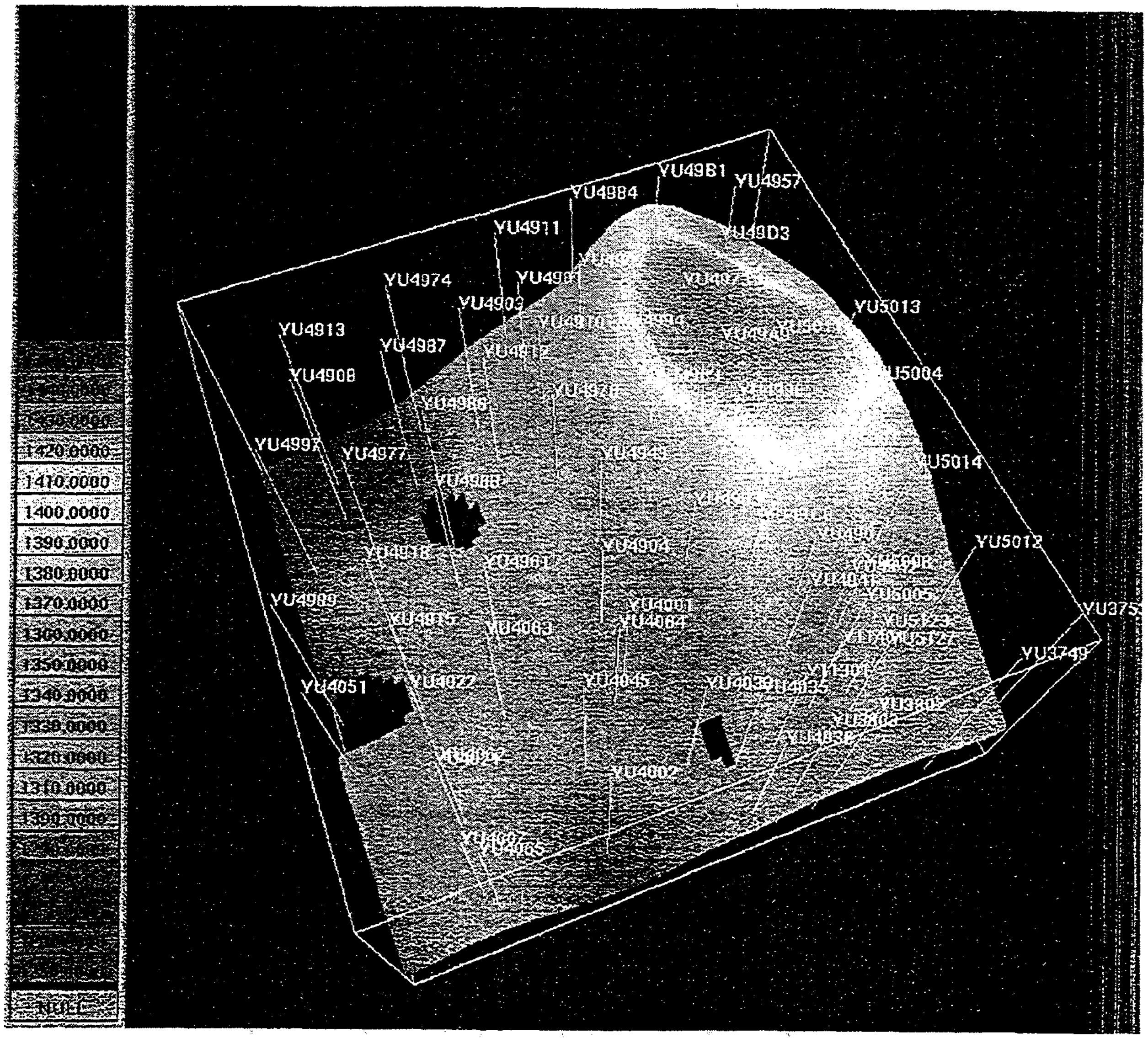

FIGURE **3-9**

STRUCTURAL MAP ALONG A CARBONATE LAYER IN THE UPPER SAN ANDRES IN TRACT 49

BDM-NIPER/FRACMAN

PROJECT NO. 963 1357.521 DRAWING NO. 72166 DATE 4/4/97 DRAWN BY CB

Golder Associates

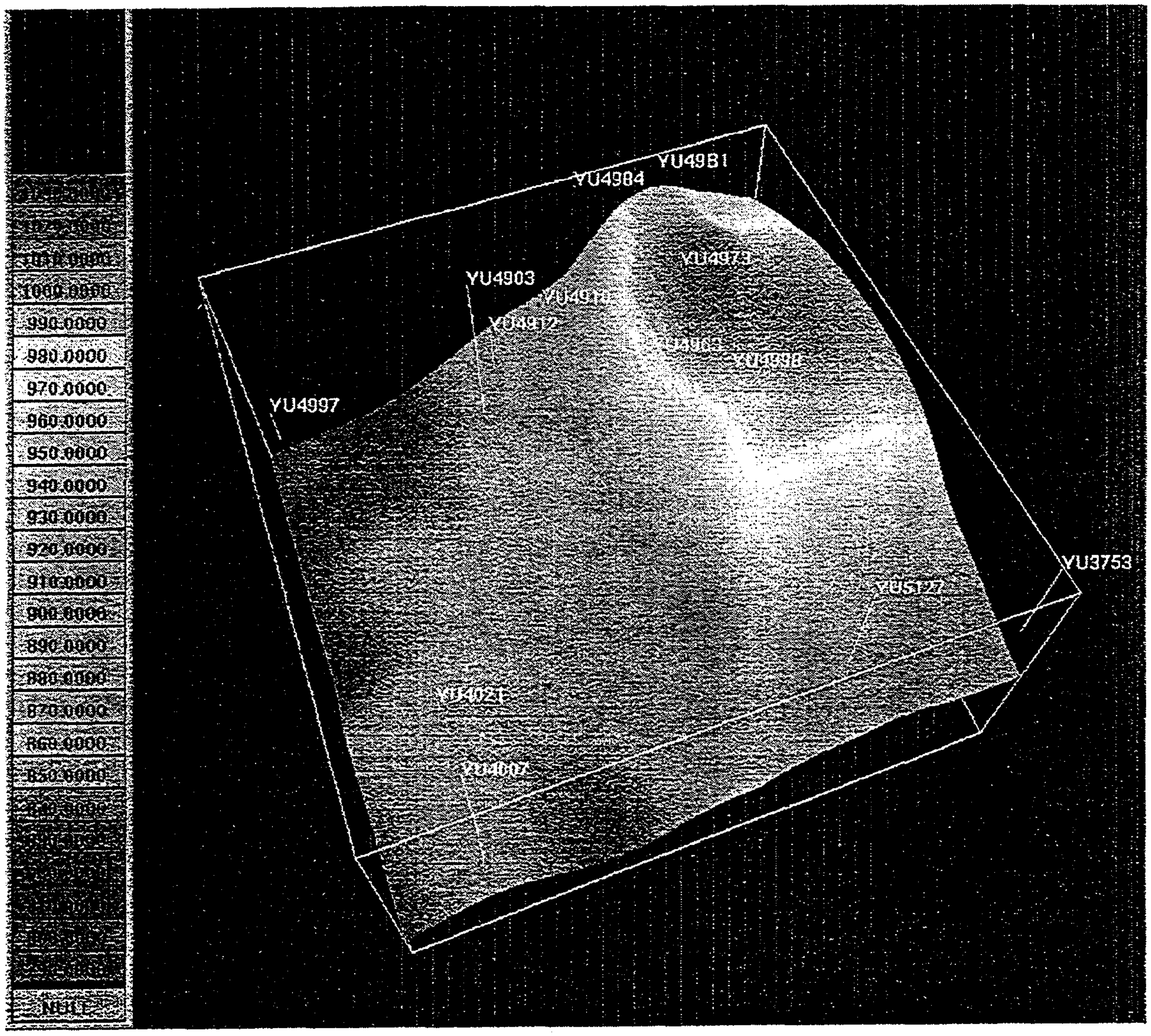

FIGURE **3-10**

STRUCTURAL MAP ALONG A CARBONATE LAYER IN THE LOWER SAN ANDRES IN TRACT 49

BDM-NIPER/FRACMAN

PROJECT NO. 963 1357.521 DRAWING NO. 72167 DATE 4/4/97 DRAWN BY CB

Golder Associates

Figures 3-11 and 3-12 illustrate the stratigraphy in tracts 17 and 49, respectively. The color scale from 1 (dark blue) to 18 (red) represents the depositional sequences from elevation 800 ft above sea level to the San Andres top (the elevation boundaries of the study area). In Figure 3-11 (wells YU1755, left, and YU1701, right) one can see to what extent erosion and compaction have changed the top surface of the San Andres carbonates. The top carbonate shoal facies is almost completely eroded at YU1701, which is the structural peak of the San Andres top in Tract 17. In Figure 3-12 (well YU4063) the formation sequences with even numbers (onlap shale facies) are completely missing. This figure illustrates the fact that in Tract 49 the San Andres lithology is almost entirely composed of dolomite (odd number carbonate shoal sequences in StrataModel).

3.3.2 Shale, Secondary Calcite, and Porosity

In the shale layers on the western side of the field 40 API gamma ray (GR) logs indicate 10% argillaceous content (Tinker and Mruk 1995). In Figure 3-13, the 3D distribution of GR response in Tract 17 is illustrated. Red color indicates locations where GR>20 API. Figure 3-14 illustrates the GR response in Tract 49 (corrected for high values due to uranium). On the same color scale, red is almost absent, once again indicating the clean dolomite in the Tract 49 area.

Figure 3-15 shows the distribution of secondary pore-filling calcite in Tract 49. In the color scale, light blue to red colors indicate the presence of higher percent calcite. Since calcite was precipitated in the pores of horizontal layers at paleo oil-water contacts, the flexure of the top calcite elevation indicates the structural deformation of the San Andres formation after the calcite deposition (Tinker and Mruk 1995).

Figure 3-16 illustrates the porosity distribution in Tract 49. Red color marks porosity higher than 22% of the rock volume. One can see the high porosity of the best reservoir rocks: dolomite packstones and grainstones on the upper east site of the Yates Field. In the deep northeastern end of Tract 49, cold color (blue) indicates the low porosity mudstones of the deep ramp and eastern slope. Figure 3-16 includes porosity due to fractures, accounting for nearly 4% in the San Andres formation in the Yates field (Tinker and Mruk 1995).

3.4 Fracture Interpretation and Modeling

One of the bases for the Hierarchical Fracture Model is the understanding of the fracture genesis mechanisms that have acted regionally in the Permian Basin and locally in the Yates field. Major points in the fracture interpretation and conceptual modeling during the year are summarized below.

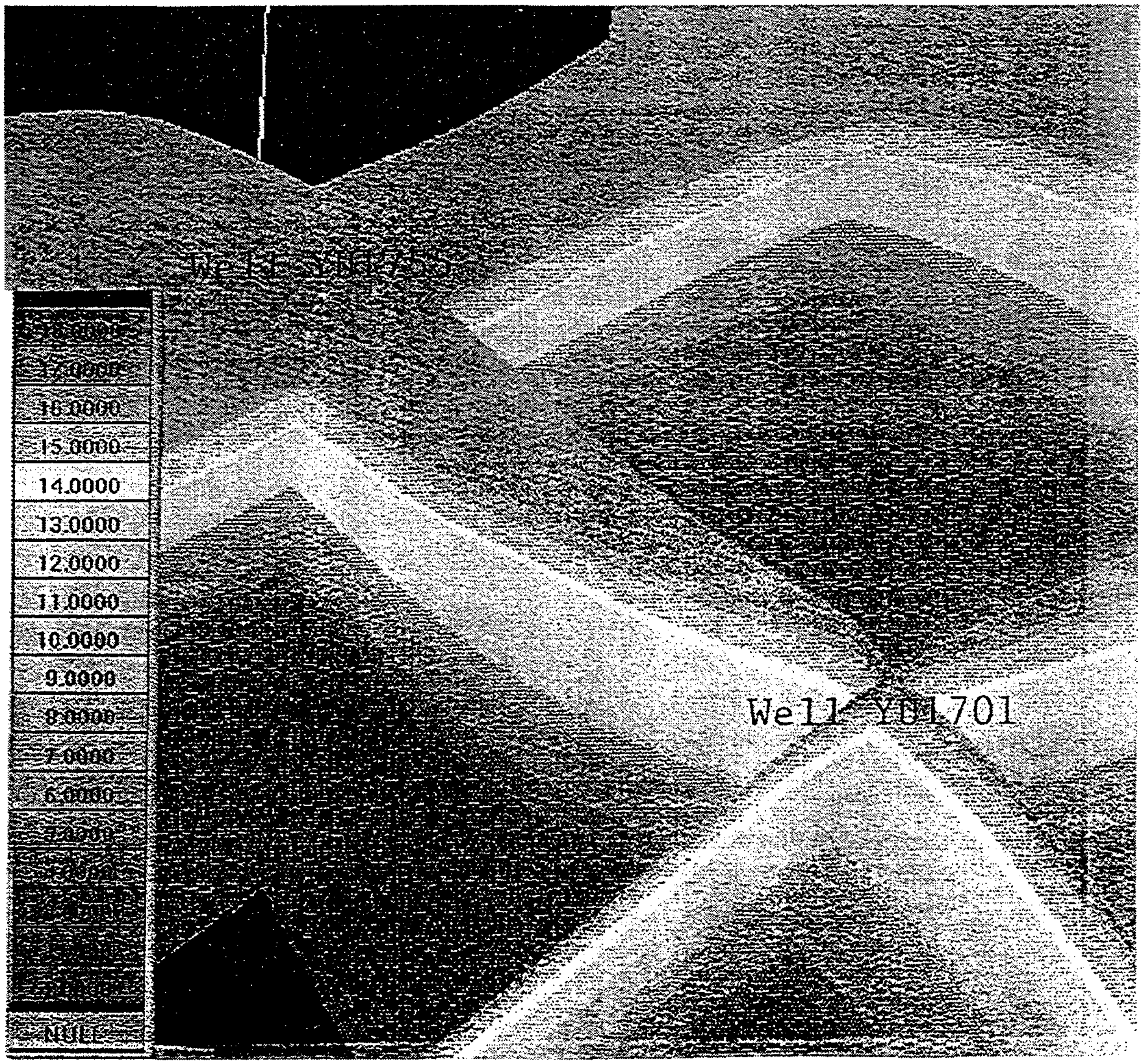

FIGURE **3-11**
FORMATION SEQUENCES IN TRACT 17
BDM-NIPER/FRACMAN

PROJECT NO. 963 1357.521 DRAWING NO. 72168 DATE 4/4/97 DRAWN BY CB

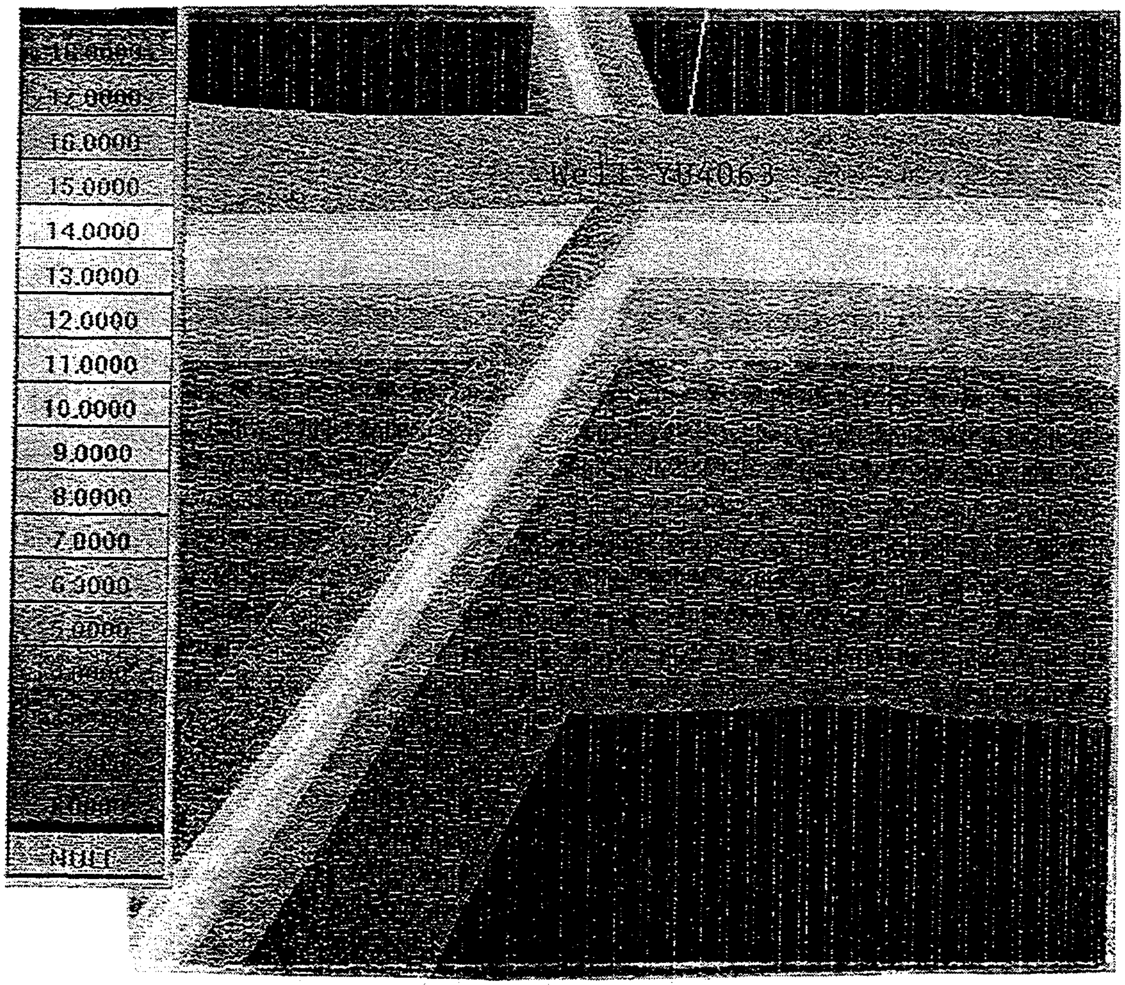

FIGURE **3-12**

FORMATION SEQUENCES IN TRACT 49

BDM-NIPER/FRACMAN

PROJECT NO. 963 1357.521 DRAWING NO. 72169 DATE 4/4/97 DRAWN BY CB

Golder Associates

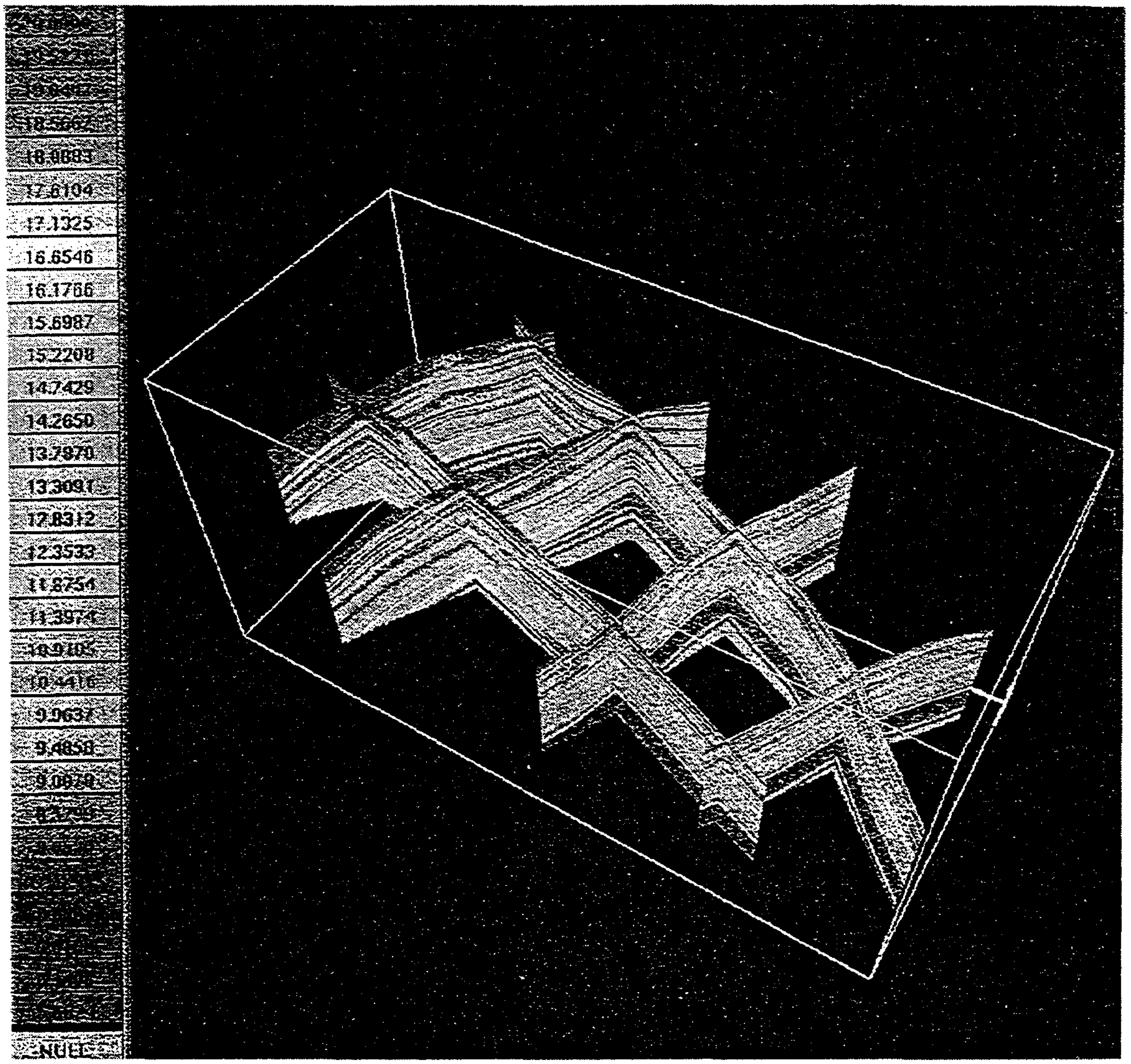

FIGURE **3-13**

SHALE DISTRIBUTION IN TRACT 17

BDM-NIPER/FRACMAN

PROJECT NO. 963 1357.521 DRAWING NO. 72170 DATE 4/4/97 DRAWN BY CB

Golder Associates

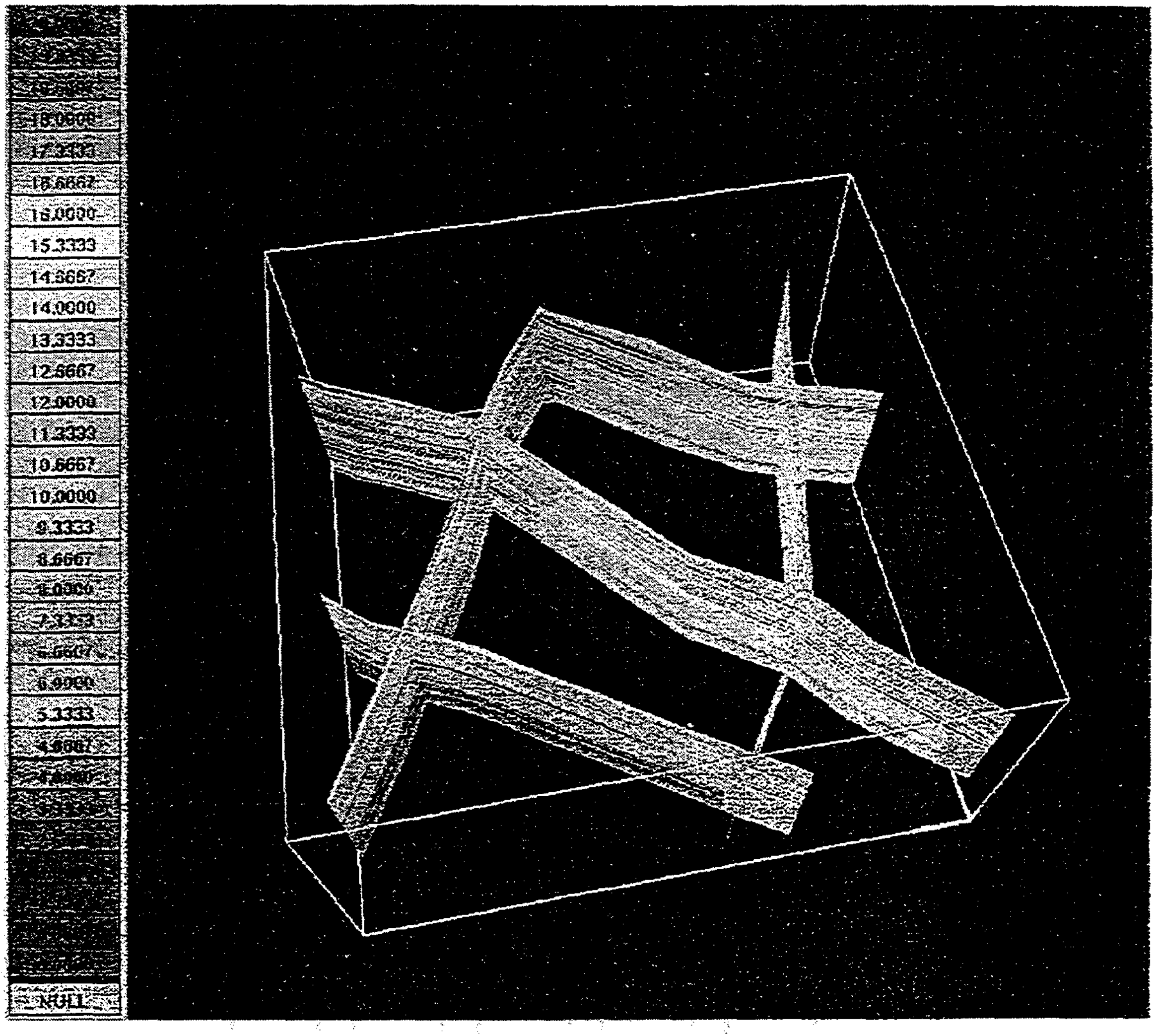

FIGURE **3-14**

SHALE DISTRIBUTION IN TRACT 49

BDM-NIPER/FRACMAN

PROJECT NO. 963 1357.521 DRAWING NO. 72171 DATE 4/4/97 DRAWN BY CB

Golder Associates

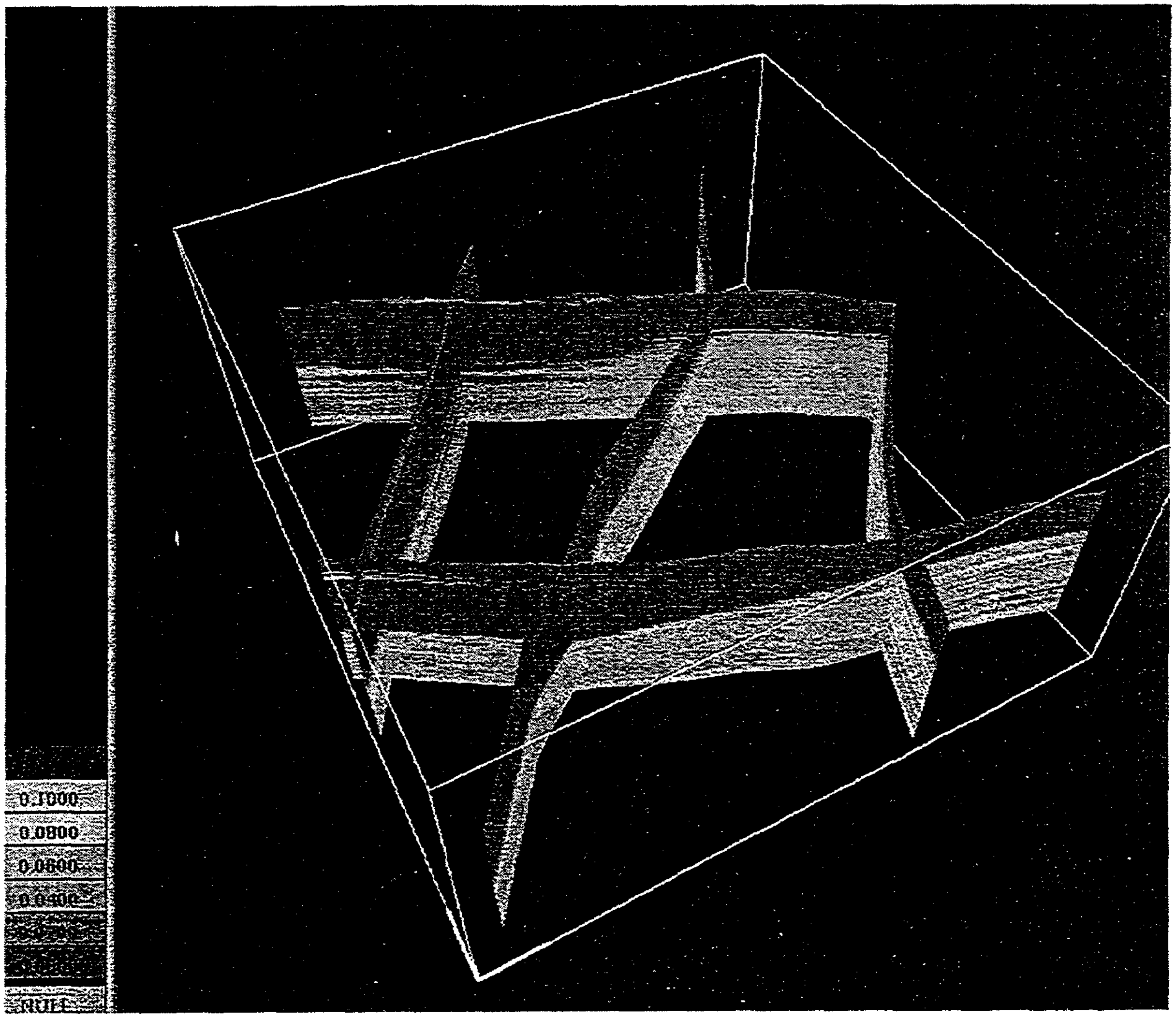

FIGURE **3-15**
CALCITE CONTENT IN TRACT 49
BDM-NIPER/FRACMAN

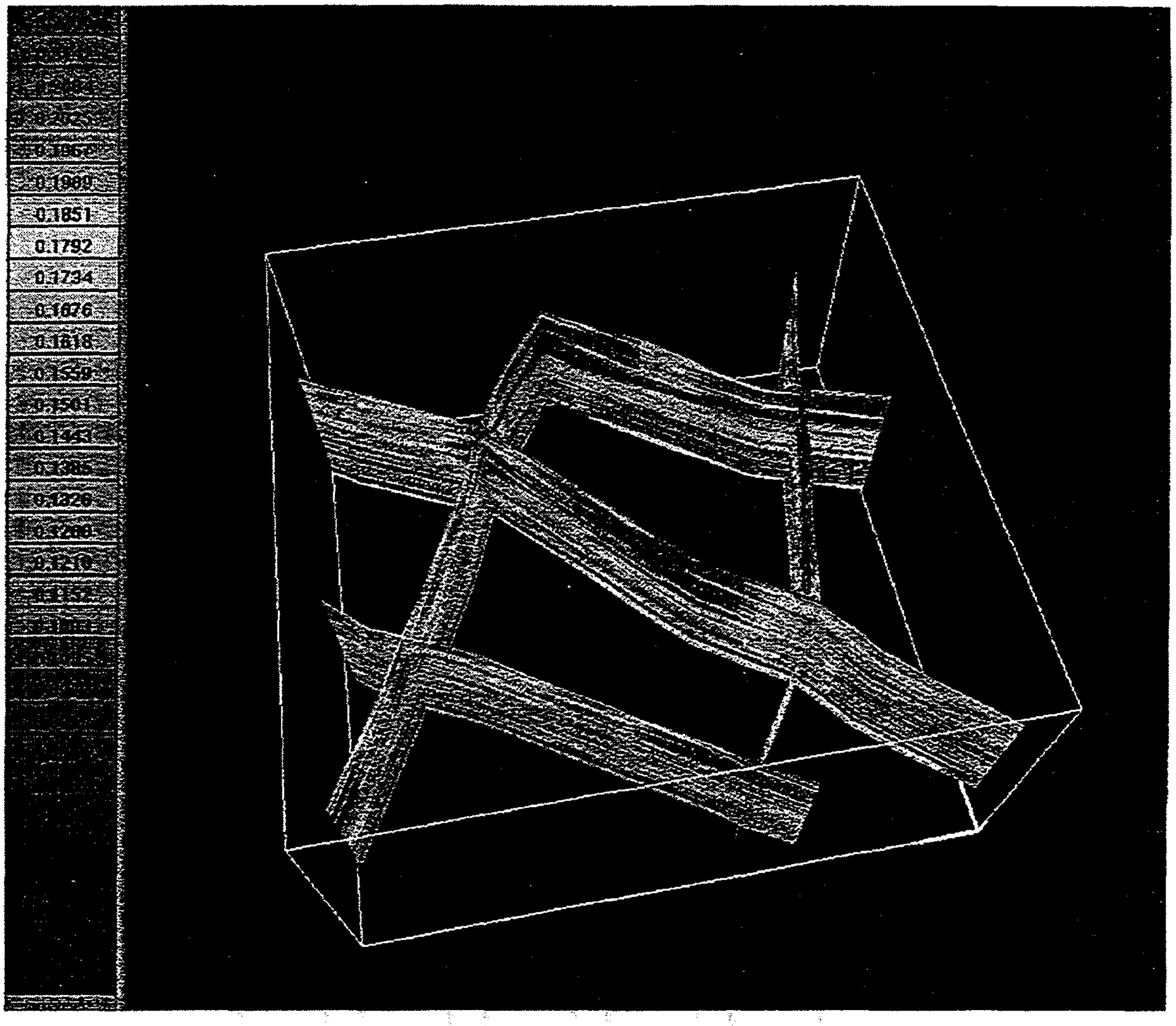

FIGURE **3-16**

POROSITY DISTRIBUTION IN TRACT 49

BDM-NIPER/FRACMAN

PROJECT NO. 963 1357.521 DRAWING NO. 72173 DATE 4/4/97 DRAWN BY CB

Golder Associates

3.4.1 Geologic Mechanisms of Fracturing in the Yates Field

Tinker and Mruk (1995) recognize three major mechanisms for fracture development in the Late Permian rocks of Yates field: (1) a regional mechanism due to activation along pre-existing planes of weakness, defined by a pre-Permian system of folds and faults; (2) a field-scale mechanism associated with the formation of the field anticline; and (3) a local mechanism on the west side of the field caused by differential compaction of shales and carbonate mudstones. Other authors (for example, Stearns and Friedman 1972) also describe regional orthogonal systems of nearly vertical fractures in reservoir sedimentary rocks.

Tinker and Mruk (1995) relate regional fracture patterns to the folds and faults developed during pre-Permian times of tectonic activity (Hills 1970). During the Late Mississippian to Early Pennsylvanian it is thought that compressive stress was approximately east-west. During this time, folds were created striking N23-35°W, and fault systems were created striking N55-80°E, and N50-65°W. In the late Pennsylvanian to Early Permian, it is thought that the regional stress reoriented from east-west to north-south. North-south strike-slip faults were created during this period, including the significant West Platform fault along the west edge of the Central Basin Platform. According to Hills (1970), the asymmetric Late Permian structures developed in relation to the older tectonic structures. Downward movement along the west side of the West Platform fault in the Late Permian (Ochoa) caused relaxation of regional stress. NW/SE striking joints and minor normal faults opened due to several post-Permian events, including Tertiary tilting of the Delaware Basin and Holocene movement along the West Platform fault.

The dominant orientations of the orthogonal regional system are N50°W (along the axis of the Central Basin Platform) and N40°E (Tinker and Mruk, 1995; Curran, Tinker, pers. comm.).

According to Tinker and Mruk (1995), the local fracture system in the Yates Field strikes parallel or perpendicular to the San Andres anticlinal structure. Since the anticlinal structure is related to pre-Permian structures, fracture strikes in the anticline-related fracture system may also have predominantly NE/SW and NW/SE directions. Fracture dips, however, probably differ from the vertical and are related to the structure curvature. The third fracture system, associated with shale compaction in the San Andres on the upper west side of the field, does not have an obvious orientation. Fractures of this system are developed in the brittle dolomites and often terminate at the more ductile shales (Tinker, pers. comm.).

3.4.2 Relation of Fracture Intensity to Rock Properties in the Yates Field

Figure 3-17 illustrates the distribution of fracture intensity (fracture counts) for four major lithology classes (Tinker and Mruk 1995). The fracture intensity in this figure is represented using histogram porosity distributions, which include the porosity due to fractures. Fracture log counts are generally lower and less reliable than fracture core counts. Fracture intensity in the Yates Field is closely related to the lithology and porosity of the Permian rocks. The greatest fracture counts are observed in dolomite mudstone and wackestone, typical for the upper west side of Yates (Tract 17). Fracture counts in dolomite increase up to 8 to 10% porosity, and then decrease with increased porosity. The higher porosity, ductile dolomite packstone and grainstone in the Yates east site (Tract 49) are less fractured than the brittle, low porosity mudstones on the east side. Fracture intensity is much lower in the San Andres shales on the west side, and in the ductile sandy dolomites of the Grayburg.

3.4.3 Parameters of the 3D Hierarchical Model for Tracts 17 and 49: Orientation and Intensity

Figure 3-18 shows an upper hemisphere pole stereoplot of 265 fractures and bedding planes picked from the log image profile at well YU1711. No Terzaghi correction has been applied. Since this well is in Tract 17, fractures may belong to any of the three fracture systems, discussed above. Open and calcite filled fractures at this well have very similar orientation distributions, demonstrated by their rosette plots in Figure 3-19a and 3-19b, respectively. The predominant strike direction is consistent with the major regional NW/SE trend, and is also perpendicular to the San Andres structure at this location. The steeply dipping fractures are perpendicular to the flat sedimentary beds. Fracture orientations in other wells, however, vary much more, indicating that the fracture genesis mechanisms are still require a more reliable interpretation.

The approximate horizontal lineaments of the regional orthogonal features in the Yates Field have been defined by B. Curran from Marathon. According to Tinker and Mruk (1995), regional fractures are confined to discrete linear zones on the west side of the field; whereas, on the east side they broaden and coalesce due to shale compaction.

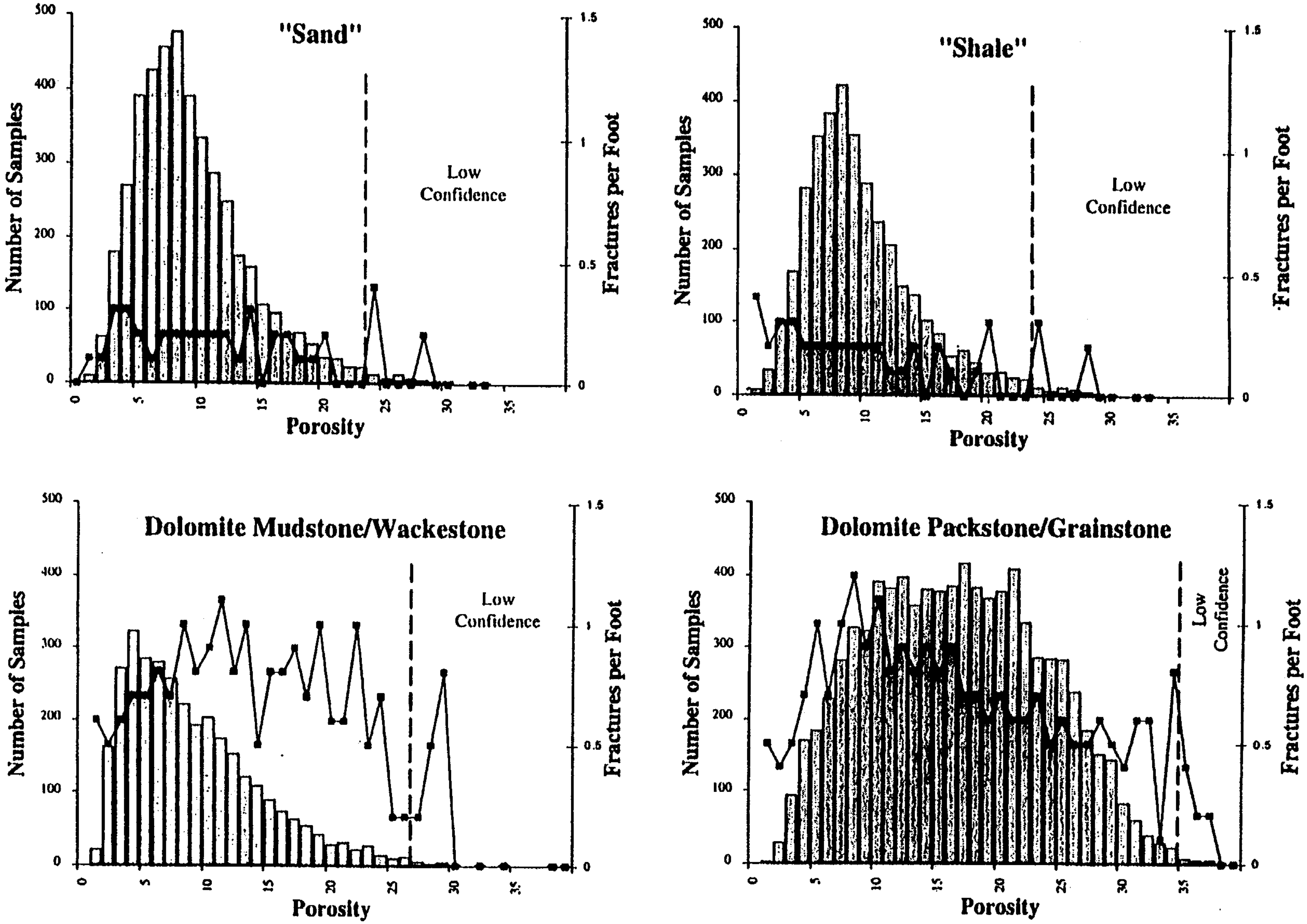

(after Tinker and Mruk 1995)

FIGURE **3-17**

FRACTURE INTENSITY IN FOUR PERMIAN LITHOLOGIES IN THE YATES FIELD

BDM-NIPER/FRACMAN

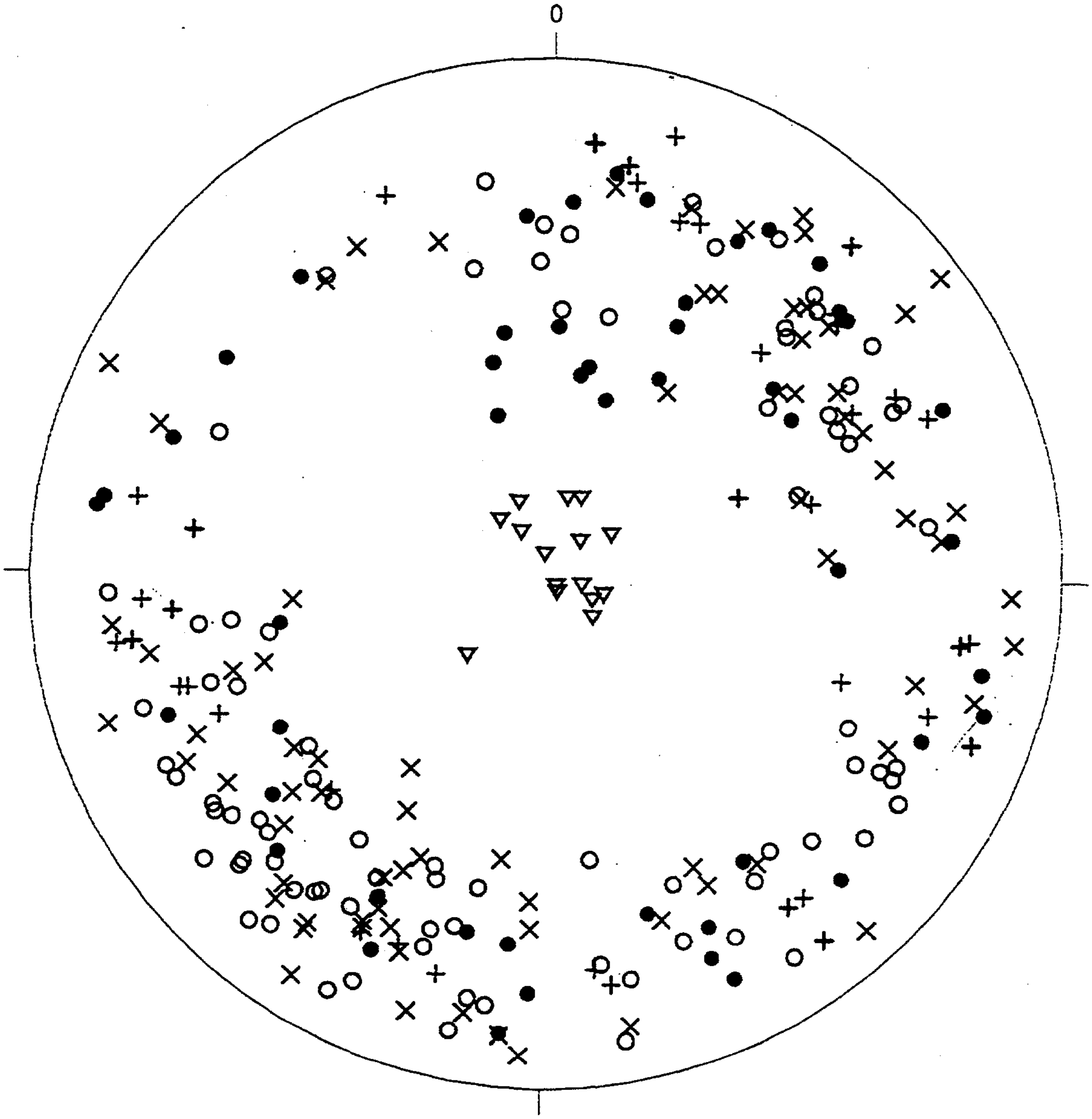

× Open fractures (observed on <5 pads: thin)
\+ Open fractures (observed on at least 5 pads)
▽ Bedding boundaries
○ Cacite filled fractures (100% mineralization)
● Calcite filled fractures (healed)

Num total: 265

FIGURE **3-18**
STEREOPLOT OF POLES TO FRACTURES AT THE LOGGED WELL YU1711
BDM-NIPER/FRACMAN

A

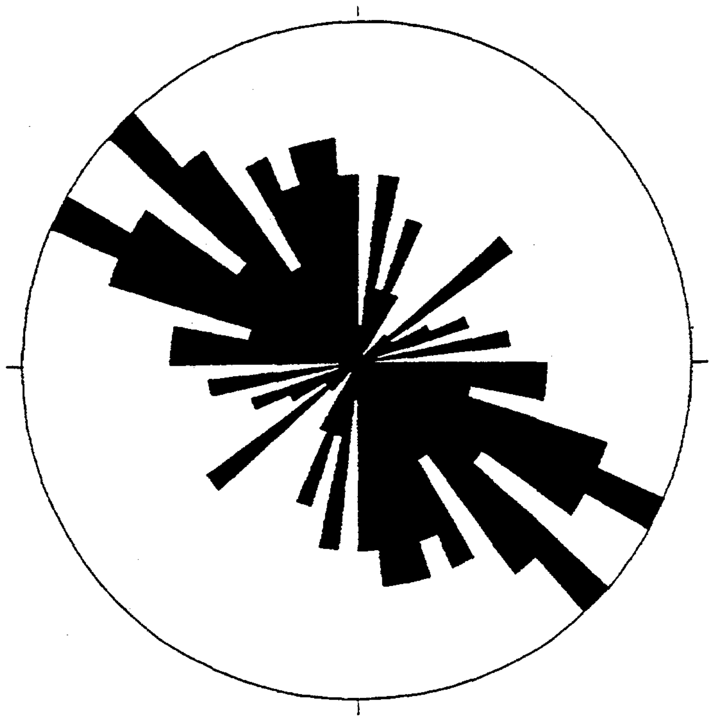

YU1711 Open Fractures

Total Number: 117

Strike Direction: 12° classes

B

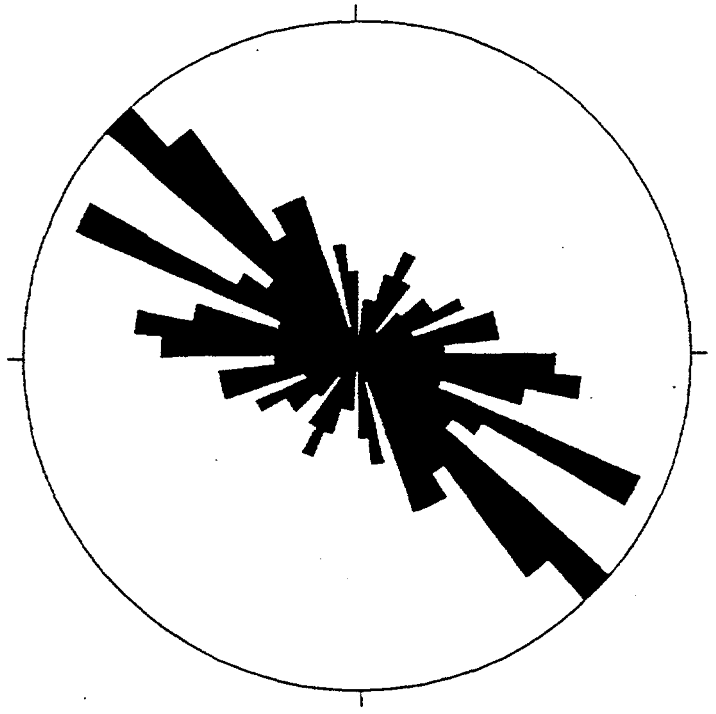

YU1711 Calcite Filled Fractures

Total Number: 133

Strike Direction: 12° classes

FIGURE **3-19**

ROSE DIAGRAMS OF FRACTURE STRIKES AT WELL YU1711

BDM-NIPER/FRACMAN

PROJECT NO. 963 1357.521 DRAWING NO. 72177 DATE 4/11/97 DRAWN BY CB

Golder Associates

The orientations of local fractures can be reproduced stochastically in relation to the regional field structure. Figure 3-20a shows the top surface of the San Andres formation in Tracts 17 and 49. Second and third order quadratic surfaces are fitted with correlation coefficients higher than 0.92 to the top of the San Andres in Tracts 17 and 49 (Figure 3-20b). These plots illustrate two major points:

- The top of the San Andres is quite flat: average dips are near 3 degrees. It may be that the formation of the anticline rotated older fractures, rather than causing the development of a new fracture system.
- It is better to relate fracture orientations to the internal structures in the San Andres, such as the clinoformal geometries of the carbonate shoals. The San Andres top is an erosional unconformity; therefore, its shape does not reflect the structural process that also formed the local fracture system.

Local fracture intensity (ratio of fractured and intact areas on potential fracture planes) will be modeled stochastically as a function of rock matrix porosity and lithology. For compaction-related fracture sets in the dolomite on the upper west side of the field, a fracture termination percent will be defined at the shale contacts.

The earlier 3D Hierarchical Fracture Model (Ivanova 1995; Ivanova et al. 1995) has been enhanced with procedures which allow greater flexibility for defining input parameters. For example, during fracture modeling of the San Andres formation in the Yates Field, fracture intensity will be defined for the first time as a function of rock matrix porosity. Other geometric procedures are currently being developed. The most important new concept is the definition of a varying mean fracture orientation. In existing stochastic models, including the old version of the 3D hierarchical model, the mean orientation is usually fixed and deviations from the mean are described by a complex mathematical expression. Orientations related to curved structures (folds) can be better modeled by a mean orientation, defined simply as a normal vector to the structure surface at any point, and a simple variation. The new enhancements of the 3D Hierarchical model add to its capability to realistically represent complex fracture networks in natural rocks.

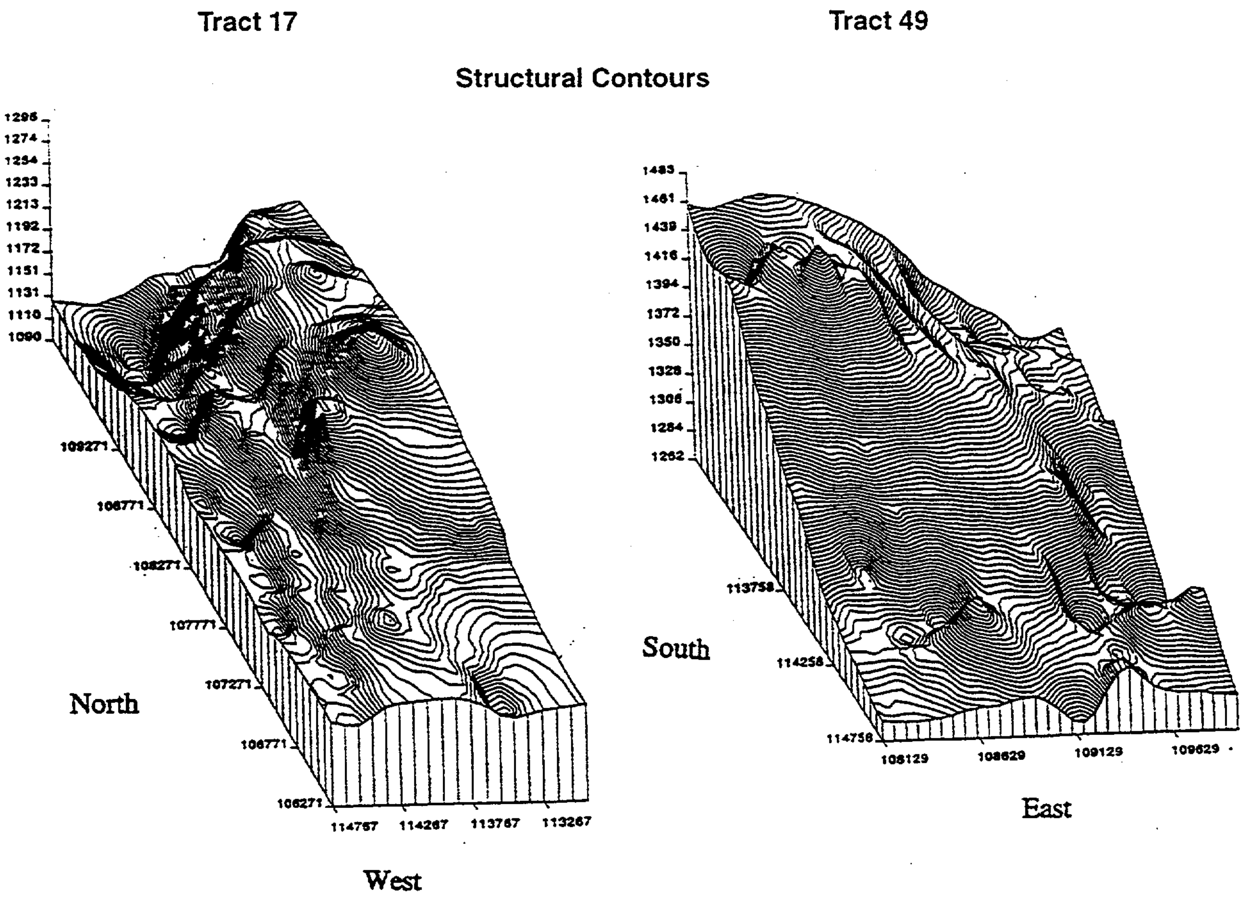

Tract 17

Tract 49

Structural Contours

Fitted Trend Surfaces

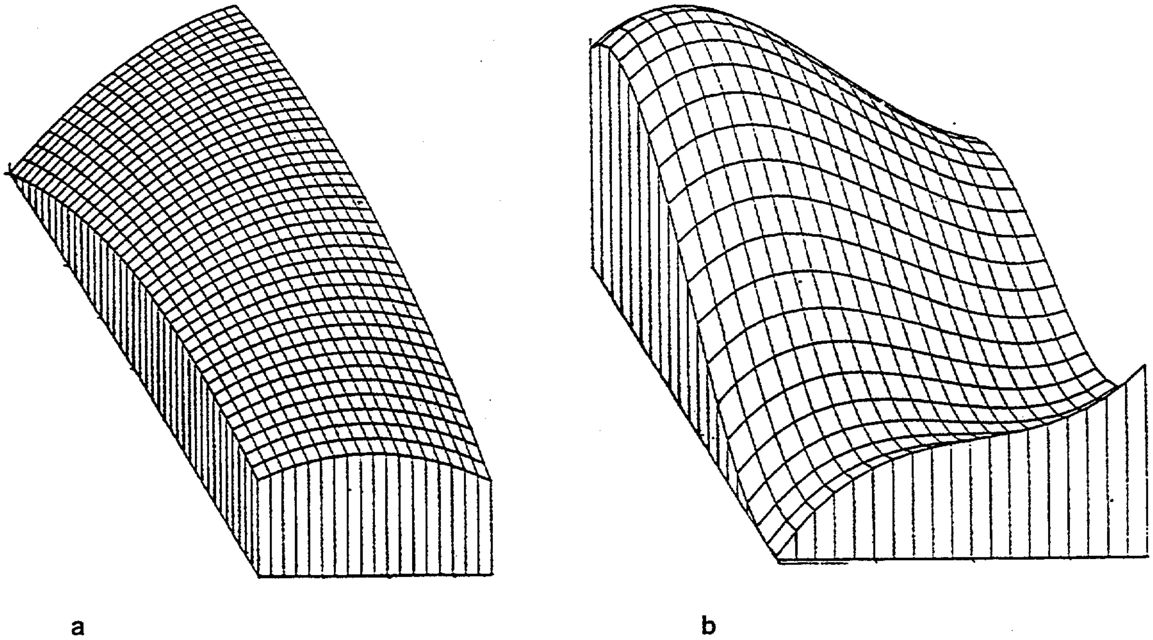

FIGURE **3-20**
STRUCTURAL CONTOURS ON THE TOP OF THE SAN ANDRES IN TRACTS 17 AND 49
BDM-NIPER/FRACMAN

4. TASK 1.3: RESERVOIR COMPARTMENTALIZATION

4.1 Task 1.3.1 Improved Matrix Block Size Estimation

4.1.1 Task 1.3.1 Implementation of Block Size Algorithms

During the year, a range of new algorithms were implemented and evaluated for estimation of rock block volume. The assessment of rock block volume is essential for efficient development and production of fractured reservoirs.

4.1.1.1 Alternative Block Size Algorithms

Reservoir simulation in dual porosity systems requires calculation of several parameters related to matrix block shape and size. The fracture surface area of matrix blocks within a cell influences the rate and quantity of fluids that can move between the matrix and the fracture system. The Z-dimension of matrix blocks influences gravity drainage mechanisms. The shape of the matrix blocks influences the choice of sugar cube, matchstick or slab idealization. A realistic description of block size and shape that can be implemented in existing dual porosity simulators will benefit not only the thermal simulation for TAGS processes, but also non-thermal simulation of injection or production in fractured reservoirs. Two algorithms have been developed and tested to compute matrix block shape and size. Both are based on geologically realistic three-dimensional fracture systems, and provide output in the form required by conventional dual-porosity simulators.

The first algorithm is a fast computational method to compute blocks based upon fracture spacing distributions in several directions. Its main advantage is the speed of calculation. Its disadvantage is that it assumes that block dimensions are uncorrelated. This algorithm is referred to as the *multidirectional spacing distribution algorithm.*

The second algorithm is based upon graph theory. Because the convex hull of points lying on fractures bounding or partially bounding a matrix block is computed, this algorithm is referred to as the *convex hull algorithm.*

4.1.1.1.1 Multi-Directional Spacing Distribution Algorithm

Figure 4-1 illustrates the multi-directional spacing (MDS) algorithm. For each realization of the discrete fracture model, a series of randomly-located lines in user-specified directions are generated. The location of fractures intersected by each line is recorded. This leads to a spacing frequency distribution in several directions. Typically, the directions include the vertical direction, in order to calculate the vertical dimension of blocks for gravity drainage considerations, and in two or three orthogonal directions that relate to simulator grid layering geometry and the fracture system.

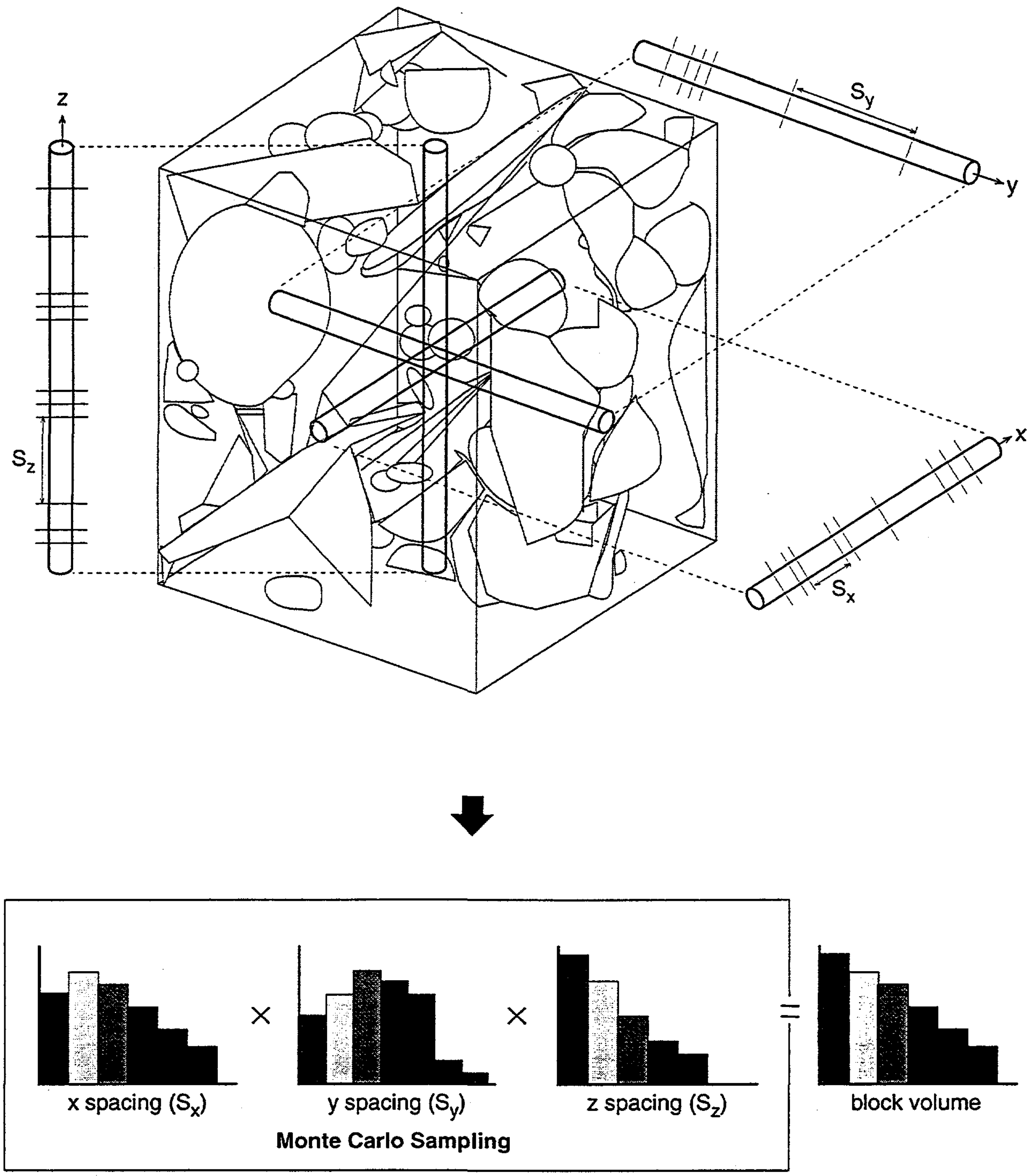

FIGURE **4-1**

MULTI-DIRECTIONAL SPACING ALGORITHM

BDM-NIPER/FRACMAN

PROJECT NO. 963 1357.521 DRAWING NO. 72179 DATE 3/28/97 DRAWN BY CB

Golder Associates

The spacing probability distributions are multiplied together using Monte Carlo sampling techniques to produce a frequency distribution of block volumes and surface areas. This is carried out by selecting X, Y and Z spacing values at random with selection probability proportional to their frequency, and multiplying them together to create a prismatic block.

The volume of the block for the i-th Monte Carlo computation is the product of the spacing values:

$$Volume_i = X_i * Y_i * Z_i \tag{4-1}$$

The surface area of the i-th block is given by:

$$SA_i = 2*(X_i * Y_i + Z_i * Y_i + X_i * Z_i) \tag{4-2}$$

The block shape is given by the ratios of the mean X, Y and Z spacings:

$$\overline{X}:\overline{Y}:\overline{Z} \tag{4-3}$$

The vertical dimension of the blocks is taken as the mean value of the Z spacing distribution:

$$Vertical\ Dimension = \overline{Z} \tag{4-4}$$

4.1.1.1.2 Convex Hull Algorithm

The convex hull (CH) algorithm is more computationally intensive, but measures the actual dimensions of the blocks, rather than reconstructing blocks stochastically from spacing frequencies. Thus, any correlations among block dimensions or non-prismatic block shapes do not present problems. The algorithm's accuracy is governed by two factors: whether in fact the matrix blocks are convex; and how many points are required to accurately characterize the convex block. The algorithm as implemented allows the user to specify the number of points for characterizing the convex block, but computation time increases as the number of points increases.

Figure 4-2 illustrates the CH algorithm. From a random point within a discrete fracture model, lines are projected out in user-specified directions until they intersect a fracture. The intersection point coordinates for all of the line intersections constitutes a sample of the matrix block. As is shown in the 2D illustration (Figure 4-2a), some of these intersection points may not all be on the block exterior. Next, a convex hull (Figure 4-2b) is calculated for the set of points. A convex hull has the property that it includes all of the points, and that it is convex. In two dimensions, the hull is a convex polygon. A convex polygon has the property that any line joining two arbitrary points within or on the boundaries of the polygon lies entirely on the boundary or in the interior of the polygon. In practice, this means that the polygon has no "holes" or embayments, and it is a single polygon, not several isolated ones. In three dimensions, the polygon is a polyhedron.

It is a simple matter to compute the volume and the surface area of the convex hull. The vertical dimension of the matrix block is taken to be the difference between the minimum and maximum Z coordinate of the convex hull. The shape of the matrix blocks approximated as convex hulls can be determined by visually displaying the hulls, or by computing the aspect ratios for the X, Y and Z directions from the hull coordinates.

The convex blocks to be analyzed are identified by projecting rays from randomly selected points within the model. Since a larger block has a proportionately greater probability of having a randomly located point within it, the algorithm overestimates the number of large blocks and underestimates the number of small blocks, particularly if multiple points are selected in the same block. The current algorithm checks to see if each new block has previously been estimated, and if so, it retains the block with the larger volume. This is because a convex hull estimate of a convex block is always equal to or less than the volume of the actual block.

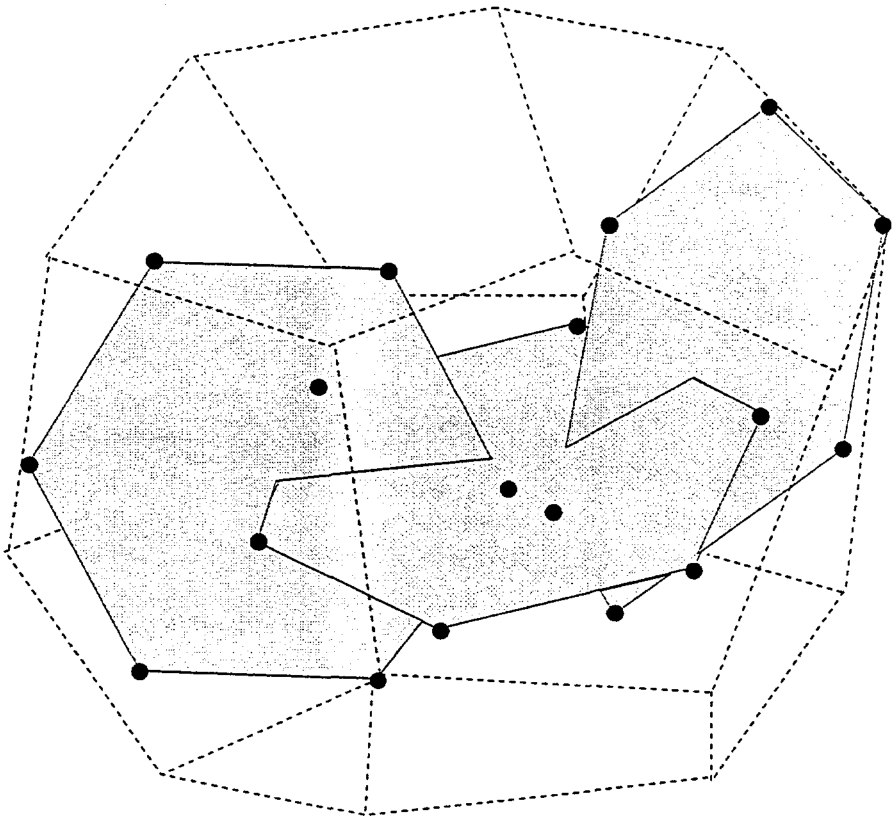

(a) Points

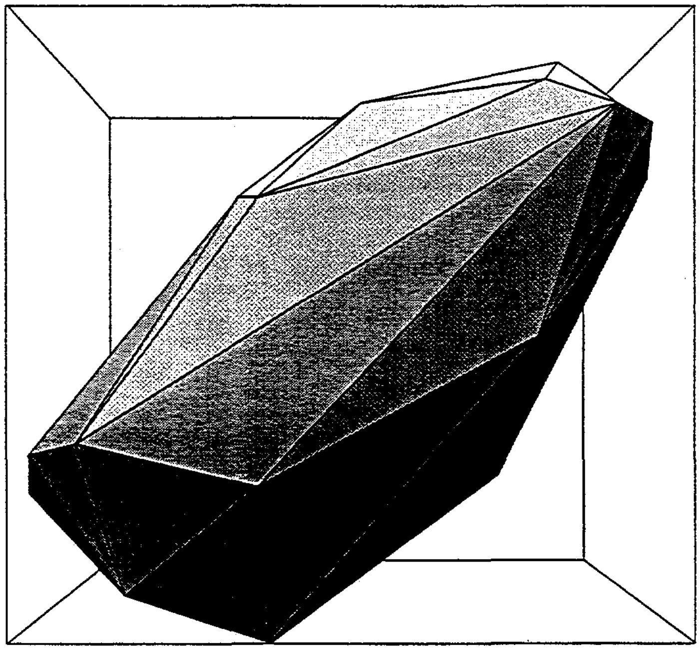

(b) Convex Hull

FIGURE **4-2**

COMPLEX HULL BLOCK SIZE ALGORITHM

BDM-NIPER/FRACMAN

4.1.1.2 Block Scale Algorithm Test Cases

Three test cases were devised to assess how well these two algorithms correctly estimated the matrix block size distribution. Cases 1 and 2, which are not geologically realistic, serve as verification and evaluation cases for the algorithms. It is not possible to calculate the true block volume distribution for Case 3, but this case illustrates how the algorithms might be applied in more realistic DFN models. Case 1 (Figure 4-3a) consists of a 202 m by 202 m by 202 m cube dissected into 8000 10 m cubes. Each cube is a matrix block, and is completely bounded by fractures. Case 2 (Figure 4-3b) consists of slabs and cubes, but of varying sizes and with dimensions that are partially correlated. The distribution of block volumes is bi-modal. These two test cases are geologically unrealistic, but clearly illustrate how well the algorithms perform. Case 3 (Figure 4-3c) is more geologically realistic. In this model, fractures do not completely isolate blocks. There are three sets in approximately three orthogonal orientations, much like the fracture pattern that develops in carbonates or other layered rocks.

Table 4-1 summarizes the values for Z dimension, specific surface area, P_{32} and volume for the three test cases. Both the specific surface area and P_{32} quantify how much fracture surface area per volume of rock there is in the model. The specific surface area is calculated by summing all of the surface area for all of the identified blocks, and dividing by the total volume. In test cases 1 and 2, this means that almost every fracture will be part of two blocks. P_{32} on the other hand, is the total amount of fracture area divided by the volume of rock, and is independent as to whether these fractures form blocks. For test cases 1 and 2, the specific fracture surface area should be approximately twice the value of P_{32}. For simulation purposes, it is necessary to use the surface area that relates to the matrix block idealization, rather than the absolute P_{32} value.

Table 4-1 Block Size Algorithm Test Case Expected Values

Test Case	Z Dimension (m)	Surface Area/Rock Volume (m^2/m^3)	P32 (m^2/m^3)	Volume (m^3)
Case 1	10.0	0.6	0.312	1,000
Case 2	mean = 22.22	0.27	0.146	mean = 10,974
Case 3	not calculated	not calculated	0.112	not calculated

Table 4-2 presents the results for MDS and CH analysis of Test Cases 1, 2, and 3. The MDS algorithm matches the correct block dimensions exactly for Case 1 when the sampling directions were chosen to be perpendicular to the block faces. In many situations involving fracturing of layered rocks, principal fracture orientations should be parallel and perpendicular to bedding, so it may be possible to choose sampling orientations that give very good matrix block volume estimates. The MDS algorithm produces reasonable estimates for Case 2, but has a tendency to somewhat overestimate the number of very small matrix blocks. Nevertheless, the MDS algorithm reproduces the shape and bimodality of the correct distribution reasonably well (Figure 4-4).

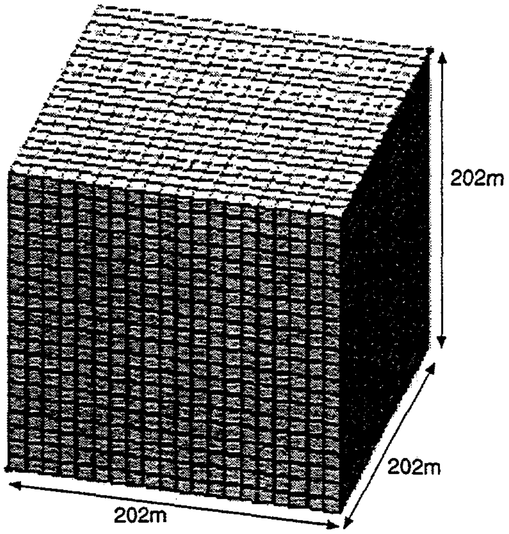

(a) Test Case 1

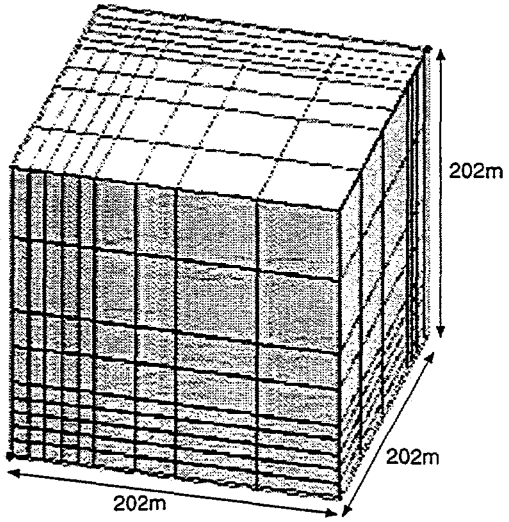

(b) Test Case 2

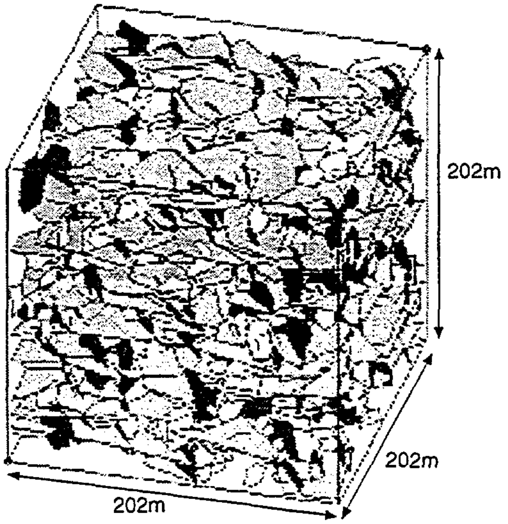

(c) Test Case 3

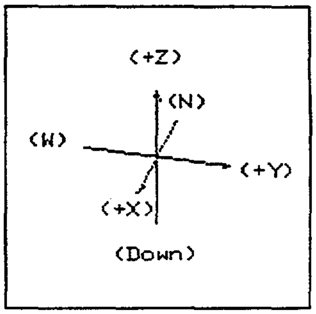

FIGURE **4-3**
BLOCK SIZE TEST CASES
BDM-NIPER/FRACMAN

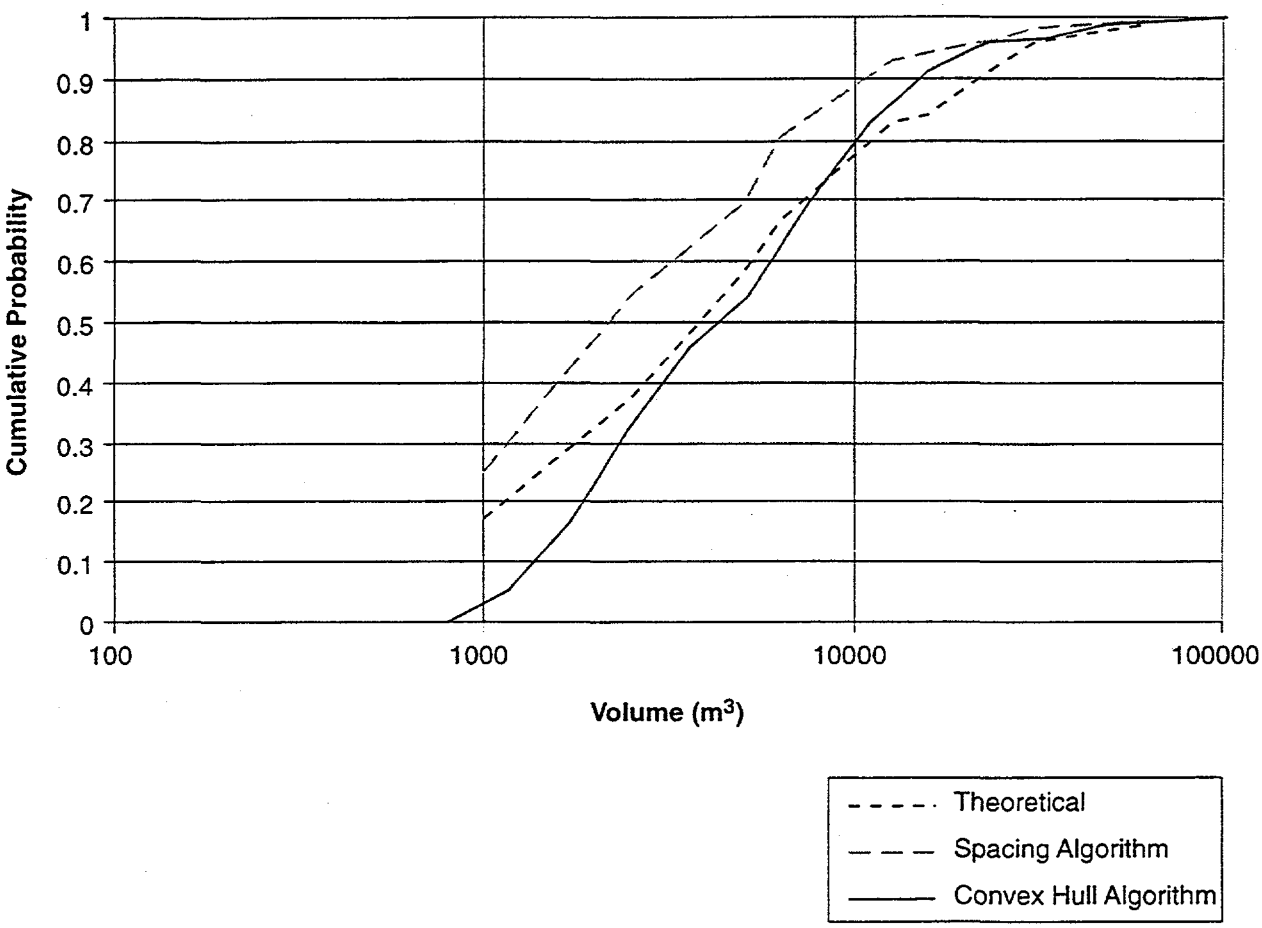

FIGURE **4-4**

BLOCK SIZE DISTRIBUTION FOR TEST CASE 2

BDM-NIPER/FRACMAN

Table 4-2 MDS and CH Block Size Algorithms

TEST CASE	Z Dimension (m)	Surface Area/Rock Volume (m^2/m^3)	P_{32} (m^2/m^3)	Volume
Case 1 - MDS	10.0 (constant)	0.60	0.312	1,000 (constant)
Case 1 - CH	14.1 (mean)	0.63	0.312	823 (mean)
Case 2 - MDS	23.4 (mean)	0.25	0.146	6,653 (mean)
Case 2 - CH	29.3 (mean)	0.32	0.146	9,154 (mean)
Case 3 - MDS	11.1 (mean)	0.36	0.112	5,484 (mean)
Case 3 - CH	43.0 (mean)	0.36	0.112	10,642 (mean)

The CH algorithm provides better results for Case 2 and worse results for Case 1. For Case 1, most convex hulls will contain a smaller volume than the cubes in which they are calculated. This is due to the fact that the convex hull is based upon a finite number of points lying on the edge surfaces of the cubes. This means that corners of the cube may be effectively "trimmed off" by calculating the hull, which in turns leads to an underestimate of block volumes. For Case 2, the median and mean block volumes are more accurately estimated by the CH algorithm than by the MDS algorithm. The inherent ability of the CH algorithm to account for the correlation in block dimensions appears to offset the tendency to underestimate the volume of cubical matrix blocks.

Case 3 is a more realistic DFN model. As horizontal and vertical cross-sections through one DFN model realization illustrate (Figure 4-5), blocks are not completely isolated on all faces by fractures. There are blocks of many different sizes, but in horizontal cross-section, the blocks are on the order of 40 m, and in vertical cross-section blocks are on the order of 10 m.

In summary, the three test cases suggest that both the MDS and CH algorithms provide reliable and consistent estimates of fracture surface area, at least for simple fracture geometries. The CH algorithm appears to provide better estimates of the mean volume of matrix blocks when block dimensions are partially correlated. Since jointing in many sedimentary rocks is characterized by pseudo-periodic spacings (e.g. ,La Pointe and Hudson, 1985), it may be preferable to use the CH algorithm to estimate block volumes. On the other hand, the geometric construction of a convex hull from a sparse data set creates hulls with slightly greater average Z-dimensions than the MDS algorithm. In both test cases 1 and 2 the MDS algorithm provided more accurate estimates of the Z-dimension. Thus, both algorithms have proven useful and necessary to provide estimates of matrix block parameters, and neither alone is completely satisfactory.

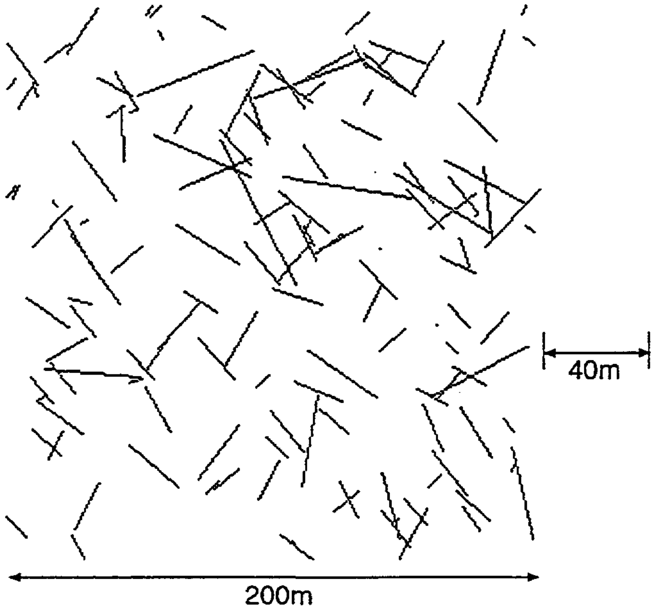

(a) Horizontal Cross Section

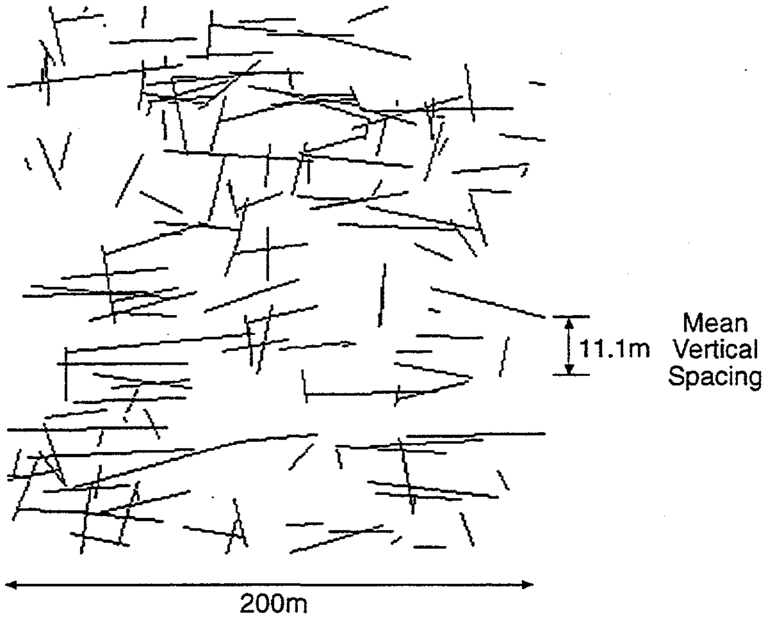

(b) Vertical Cross Section

FIGURE **4-5**
CROSS SECTION THROUGH TEST CASE 3
BDM-NIPER/FRACMAN

4.2 Task 1.3.2 Drainage Volume Analysis

4.2.1 Task 1.3.2 Drainage Volume Analysis

Tributary drainage volume is related to both block size and compartmentalization. Tributary drainage volume is the estimated volume of matrix that a fracture system intersected by a well or perforated zone can access. In those reservoirs in which the matrix provides the storage, and the fracture system the reservoir permeability, the amount of hydrocarbon that can be produced is a function of the fracture network connectivity and geometry.

Nonetheless, the mobilization and drainage of oil due to pressure depletion occurs in many fractured reservoirs. Improving forecasts of the potential volume of reservoir that a well can drain through the connected fracture system is useful for planning field development in many fractured reservoirs.

4.2.1.1.1 Algorithm

The algorithm developed to compute the tributary drainage volume is divided into two steps:

Step 1. Identify the fracture networks connected to a well or perforated zone of interest

Step 2. Estimate the volume of matrix within that could be produced

Step 1 utilizes the algorithm developed for compartmentalization analysis, as described in Section 5.4 below. As in the compartmentalization algorithms, it is possible to process the fractures in a DFN model to identify those fractures which are connected to a well or a portion of a well.

There are different ways that might be used to accomplish Step 2. If the fracture network were very dense, then the volume of the matrix accessed by the fracture network will be closely approximated by the volume of the convex hull enclosing the network. In essence, this means that the compartment volume is equal to the tributary volume. However, there is no reason to expect that all fracture networks will be sufficiently dense that the convex hull method produces the best estimate. In less dense fracture networks, some or maybe a significant portion of the volume inside the convex hull will be too far from any of the fractures to be easily produced (Figure 4-6).

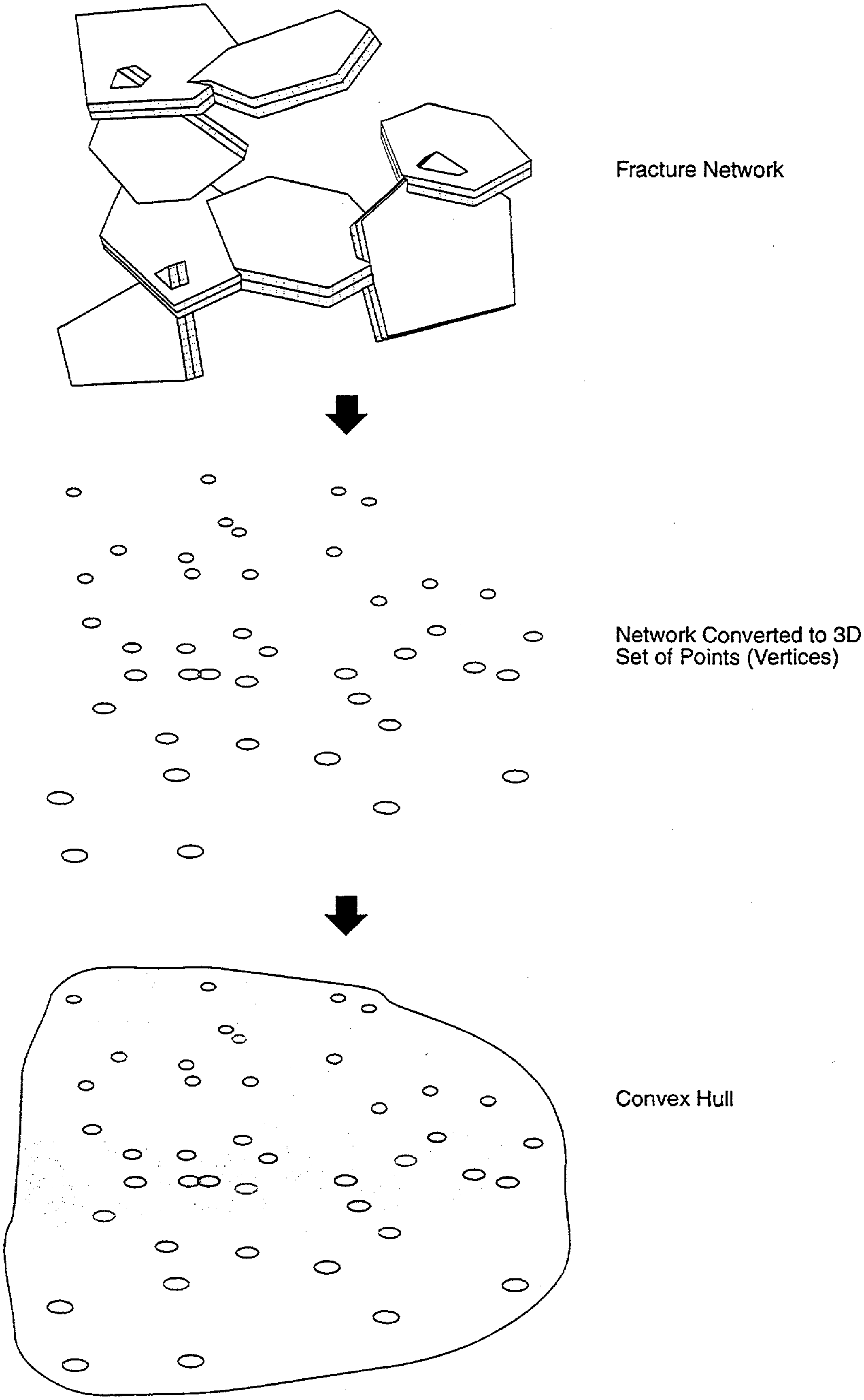

FIGURE **4-6**
TRIBUTARY DRAINAGE VOLUME BY CONVEX HULL
BDM-NIPER/FRACMAN

PROJECT NO. 963 1357.521 DRAWING NO. 69420 DATE 4/11/97 DRAWN BY CB

Golder Associates

A better estimate of tributary drainage volume would not include matrix that might not be efficiently produced through pressure depletion drainage. Figure 4-7 illustrates a possible alternative algorithm to achieve this. In this algorithm, each fracture is circumscribed by a prism that is calculated from the area of the fracture and the distance away from the fracture over which drainage might be effective. For pressure depletion mechanisms, the fracture forms the midplane of the prism.

An obvious problem with this algorithm is to avoid double-counting the volume of overlap between prisms. Volume calculations based upon solid geometry which account for the overlap are time-consuming for the number of fractures that might commonly be encountered in a fracture network. A simpler, more efficient method has been devised, although it is not as numerically exact.

An approach based on the use of grid cells is illustrated in Figure 4-8. The prism enclosing each fracture is approximated by a series of cells that are referenced to a global origin. All of the cells whose centers lie within the prism are said to belong to the prism. Initially, all cells have the value of "0". Each fracture is processed in turn, and all cells belonging to the fracture prism are incremented by the value "1". If a cell belongs to more than one fracture prism, then its counter is incremented to a number equal to the number of prisms it belongs to. After all of the fractures are processed, the total number of non-zero cells multiplied by the cell volume is taken as the estimate of the tributary volume, or:

$$Volume = \sum_{i=1}^{n} \delta(i) dxdydz \qquad (4\text{-}5)$$

where $\delta(i)$ is the Dirac function which is equal to 1.0 if the cell has a value greater than 0.0, and is set to 0.0 if the value in the cell is 0.0,

n is the number of cells, and

dx, dy, dz are the cell dimensions.

An example of this calculation for a simple, verifiable test case is shown in Figure 4-9. The model consists of three horizontal fractures with partial horizontal overlap. Expected and actual results for Test Case 1 are shown in Table 4-3.

Table 4-3 Drainage Volume Algorithm, Test Case 1

Case 1 (half-thicknesses, in meters)	Expected Volume (m^3)	Estimated Volume (m^3)	Percent Difference
1.0	600	600	0.0%
2.0	1000	1000	0.0%
8.0	3400	3400	0.0%

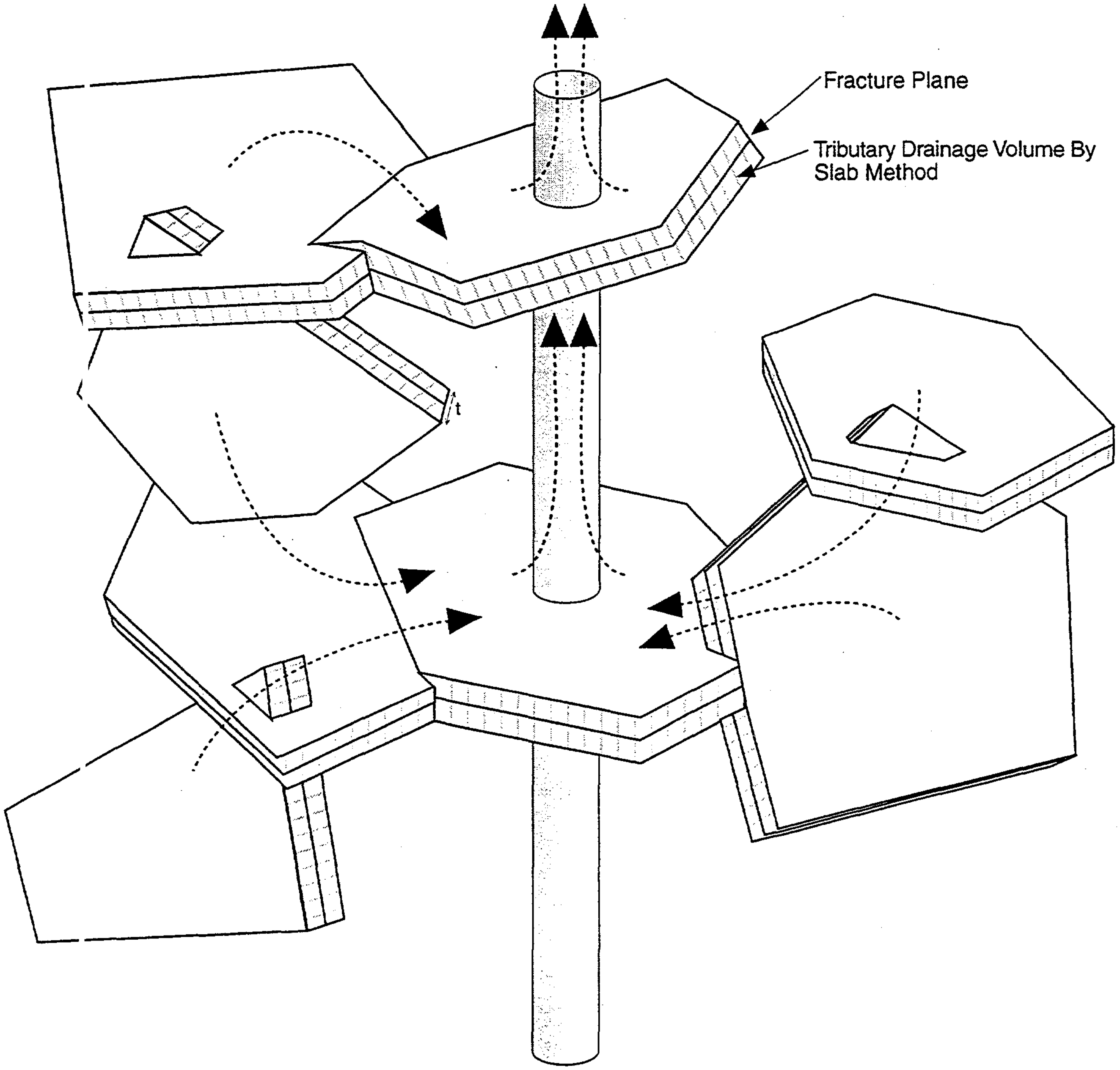

FIGURE **4-7**
TRIBUTARY DRAINAGE VOLUME BY SLAB ALGORITHM
BDM-NIPER/FRACMAN

PROJECT NO. 96: 1357.521 DRAWING NO. 69421 DATE 4/4/97 DRAWN BY CB

Golder Associates

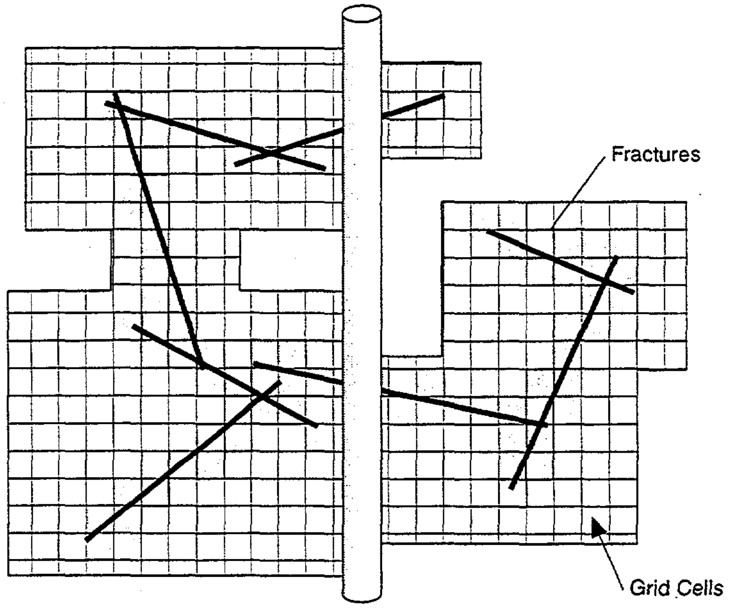

(a) 2D Visualization

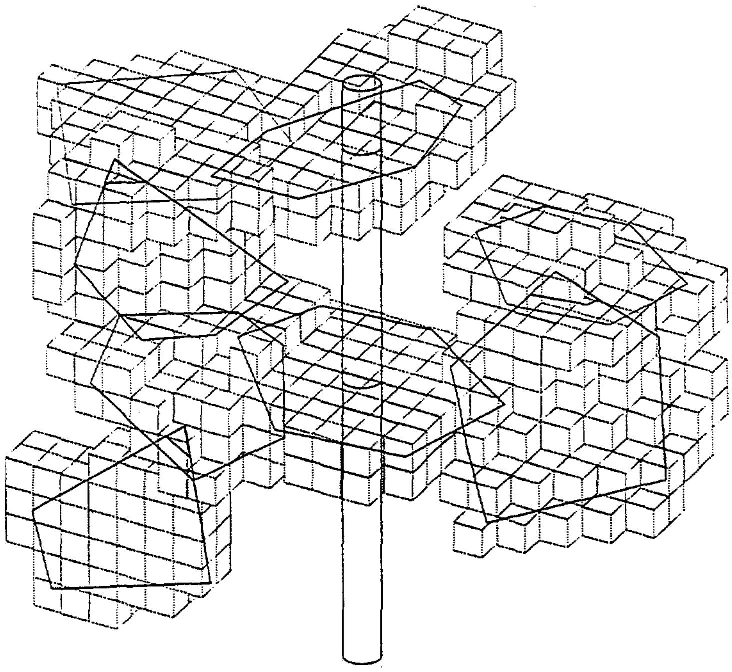

(a) 3D Visualization

FIGURE **4-8**
GRID CELL ALGORITHM
BDM-NIPER/FRACMAN

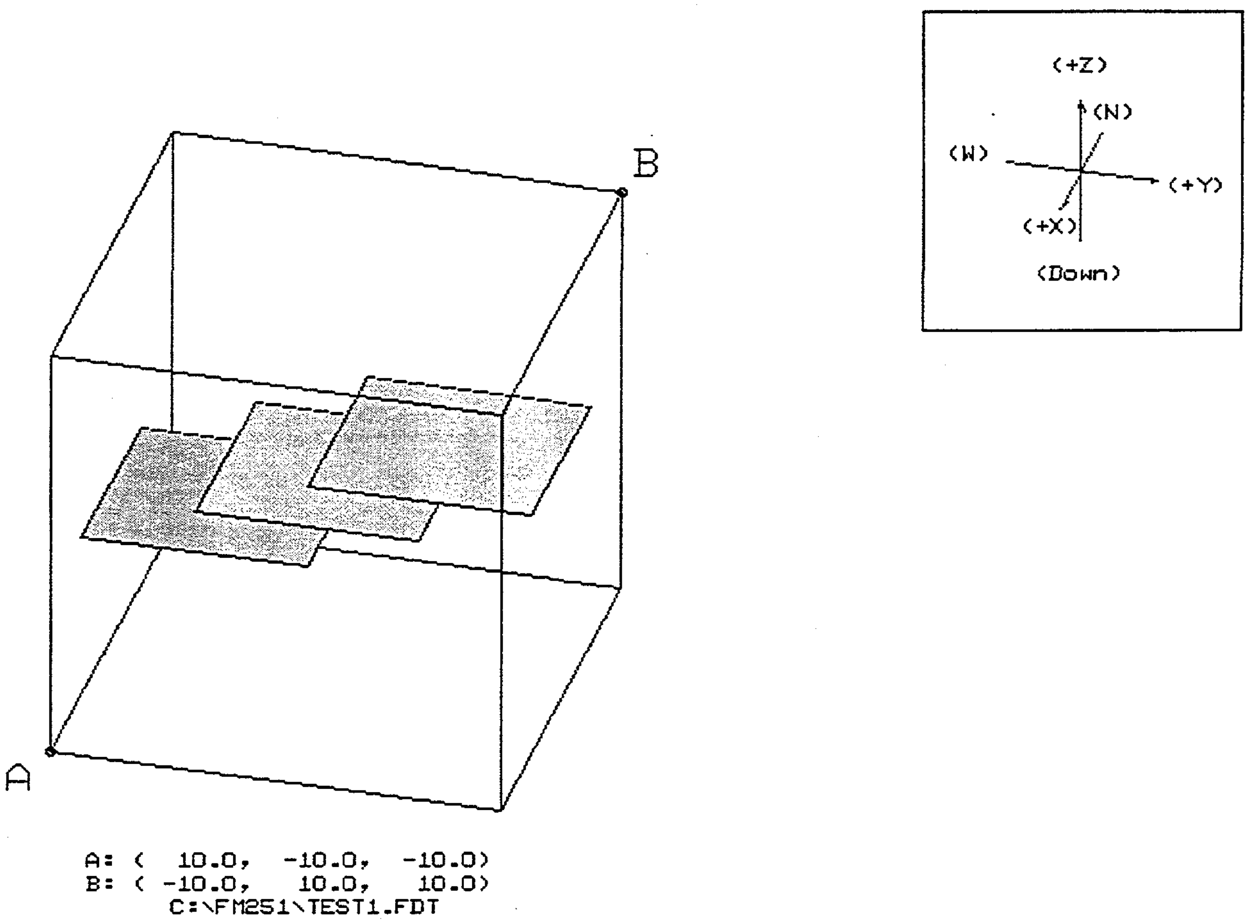

FIGURE **4-9**

DRAINAGE VOLUME TEST CASE 1

BDM-NIPER/FRACMAN

PROJECT NO. 96 1357.521 DRAWING NO. 72157 DATE 4/4/97 DRAWN BY CB

Golder Associates

These series of verification cases are simplistic, but demonstrate that the algorithm correctly computes the volume and does not double-count when the tributary fracture volumes overlap. The reason for the exact match between expected and predicted volumes is that the fractures are horizontal, making the prisms exactly approximated by a series of stacked cells, and the cell size (1.0 m cubes) were evenly divisible into the prism thickness. For example, if a cell size of 3 m were used, then the algorithm would underestimate the volume. The predicted underestimates and the actual results are shown in Table 4-4.

Table 4-4 Expected Errors for Drainage Volume Algorithm, Test Case 1

Case 1 (half-thicknesses, in meters)	**Expected Underestimated Volume (m^3)**	**Estimated Volume (m^3)**	**Percent Difference with True Volume**
1.0	567	567	-5.5%
2.0	972	972	-2.8%
8.0	3240	3240	-4.7%

These cases verify that the algorithm functions as intended, and shows that a poorly chosen cell size can lead to a mis-estimation on the order of 5%.

Test Case 2 is designed for demonstration purposes, because there is no analytical solution for the case of incompletely constrained blocks in discrete fracture networks. Test Case 2 is defined using the fracture geometry for fractures connected to a vertical well drilled in the center of Block Size Test Case 3 (Figure 4-3). For this analysis we assume that the prism surrounding the fracture is of variable thickness, similar to the increasing volume of matrix produced through time as the reservoir is depleted. The measuring cells are cubes with edges of length 1.0 m. Results are shown in Table 4-5.

Table 4-5 Drainage Volume Algorithm, Test Case 2

Case 2 (half-thicknesses, in meters)	**Volume from Drainage Volume Algorithm (m^3)**
1.0	2908
2.0	5735
8.0	21840

Table 4-5 shows that the tributary volume does not scale linearly with increasing prism thickness, due to the overlap of the drainage regions for each fracture.

5. TASK 2.1: TECHNOLOGY DEVELOPMENT

5.1 Task 2.1.1 Fracture Set Analysis

During the year, we developed a neural net technology for fracture set analysis. This section describes this technology development.

5.1.1 Background

Neural networks are a sophisticated form of non-linear pattern recognition that are used in such diverse areas as stock market analysis, loan application screening, diseases diagnosis, and medical expert systems (Eberhart & Dobbins, 1993). They are particularly well-suited for problems in which the input and output variables vary spatially and in scale of importance, are of different mathematical types (e.g., class, ordinal, and continuous variables) and are complexly interrelated. Neural network have found geologic application in a variety of areas including slope stability analysis (Xu & Huang, 1994), rock and soil mechanics (Ellis et al., 1995; Feng, 1995; Lee & Sterling, 1992), fracture network hydrology (La Pointe et al., 1995; Thomas & La Pointe, 1995) and prediction of earthquake intensity and liquefaction (Goh, 1994; Tung et al. 1994).

There are many types of neural networks, but all share a common architecture consisting of *neurons* and *synapses* (Figure 5-1). A neuron is simply a node in the network which uses a non-linear transfer function to convert an input signal (value) to an output signal. Neurons are connected by synapses. A synapse takes the output signal from one neuron, multiplies it by a *synaptic weight*, and passes the modified signal to an adjacent neuron as input. Depending on the number of incoming and outgoing synapses connected to it, a neuron can be classified into one of three categories:

1. *Input neurons* have zero incoming synapses and one or more outgoing synapses. They are used to represent input variables, and take the variable value as their output.
2. *Output neurons* have one or more incoming synapses and zero outgoing synapses. They are used to represent output variables, and produce an output signal which equals the predicted variable value.
3. *Hidden neurons* have one or more incoming synapses and one or more outgoing synapses. They sit between the input and output neurons and pass signals through the network.

A distinct advantage of neural networks over other classification methods is their ability to learn the relative importance and complex interrelations among input and output variables. By changing the neuron transfer functions, the synaptic weights, or the network connectivity, a neural network can be conditioned to provide the expected response for a given input pattern. Once trained, a neural network can then be used to make predictions for input patterns whose correct classification is unknown.

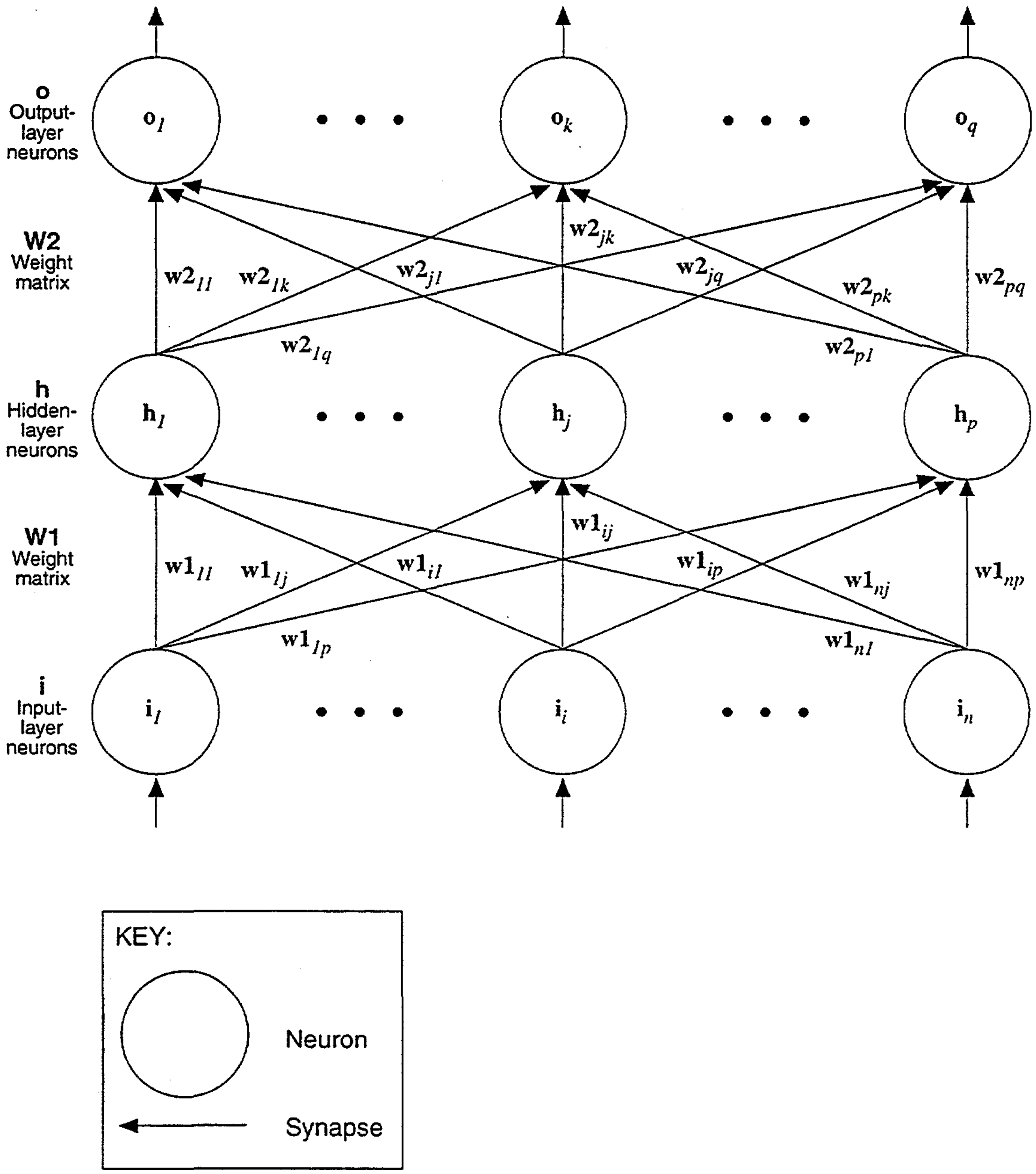

FIGURE **5-1**

NEURAL NETWORK TOPOLOGY

BDM-NIPER/FRACMAN

PROJECT NO. 963 1357.521 DRAWING NO. 69413 DATE 4/4/97 DRAWN BY CB

Golder Associates

Fracture conductivity studies may be considered an exercise in discriminant analysis: given a variety of geological and environmental parameters, is a particular fracture likely to be conductive or not? Backpropagation neural networks are well-suited for this purpose. In a backpropagation neural network, the input, hidden, and output nodes are arranged in layers. A single *input layer*, consisting only of input neurons, is connected to an *output layer*, consisting only of output neurons, through one or more *hidden layers*, consisting only of hidden neurons (Figure 5-1). Each neuron in a given layer is connected to all neurons in the preceding and following layers by synapses, which are characterized by their *synaptic weight*.

As an example, consider a fracture conductivity dataset consisting of the input and output parameters listed in Table 5-1. Of the five input variables, three are continuous, one is of class type, and the remaining one is boolean. The single output parameters is of class type, indicating the fracture set. A backpropagation neural network constructed for this problem would require at least five input nodes, one output node, and perhaps a single hidden layer containing three or so hidden nodes (Figure 5-2).

Table 5-1 Input and Output Parameters for Fracture Conductivity Study

Parameter	**Type**	**Range**	**Units**
Input Parameters			
Strike	Continuous	0 - 360	degrees
Dip	Continuous	0-90	degrees
Mineralization	Class	Calcite, quartz, epidote, ...	N/A
Aperture	Continuous	≥ 0	mm
Open (or closed)?	Boolean	true, false	N/A
Output *Parameters*			
Fracture Set?	Class	Set Number	N/A

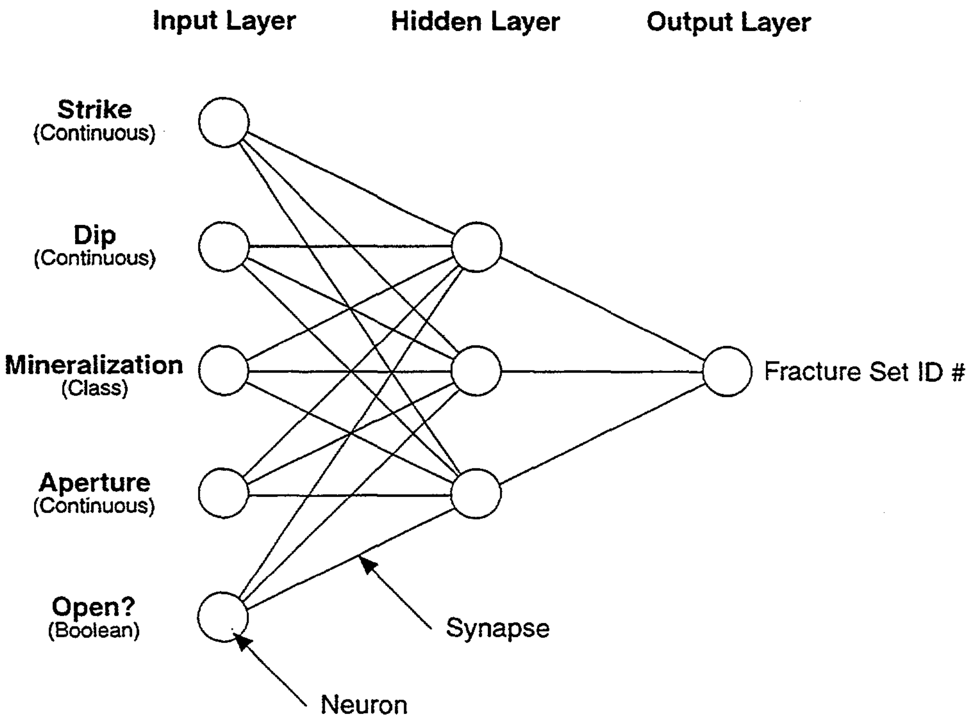

FIGURE 5-2
EXAMPLE NEURAL NETWORK FOR FRACTURE SET ASSIGNMENT
BDM-NIPER/FRACMAN

In a backpropagation network, the network connectivity and the neuron transfer function are held constant, and network behavior is modified by adjusting synaptic weights. Initial synaptic weights are assigned from a random distribution. The neural network is then presented with a series of training patterns, and an error signal is computed from the difference between the network's output signal and the desired output signal. In an iterative procedure known as back propagation of errors, the synaptic weights connecting each layer are modified so as to reduce the output error. In this way, the network is trained to successfully classify the training data. Any backpropagation network with one or more hidden layers using a non-linear neuron transfer function is capable of learning complex non-linear mappings (Eberhart and Dobbins, 1990). Once trained, a neural network can be used to make predictions for data sample whose output parameters are unknown (e.g., assignment of additional fractures to sets).

Additional information can be obtained by examining the synaptic weights of a trained neural network. These weights provide a record of the network's classification strategy and of the input parameters most important for classification. Synaptic weights can be viewed graphically using a Hinton diagram (Figure 5-3), or examined quantitatively by computing the neural network's relation factors. Of these, the simplest is *relation factor one*, which indicates the strength of the output signal produced by a single neuron.

The probabilistic neural network (Specht, 1990) is based on a combination of probability theory and Bayesian statistics, and was developed primarily for solving multivariate classification problems (Masters, 1993). The definition of fracture sets can be considered a classical classification problem, with the following special attributes:

- The combination of diverse data types, including orientations, vectors, real, integer, and ordinal values, and classes
- The need to consider both upper and lower hemisphere orientation vectors when defining distances between orientation values
- The bias toward definition of sets with distinctive mean orientations and minimized dispersion
- The need to consider geologists judgment for definition of prior distribution assumptions

The probabilistic neural network algorithm is designed to provide a classification which minimizes mis-classification of fractures to the wrong set. The classification system which has the minimum "cost" of mis-classification is termed "Bayes Optimal" (Parzan, 1962).

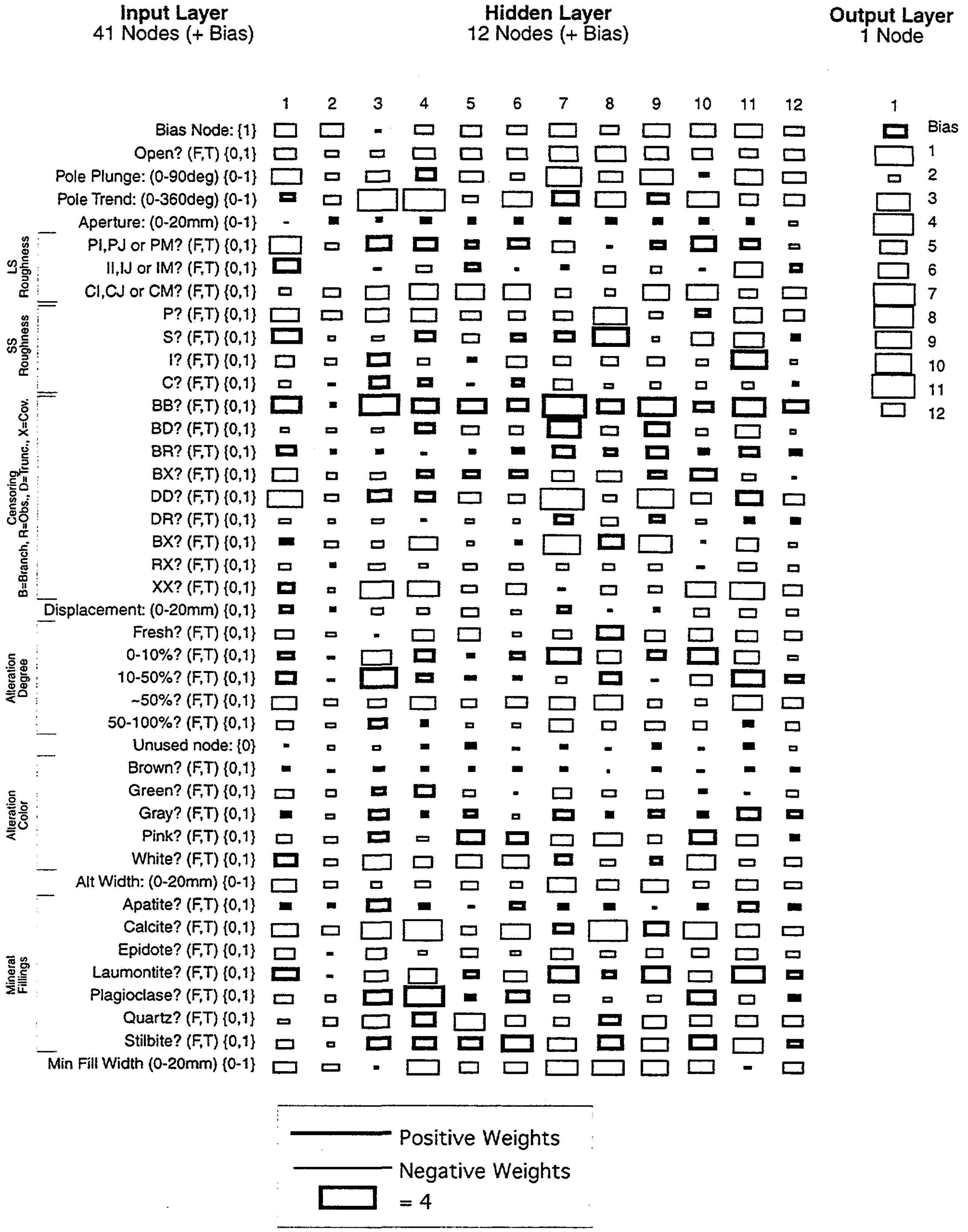

FIGURE **5-3**

HINTON DIAGRAM USING CONTINUOUS VARIABLES

BDM-NIPER/FRACMAN

PROJECT NO. 963 1357.521 DRAWING NO. 69415 DATE 4/4/97 DRAWN BY CB

The algorithm for the implemented probabilistic neural network is illustrated in Figure 5-4. The algorithm proceeds as follows.

1. The user evaluates the data to define the variables to be considered in set classification.
2. The user evaluates the data to define prior distributions for each of the sets. Fractures with these distributions of properties are then generated to constitute the "training set".
3. The user specifies weightings w_i for each of the classification variables, for use in the utility function for evaluation of set classification.

   $$V(c) = \sum W_i \sum D_i(j|c)$$

   where V(c) is the utility for classification c, W_i is the weighting for variable i, and $D_i(j|c)$ is the euclidian distance from the data point j for its classification c,
4. The neural network algorithm uses the minimum distance V(c) for each data point to determine which set it should be assigned to. Each fracture is evaluated for its probability of membership in each of the defined sets, and is assigned to those sets.
5. The statistics for each set are reported based on the fractures assigned to each set.
6. Set statistics and graphical displays are provided.

The classes of fracture properties which can be used in this algorithm are provided in Table 5-2.

Table 5-2 Fracture Property Classes

Property Class	Description	Example
Real	Real valued number	Trace length, aperture
Integer	Integer valued number	JRC, RQD
Orientation	Trend (θ)on [0,360) and Dip (ϕ) on (0,90) for the dip vector (D) or pole vector (P). For calculation of sperical angles the minimum angle of either the upper or lower hemisphere orientation vector is used. The default is lower hemisphere	Fracture orientation, striation orientation, foliation orientation.
Vector	Similar to orientation, but uses only lower hemisphere values	
Class	Membership in a group, as a logical (0,1) cvalue	Rock type, fracture termination mode
Ordinal	Positive, integer value	Fracture Set Number

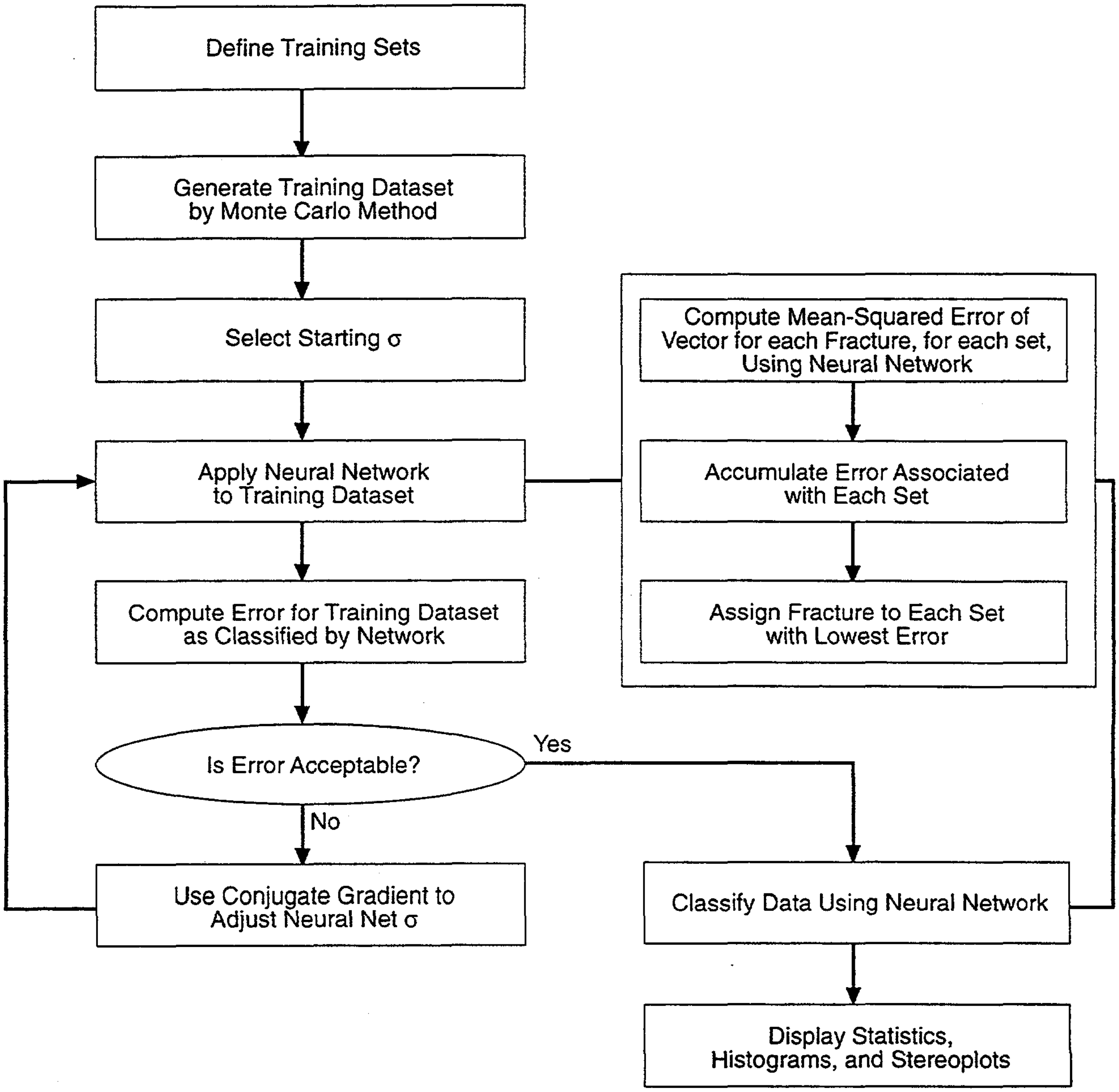

NOTE: Weighting uses the Kernal $W(Z) = e^{-z^2}$ where Z is the "difference between data vectors. "Difference" is defined appropriately for each data type.

FIGURE **5-4**

PROBABILISTIC NEURAL NETWORK ALGORITHM

BDM-NIPER/FRACMAN

5.1.2 Verification Case

The verification case was defined by generating two overlapping Fisher distributed fracture sets using the statistics given in Table 5-3. The stereoplot before fracture separation by ISIS/N is provided in Figure 5-5. The statistics for the fracture sets following neural network analysis, and the stereoplots for the fractures assigned to the sets are provided in Figure 5-6.

Table 5-3 NeurIsis Verification Case

Set	**Orientation Distribution**	**Mean Pole (Trend, Plunge)**	**Dispersion κ**
1	Fisher	36.67, 89.45	10
2	Fisher	-0.28, 59.65	20

5.2 Task 2.1.2 Spatial Location Analysis

Spatial analysis of fracture patterns is an essential aspect of the discrete feature network modeling processes. Current spatial analysis methods include geostatistical (Isaaks and Srivastava, 1985), spatial statistics (Ripley, 1982), and fractal (La Pointe and Barton, 1995). Rule-based methods developed within the scope of this project provide an important additional tool for use in defining structural patterns.

The key to spatial fracture analysis of discrete features is the recognition that fracture formation is not a purely stochastic process. Rather, there is a physical, mechanical basis for every fracture's location and geometry. While it is frequently not productive to attempt to understand the entire stress-strain and material property history related to each fracture, the basic rules of fracture formation can be used to derive more realistic DFN model spatial location processes.

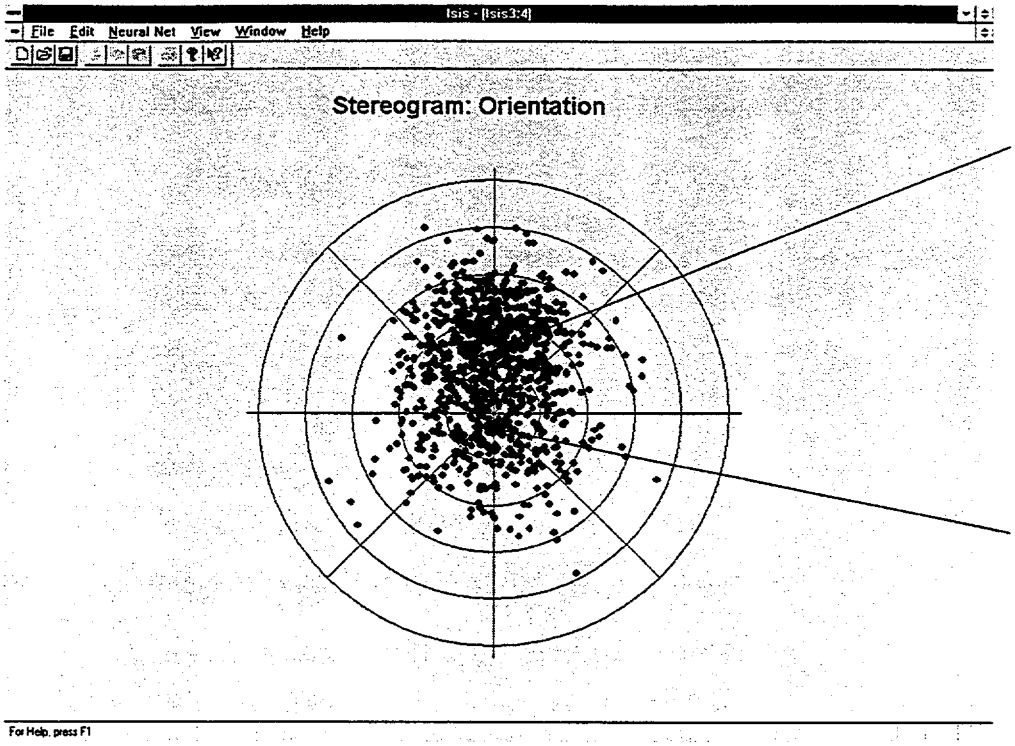

SET #2
Fisher Distribution
Mean Pole Trend θ = 0°
Men Pole Plunge ϕ = 60°
Dispersion κ = 20

SET #1
Fisher Distribution
Mean Pole Trend θ = 37°
Men Pole Plunge ϕ = 90°
Dispersion κ = 10

FIGURE **5-5**

NeurIsis VERIFICATION CASE

BDM-NIPER/FRACMAN

PROJECT NO. 963 1357.521 DRAWING NO. 72184 DATE 4/7/97 DRAWN BY CB

Golder Associates

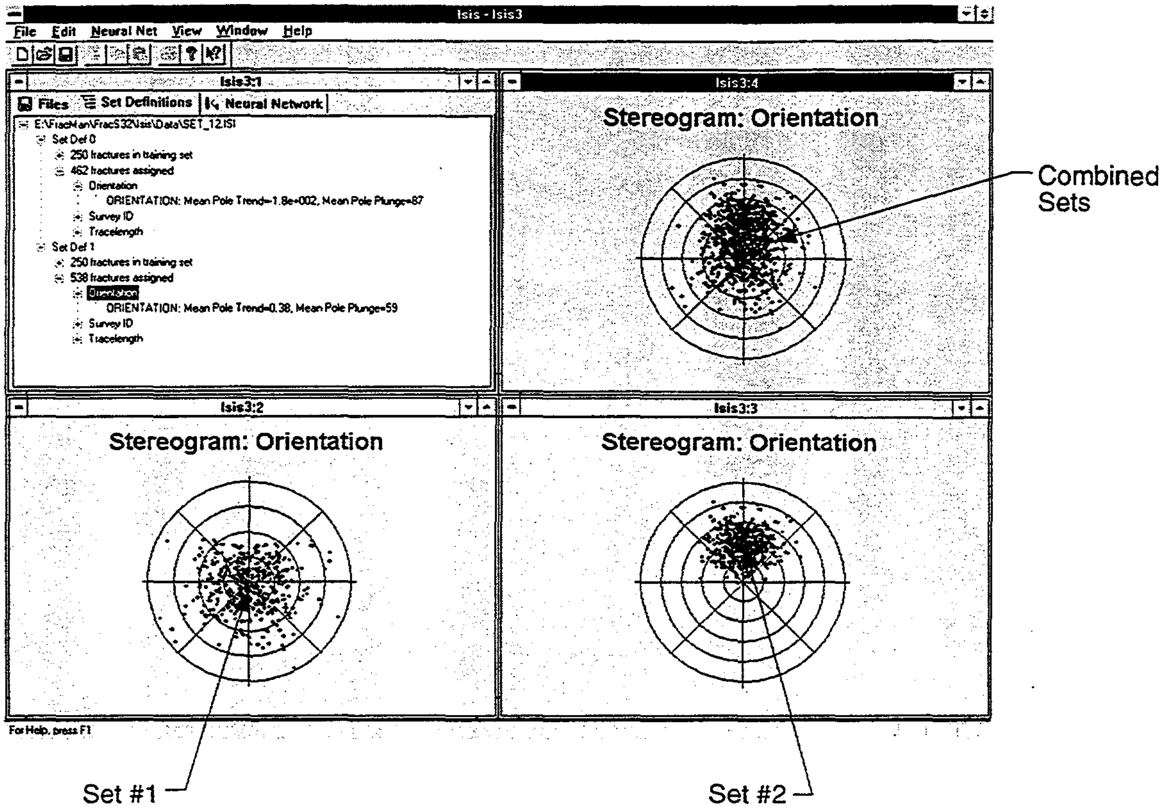

```
E:\FracMan\FracS32\Isis\Data\SET_12.ISI
  Set Def 0
    250 fractures in training set
    462 fractures assigned
      Orientation
        ORIENTATION: Mean Pole Trend=1.8e+002, Mean Pole Plunge=87
      Survey ID
      Tracelength
  Set Def 1
    250 fractures in training set
    538 fractures assigned
      Orientation
        ORIENTATION: Mean Pole Trend=0.38, Mean Pole Plunge=59
      Survey ID
      Tracelength
```

FIGURE **5-6**

VERIFICATION CASE STATISTICS

BDM-NIPER/FRACMAN

PROJECT NO. 953 1357.521 DRAWING NO. 72185 DATE 4/4/97 DRAWN BY CB

Golder Associates

Spatial pattern analysis is looking for correlation structures which can be used to explain the location, size, and orientation of discrete features. In a rule-based approach, we rely on geologically based correlations rather than on purely statistical or stochastic/fractal process based correlations. The geological correlations behind fracture spatial patterns can be expressed quantitatively as (Figure 5-7):

- precedence: the relative order in the sequence of fracture creation
- intensity trends: the variation of fracture intensity with distance from specific types of pre-existing features, or in a specific direction
- orientation trends: the variation of orientation with distance from specific types of pre-existing features, or in a specific direction
- size trends: the variation of orientation with distance from specific types of pre-existing features, or in a specific direction

These correlation structures provide the underlying underpinings for the Hierarchical Fracture Model (see Chapter 3). The rule-based spatial analysis approach quantifies spatial trends and correlations to provide input parameters for hierarchical fracture models.

5.2.1 Algorithm

The rule-based algorithm developed for analysis of spatial fracture patterns is illustrated in Figure 5-8. The algorithm proceeds as follows:

1) **Set Definition:** The first step in the algorithm is to preprocess fractures into sets using a method which allows definition of fracture sets in terms of precedence and geological characteristics as well as orientation. Examples of these algorithms include the Neural network (Figure 5-4; Dershowitz et al, 1997), and stochastic/probabilistic methods (Figure 5-9; Dershowitz et al, 1996).

2) **Same-Set Trends:** The second step in the algorithm is to identify possible spatial trends in intensity, size, and orientation for each set. This is done by calculating the statistics for the set on a grid (Figure 5-10).

3) **Prior Set Correlations:** Once a list of possible spatial trends have been established, the algorithm looks for prior-set features which could explain the trends. Examples of prior set correlation include, for example, decreases in intensity away from identified "fracture zones", and increased intensity within identified "fracture zones" (Figure 5-11).

4) **Between Set Correlations:** The fourth step is to determine whether there are correlations between the trends observed for different sets. For example, the spatial variation in intensity or orientation should correlate strongly for conjugate shears (Figure 5-12).

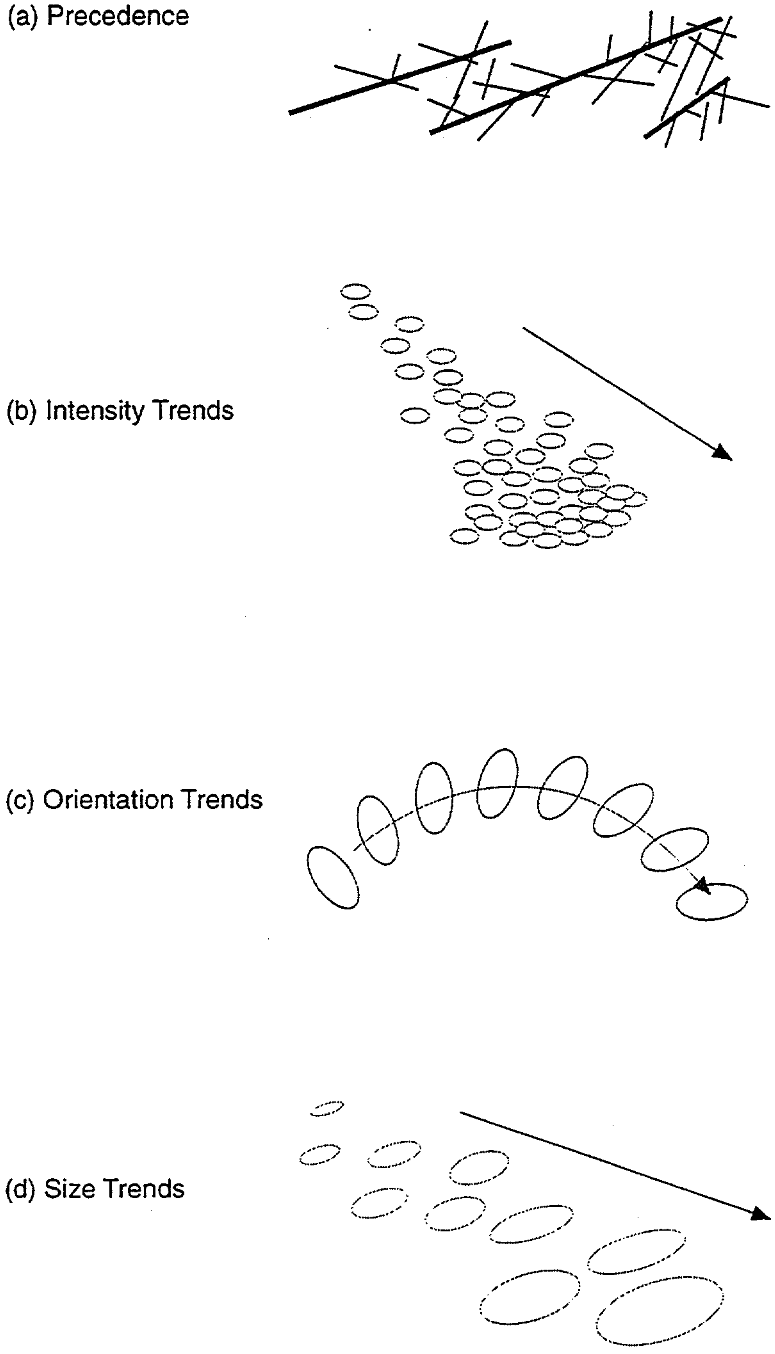

FIGURE **5-7**
SPATIAL CORRELATIONS
BDM-NIPER/FRACMAN

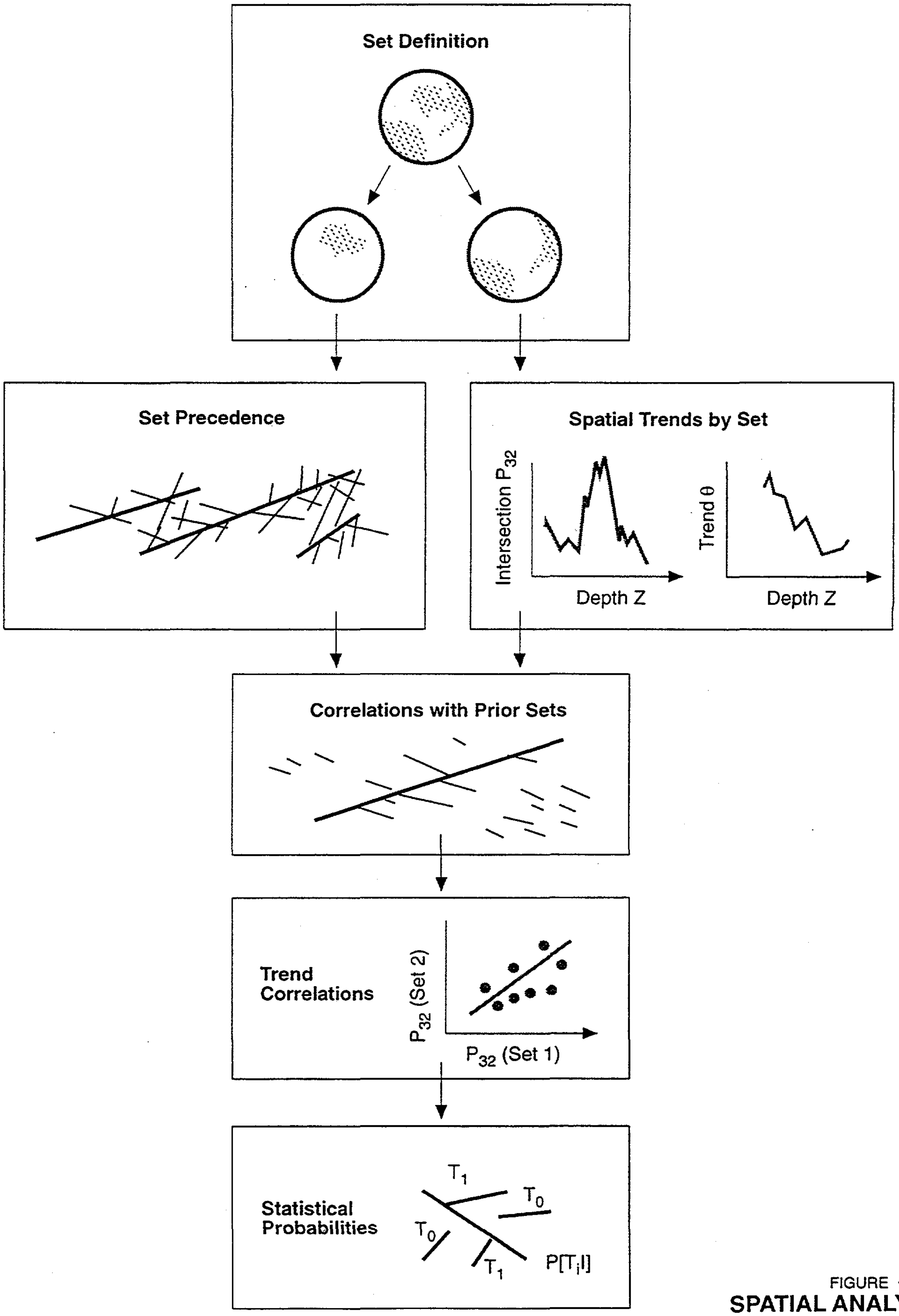

FIGURE **5-8**

SPATIAL ANALYSIS ALGORITHM

BDM-NIPER/FRACMAN

PROJECT NO. 963 1357.521 DRAWING NO. 69401 DATE 4/11/97 DRAWN BY EA

Golder Associates

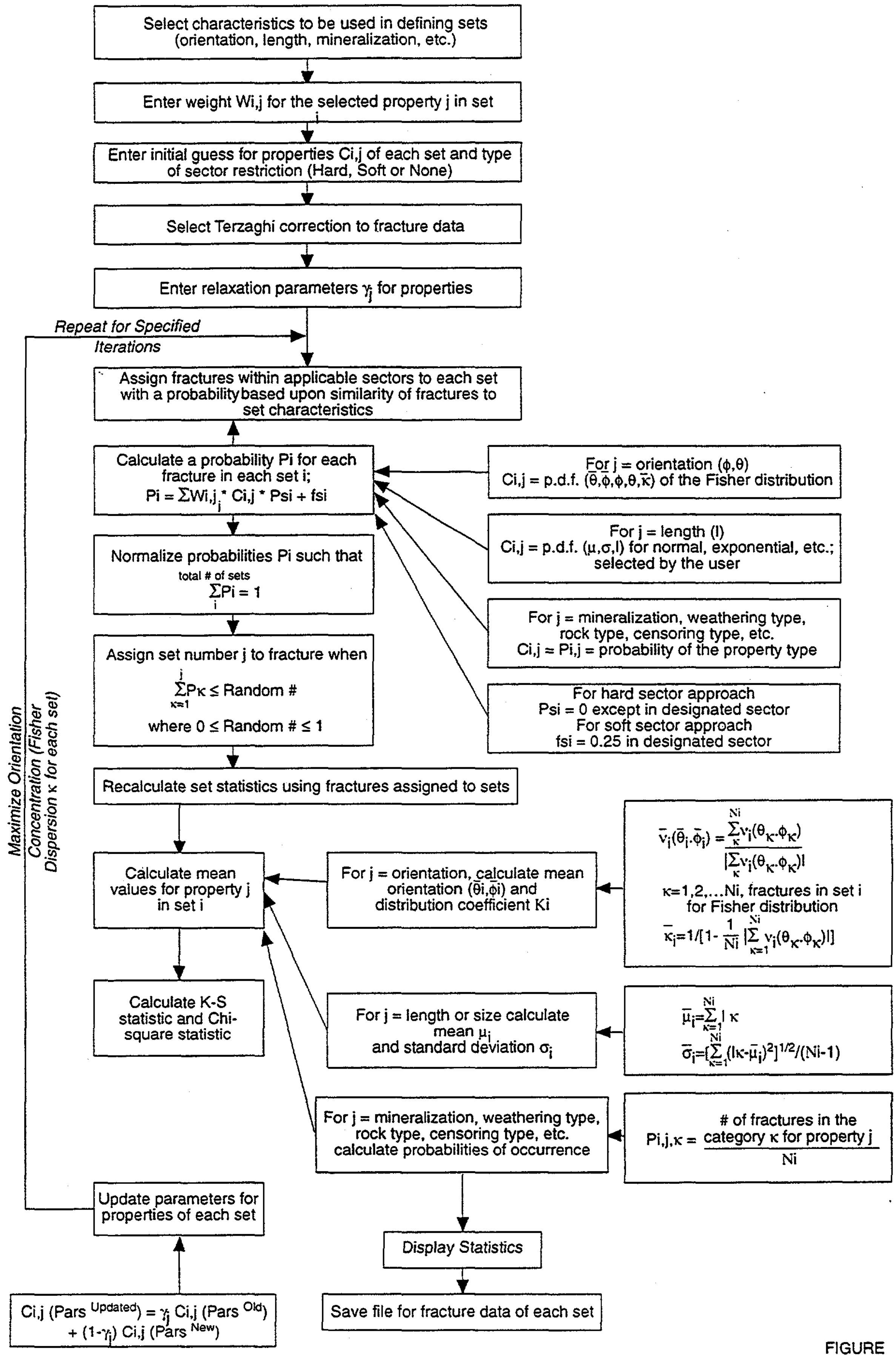

FIGURE **5-9**

STOCHASTIC/PROBABILISTIC SET DEFINITIONS

BDM-NIPER/FRACMAN

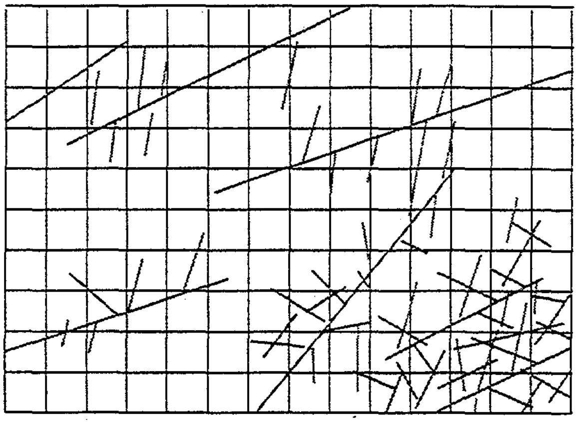

(a) Gridded Fracture Data

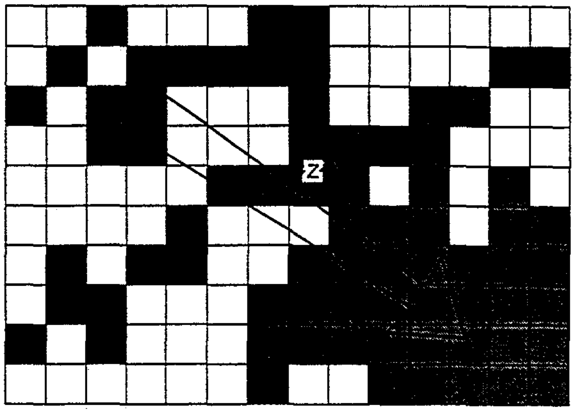

(b) Intensity Values on Grid

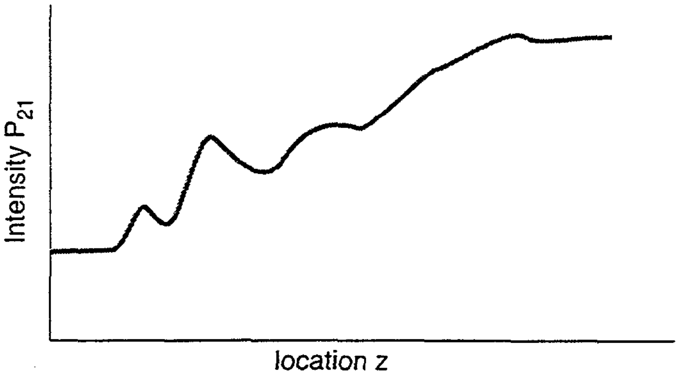

(c) Spatial Trends

FIGURE **5-10**
INTENSITY TREND ON GRID
BDM-NIPER/FRACMAN

PROJECT NO. 963 1357.521 DRAWING NO. 69400 DATE 4/11/97 DRAWN BY EA

Golder Associates

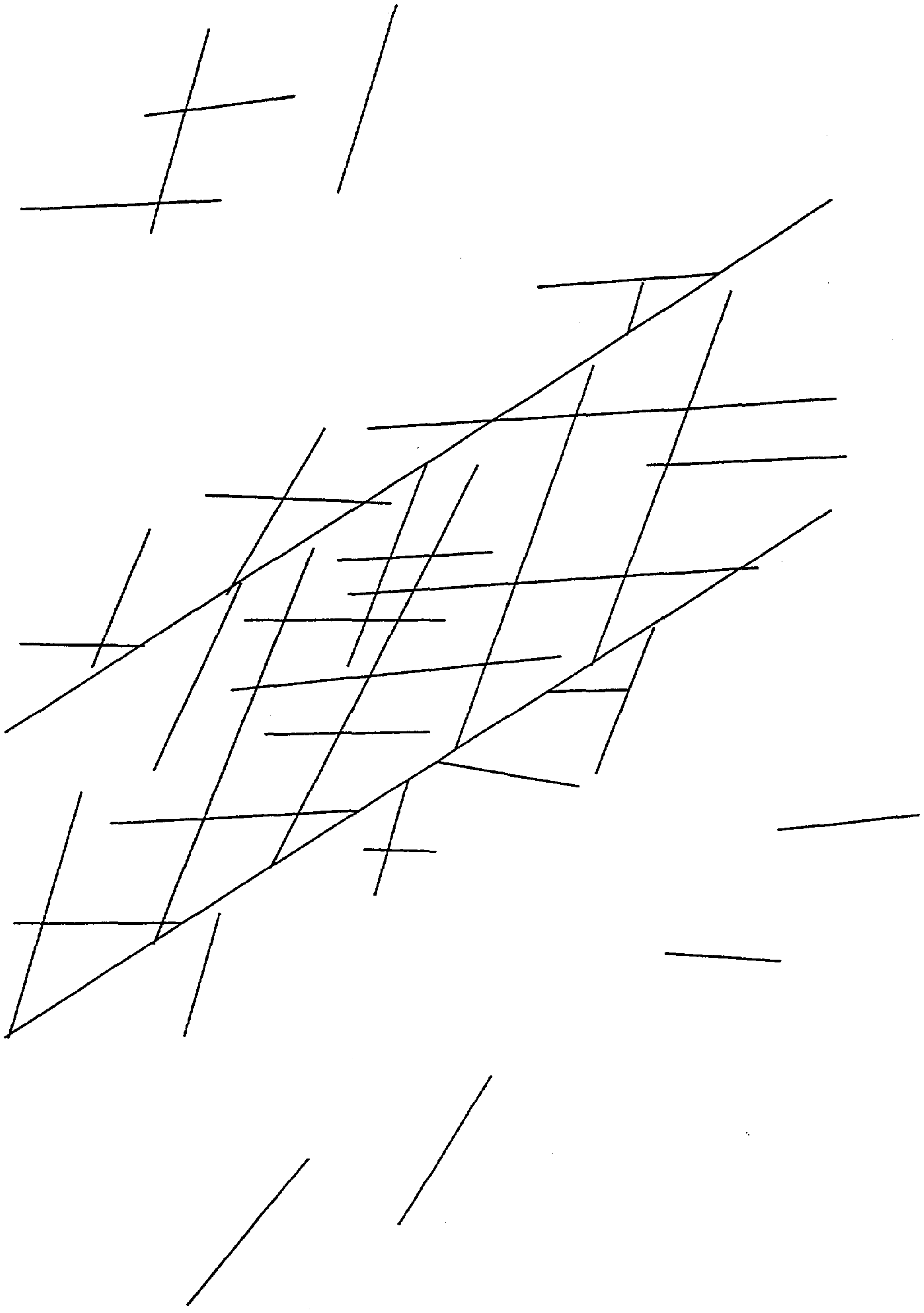

FIGURE **5-11**

PRIOR SET CORRELATION

BDM-NIPER/FRACMAN

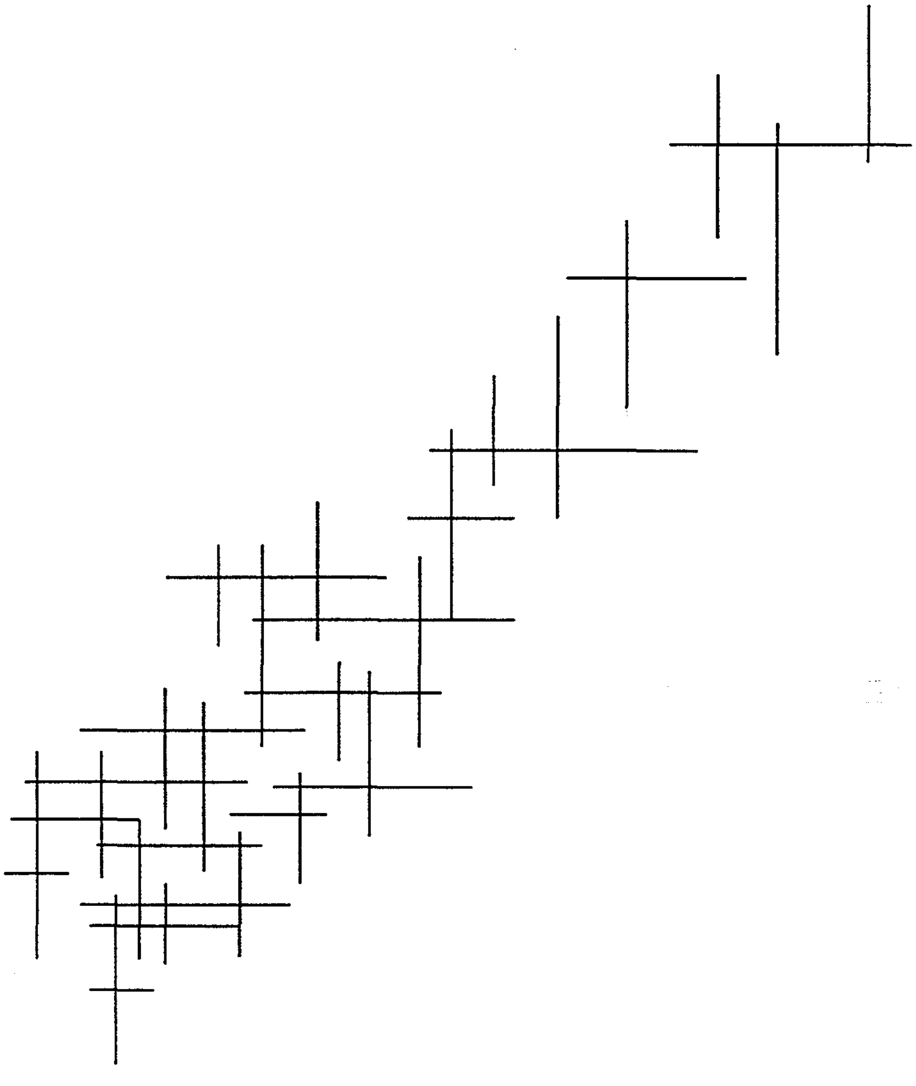

FIGURE **5-12**

CORRELATION BETWEEN CONJUGATE SHEARS

BDM-NIPER/FRACMAN

5) **Statistical Probabilities:** For each of the possible correlations, and trends identified in (2), (3), and (4) above, the algorithm calculates the probability that the correlation will apply for a particular fracture generation. The rules and statistical probabilities are then reported.

The algorithm described above is still under development, and will be verified, implemented and applied during the next project year.

5.3 Task 2.1.3 Hydraulic Parameter Analysis

Hydraulic pathways through fractured rock are frequently formed by a combination of matrix permeability, flow in planar features such as fractures and fracture zones, and flow through one-dimensional channels such as those formed by selective mineralization, dissolution, and fracture intersection processes (Figure 5-13). This combination of flowing features of different dimensionality is referred to as "fractional dimension response" (Barker, 1988; Doe and Chakrybarty, 1996), as illustrated in Figure 5-14. At the Yates Field project study site, for example, there are indications that one- and two-dimensional solution features play a significant role in fluid transport to production boreholes.

An approach was developed for analysis of DFN to obtain simulated distributions of flow dimension to ensure that the simulated DFN have the same connectivity and heterogeneity structure as the *in situ* reservoir rock. This method provides an integrated approach to analysis of hydraulic tests in fractured rocks exhibiting this type of "fractional dimension" (Barker, 1988) and heterogeneously connected behavior.

The approach developed combines fractional dimension type curve analysis (Doe and Chakrybarty, 1996) with discrete fracture network simulation (Dershowitz et al, 1996) and the "OxFilet" approach for derivation of fracture properties by deconvolution of hydraulic test results. A paper describing the approach is provided in Appendix A (Dershowitz and Doe, 1997).

5.3.1 Fractional Dimension Analysis

The main geometric feature which distinguishes different flow dimensions is the power law change in flow area with radial distance. This is second power relationship for spherical flow, first power relationship for cylindrical flow, and zero power (or constant) for linear flow. The dimension is simply the power of the radial variation plus one. As pointed out by Doe and Geier (1991), power law variability of hydraulic properties can also produce dimensional behavior. We can combine the joint effects of area and property by considering the two effects together as a conductance, which is the product of area and hydraulic conductivity.

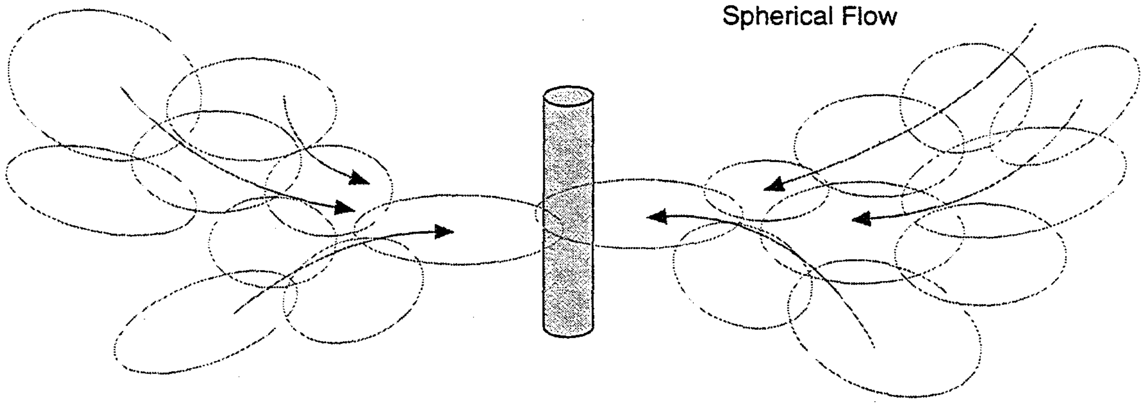

(a) Dimension 3

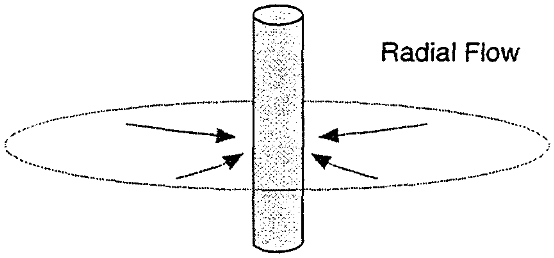

(b) Dimension 2

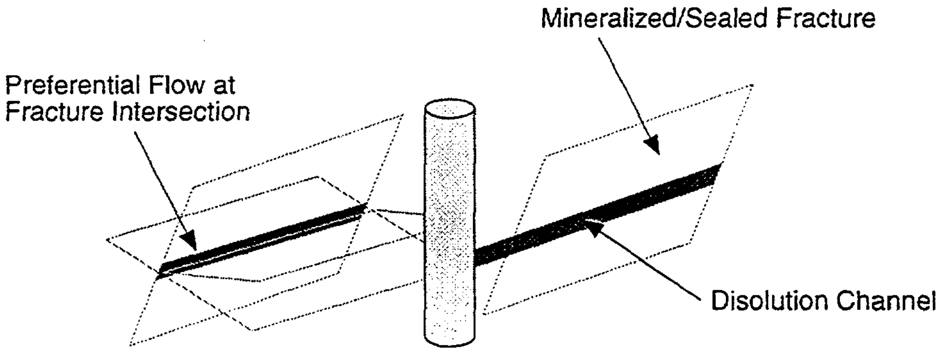

(c) Dimension 1

FIGURE **5-13**
HYDRAULIC PATHWAY FLOW DIMENSION
BDM-NIPER/FRACMAN

PROJECT NO. 963 1357.521 DRAWING NO. 69396 DATE 4/4/97 DRAWN BY EA

Golder Associates

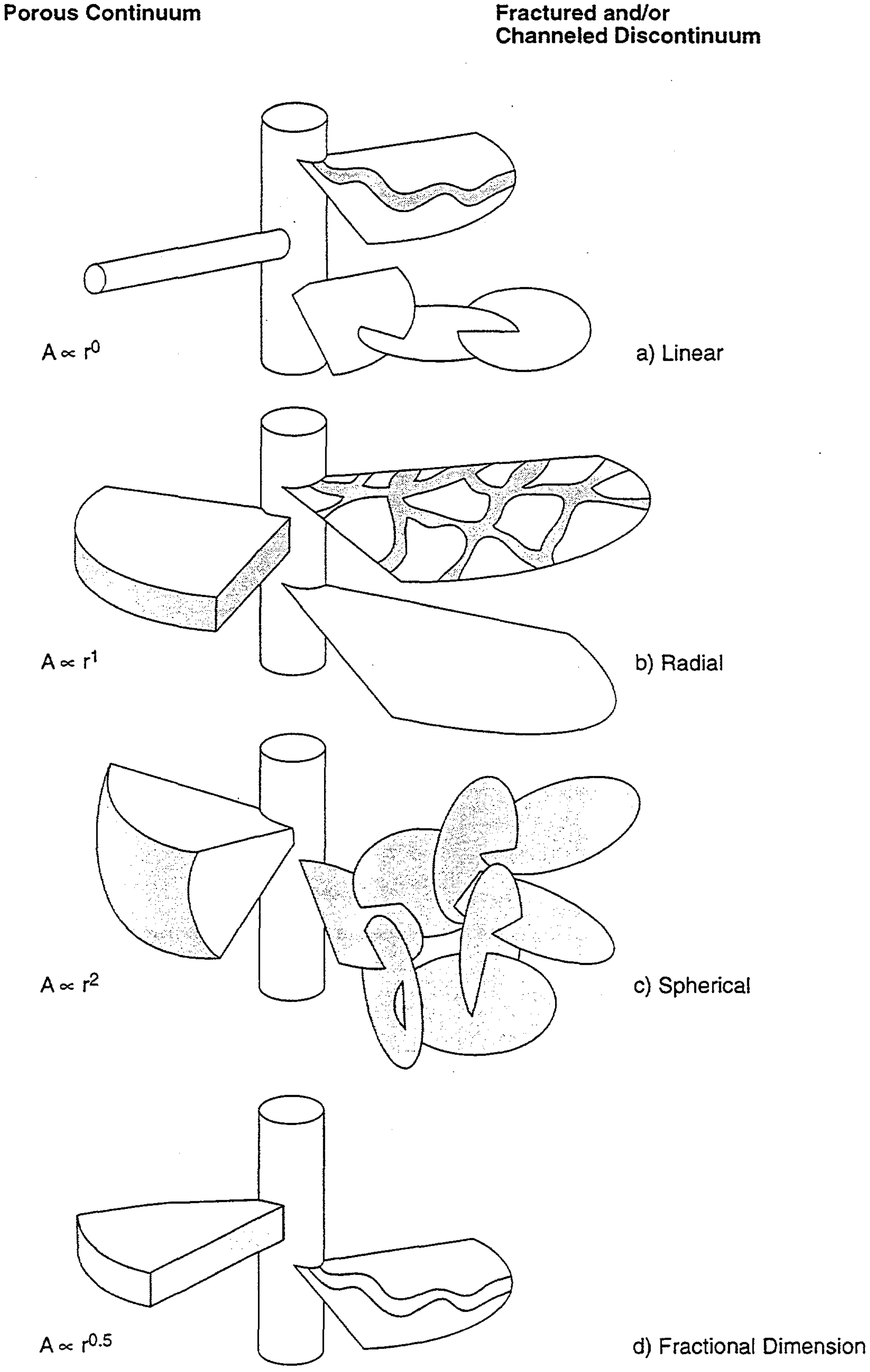

FIGURE **5-14**

FRACTIONAL DIMENSIONAL FLOW

BDM-NIPER/FRACMAN

The dimension of the well test contains very fundamental and useful information about the hydraulic geometry of fracture networks. One-dimensional flow may indicate a single channel within a fracture, or a chain of channels forming a linear network. Two-dimensional flow may indicate a single fracture normal to the borehole, or a network of fractures that is confined to a planar zone, such as a fracture zone or a highly fractured sedimentary bed. Three-dimensional flow may indicate well-connected, a space-filling network of discrete fractures or channels. Finally, non-integer dimensions will appear between these cases where the fracture pattern does not fill a particular space, as in a fractal or power-law network geometry.

Differently dimensioned flow systems have significantly different behavior. In addition, since the systems are fractured, they can be both scale dependent and heterogeneously connected. Research was carried out toward development of procedures for analysis of fractional dimension type curve responses, using Laplace transform solutions for the equation of fractional dimensional flow.

The main assumptions made in the course of developing the models for transient rate and pressure behavior in a two-zone composite system are as follows:

1. Transient Darcian flow takes place in the system, the near flow direction is radial
2. The ith zone is characterized by flow dimension n_i ($i = 1$ for the inner zone and $i = 2$ for the outer zone), where n_i is not necessarily an integer; the source well is an n_1-dimensional "sphere" projected through three-dimensional space
3. The ith zone is characterized by hydraulic conductivity and specific storage K_i and S_{si}, respectively ($i = 1$ for the inner zone and $i = 2$ for the outer zone)
4. The system is infinite, and either a constant-rate or a constant-pressure condition is imposed at the source well
5. Wellbore/source storage capacity is non-negligible

The radial flow behavior of water in a two-zone composite system is governed by the following equations (Barker, 1988):

$$\frac{\partial^2 h_{D1}}{\partial r_D^2} + \left(\frac{n_1 - 1}{r_D}\right)\frac{\partial h_{D1}}{\partial r_D} = \frac{\partial h_{D1}}{\partial t_D}, \quad 1 \le r_D \le r_{D1} \tag{5-1a}$$

and

$$\frac{\partial^2 h_{D2}}{\partial r_D^2} + \left(\frac{n_2 - 1}{r_D}\right)\frac{\partial h_{D2}}{\partial r_D} = \mathrm{D_r}\frac{\partial h_{D2}}{\partial t_D}, \quad r_{D1} \le r_D < \infty \tag{5-1b}$$

respectively, where

$$D_r = \frac{K_1 / S_{s1}}{K_2 / S_{s2}} \tag{5-1c}$$

In terms of the dimensionless variables, the initial and boundary conditions become

$$h_{D1}(r_D,0) = h_{D2}(r_D,0) = H_D(0) = 0 \tag{5-2a}$$

$$S_{wD}\,\frac{d\,H_D}{d\,t_D} = 1 + \frac{\partial h_{D1}}{\partial r_D}\Big|_{r_D = 1} \tag{5-2b}$$

$$h_{D2}(r_D \to \infty, t_D) = 0 \tag{5-2c}$$

$$h_{D1}(r_{D1}, t_D) = h_{D2}(r_{D1}, t_D) \tag{5-2d}$$

and

$$\sigma\,\frac{\partial h_{D1}}{\partial r_D}\Big|_{r_{D1}} = \frac{\partial h_{D2}}{\partial r_D}\Big|_{r_{D1}} \tag{5-2e}$$

where

$$S_{wD} = \frac{S_w}{S_{s1}\; b^{3-n_1}\; \alpha_{n_1}\; r_w^{n_1}} \tag{5-2f}$$

$$\sigma = \frac{K_1\;(b / r_1)^{n_2 - n_1}}{K_2}\,\frac{\alpha_{n_1}}{\alpha_{n_2}} \tag{5-2g}$$

and

$$r_{D1} = r_1 / r_w \tag{5-2h}$$

Laplace transforms can be used to solve the system of partial differential equations. The subsidiary equations are

$$\frac{d^2\,\overline{h}_{D1}}{d\,r_D^2} + \frac{n_1 - 1}{r_D}\frac{d\,\overline{h}_{D1}}{d\,r_D} = p\;\overline{h}_{D1},\; 1 \le r_D \le r_{D1} \tag{5-3a}$$

and

$$\frac{d^2\,\overline{h}_{D2}}{d\,r_D^2} + \frac{n_2 - 1}{r_D}\frac{d\,\overline{h}_{D2}}{d\,r_D} = p\;\mathrm{D}_r\;\overline{h}_{D2},\; r_{D1} \le r_D < \infty \tag{5-3b}$$

After transforming the boundary conditions, Equations (2-3a) and (2-3b) are solved simultaneously. The solutions in Laplace space are

$$\bar{h}_{D1}(r_D, p) = \frac{\Delta_2 K_{\nu_1}(r_D\sqrt{p}) + \Delta_1 I_{\nu_1}(r_D\sqrt{p})}{p\,(\Delta_1 \lambda_2 + \Delta_2 \lambda_1)} \tag{5-4a}$$

$$1 \le r_D \le r_{DI}$$

and

$$\bar{h}_{D2}(r_D, p) = \frac{\left[\Delta_2 K_{\nu_1}(r_{D1}\sqrt{p}) + \Delta_1 I_{\nu_1}(r_{D1}\sqrt{p})\right] K_{\nu_2}(r_D\sqrt{D_r\, p})\; r_{D1}^{\nu_1-\nu_2}\; r_D^{\nu 2}}{p\, K_{\nu_2}(r_{D1}\sqrt{D_r\, p})\, (\Delta_1\lambda_2 + \Delta_2\lambda_1)}$$

$$r_{D1} \le r_D < \infty \tag{5-4b}$$

where

$$\Delta_1 = \frac{\sigma}{\sqrt{D_r}} K_{\nu_1 - 1}(r_{D1}\sqrt{p})\, K_{\nu_2}(r_{D1}\sqrt{D_r\, p}) -$$

$$K_{\nu_2 - 1}(r_{D1}\sqrt{D_r\, p})\, K_{\nu_1}(r_{D1}\sqrt{p}) \tag{5-5a}$$

$$\Delta_2 = \frac{\sigma}{\sqrt{D_r}} I_{\nu_1 - 1}(r_{D1}\sqrt{p})\, K_{\nu_2}(r_{D1}\sqrt{D_r\, p}) +$$

$$K_{\nu_2 - 1}(r_{D1}\sqrt{D_r\, p})\, I_{\nu_1}(r_{D1}\sqrt{p}) \tag{5-5b}$$

$$\lambda_1 = p\, S_{wD}\, K_{\nu_1}(\sqrt{p}) + \sqrt{p}\, K_{\nu_1 - 1}(\sqrt{p}) \tag{5-5c}$$

$$\lambda_2 = p\, S_{wD}\, I_{\nu_1}(\sqrt{p}) - \sqrt{p}\, I_{\nu_1 - 1}(\sqrt{p}) \tag{5-5d}$$

and

$$\nu_i = 1 - \frac{n_i}{2}, \; i = 1, 2 \tag{5-5e}$$

Using equations 5-1 through 5-5 and the related type curves of Figures 5-15 through 5-17, it is possible to derive both transmissivity, storativity, and flow dimension as a function of distance from the well bore from well tests. Of these, the flow dimension as a function of distance may prove to be the most important for reservoir design, since lower flow dimensions indicate that only a small portion of the reservoir is being accessed.

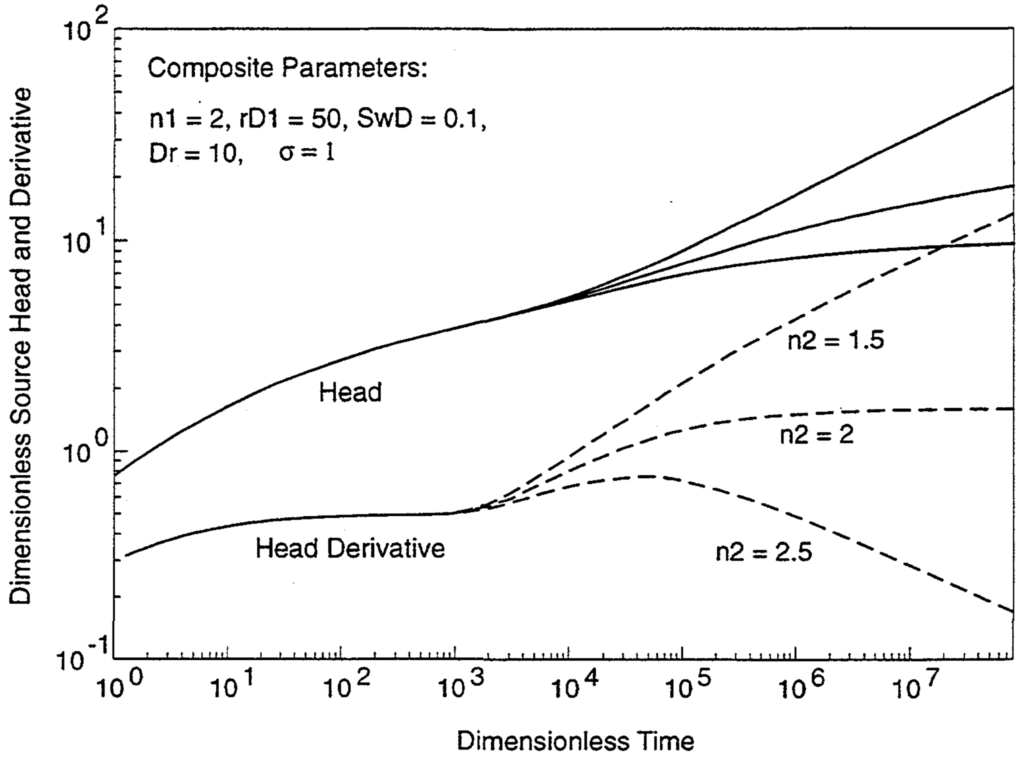

a) Dimensionless head and head derivative in source well vs. time with different outer zone flow dimensions

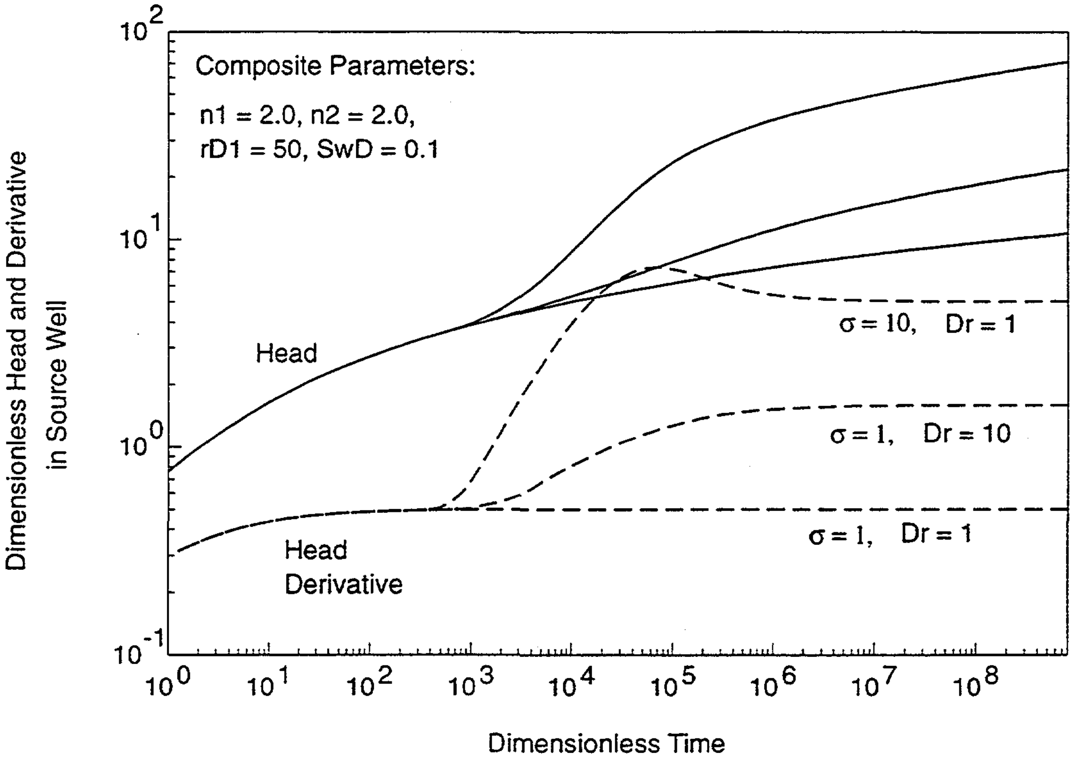

b) Dimensionless plot of head and head derivative in source well vs. time for different values of σ and Dr: n1 = n2 = 2

FIGURE **5-15**

FRACTIONAL DIMENSION TYPE CURVES

BDM-NIPER/FRACMAN

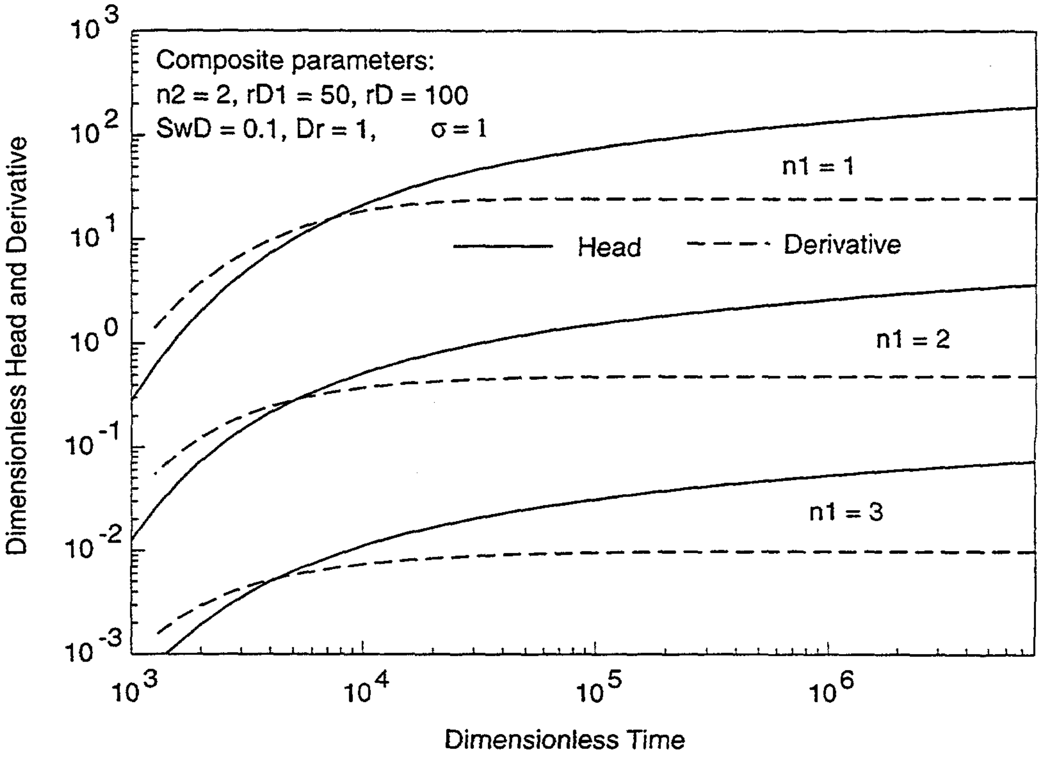

Constant rate interference test solution with varying inner zone flow dimension: observation well in outer zone

FIGURE **5-16**

FRACTIONAL DIMENSION TYPE CURVES

BDM-NIPER/FRACMAN

PROJECT NO. 963 1357.521 DRAWING NO. 69430 DATE 4/4/97 DRAWN BY CB

Golder Associates

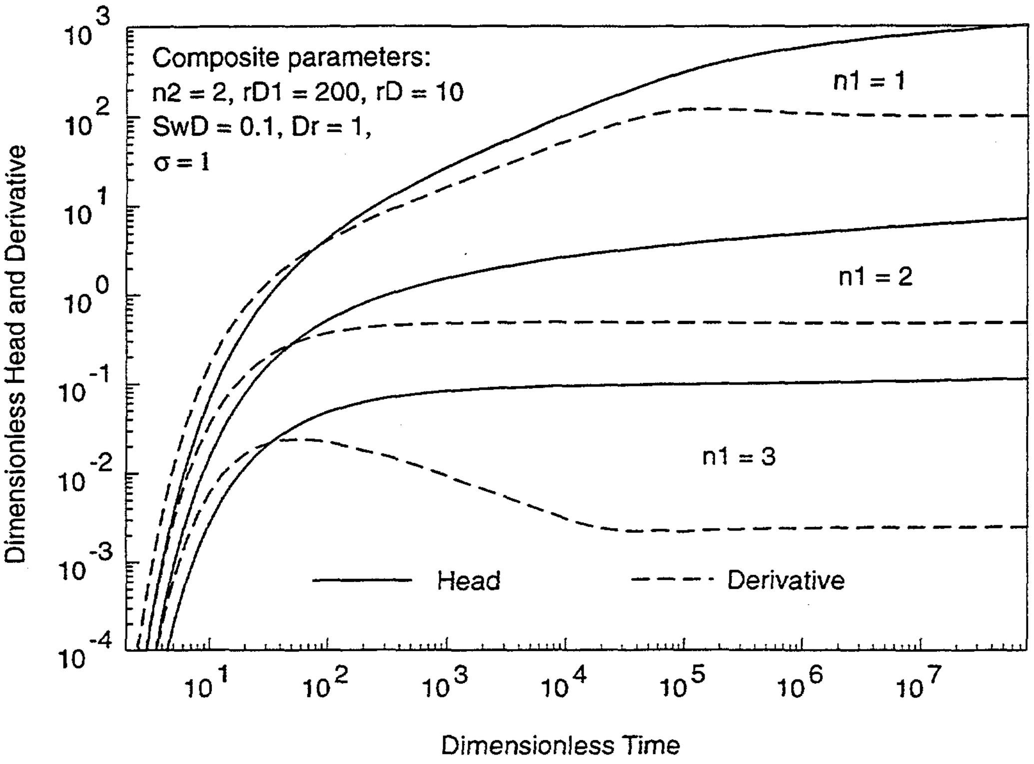

Constant rate interference test solution with varying inner zone flow dimension: observation well in inner zone

FIGURE **5-17**

PRODUCTION FROM FRACTIONAL DIMENSION RESERVOIRS

BDM-NIPER/FRACMAN

PROJECT NO. 963 1357.521 DRAWING NO. 69431 DATE 4/4/97 DRAWN BY CB

Golder Associates

5.3.2 Integration of DFN and Fractional Dimension Flow Approaches

Just as heterogeneous fractured rock masses are not limited to integer flow dimensions, a series of well tests from different locations in a fracture networks may exhibit a distribution of flow dimensions rather than a single, characteristic flow dimension. This distribution of flow dimensions is thus a valuable measure of rock mass heterogeneity and connectivity. Flow dimension distributions from well test analyses of large data sets from Japan and Sweden (Geier et al., 1995; Winberg et al., 1996) are shown in Figure 5-18. Each of these sites shows a unique distribution of transmission and flow dimension which is indicative of the rock mass heterogeneity and connectivity.

Figure 5-19 illustrates the approach developed during the current project year to use well test results in terms of transmissivities and flow dimension distributions to develop DFN models with consistent fracture network connectivity and hydraulic properties.

The analysis starts with:

1. **Hydraulic Test Results:** A file containing the results of transient packer test or drill-stem hydraulic test results, expressed as distributions of interval transmissivity and flow dimension, similar to those illustrated in Figure 5-18. These are derived from packer test transient results using fractional dimensional type curve analyses (Doe, 1991).

2. **DFN Model:** A discrete fracture network (DFN) conceptual model implemented as a spatial location model, distributions for orientation, intensity, size, and shape, and analysis of any correlations between these.

The forward modeling approach presented here attempts to reduce the effort required to get the distribution of dimensions from the DFN model. The approach concentrates on the variation in the flow path conductance as a function of radial distance, rather than using simulated hydraulic tests.

As discussed above and by consequence of Equations 5-1 through 5-5, the flow dimension is a measure of the power law variation of flow area or conductance with radial distance. The relationship between the variation in flow path area, (which is an analog for conductance) with radial distance and the flow dimension is illustrated in Figure 5-20.

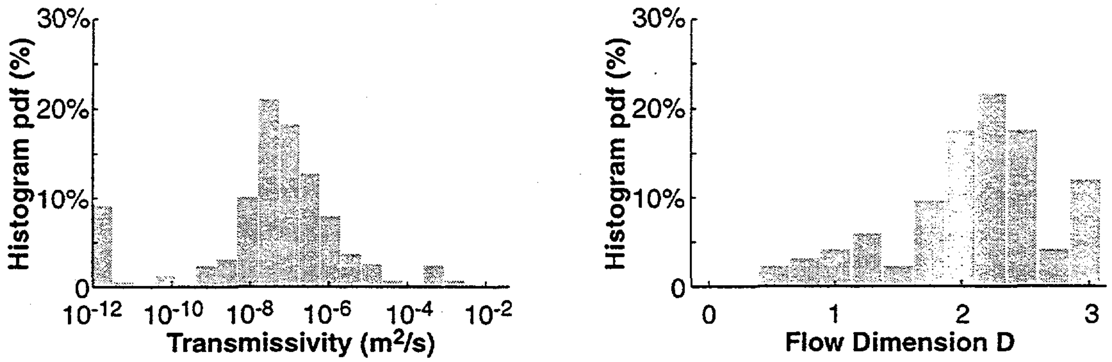

(a) Finnsjon, Sweden (after Geier et al., 1995)

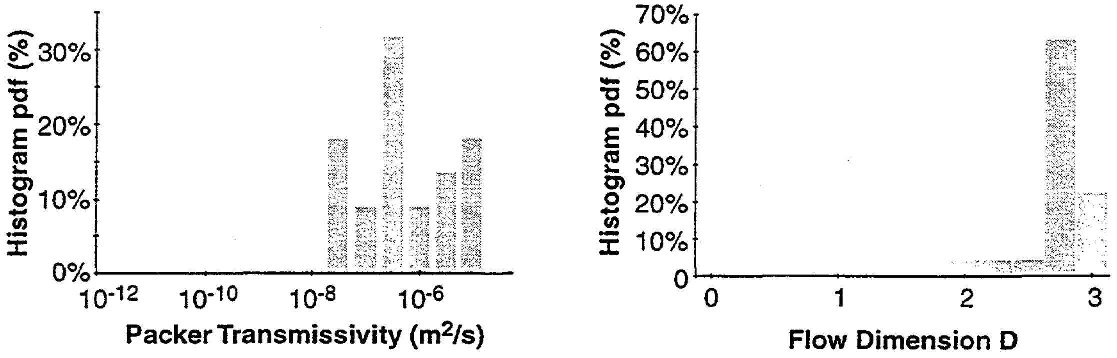

(b) Äspö "TRUE-1" Block (after Winberg et al., 1996)

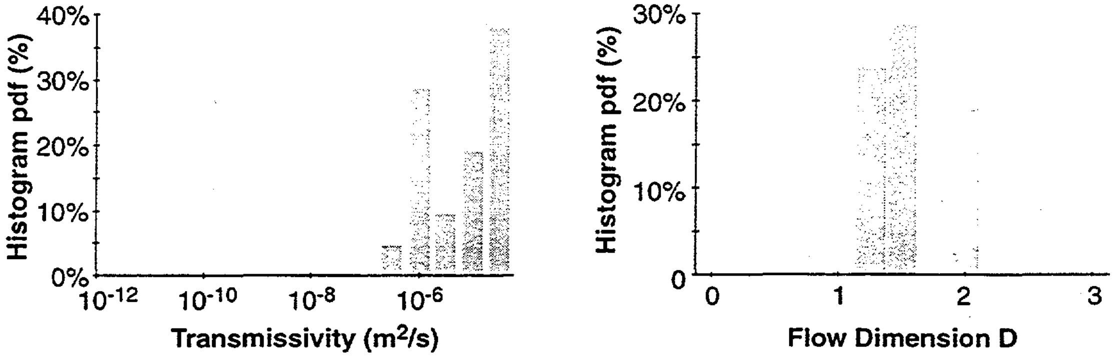

(c) Kamaishi KD-90 Area

FIGURE **5-18**

DISTRIBUTION OF FLOW DIMENSION, FINNSJON AND ÄSPÖ, SWEDEN AND KAMAISHI, JAPAN

BDM-NIPER/FRACMAN

PROJECT NO. 9(3 1357.521 DRAWING NO. 69395 DATE 4/4/97 DRAWN BY EA

Golder Associates

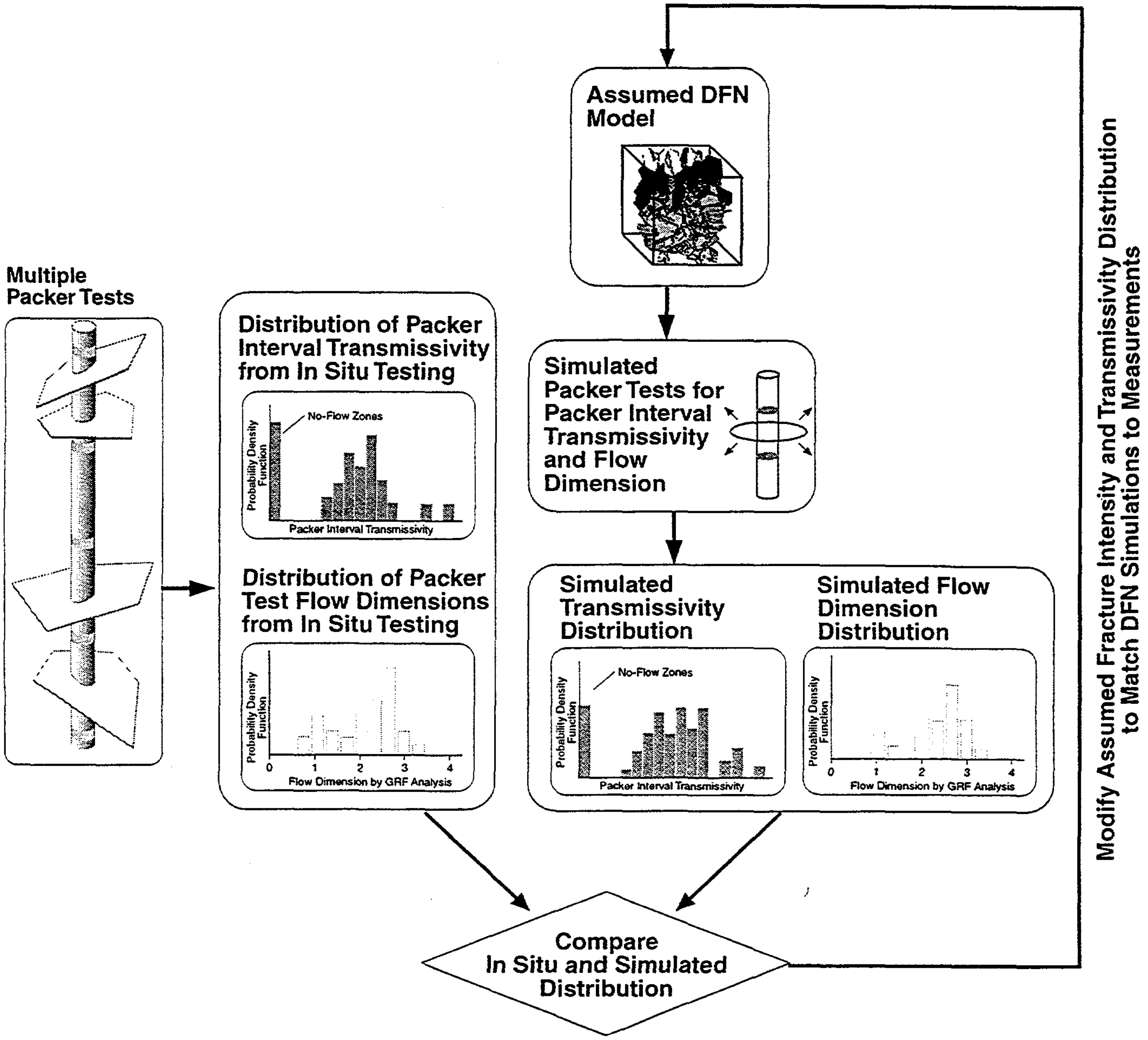

FIGURE **5-19**

CALIBRATION OF DFN TO HYDRAULIC TESTS

BDM-NIPER/FRACMAN

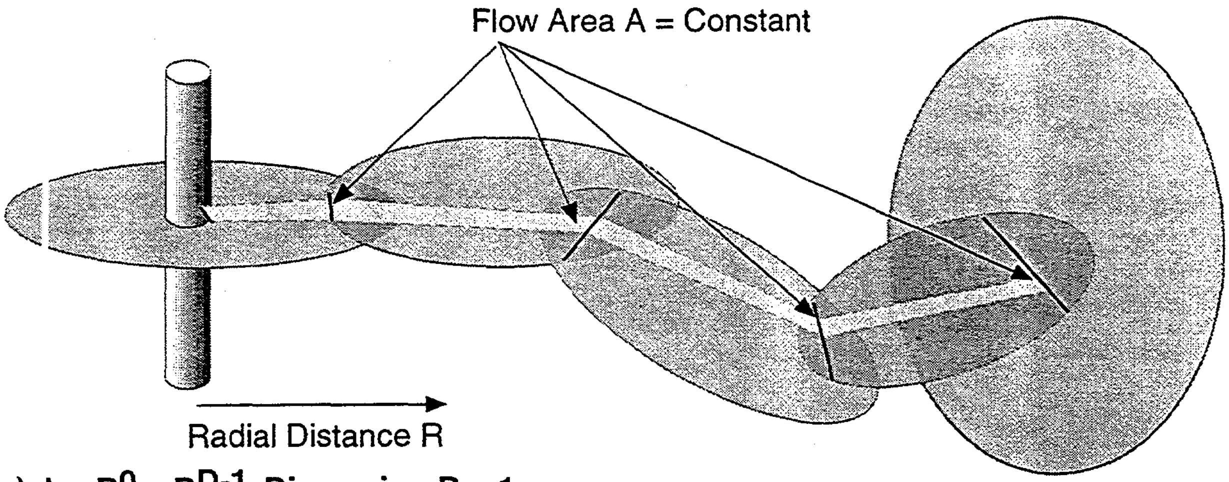

(a) A = R^0 = R^{D-1}, Dimension D = 1

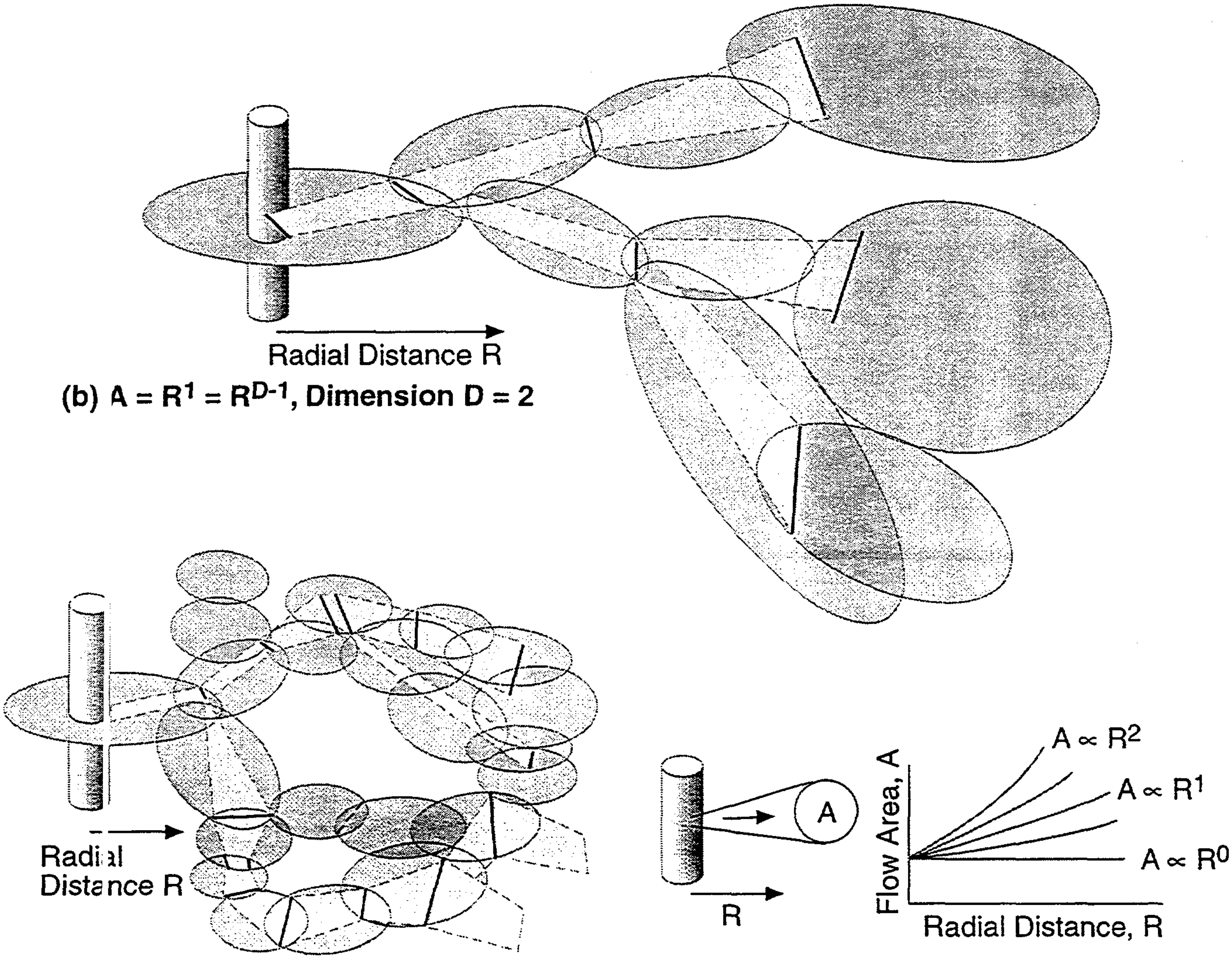

(b) A = R^1 = R^{D-1}, Dimension D = 2

(c) A = R^2 = R^{D-1}, Dimension D = 3

(d) Flow Area Function

FIGURE **5-20**
FLOW AREA VS. RADIAL DISTANCE
BDM-NIPER/FRACMAN

PROJECT NO. 96 1357.521 DRAWING NO. 69393 DATE 4/4/97 DRAWN BY EA

Golder Associates

- For linear (1D) flow, the area (conductance) is constant with radial distance
- For radial (2D) flow, the area (conductance) increases linearly with radial distance
- For spherical (3D) flow, the area (conductance) increases as radial distance squared
- For generalized radial flow (nD), the flow area A_f (as an analog of conductance C) increases as a power of radius R equal to the one less than the flow dimension, according to

$$C \propto A_f \propto R^{D-1} \tag{5-6}$$

In the forward simulation approach, a graph theory search is used to work out from the borehole into the fracture network to calculate the variation in conductance with distance from the borehole. This search is carried out as follows:

1. **DFN Simulation:** A series of realizations of a discrete fracture network model are generated, using assumed distributions for parameters based on initial data analysis. The same wells used in the field testing are "completed" into each of the DFN simulations.

2. **Cluster Analysis:** A cluster analysis is used to identify all the fractures which exceed a specified size or transmissivity threshold and which are connected to well test interval in the simulated well. The result of the cluster analysis may contain the entire network or it may be only a few fractures depending on the connectivity of the fracture network.

3. **Graph Analysis:** The fracture pattern is converted to a pipe network graph, with each graph element i assigned a length L_i and pipe conductance C_i. The pipe conductance is calculated as

$$C_i = W_i \, T_i \tag{5-7}$$

where W_i is the flow width achieved in the fracture, and T_i is the transmissivity of the fracture containing the pipe.

A number of algorithms are available to calculate the flowing width in the fracture from the geometry of fractures and fracture intersections. For the present demonstration, the width is calculated based on the geometry of the traces formed by fracture intersections, with an applied channeling factor F_i,

$$W_i = \tfrac{1}{2} F_i \, (L_{1i} + L_{2i}) \tag{5-8}$$

L_{1i} and L_{2i} are the lengths of the two traces which define the fracture intersections (Figure 5-21).

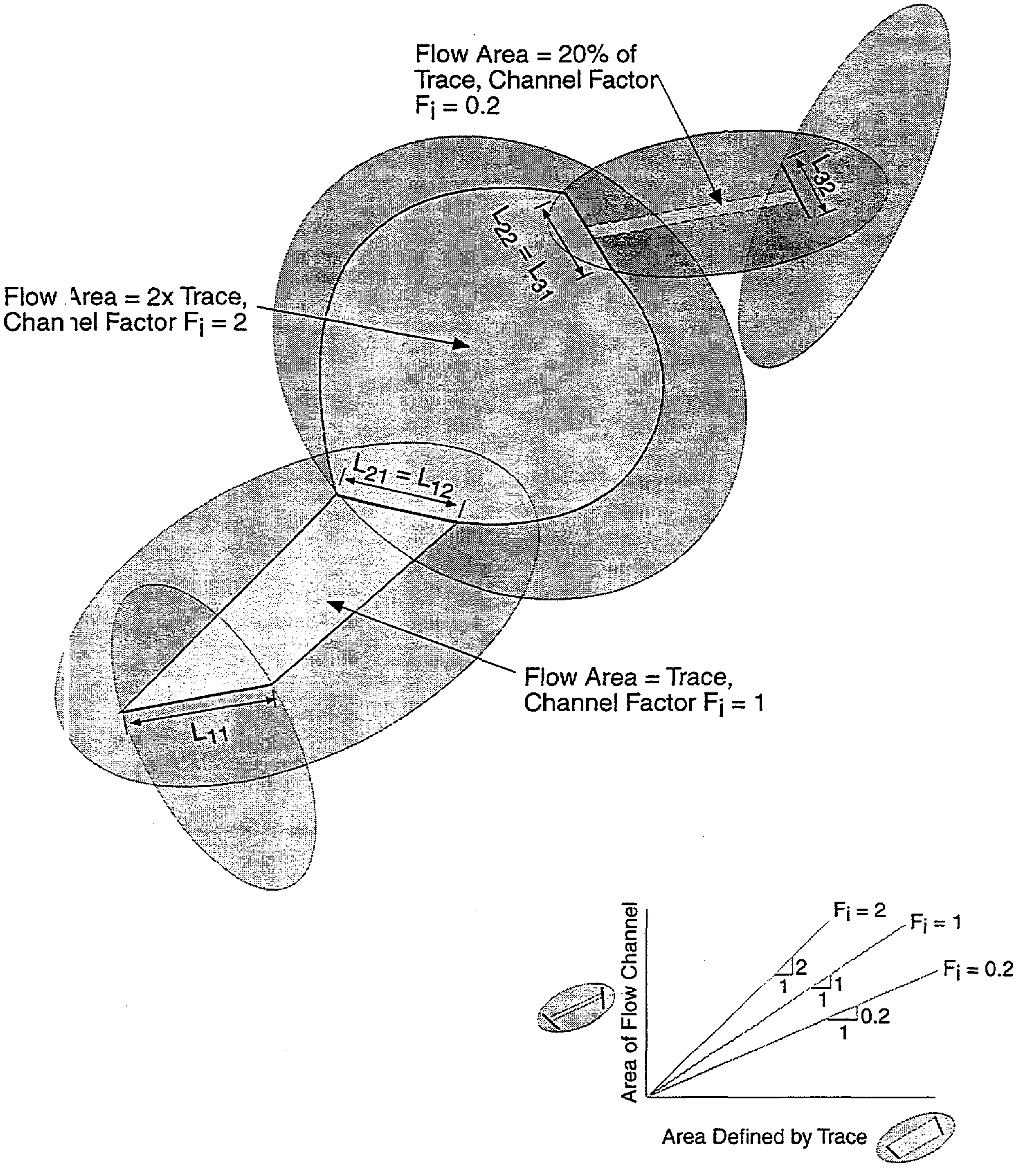

FIGURE **5-21**

FLOW WIDTH CHANNELING FACTOR F_i

BDM-NIPER/FRACMAN

4. **Flow Dimension:** Using this approach, a plot of radial distance from the well against conductance can be derived for any borehole configuration and DFN model. The slope S of this relationship on a log-log plot provides an estimate of the flow dimension as,

$$D = 1+S \tag{5-9}$$

where S is the non-linear regression fit to the radial distance vs. conductance plot. Examples of this calculation are provided in Figure 5-24.

By carrying out this analysis on a series of stochastic realizations of the DFN model, one can obtain a distribution of packer test flow dimension.

5. **Packer Test Transmissivity:** The packer test transmissivity T_{pi} for each network realization can be approximated by,

$$T_{pi} = f\,(\,\sum T_{fj}, D_i) \tag{5-10}$$

where T_{fj} is the transmissivity of each fracture intersecting the interval and D_i is the packer interval flow dimension calculated by equation 5-9 above.

6. **Comparison and Optimization:** The distributions of simulated and measured packer test transmissivity and flow dimension can then be compared to determine the match between the hydrogeological heterogeneity and connectivity of the simulated DFN and the *in situ* rock mass. The DFN can then be calibrated or conditioned to match the observed behavior.

5.3.3 Example Application

The approach described above has not yet been applied to *in situ* data. The demonstration described here is based on the example fracture network illustrated in Figure 5-22. The stochastic fracture network parameters used to generate this fracture pattern are given in Table 5-4.

Ten meter packer tests in the rock block were simulated using the method described above. Figure 5-23 illustrates the resulting plot for radial distance vs. conductance for each of the realizations of the fracture network model. Figure 5-24 illustrates the calculation of flow dimension from the slope of the log-log plot of radial distance against conductance for three of the realizations. Figure 5-25 presents a histogram of simulated 10 meter packer test flow dimension derived in this manner.

In the present simulation, the mean flow dimension is calculated at 2.4, with a standard deviation of 0.7. This degree of flow dimension variability is consistent with a relatively heterogeneous system in which each well test behaves in a different manner. In general, however, the network is sufficiently well connected that the flow dimension approaches three for many of realizations. As a result, reservoir production could be better than would be predicted by a radial (D=2) analysis of flow.

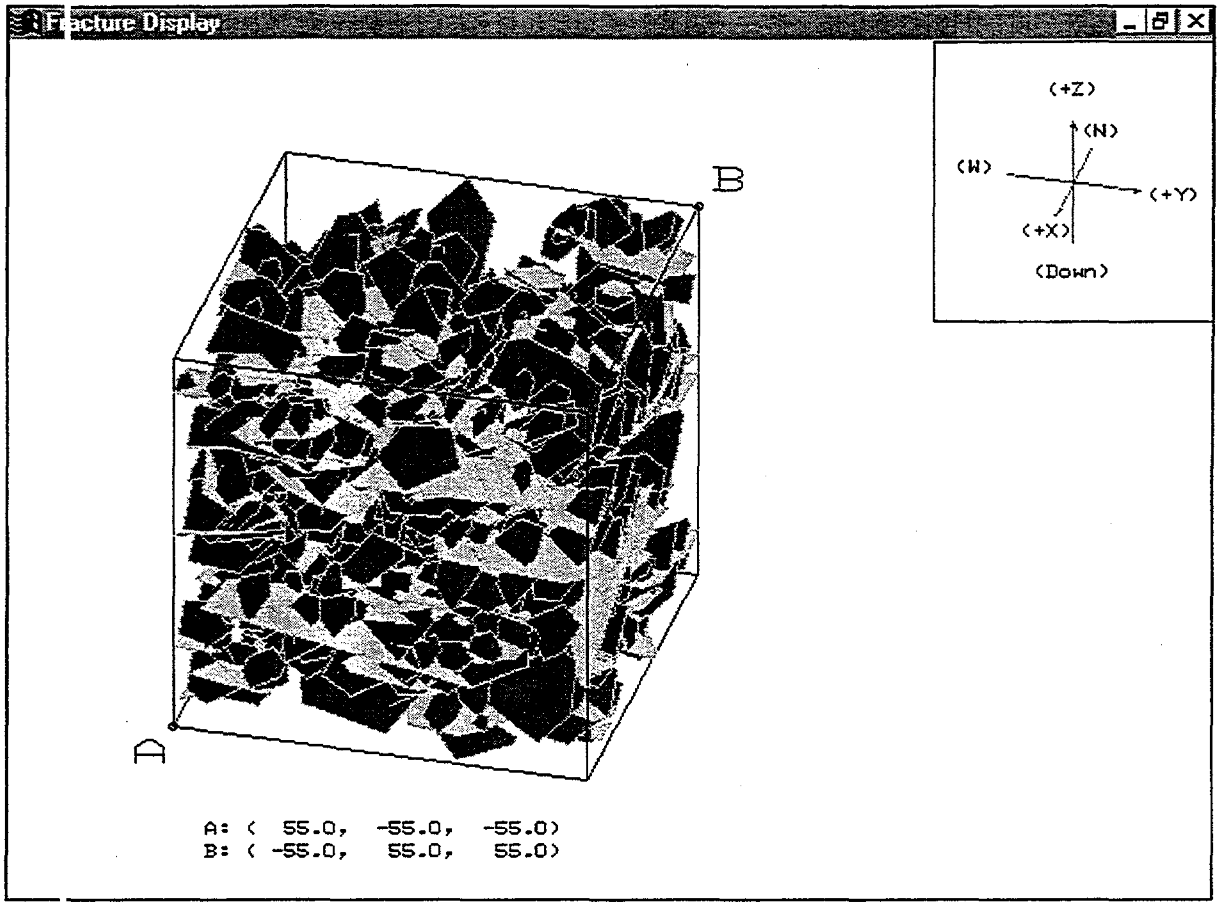

```
A: (  55.0,  -55.0,  -55.0)
B: ( -55.0,   55.0,   55.0)
```

FIGURE **5-22**
FRACTURE NETWORK MODEL USED FOR SIMULATION
BDM-NIPER/FRACMAN

PROJECT NO. 963 1357.521 DRAWING NO. 69391 DATE 4/4/97 DRAWN BY EA

Golder Associates

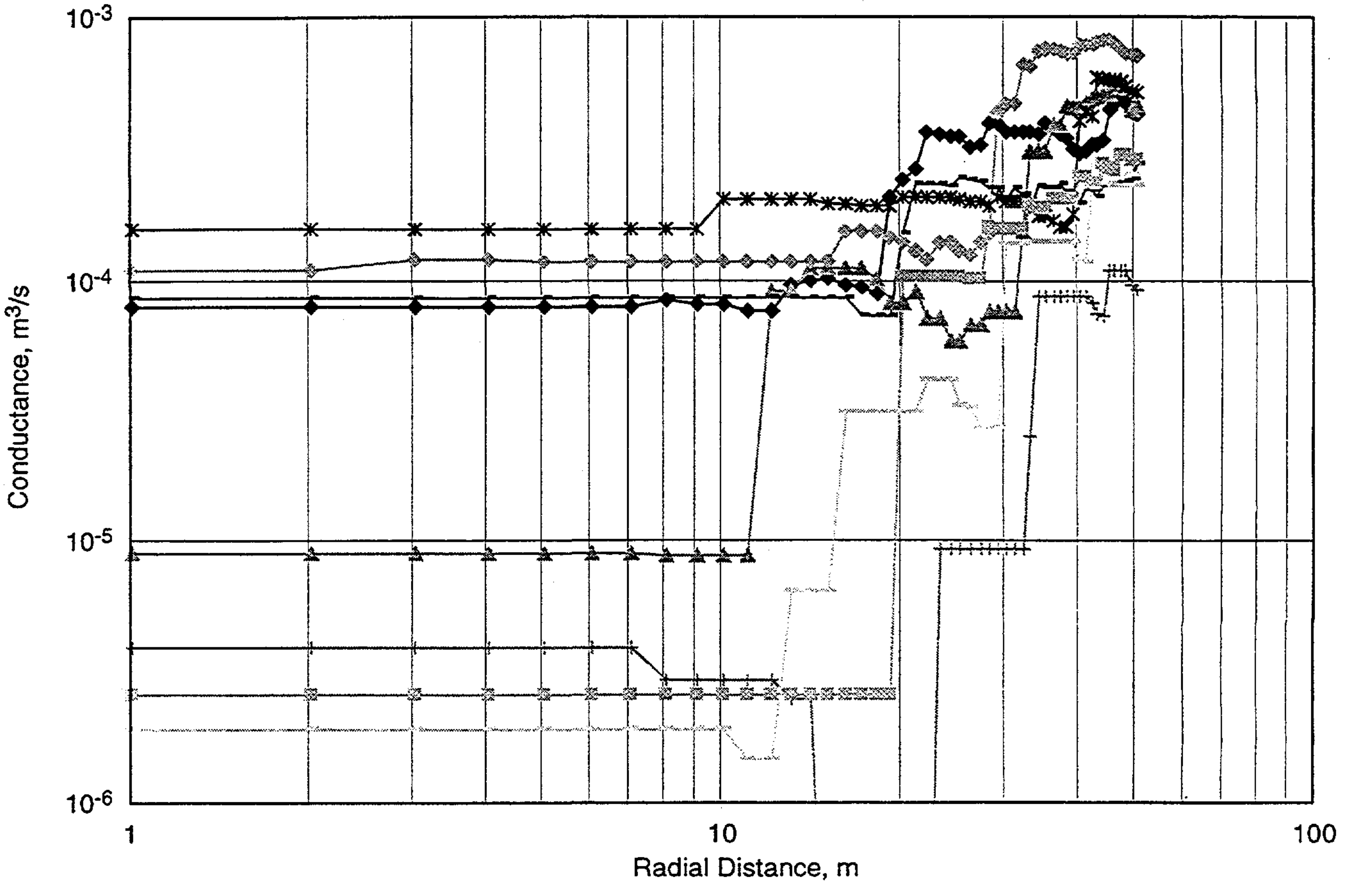

FIGURE **5-23**

CONDUCTANCE VS. RADIAL DISTANCE FROM SIMULATIONS

BDM-NIPER/FRACMAN

PROJECT NO. 963 1357.521 DRAWING NO. 69390 DATE 4/4/97 DRAWN BY EA

Golder Associates

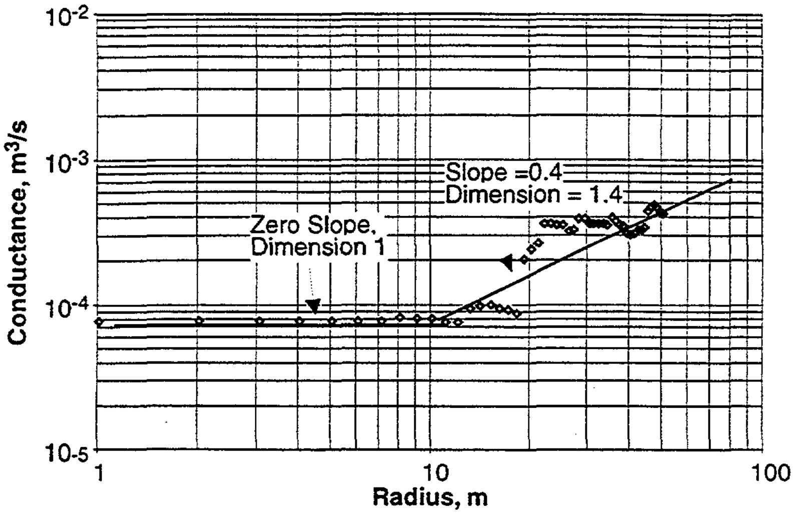

(a) Realization 1, Dimension = 1.4

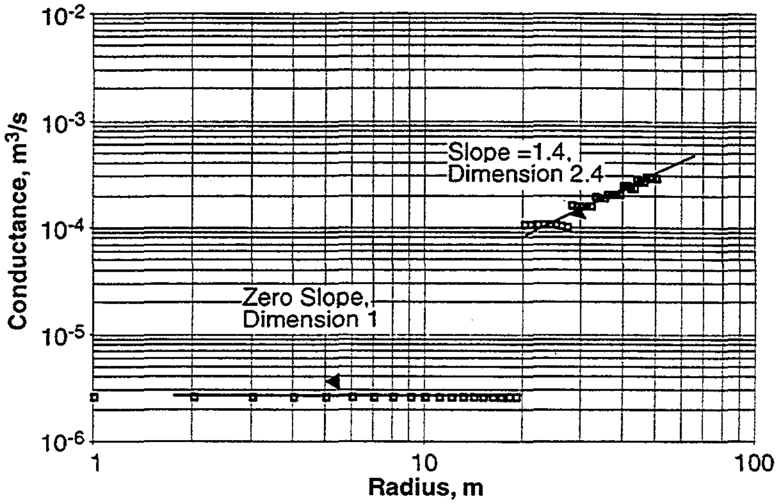

(b) Realization 10, Dimension = 2.4

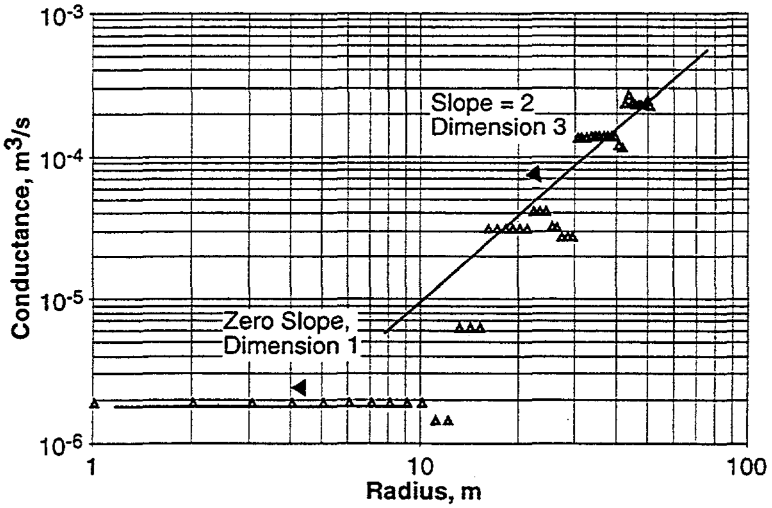

(c) Realization 8, Dimension = 3

FIGURE **5-24**

CALCULATION OF FLOW DIMENSION FROM CONDUCTANCE VS. RADIAL DISTANCE PLOTS

BDM-NIPER/FRACMAN

PROJECT NO. 963 1357.521 DRAWING NO. 69388 DATE 4/4/97 DRAWN BY EA

Golder Associates

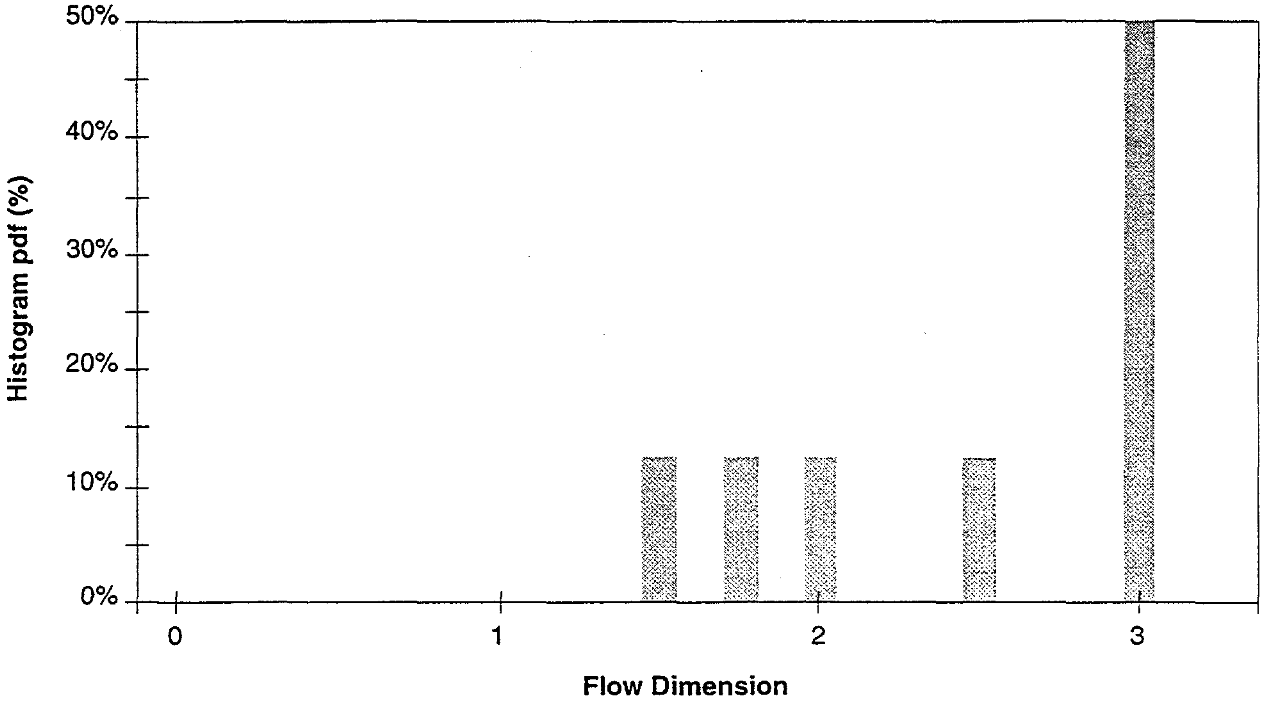

FIGURE **5-25**
DISTRIBUTION OF FLOW DIMENSION FROM ANALYSIS OF SIMULATIONS
BDM-NIPER/FRACMAN

Table 5-4 DFN Parameters for Demonstration Fracture Network

Parameter	Set 1	Set 2
Spatial Model	Baecher (Dershowitz et al., 1996)	BART (Dershowitz et al., 1996)
Size	Log Normal Distribution Mean Radius = 10m Std Dev. Radius = 7m	Log Normal Distribution Mean Radius = 7m Std Dev. Radius = 3m
Intensity	P_{32} (Area/Volume) = 0.05 m^2/m^3	P_{32} (Area/Volume) = 0.10 m^2/m^3
Orientation	Mean Pole Trend $\theta = 0$ Mean Pole Plunge $\phi = 90$ Fisher Distribution, $\kappa = 30$	Mean Pole Trend $\theta = 45°$ Mean Pole Plunge $\phi = 45°$ Fisher Distribution, $\kappa = 30$
Termination	0%	100%
Transmissivity	Log Normal Distribution Mean = 10^{-6} m^2/s St. Dev. = 5×10^{-7} m^2/s	Log Normal Distribution Mean = 10^{-6} m^2/s St. Dev. = 5×10^{-7} m^2/s

For analysis of a site with calculated flow dimension distributions from *in situ* data, the simulated distribution of packer test transmissivity and flow dimension could be compared directly to measured distributions of packer test transmissivity and flow dimension. The DFN parameters could then be adjusted to obtain a DFN model with the same hydrological connectivity and heterogeneity as in the rock mass itself. For a site in which *in situ* flow dimensions are not available, the analysis above could be used with a DFN model based on other data to predict or estimate the flow dimension of the rock mass for specific well test geometries.

5.4 Task 2.1.4 Compartmentalization Analysis

During the year, software as well as algorithms was implemented corresponding to the compartmentalization analysis, tributary volume analysis, and reservoir block volume.

5.4.1 Algorithms

Compartmentalization in reservoirs where fractures dominate permeability often leads to wells that produce at different rates and volumes than expected. Within compartments, pressure communication can be nearly instantaneous, while nearby wells in different compartments may have very little communication. This situation can lead to several undesired consequences, among them, unanticipated interference among wells, reduced recovery efficiency, and increased production uncertainty. Estimating the degree of compartmentalization is important at all stages of field development in order to properly engineer the field and to provide realistic recovery estimates and rates for financial decisions.

Compartmentalization may be due to several factors: fault offset of the producing horizon; the existence of high permeability sub-vertical faults that form barriers to lateral migration; the reduction in permeability of fractures due to mineralization; and the natural geometrical clustering of joint and smaller fault networks when matrix permeability is low. In terms of thermal recovery projects, there is an additional type of compartmentalization that is dynamic. Injected steam loses heat to the matrix and condenses. This condensation "front", which may be less of a definable surface than it is a series of fingers reaching out from the well along fracture paths, forms the steam "compartment". Knowledge of the shape and extent of this compartment is crucial to optimizing production. It is a combination of the natural geometrical compartmentalization of the fracture networks, and the ability of the fractures in the networks to exchange heat with the matrix. The geometry of the fracture networks places constraints on the steam compartments; the steam compartments can never be bigger than the networks themselves.

It is usually possible to identify large-scale fault-bounded reservoir compartments from seismic or production histories. It is far more difficult to assess the compartmentalization due to joint network geometry and connectivity, for which seismic is of little use. Joint network compartmentalization is often suspected when static and dynamic calculations of recoverable oil or gas do not agree, and their is no evidence for fault-offset or others types of fault-related compartmentalization in a fractured reservoir.

For this reason, two approaches have been developed and are being evaluated to address the more general problem of joint network compartmentalization for non-thermal applications, and also to extend the calculation for steam injection applications.

Figure 5-26 shows a hypothetical discrete fracture network. In this model, there are clusters of fractures, despite the apparent high density of fracturing. Each well shown in the model intersects a different cluster. In other words, these wells could only communicate with each other through the matrix. If this were a field, it would be important to determine the volumes of these compartments, which ultimately relates to the amount of hydrocarbon that a well can produce, and the horizontal dimensions of these compartments, which relates to optimal well spacings and the efficiency of primary or secondary recovery for a specified well pattern.

This task is focused on development of the technology for analysis of compartmentalization in fractured rock masses, where the compartmentalization is controlled by such fracture location heterogeneity. This task is related to Tasks 1.3.1 and 1.3.2, which address similar issues of fracture geometry, and Task 2.1.2, which deals with fracture spatial location distributions.

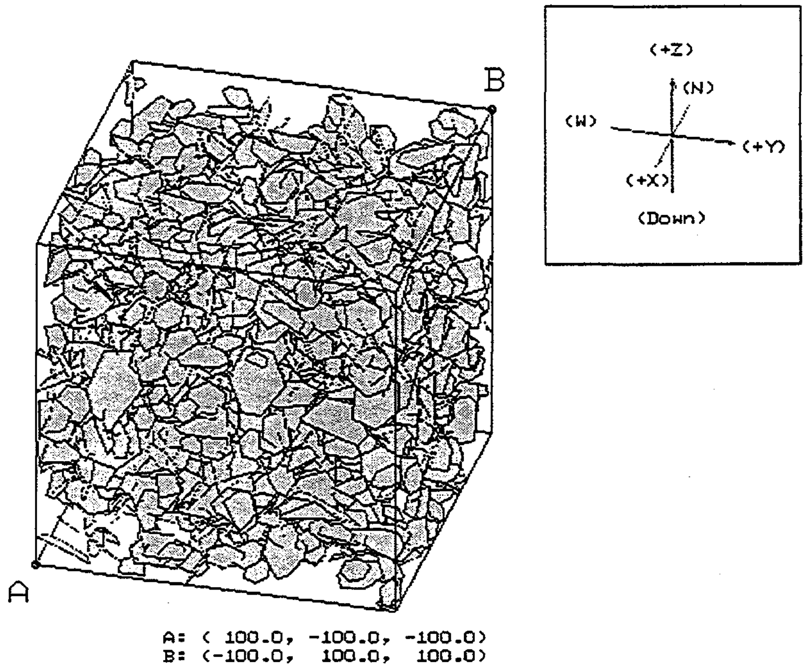

(a) Fracture Pattern

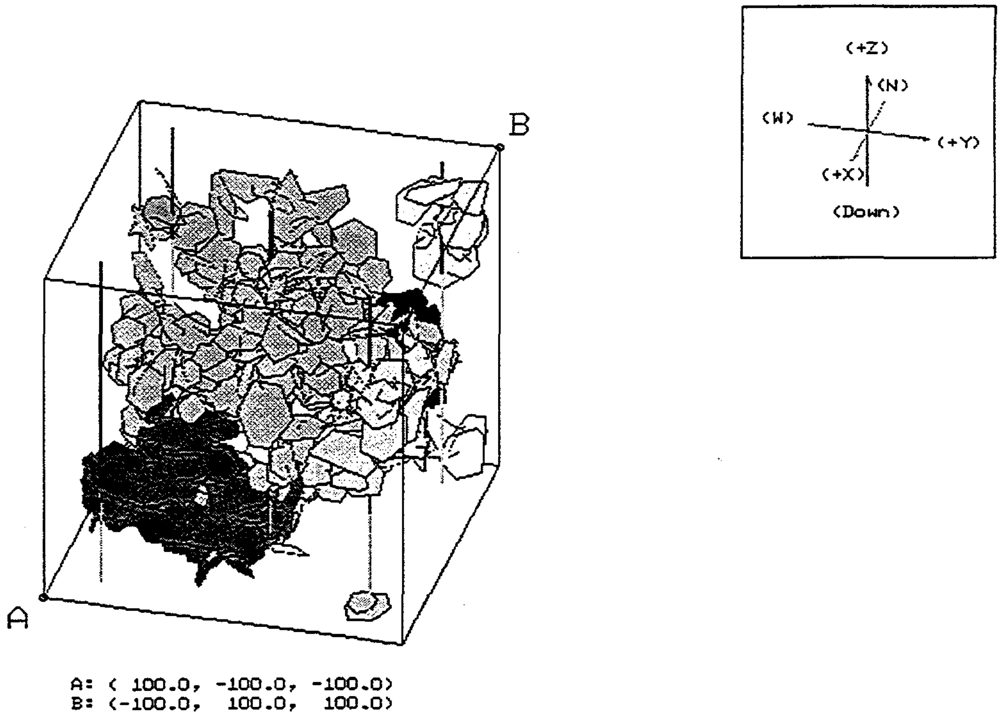

(b) Compartmentalization

FIGURE **5-26**
COMPARTMENTALIZATION OF INTENSITY, FRACTURED RESERVOIR
BDM-NIPER/FRACMAN

PROJECT NO. 9 3 1357.521 DRAWING NO. 69417 DATE 4/11/97 DRAWN BY CB

Golder Associates

5.4.2 Algorithm to Compute the Volume and Horizontal Extent of Fracture Network Compartments

The computation of the volume and horizontal extent of joint network compartments is a three-step process:

Step 1. Identify individual fracture networks within the DFN model

Step 2. Compute the bounding surface for each identified network

Step 3. Calculate the volume of the bounding surface and the horizontal extent of the network

The identification of the individual fracture networks is a straightforward process for which robust algorithms have been developed. After the DFN model has been created, the intersections among the fractures is calculated. This leads to a symmetrical matrix of "1"'s and "0"'s, where "1" indicates an intersection. This connectivity matrix is then searched beginning with fracture number 1 in a standard tree search. This search process is repeated for all fractures that do not belong to any previously identified cluster until all fractures in the model have been processed. The results of this first step are saved as a list of fractures belonging to each cluster.

The second step is the calculation of the bounding surface for each cluster. Each network may be irregular. While it would be possible to compute the "bounding box" (Figure 5-27) for a network, and use this box volume and horizontal cross-section as surrogates for compartment volume and horizontal extent, this would lead to an overestimation in most cases of both volume and cross-section. This in turn would produce overestimates of the ultimate recovery from wells, and suggest greater well spacings and recovery efficiencies than would actually be the case (Figure 5-28).

To reduce the potential for overestimates, it is necessary to calculate a bounding surface that better approximates the outer limits of the network. A convex hull, as described in Section 4.1.1.1.2 meets these requirements.

Figure 5-29 shows the three-dimensional convex hull calculated using the QuickHull algorithm and the Qhull software package (Barber et al., 1995). As this figure shows, the shapes of the discrete fracture network (DFN) of Figure 5-26 would not be well-approximated by a bounding box for many of the networks.

The final step is to compute the volume and cross-sectional area of each hull. This is easily done. First, Qhull contains options to compute the volume of the hull, and to output the coordinates of vertices belonging to the hull. From these vertices, it is possible to compute another convex hull which represents the horizontal extent (Figure 5-29).

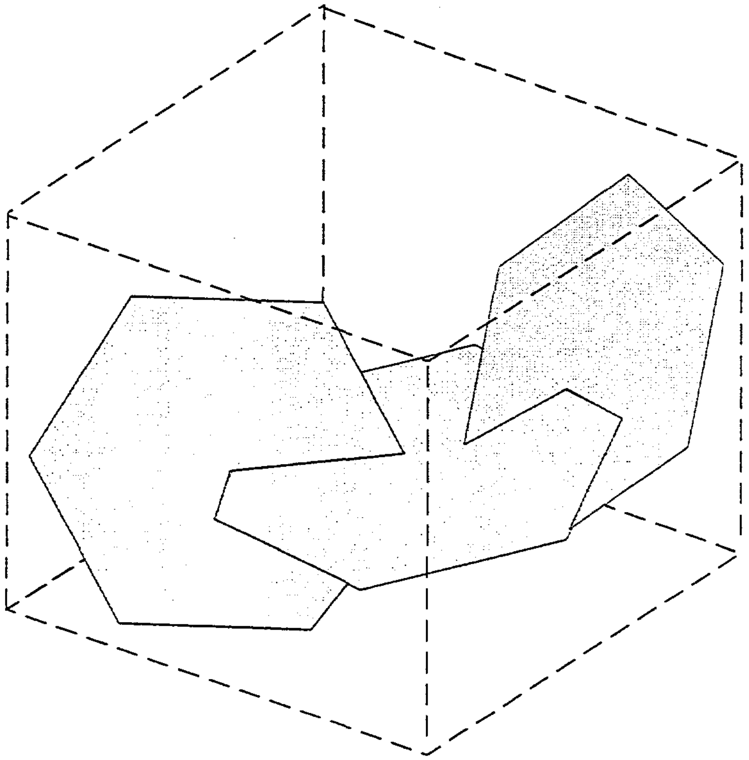

FIGURE **5-27**

FRACTURES IN BOUNDING BOX

BDM-NIPER/FRACMAN

PROJECT NO. 963 1357.521 DRAWING NO. 69418 DATE 4/4/97 DRAWN BY CB

Golder Associates

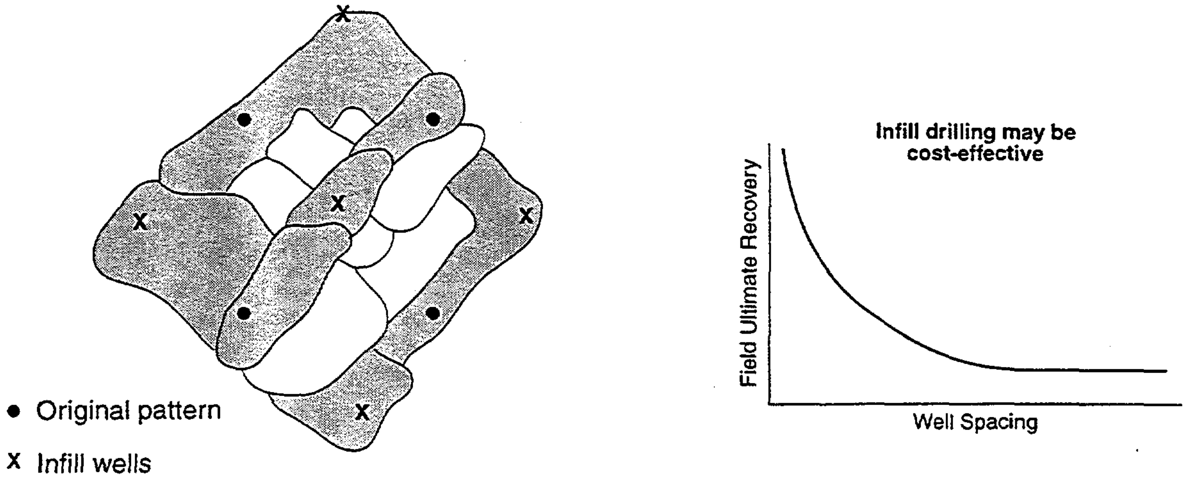

(a) Compartments Smaller than Well Spacing

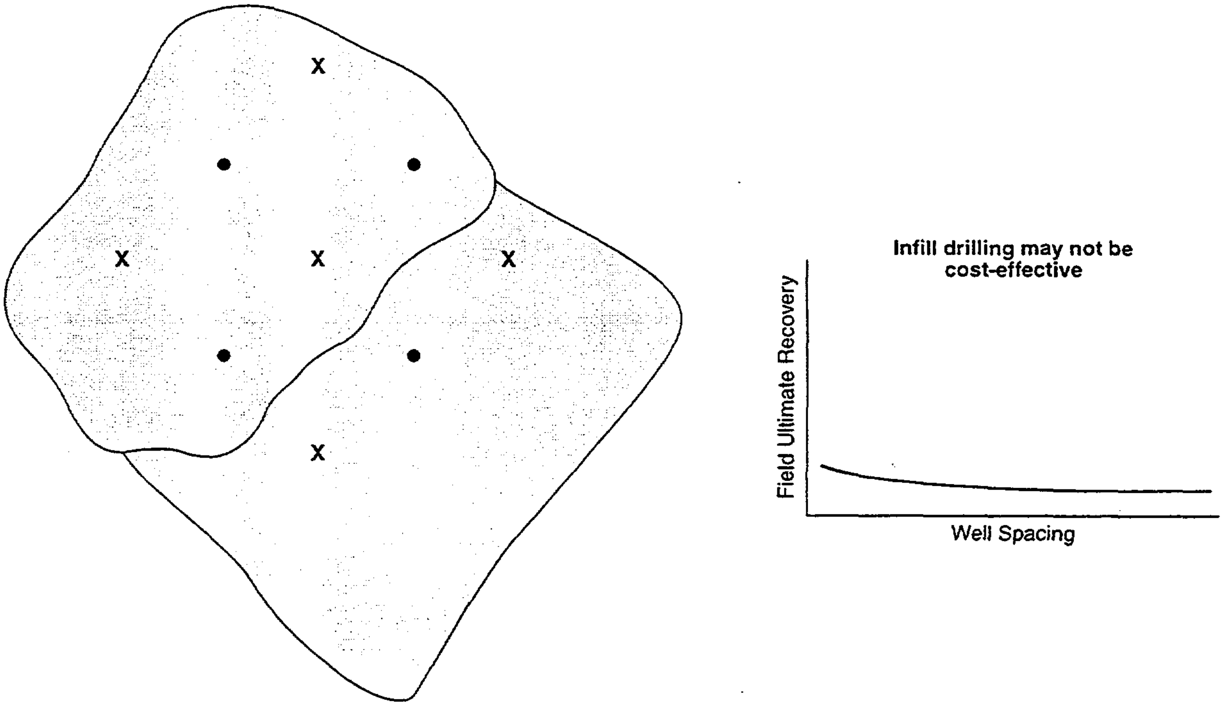

(b) Compartments Larger than Well Spacing

FIGURE **5-28**

IMPORTANCE OF COMPARTMENT SIZE FOR WELL PATTERN OPTIMIZATION

BDM-NIPER/FRACMAN

PROJECT NO. 963 1357.521 DRAWING NO. 69419 DATE 4/4/97 DRAWN BY CB

Golder Associates

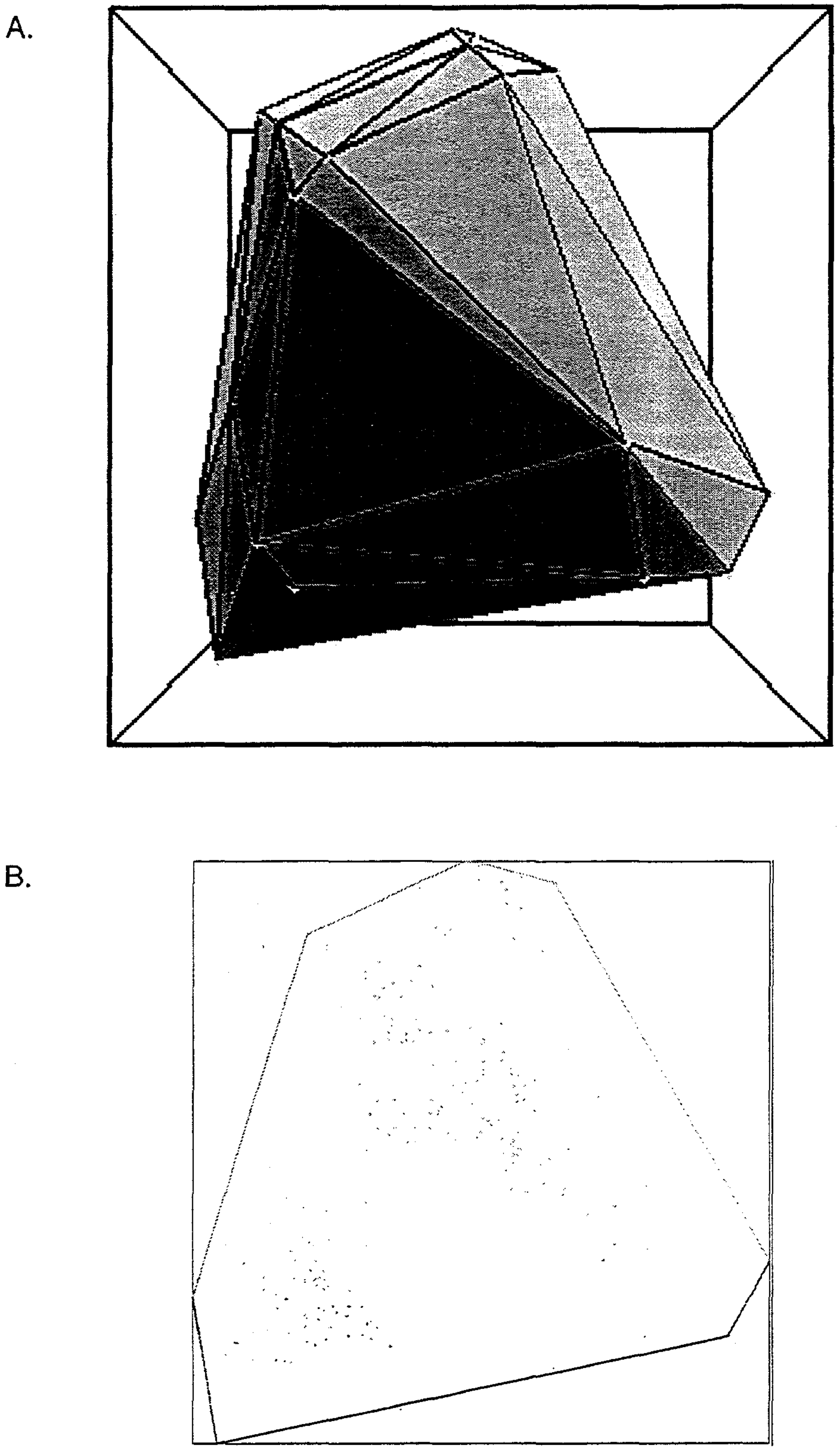

FIGURE **5-29**
THREE DIMENSIONAL CONVEX HULL
BDM-NIPER/FRACMAN

For vertical wells, the probability of whether the well will intersect an underlying cluster (given that the well will be drilled deeply enough to intersect the cluster) does not depend upon the Z-coordinates of the cluster. The intersection probability is only a function of the X- and Y-coordinates. The shape and area of this horizontal extent is easily determined by calculating the two-dimensional convex hull of the (X,Y) data points belonging to the three-dimensional convex hull that bounds the network cluster. This algorithm can easily be extended to non-vertical wells by projecting the coordinates of the three-dimensional hull onto a plane that is perpendicular to the well trajectory.

Results for the volume and horizontal extent for the hypothetical model are shown in Table 5-5.

Table 5-5 Calculation of Volume and Horizontal Extent for Hypothetical Model

Volume (m^3)	156,789
Horizontal Area (m^2)	4369.0
Bounding Box (m)	81.0 x 82.4
Hull/Bounding Box	65%

5.4.3 Algorithm to Compute Steam Compartmentalization

The compartmentalization defined by the condensation front of injected steam is a dynamically-changing process. As the matrix heats up with time due to steam injection, the condensation front moves downstream into new fractures. Not all of the matrix encompassed by the fracture compartment defined by fracture geometry is immediately heated by injected steam. Factors such as the conductivity of the fractures, their surface area, and the adjacent rock temperature gradient influence this process.

While it is not possible to carry out a detailed, dual-phase, dual-porosity simulation of this process for large fracture networks, it is possible to capture first-order effects of this process for the purposes of estimating steam compartmentalization.

The algorithm builds upon the geometrical clusters identified in the previous steps. To evaluate the rate and shape of compartment growth, a well is inserted into one of the geometric network clusters. Heat "particles" are injected into the well in the same way that tracer particles are injected in particle-tracking schemes in groundwater flow modeling codes. Miller et al. (1995) describe the MAFIC code which carries out this type of particle-tracking simulation for tracers. The equations for tracer transport and heat transport (as hot water) are identical, except for the need to have heat capacity for the fracture and a heat capacity for the effective bulk matrix. To simplify the process, diffusive transport within the fracture flows is neglected. We assume that the dominant mechanism for heating the matrix is conduction of heat from the fracture to the matrix, and that other heat transfer mechanisms are less important.

In this initial effort, overburden heat losses are ignored. Eventually, it may be necessary to modify the algorithm to represent conduction of heat into semi-infinite media to account for this heat loss mechanism.

This algorithm represents a first stage in modeling steam compartment formation through time. Clearly, flow of condensing steam is not the same as flow of an incompressible, single phase fluid, but the single-phase approximation used in this algorithm is a reasonable starting point to learn about heat transfer in a complicated discrete fracture network. In reality, as steam condenses in the fractures, the velocity of flow changes due to steam collapse and density contrasts near the periphery of the steam zone. It may be possible to use an effective viscosity approach to model the moving steam in a way that accounts for the change in steam quality with distance. The effective viscosity would depend upon steam quality, which in turn, is a function of the heat balance along the fracture.

6. TASK 3.1 LINKAGE TO STATIGRAPHIC RESERVOIR MODELS

The linkage between reservoir and DFN simulators will be the focus of the second year of this research project. During the first year, initial discussions were carried out between Golder Associates and Marathon Oil to define the linkage to be made between three discrete fracture network (DFN) models and the StrataModel stratigraphic analysis package.

6.1 Task 3.1.1 StrataModel/DFN Integration

Initial development of the link between DFN and reservoir models focused on definition of DFN and StrataModel file formats and underlying concepts. Two fundamental concepts are under development:

- Mapping individual discrete features into StrataModel using custom file formats
- Converting fracture networks to material zones which can be directly displayed and manipulated in StrataModel

6.1.1 Discrete Fracture Mapping

StrataModel uses information on stratigraphy and structure to define the geometry of cells and to assign cell attributes. Faults are often used as boundaries for groups of cells, or as control surfaces for interpolating stratigraphy and lithology. Indeed, StrataModel contains sophisticated algorithms for modeling cells near faults represented as discrete surfaces that die out laterally and vertically.

Both large displacement faults and smaller displacement faults can compartmentalize reservoir units There faults influence sweep efficiency, production rates and ultimate recovery.

Major faults can frequently be identified deterministically through seismic reflection and well penetrations. In addition to these known features, there are frequently faults with smaller displacements which are difficult to resolve from seismic data, and need to be characterized and analyzed stochastically. Faults which are outside of range of the seismic characterization program must also be characterized and analyzed stochastically.

In such cases, DFN models can be used to generate faults using a conditioned deterministic/stochastic approach in which known large displacement faults are combined with stochastically realized smaller displacement faults (Dershowitz and La Pointe, 1995). As an example of conditioning, consider a site where field measurements indicate that a particular set of faults has a statistical distribution of sizes, described by a lognormal distribution with mean 90,000 m^2 and a standard deviation of 50,000 m^2.

Conditional simulation starts with a stochastic DFN realization of this fault population (Figure 6-1). Figure 6-2 illustrates the simulated trace map generated by a horizontal section through this DFN. This can represent either a vertical seismic section or a top of reservoir structure map. These fault traces can then be censored to remove trace lengths less than the smallest one mapped. The remaining traces can then be compared against the actual fault trace length distribution. The mean and standard deviation are adjusted using a grid search until the truncated synthetic trace length distribution approximately matches the observed. In this method, it is assumed that the truncated traces correspond to fractures either lying outside of the seismic grid, or are small enough that they were not intersected by seismic profiles. Thus, it is possible to generate stochastic realizations of the faults using these size parameters. The faults above the truncation threshold are removed and replaced by the actual faults detected through seismic. The faults below the truncation threshold are retained.

Thus, it is possible to generate a better reservoir model than one which only contains the faults directly detected by the seismic grid. These stochastic faults are put into the StrataModel reservoir model in the same way that the seismically-detected faults are incorporated. If desired, several stochastic StrataModel realizations can be generated using this procedure, and used to form the basis of reservoir models that more accurately capture faulting in the reservoir and also account for uncertainty in faulting not detected through seismic.

6.1.2 Material Zone Mapping

StrataModel can represent three-dimensional geology using a cellular data structure. This package is often used as a system for building input for reservoir simulators, as well as a reservoir or basin visualization tool. The advantage of a software tool like StrataModel is that it conditions the properties of each cell to complex internal stratigraphic and structural reservoir architecture, and makes it possible to guide the distribution of reservoir data throughout the model.

Software linking between DFN models and reservoir simulators such as ECLIPSE and THERM-DK requires that the DFN models be adapted to provide the parameters needed for input for each simulator grid cell. The input for the simulators, in turn, often derives from a cellular reservoir modeling system like StrataModel. Figure 6-3 illustrates this process.

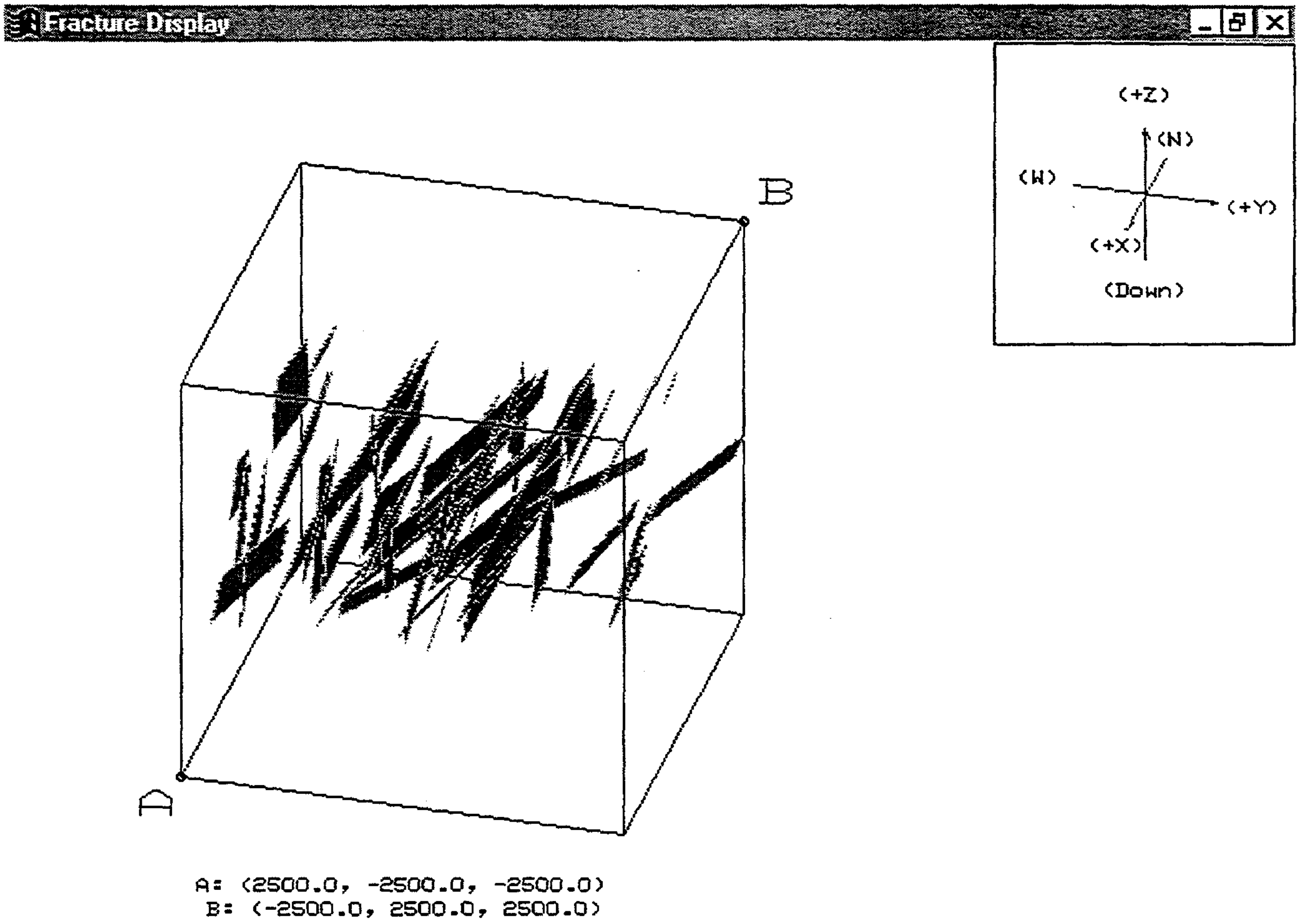

```
A: (2500.0, -2500.0, -2500.0)
B: (-2500.0, 2500.0, 2500.0)
```

FIGURE **6-1**
EXAMPLE DFN MODEL FOR STRATA MODEL LINKING
BDM-NIPER/FRACMAN

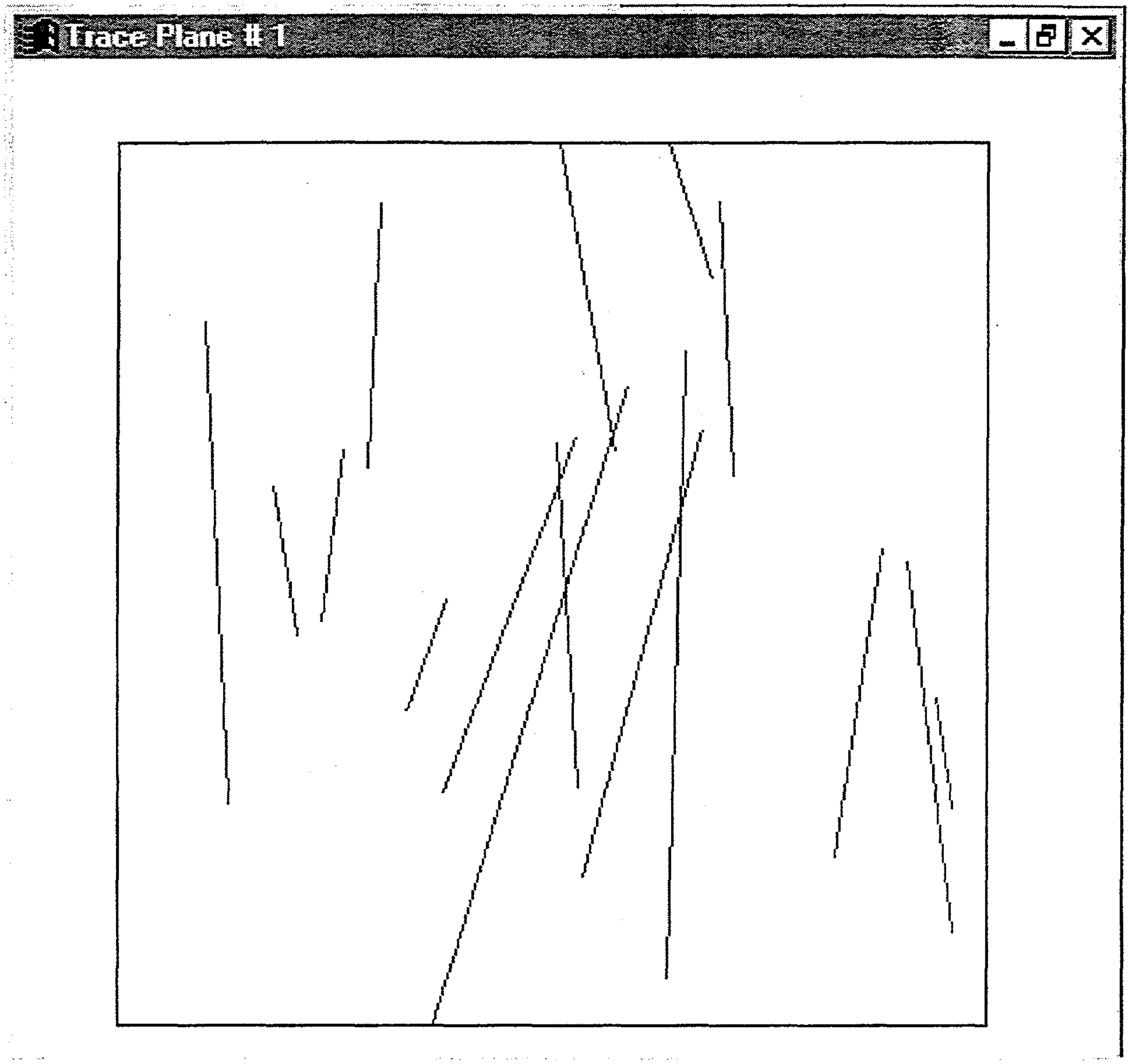

FIGURE **6-2**

SIMULATED HORIZONTAL SECTION

BDM-NIPER/FRACMAN

PROJECT NO. 963 1357.521 DRAWING NO. 69440 DATE 4/7/97 DRAWN BY EA

Golder Associates

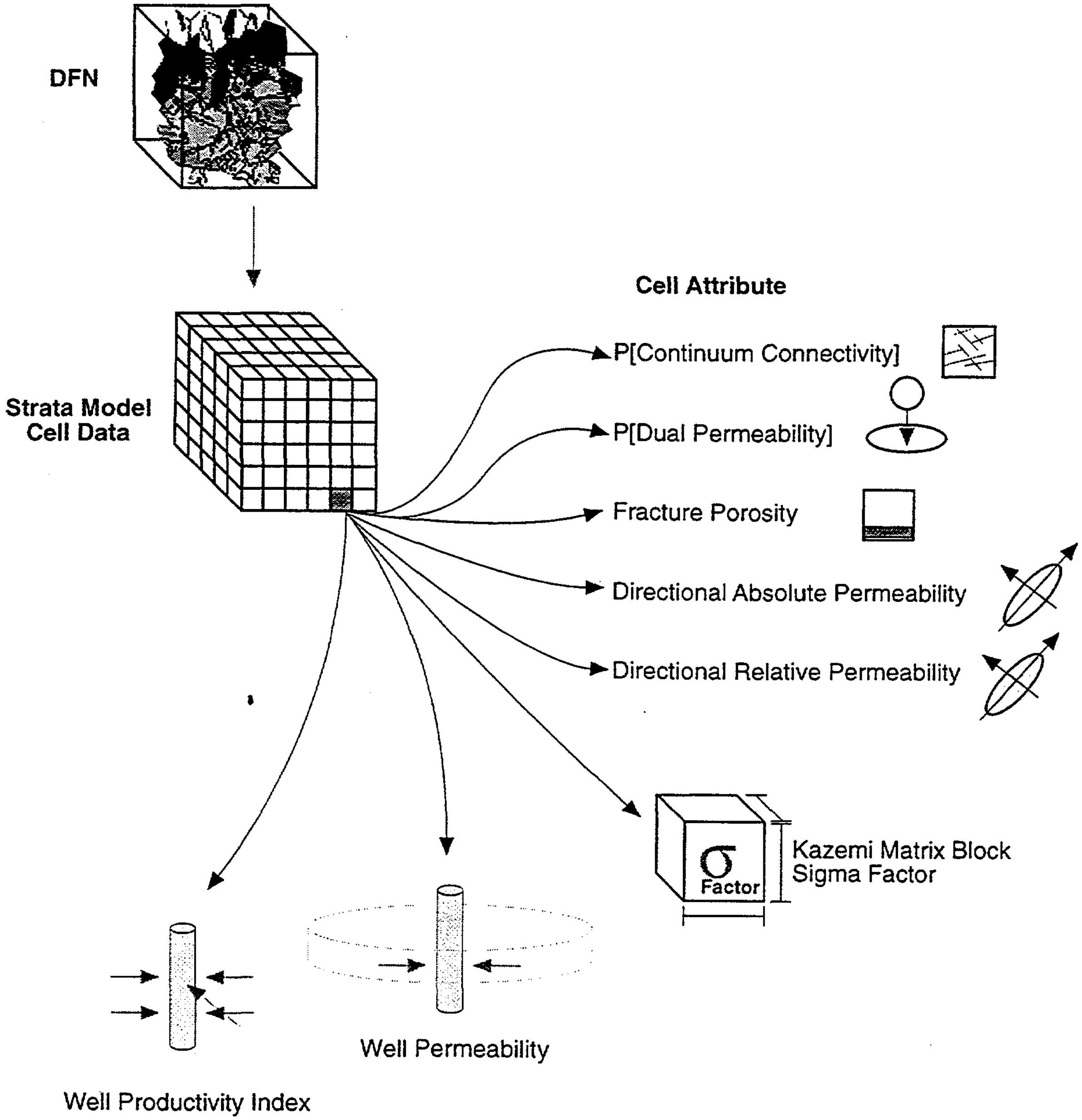

FIGURE **6-3**

STRATA MODEL ↔ DFN LINKING

BDM-NIPER/FRACMAN

PROJECT NO. 963 1357.521 DRAWING NO. 69441 DATE 4/11/97 DRAWN BY EA

Golder Associates

Eight fracture network properties have been identified during the first year of this project which can be derived from a DFN model and incorporated as attributes in StrataModel, which then can be used for reservoir simulation. The eight attributes for each cell are:

- Probability that a particular cell contains sufficient fracture connectivity to be modeled as a continuum,
- Probability that a particular cell contains sufficient fractures to be modeled as a dual-permeability material,
- Fracture porosity,
- Directional absolute permeability in user-specified directions,
- Directional relative permeabilities,
- Matrix-fracture coupling, as expressed by typical X, Y and Z matrix block dimensions and a formula such as Kazemi et al.'s (1976) Sigma factor,
- Well permeability, and
- Well productivity/injectivity index.

The strategy developed for calculation of these attributes from a DFN model is summarized as follows.

The first step is to define domains within the DFN model that have statistically homogeneous fracturing. This information is generated during DFN model construction, and is equivalent to the boundaries of the fracture generation regions specified during DFN model construction.

Next, each fracture generation region or domain is processed in turn to yield the eight attributes listed above. For each domain, fracturing is statistically homogeneous, so location within the domain does not matter by definition. However, many of the attribute values will be sensitive to cell size within the domain. The user specifies a cell size range for each domain to compute the eight attributes. For a given cell size, several random samples of the DFN model are extracted from the generation region. First, the geometrical attributes are calculated. Porosity is calculated as:

$$\phi_{cell} = \sum_{i=1}^{n} A_i * t_i \tag{6-1}$$

where A_i is the area of the ith fracture, n the cell, and t_i is the aperture of the ith fracture.

Matrix-fracture coupling is represented as the Sigma factor:

$$\sigma_{cell} = 4*\left(\frac{1}{L_x^2}+\frac{1}{L_y^2}+\frac{1}{L_z^2}\right) \tag{6-2}$$

where L_x, L_y and L_z represent the average X-, Y- and Z-direction fracture spacings in the cell.

The probability that there is no component of fracture permeability in the cell is based upon fracture connectivity from one side of the cell to the opposite side for all six cell faces. It is based on computing the connectivity in three directions for a series of random samples from the DFN model, and is computed as:

$$\Pr(no\ K_f\ in\ direction\ j) = \frac{\sum cells\ with\ no\ connectivity}{\sum cells} \tag{6-3}$$

Connectivity is calculated using the tools developed for compartmentalization analysis during the project's first year.

The computation of the probability that the cell can be reasonably modeled as a continuum, the directional absolute and relative cell permeabilities, and the well productivity/injectivity index requires MAFIC (Miller et al, 1995) DFN flow simulations, as described in Table 6-1 (also see Chapter 7). Well inflow performance in Eclipse as well as other simulators is described by an equation of the form (Intera, 1994):

$$q_{pj} = T_{wf} M_{pj}\left(P_j - P_w - H_{wj}\right) \tag{6-4}$$

where

q_{pj} is the volumetric flow rate of phase p in connection j at stock tank conditions,
T_{wj} is the connection transmissibility factor, defined below,
M_{pj} is the phase mobility at the connection,
P_j is the nodal pressure in the grid block,
P_w is the bottom hole pressure, and
H_{wf} is the well bore pressure head between the connection and the well's bottom hole datum depth.

The well permeability, k_h, enters into the connection transmissibility factor as:

$$T_{wj} = \frac{c\theta k_h}{\ln(r_o / r_w) + S} \tag{6-5}$$

where:

c is a unit conversion factor,
θ is the angle of the segment connecting the well, in radians,
k_h is the effective permeability times thickness of the connection,
r_o is the "pressure equivalent radius",

r_w is the well bore radius,
and S is the skin factor.

The permeability, k_h, is computed using the Flare approach described in Section 5.3 above. The well injectivity/productivity index is computed using the methods described in the La Pointe et al.(1996) prepared during the first year of the project. These attributes are then assigned to each cell in StrataModel for each generation region based upon cell size.

7. TASK 3.2 INTEGRATED FRACTURED RESERVOIR DISCRETE FRACTURE MODEL

The integration of discrete feature network (DFN) modeling approaches will be a prime focus of the second year of this research project. During the first year, preliminary steps were made toward these tasks.

7.1 Task 3.2.1 MS Windows 95 Fracture Data Analysis System

The fracture data analysis procedures developed in the context of Task 2 are being implemented as MS Windows 95 applications. Figure 7-1 illustrates the fracture data analysis components within the context of the data needs for DFN modeling. Progress was made on development of the following software versions which will be released during the second project year:

- **NeurIsis b1.0:** Fracture set clustering based on neural network algorithms,
- **FlowDim b1.0:** Fractional dimension type curve analysis
- **Flare b1.0:** Calculation of flow area and conductance in simulated fracture networks
- **Fractal b1.0:** Analysis of spatial patterns
- **FraCluster b1.0:** Analysis of clustering, tributary volume, and block size.

7.1.1 NeurIsis b1.0: Fracture Sets by Neural Nets

NeurIsis will be based on the program ISIS/N described in our second quarter progress report.

7.1.1.1 User Instructions

The user interface for NeurIsis is illustrated in Figure 7-2. The user interface is designed based on an "object oriented", tree structure model. Each fracture can have any number of properties, defined according to the class-types of Table 5-2 above. The menu options are listed in Table 7-1.

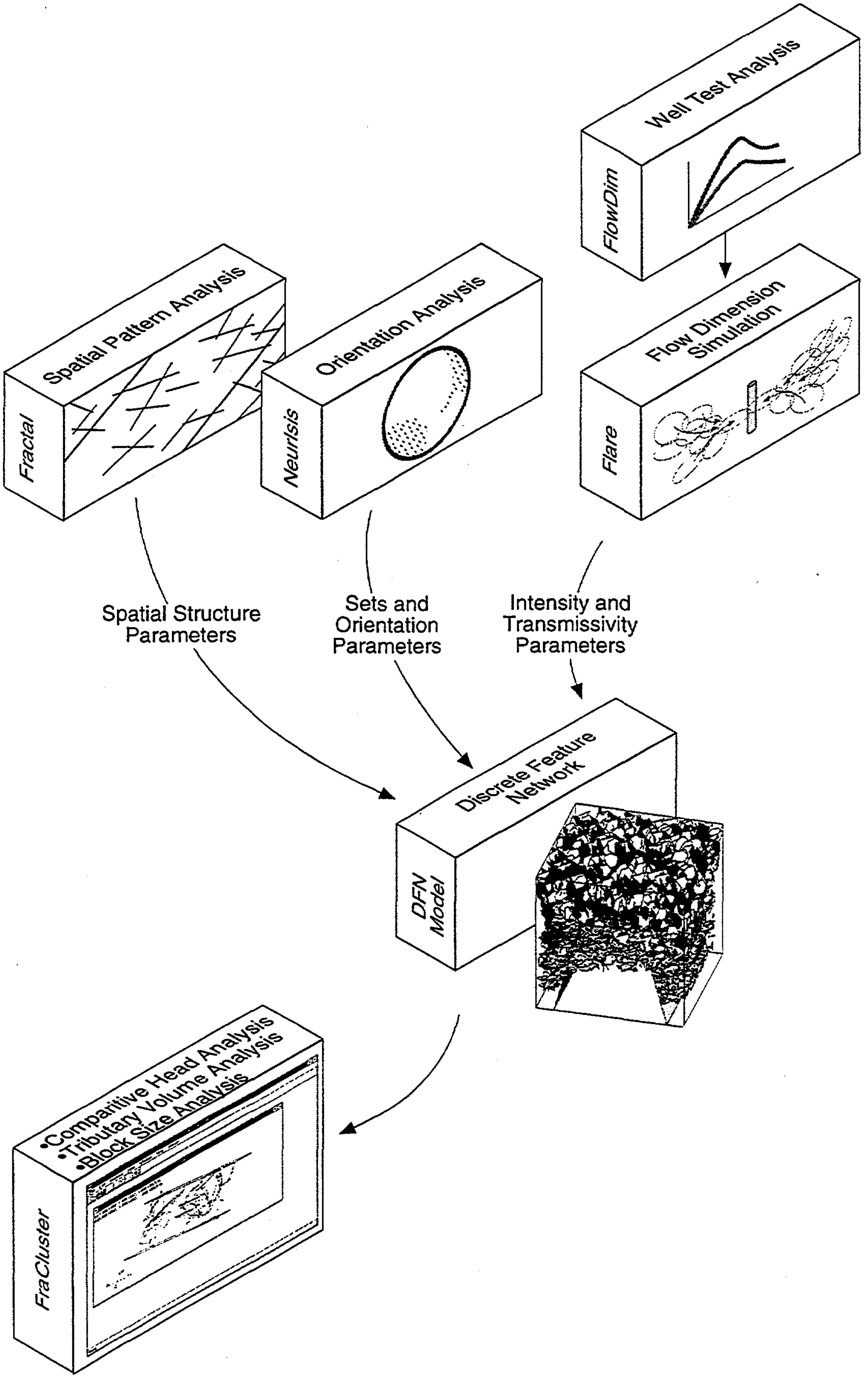

FIGURE **7-1**

FRACTURE DATA ANALYSIS SYSTEM

BDM-NIPER/FRACMAN

PROJECT NO. 963 1357.521 DRAWING NO. 69402 DATE 4/4/97 DRAWN BY EA

Golder Associates

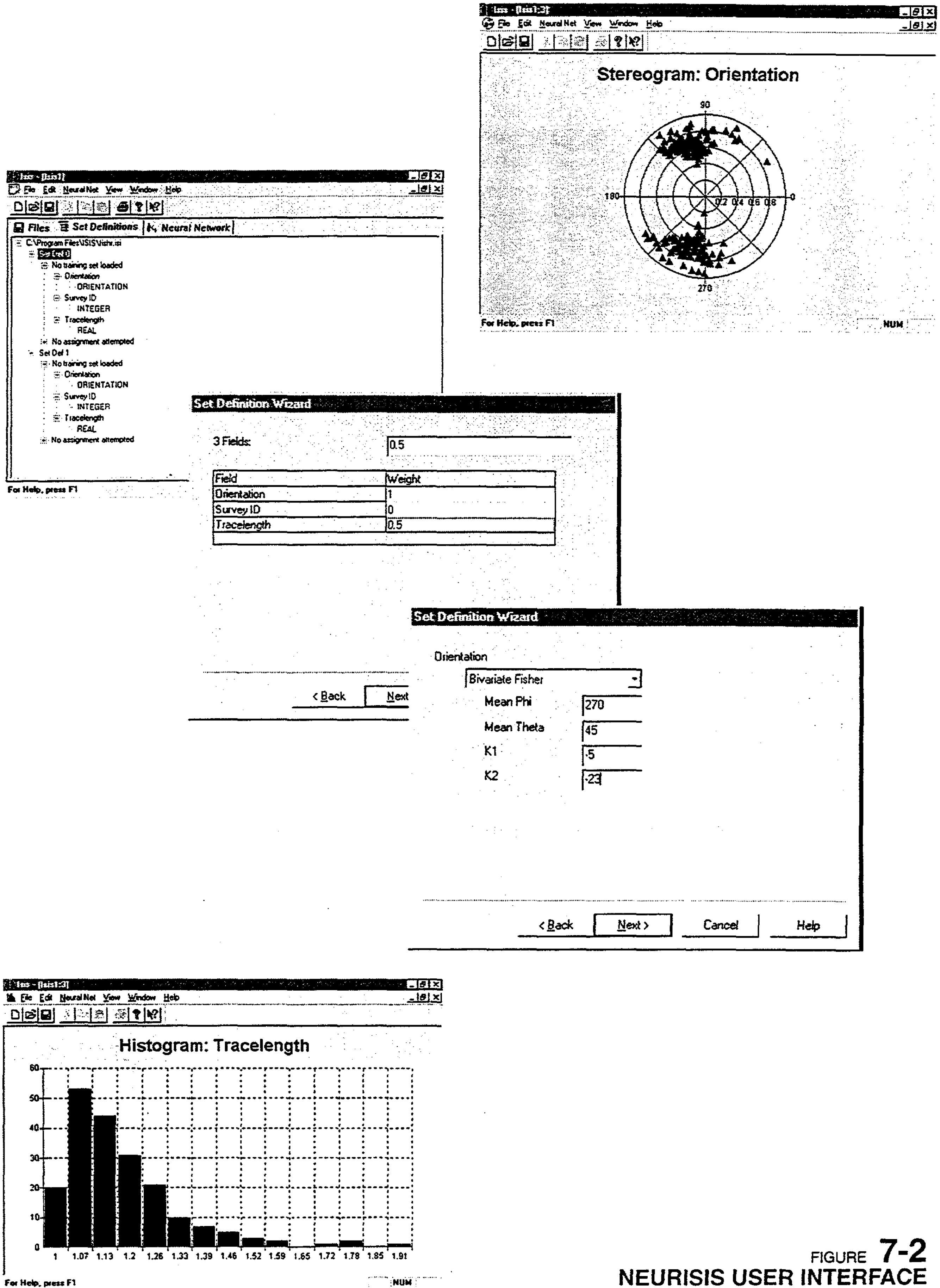

C:\Program Files\ISIS\ishr.isi
- Set Def 0
  - No training set loaded
    - Orientation
      - ORIENTATION
    - Survey ID
      - INTEGER
    - Tracelength
      - REAL
  - No assignment attempted
- Set Def 1
  - No training set loaded
    - Orientation
      - ORIENTATION
    - Survey ID
      - INTEGER
    - Tracelength
      - REAL
  - No assignment attempted

3 Fields: 0.5

Field	Weight
Orientation	1
Survey ID	0
Tracelength	0.5

Orientation: Bivariate Fisher

Mean Phi: 270

Mean Theta: 45

K1: -5

K2: -23

FIGURE **7-2**

NEURISIS USER INTERFACE

BDM-NIPER/FRACMAN

PROJECT NO. 963 1357.521 DRAWING NO. 72187 DATE 4/4/97 DRAWN BY TK

Golder Associates

Table 7-1 NeurIsis User Interface

Primary Menu Item/ Command	Secondary Menu Item/ Command	Action
File	New	Create a new analysis (the previous analysis will be kept open)
	Open	Open an .ISI data file, and the .SAM file describing the boreholes and traceplanes the data was collected from
	Close	Close the current analysis
	Save	Save the fracture set definitions as .ISI, and .ORS files, and save the statistical reports as .STS files. Save using default file names
	Save As	Save the fracture set definitions as .ISI, and .ORS files, and save the statistical reports as .STS files. Save using user provided file names
	Print	Print the contents of the current window, which can be either (a) data, (b) the analysis object tree, or (c) stereoplot visualizations
	Print Preview	Display on-screen a preview of the items to be printed
	Print Setup	Setup the printer
	Exit	Leave ISIS/N
Edit	Undo	Undo the previous text entry
	Cut	Cut the selected text field
	Copy	Copy the selected text field
	Paste	Paste the copied text field at the selection
	Terzaghi	Carry out a Terzaghi correction on the selected data
	Define New Set	Define the properties, default values, and weights to be used for the next set in the current analysis
Neural Net	Select Data Set	Select a subset of the currently open data file for analysis
	Generate Training Set	Generate training sets based on the specified set statistics
	Load Training Set	Load a previously defined training set
	Train	Run the neural network on the training set to create a neural network
	Classify	Classify the fractures to sets using the neural network developed from the training set
View	Toolbar	Display the toolbar on screen
	Status Bar	Display the status bar on screen
	Stereoplots	Display a window containing a stereoplot of the current data
Window	New Window	Create a new analysis (as with the New menu item)
	Cascada	Cascade the windows
	Tile	Tile the windows
	Arrange Icons	Arrange icons neatly for the minimized windows
	<File Name>	Switch to the main analysis window for the analysis of the file name displayed
Help	Help Topics	Provide context sensitive help
	About ISIS	Provide information about ISIS.

The procedure for set definition using NeurIsis is as follows:

1. **Dataset:** Define the fracture data in the required format. This file includes a definition of each of the fields in the file, and the data in tabular form.

2. **File/Open:** Open the .ISI data file and the .SAM file describing the orientation and geometry of the fractures.

3. **Neural Net/Select Dataset:** Choose a Subset to analyze (if desired).

4. **Edit/Terzaghi:** Apply the Terzaghi correction to the selected data. A warning will be issued if the data has already been Terzaghi corrected.

5. **View/Stereoplot:** Produce stereoplots of the current data, with Terzaghi corrections (if selected).

6. **Edit/Define New Set:** Based on the visual analysis of the data, and statistical analysis of the data files, select properties to be used in the set assignments for the first set. Provide a weighting (0 to 1) for each of the available properties, and the initial distribution assumptions for each property. Distributions are specified by a distributional form (e.g., normal or log-normal), and moments (e.g., mean and standard deviation or dispersion).

7. **Repeat** the Edit/Define New Set for each set to be generated for the training set.

8. **Neural Net/Generate:** Generate training sets according to the statistical descriptions provided using Edit/Define New Set. Specify the number of fractures to be generated for each set.

9. **Neural Net/Train:** Use the probabilistic neural network algorithm to generate a neural network based on the assumed fracture set definitions.

10. **Neural Net/Classify:** Use the neural network generated in the previous step to classify every fracture into one of the sets. Calculate the statistics of each set based on the fractures assigned to the sets.

11. **View/Stereoplot:** Produce stereoplots of the fracture sets as assigned by the neural network.

12. **File/Save As:** Save statistical reports and files containing the individual fracture sets.

7.1.2 FlowDim b1.0: Fractional Dimension Type Curves

FlowDim b1.0 is illustrated in Figure 7-3. The purpose of FlowDim b1.0 is to provide type curve analysis, consistent with the fractional dimension approach described in Chapter 5 above. FlowDim takes welltest input expressed as drawdown vs. time for a constant extraction rate test. The program plots the normalized time/distance-drawdown curve for the well test, and fits it against type curves to derive the flow dimension.

FlowDim uses the generalize radial flow solution for fractional dimension flow, first developed in the groundwater flow literature by Barker (1988). Barker (1988) defined the radial flow diffusion equation for variable dimensioned flow as

$$\frac{\partial^2 h^*}{\partial r^*} + \frac{D-1}{r^*}\frac{\partial h^*}{\partial r^*} = \frac{\partial h^*}{\partial t^*}, \text{ and} \tag{7-1}$$

$$h^* = \frac{2\pi^{D/2} hKb^{3-D} r_w^{D-2}}{\Gamma\left(\frac{D}{2}\right) Q}$$

where

r^* = dimensionless radius (r/r_w),
h^* = dimensionless head,
t^* = dimensionless time, $tK/4Sr_w^2$,
D = flow dimension,
Q = flow rate (m^2/s),
h = head (m),
K = hydraulic conductivity (m/s),
b = thickness, r_w = well radius, and
Γ = gamma function.

Barker (1988) noted that the solution of Equation 7-1 for transient head or head versus radius during constant-rate well tests is the incomplete gamma function which reduces to the exponential integral (Theis) curve for two-dimensional flow.

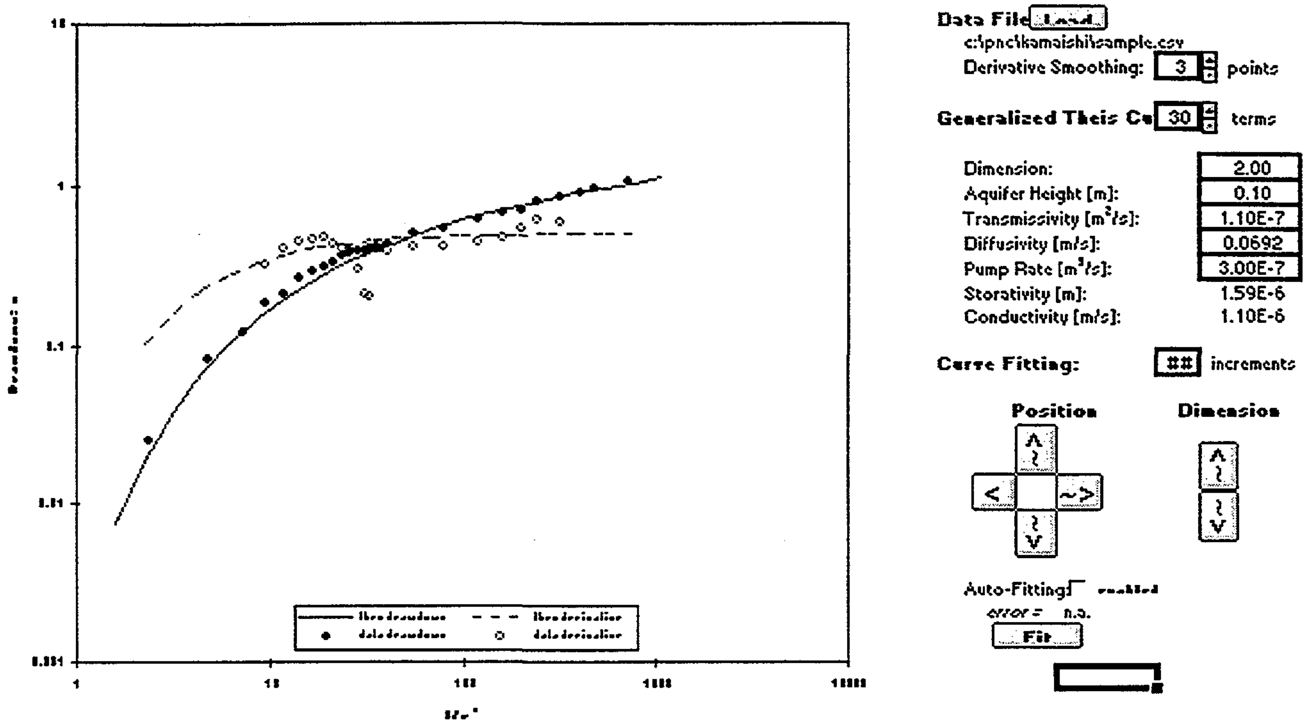

Data File
c:\pnc\kamaishi\sample.csv
Derivative Smoothing: 3 points

Generalized Theis Co 30 terms

Dimension:	2.00
Aquifer Height [m]:	0.10
Transmissivity [m²/s]:	1.10E-7
Diffusivity [m/s]:	0.0692
Pump Rate [m³/s]:	3.00E-7
Storativity [m]:	1.59E-6
Conductivity [m/s]:	1.10E-6

Curve Fitting: ## increments

Position **Dimension**

Auto-Fitting: ☐ enabled
error = n.a.

FIGURE 7-3
FLOWDIM USER INTERFACE
BDM-NIPER/FRACMAN

PROJECT NO. 963 1357.521 DRAWING NO. 69385 DATE 4/4/97 DRAWN BY EA

Golder Associates

The dimension of fractional dimension flow is easy to recognize in either constant-rate or constant-pressure well tests. For dimensions between one and two, the late time behavior of constant-rate tests can be defined using a power function with a logarithmic slope $\frac{\partial h}{\partial(\log t)}$ of ½ (2-D). For the pressure derivative for constant pressure tests, the slope given by inverse flow derivative $\frac{1}{q\partial(\log t)}$ can also be defined using a power function with a logarithmic slope of ½ (2-D). Logarithmic plots of pressure versus the pressure derivative (for constant rate tests) or the inverse flow derivative (for constant pressure tests) have slopes of ½ for linear flow, zero slopes for cylindrical flow, and slopes of -½ for spherical flow. Partial dimensions between one and three have straight-line slopes between these values.

Figure 7-4 shows calculated head curves for a constant rate test with the values shown on the figure. The curves show either the variation of head with time at a fixed radius, or the variation of head with distance for a fixed time. In either case, the straight line behavior appears very clearly. By showing these curves in real units rather than dimensionless units, as is commonly done for type curves, one can see the offset of the curves along both the time-distance and the head axis directions. Because of this offset, the analysis of data using an inappropriate type curve can lead to large errors in the calculation of hydraulic properties.

7.1.3 Flare b1.0: Flow Dimension Analysis for Simulated Fracture Networks

Flare b1.0 will implement the flow dimension analysis of simulated fracture network described in Section 5.3 above. For any given fracture network and borehole configuration, Flare will calculate the flow dimension based on a plot of conductance vs. distance from the well, as illustrated in Figures 5-20 and 5-24. A prototype user interface for Flare is shown in Figure 7-5.

7.1.4 Fractal b1.0: Analysis of Spatial Structures

The purpose of Fractal b1.0 is to support the analysis of fracture spatial structures as described in Section 5.2 above. The generalized flow-chart for Fractal is illustrated in Figure 5-8. Fractal will proceed as follows:

1. **Input:** The input will be defined by a lineament map of fractures, assigned to sets using e.g., NeurIsis (Section 7.1.1 above).

2. **Gridding:** All data will be allocated to a user-specified spatial grid. In each grid cell, the intensity of each set will be calculated, together with the mean orientation and size of fractures occurring in that grid cell.

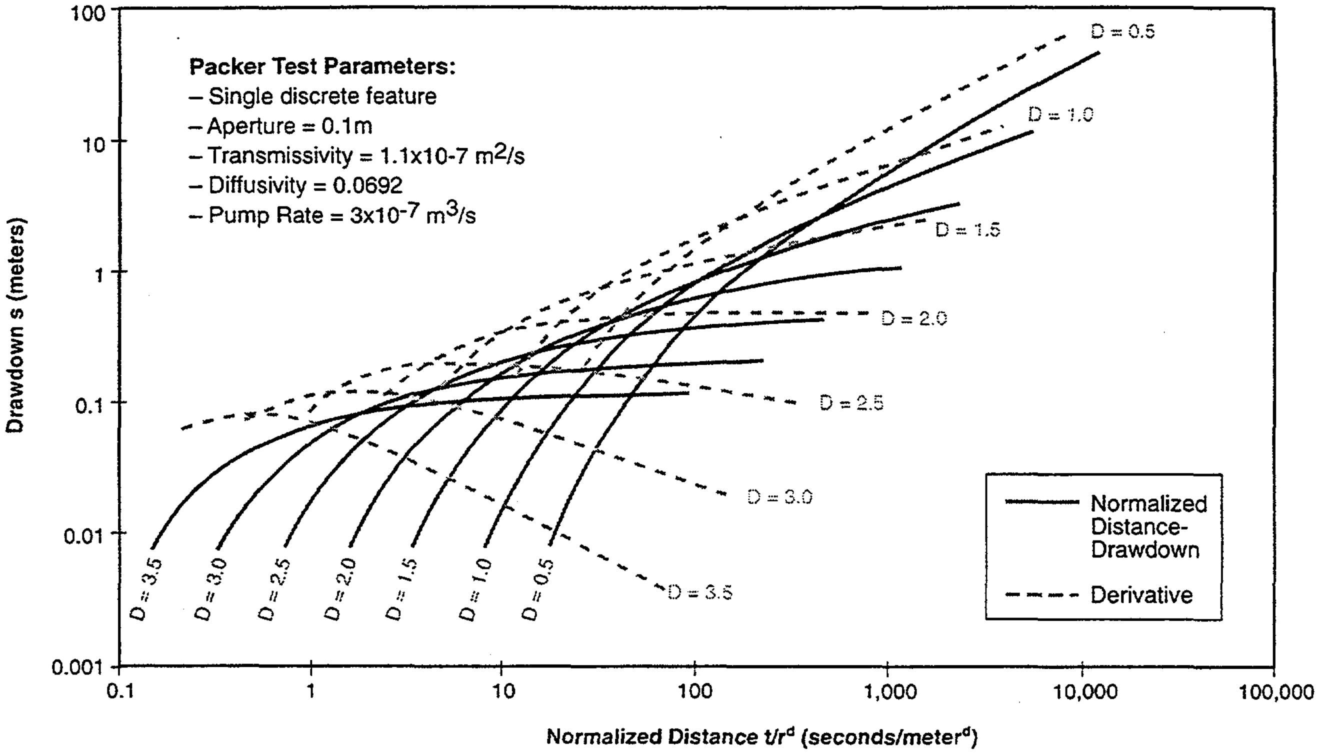

FIGURE **7-4**

DISTANCE-DRAWDOWN RESPONSE FOR DIFFERENT FLOW DIMENSIONS

BDM-NIPER/FRACMAN

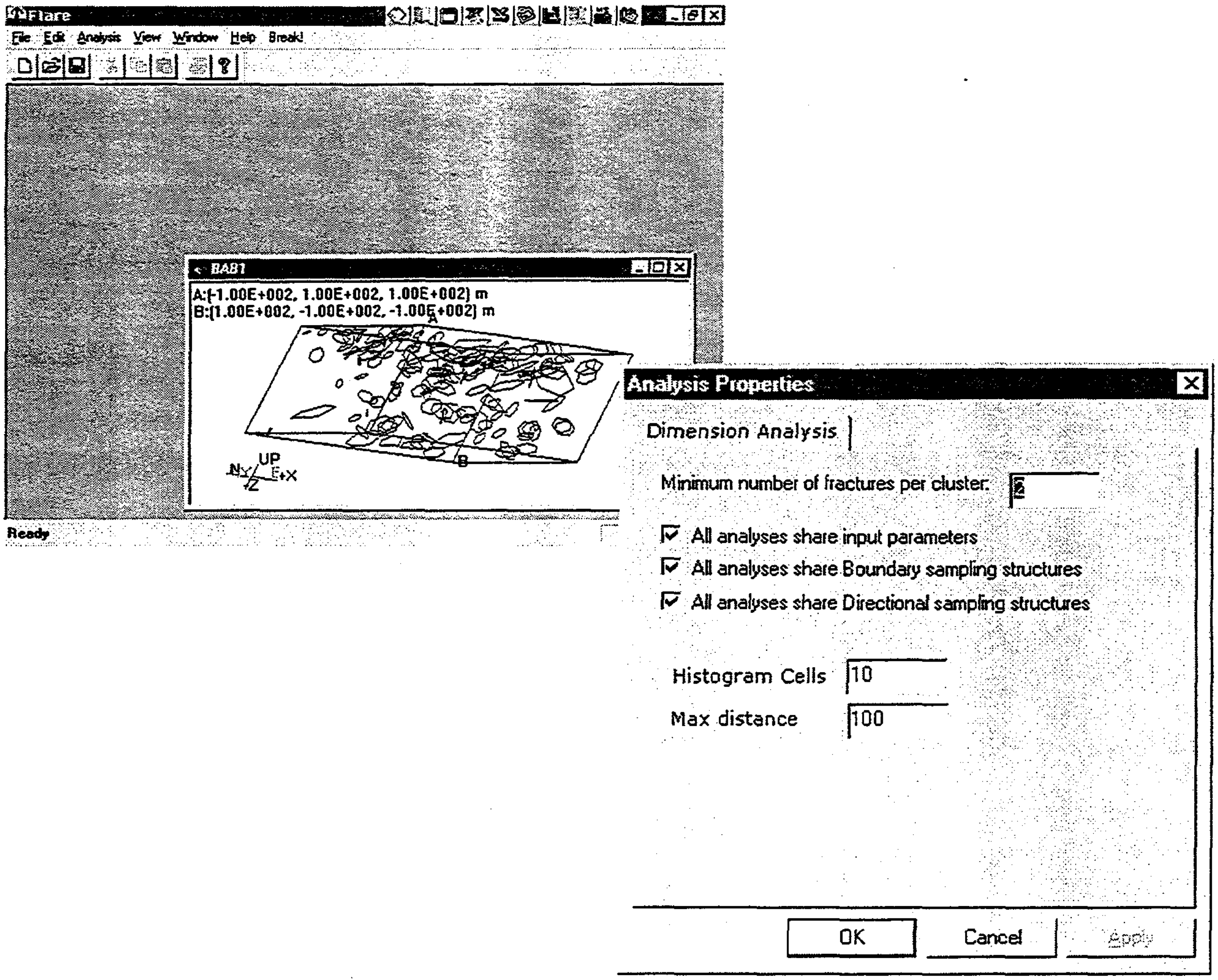

A:[-1.00E+002, 1.00E+002, 1.00E+002] m
B:[1.00E+002, -1.00E+002, -1.00E+002] m

Analysis Properties

Dimension Analysis

Minimum number of fractures per cluster: 2

☑ All analyses share input parameters
☑ All analyses share Boundary sampling structures
☑ All analyses share Directional sampling structures

Histogram Cells: 10
Max distance: 100

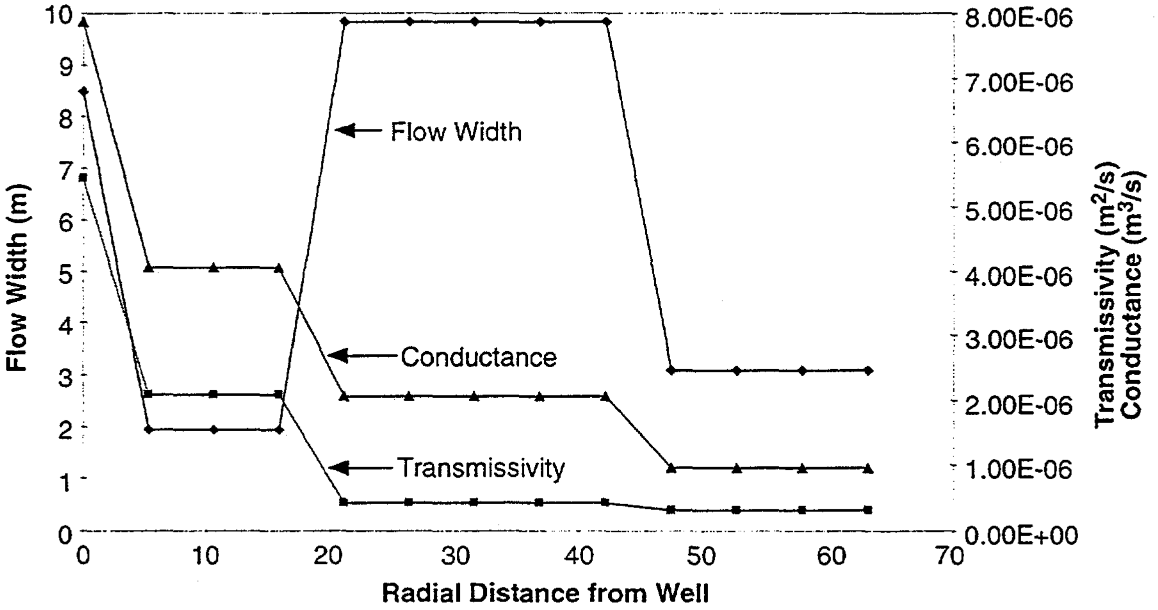

FIGURE **7-5**

FLARE USER INTERFACE

BDM-NIPER/FRACMAN

PROJECT NO. 963 1357.521 DRAWING NO. 69386 DATE 4/7/97 DRAWN BY EA

Golder Associates

3. **Trend Analysis:** The gridded data will be analyzed for spatial trends by set.
4. **Correlation Analysis:** The gridded data and identified spatial trends will be evaluated for correlations
5. **Reporting:** The possible spatial trends and correlations will be reported for use in quantifying location conceptual models.

7.1.5 FraCluster b1.0: Reservoir Compartmentalization

FraCluster b1.0 was implemented to provide the analyses described in Sections 4.1, 4.2, and 5.4.

7.1.5.1 FraCluster Features

FraCluster includes the following features:

- Identification of fracture clusters within stochastically generated fracture networks,
- Calculation of compartment volume distributions corresponding to fracture clusters using the convex hull algorithm,
- Calculation of tributary drainage volumes for fracture clusters intersected by specific borehole configurations, and
- Calculation of reservoir block size distributions.

These features make it possible for reservoir engineers to rapidly define key reservoir engineering parameters for fractured reservoirs from discrete fracture network models. The algorithms implemented are described in La Pointe et al (1996).

The FraCluster user interface is illustrated in Figures 7-6, 7-7, 7-8, and 7-9.

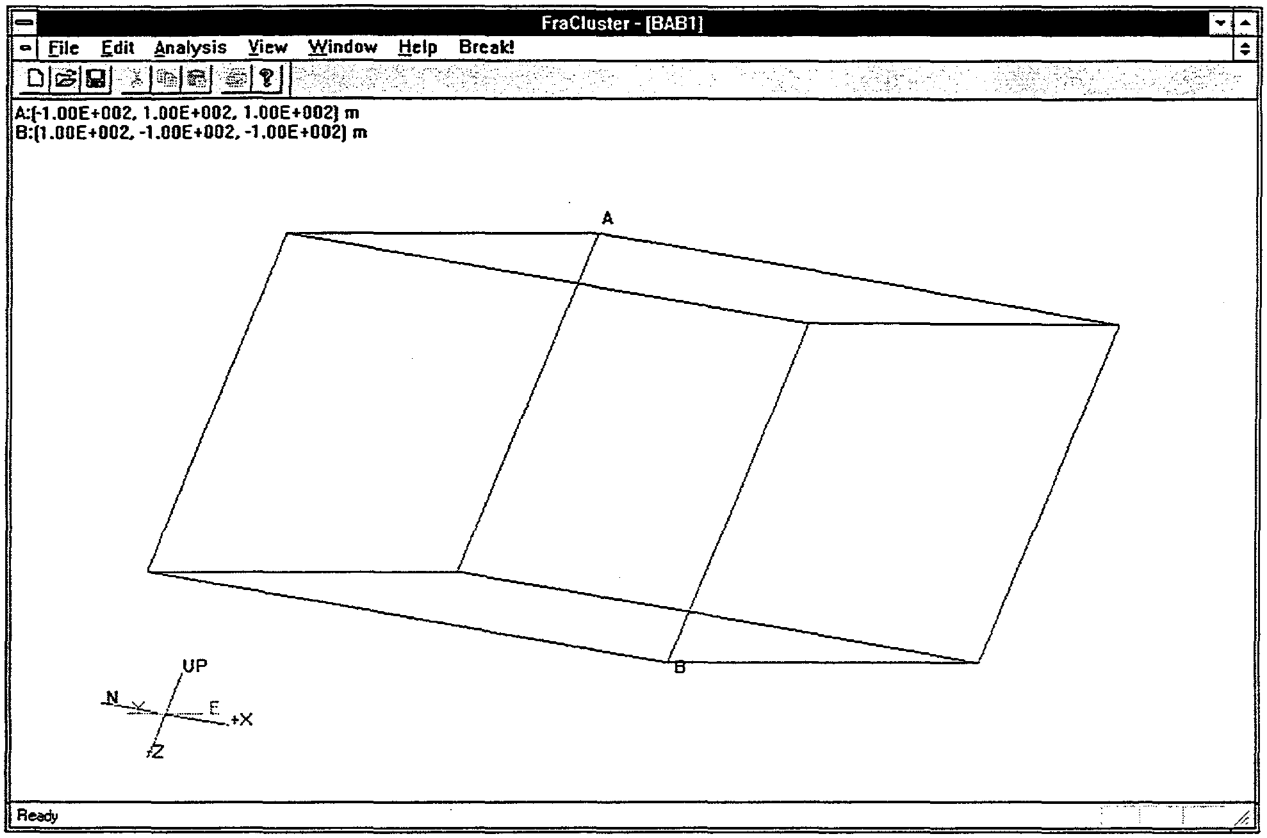

A:(-1.00E+002, 1.00E+002, 1.00E+002) m
B:(1.00E+002, -1.00E+002, -1.00E+002) m

FIGURE **7-6**
FraCluster MAIN MENU
BDM-NIPER/FRACMAN

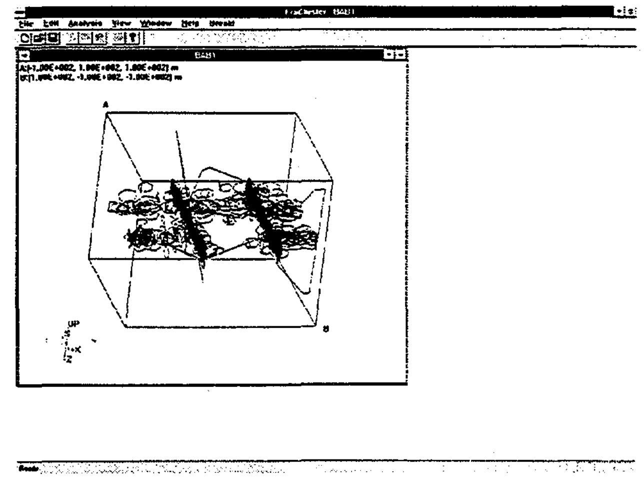

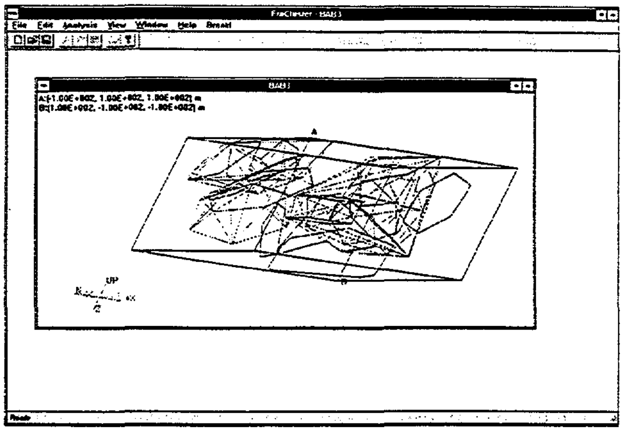

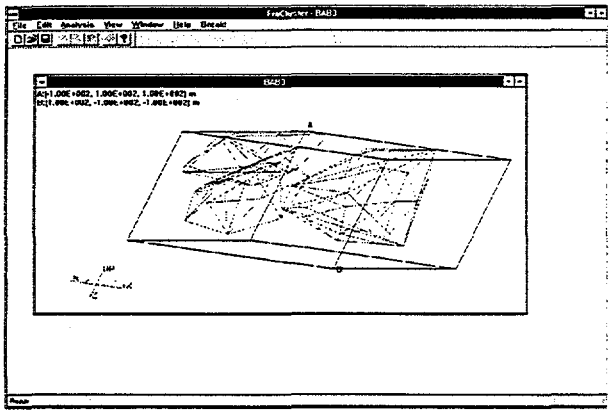

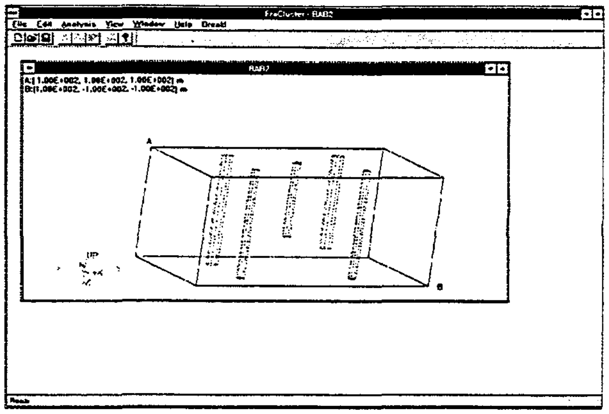

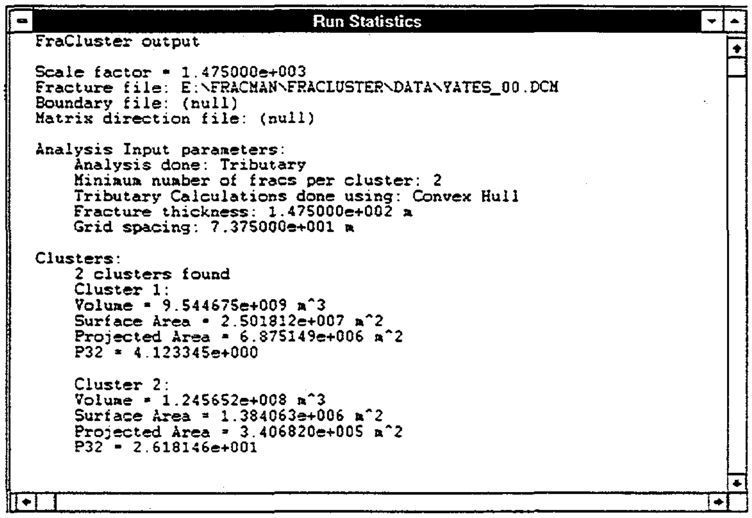

```
FraCluster output

Scale factor = 1.475000e+003
Fracture file: E:\FRACMAN\FRACLUSTER\DATA\YATES_00.DCM
Boundary file: (null)
Matrix direction file: (null)

Analysis Input parameters:
    Analysis done: Tributary
    Minimum number of fracs per cluster: 2
    Tributary Calculations done using: Convex Hull
    Fracture thickness: 1.475000e+002 m
    Grid spacing: 7.375000e+001 m

Clusters:
    2 clusters found
    Cluster 1:
    Volume = 9.544675e+009 m^3
    Surface Area = 2.501812e+007 m^2
    Projected Area = 6.875149e+006 m^2
    P32 = 4.123345e+000

    Cluster 2:
    Volume = 1.245652e+008 m^3
    Surface Area = 1.384063e+006 m^2
    Projected Area = 3.406820e+005 m^2
    P32 = 2.618146e+001
```

FIGURE **7-7**

FraCluster VIEWS

BDM-NIPER/FRACMAN

PROJECT NO. 963 1357.521 DRAWING NO. 69424 DATE 4/4/97 DRAWN BY CB

Golder Associates

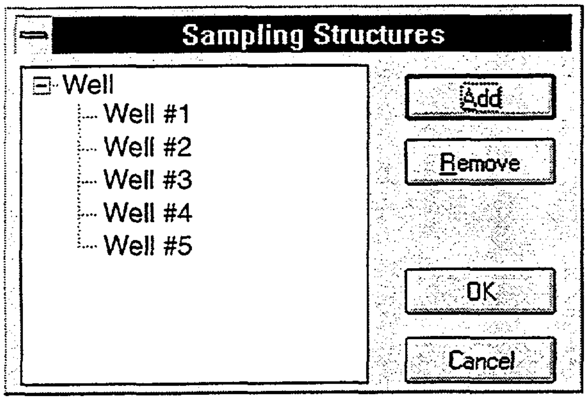

- Well
  - Well #1
  - Well #2
  - Well #3
  - Well #4
  - Well #5

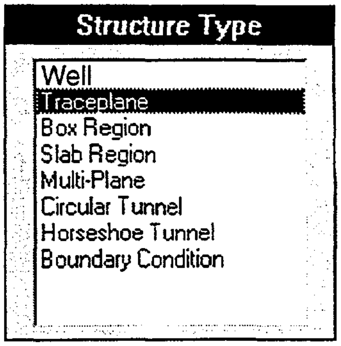

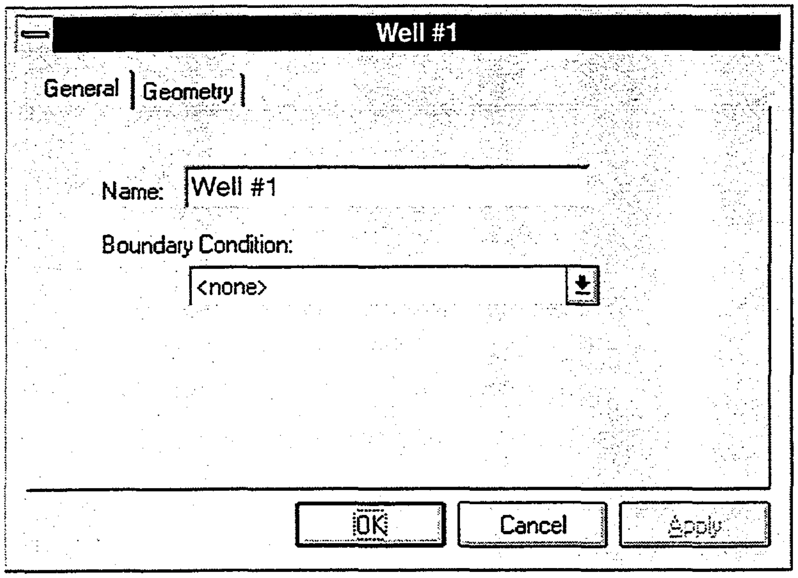

Name: Well #1

Boundary Condition: <none>

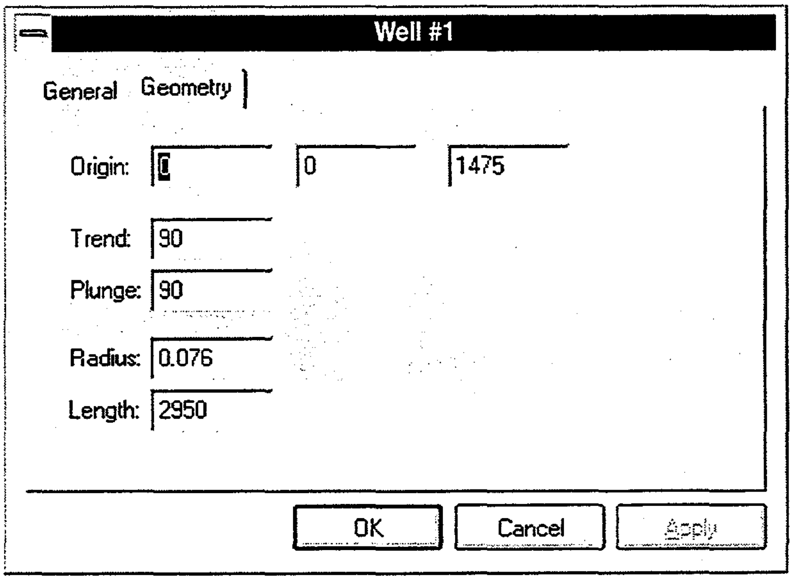

Origin: 0 0 1475

Trend: 90

Plunge: 90

Radius: 0.076

Length: 2950

FIGURE **7-8**

FraCluster EXPLORATION OBJECTS

BDM-NIPER/FRACMAN

PROJECT NO. 963 1357.521 DRAWING NO. 69425 DATE 4/4/97 DRAWN BY CB

Golder Associates

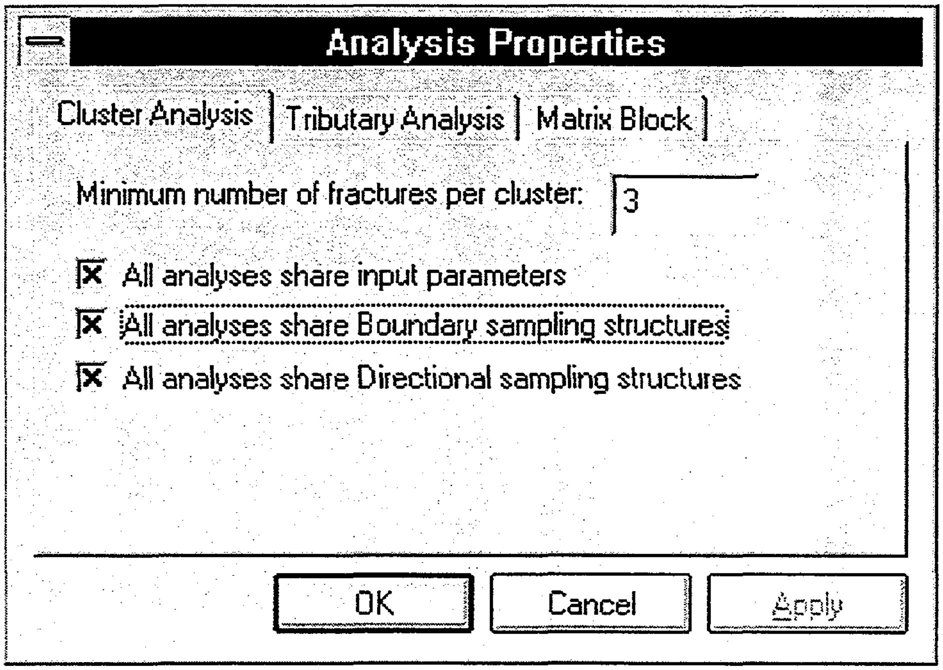

Minimum number of fractures per cluster: 3

☒ All analyses share input parameters

☒ All analyses share Boundary sampling structures

☒ All analyses share Directional sampling structures

FIGURE **7-9**

FraCluster ANALYSIS SETTINGS

BDM-NIPER/FRACMAN

7.2 Task 3.3.2 Discrete Fracture Analysis for the TAGS Process

During the current project year, preliminary discrete fracture analysis in support of the TAGS process focused on applications of the compartmentalization analysis.

7.2.1 Application to Yates Field Data

7.2.1.1 Reference Discrete Fracture Network

Although a complete reservoir model for Yates has not yet been developed, a preliminary model of some of the important fracture zones correlated with production and flexure trends have been created. These fracture zones will form a component of the final model. In order to illustrate the application of the new fracture technologies, compartment, tributary and matrix block analyses were carried out on the fracture zones. The fracture zone DFN model is summarized in Figures 7-10, 7-11, 7-12 and Table 7-2.

Fracture zone architecture is both variable and complex, and is a subject of much current research worldwide in both petroleum reservoir development and nuclear waste disposal (for example, see Mazurek et al. 1995; Caine et al. 1996). Studies have shown that many fracture zones are composed of thousands of anastamozing discrete fractures. Many of these fractures are on the order of meters or less, and probably do not play a significant role in the regional fault zone permeability (Pusch 1995). For this reason, the DFN model of the fracture zones only includes the larger fractures and those with a transmissivity above a threshold typical of conductive fractures in fracture zones. The analyses carried out consisted of fractures with radius greater than 75m, which also corresponds to a transmissivity greater than 0.00075 m^2/s.

Table 7-2 Yates Field Reference DFN Fracture Zone Model

		Set 1	Set 2	Set 3	Set 4	Set 5	Set 6	Set 7	Set 8
Slab Region	(L,W,H) [m]	2955, 40 ,150	2955, 40, 150	2324, 40, 50	647, 40, 150	1125, 40, 150	668, 40, 150	2950, 2950, 100	2950, 2950, 101
Slab Orientation	(Trend, Plunge)	179,0	179,0	273,0	93,0	269,0	88,0	0,0	0,1
Slab Origin	(X,Y,Z) [m]	-1475, -856, 0	-1475, 318, 0	-543, 1475 ,0	-415 -1475, 0	759, 1475, 0	818, -1475, 0	1475, 0, 0	1475, 0, 1
Mean Pole	(Trend, Plunge)	269,0	269,0	183,0	183,1	269,0	178,0	0,0	90,0
Dispersion	Fisher Distrib K	70	70	70	70	70	70	85	65
Mean Radius	[m]	100	100	100	100	100	100	40	32
Radius StDev	[m]	45	45	45	45	45	45	23	17
Min Radius	[m]	75	75	75	75	75	75	75	75
Dir of Elong(tr,pl)	Constant	179,0	179,0	273,0	93,0	89,0	88,0	90,0	0,0
Aspect Ratio		1.2	1.2	1.2	1.2	1.2	1.2	1.2	1.2
Termination %		35	35	35	35	35	35	70	85
Intensity P_{32}	[m^2/m^3]	0.5	0.5	0.5	0.5	0.5	0.5	0.00425	0.000877

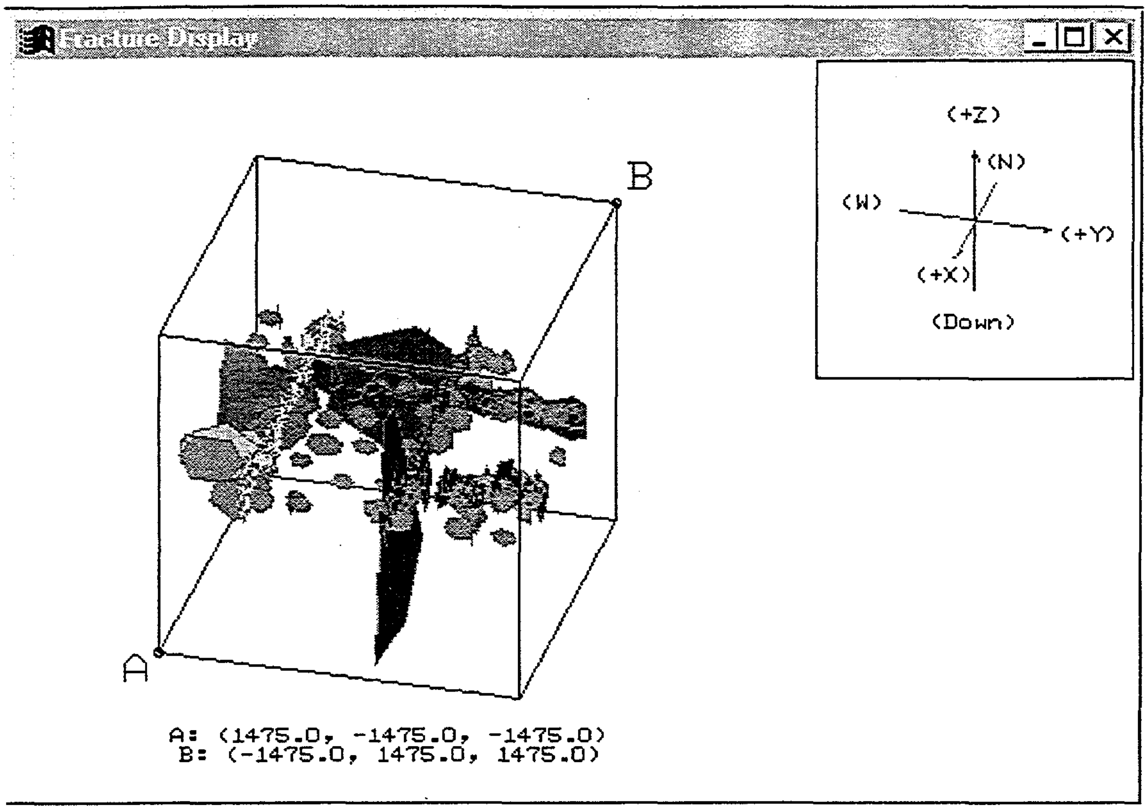

A: (1475.0, -1475.0, -1475.0)
B: (-1475.0, 1475.0, 1475.0)

FIGURE **7-10**
YATES REFERENCE CASE
BDM-NIPER/FRACMAN

PROJECT NO. 963 1357.521 DRAWING NO. 72143 DATE 4/4/97 DRAWN BY CB

Golder Associates

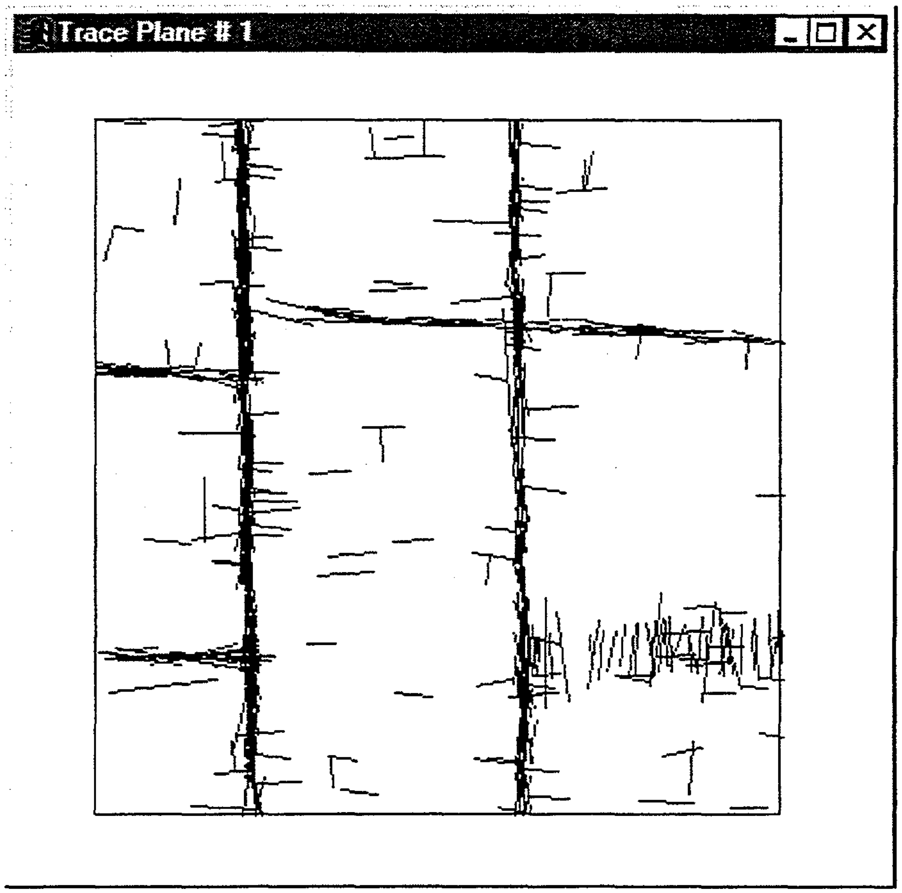

FIGURE **7-11**
2D VIEW, YATES REFERENCE CASE
BDM-NIPER/FRACMAN

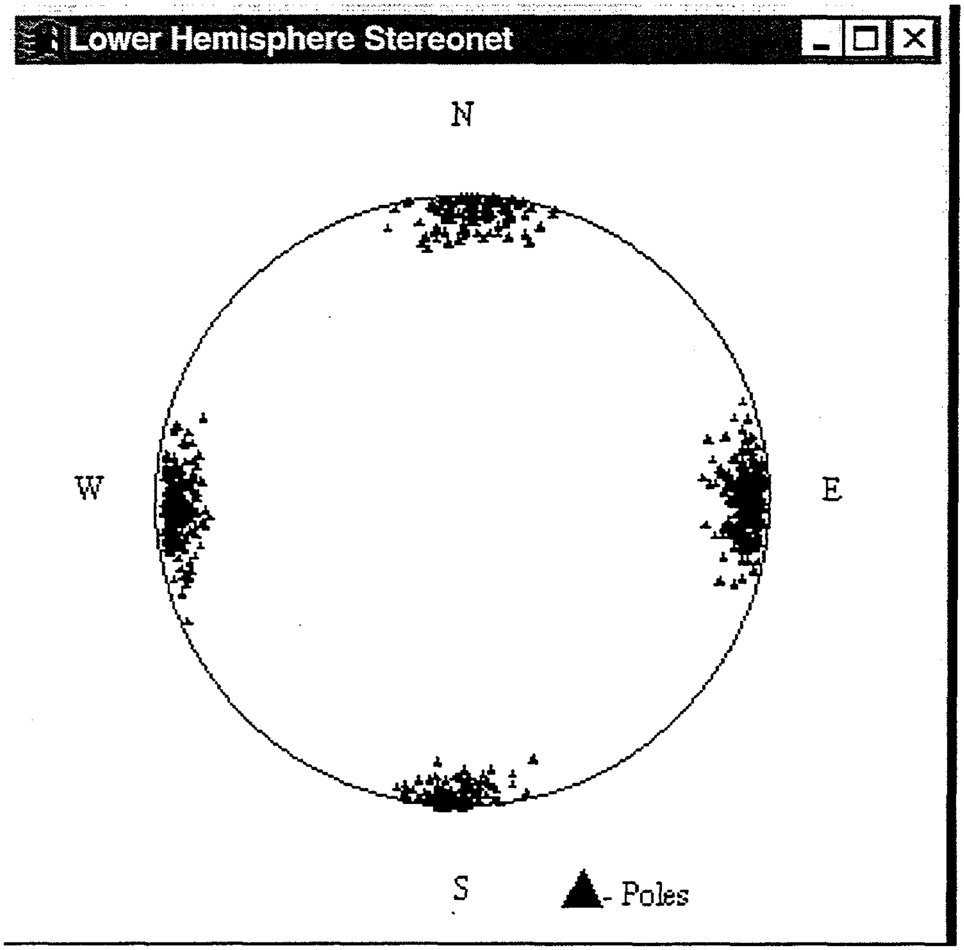

FIGURE **7-12**
STEREOPLOT OF FRACTURES, YATES REFERENCE CASE
BDM-NIPER/FRACMAN

7.2.1.2 Compartmentalization Analysis

Compartmentalization analysis for the reference DFN are summarized in Table 7-3. Out of a total of approximately 600 fractures in the 2950 ft by 2950 ft by 100 ft reservoir block, FraCluster found 49 networks. The distributions of compartment volume and horizontal plane projection area by the convex hull algorithm are given in Figure 7-13.

Table 7-3 Statistics for Reservoir Compartments by Convex Hull Algorithm

	Area (m^2)	Volume (m^3)
Mean	1.44E+06	2.23E+09
Standard Error of Mean	3.54E+05	6.80E+08
95% Confidence Level on Mean	7.11E+05	1.37E+09
Median	1.19E+05	2.60E+07
Standard Deviation	2.48E+06	4.76E+09
Sample Variance	6.13E+12	2.26E+19
Kurtosis	1.29E+00	2.69E+00
Skewness	1.67E+00	2.07E+00
Minimum	6.17E+03	6.23E+05
Maximum	7.66E+06	1.54E+10

7.2.1.3 Drainage Volume Analysis

Drainage volume analysis was performed for a well intersecting the DFN model of the fracture zone. The majority of the fractures were connected to the well directly or through other fractures. Figure 7-14 shows the results of the volume of matrix that could be mobilized for three values of mobilization distance. Such a graph might represent the increasing amount of mobilized matrix through time due to pressure depletion drive. The graph behaves as it should; the volume mobilized does not increase linearly with mobilization distance due to overlap between the polyhedrons.

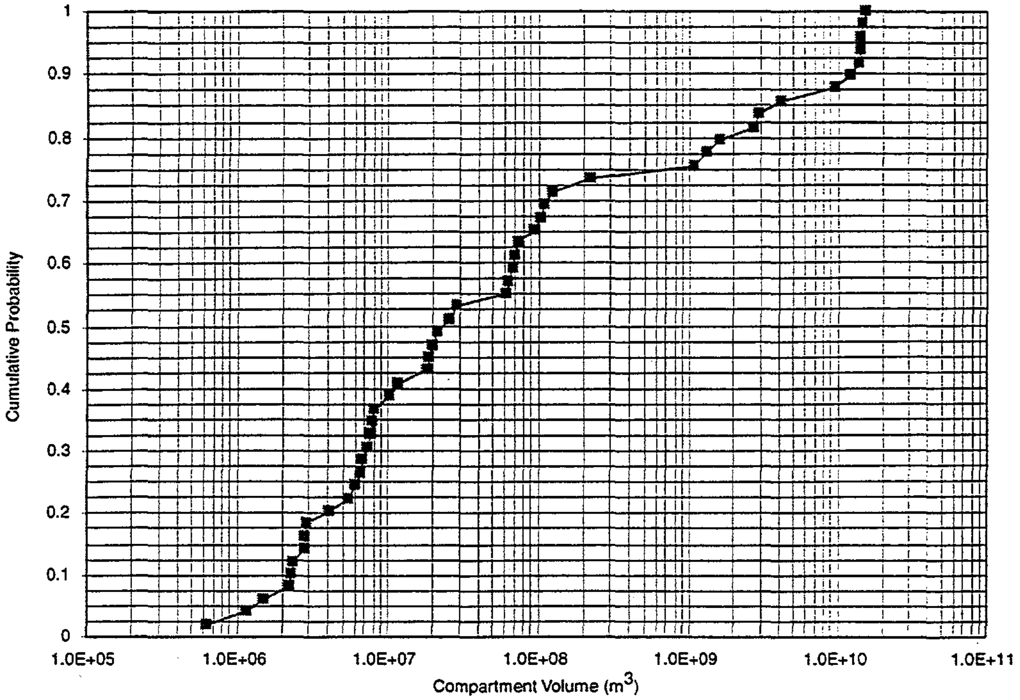

(a) Cumulative Density Function for Compartment Volume

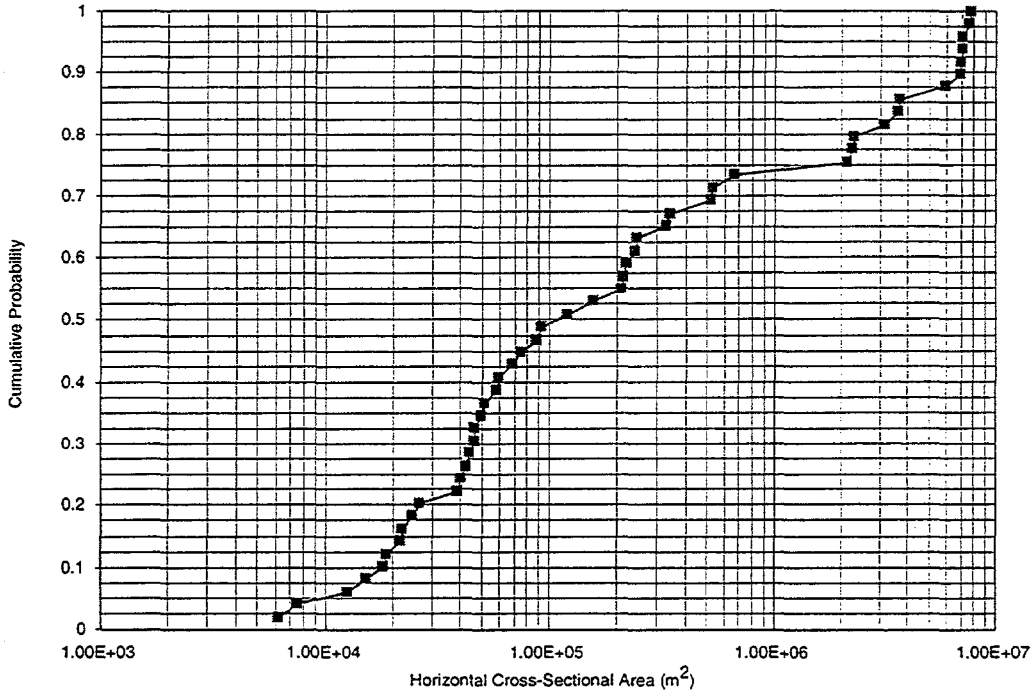

(b) Cumulative Probability Density for Cross Sectional Area

FIGURE **7-13**

COMPARTMENT ANALYSIS FOR YATES REFERENCE CASE

BDM-NIPER/FRACMAN

PROJECT NO. 963 1357.521 DRAWING NO. 72146 DATE 4/4/97 DRAWN BY CB

Golder Associates

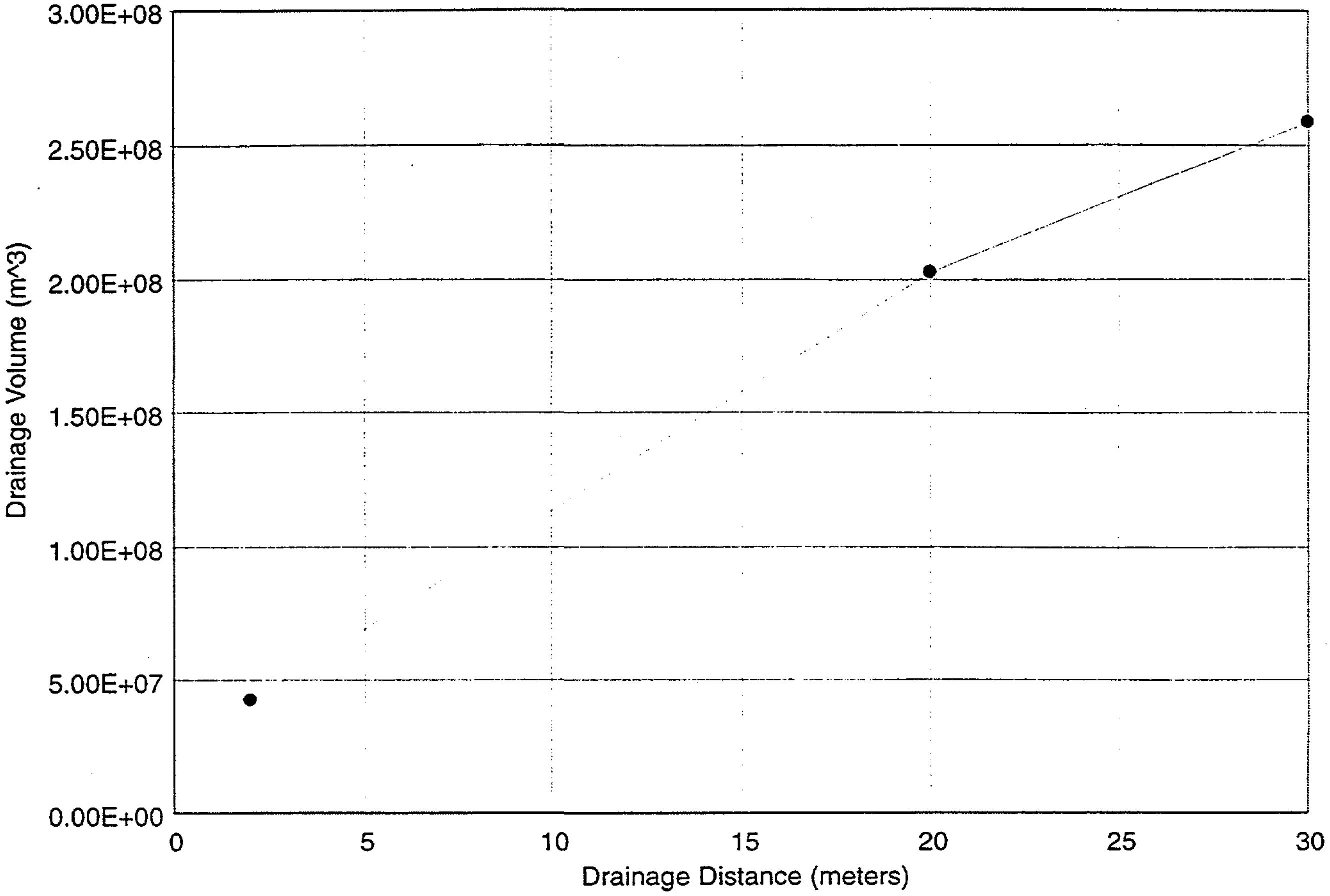

FIGURE **7-14**

ESTIMATED TRIBUTARY VOLUME VS. DRAINAGE DISTANCE

BDM-NIPER/FRACMAN

7.2.1.4 Block Size Analysis

Block size analysis was carried out using both the multi-directional spacing algorithm (MDS) and the convex hull algorithm (CH). The results are summarized in Tables 7-4 and 7-5. Probability distributions for volume, surface area, sigma factor, and Z-dimension for the two algorithms. The tables indicate that the MDS algorithm estimates mean blocks that are about an order of magnitude bigger than the CH algorithm. The higher standard deviation for the MDS algorithm together with the larger block size estimate suggests that the actual blocks have correlated dimensions. Regression analysis on the dimensions yields a R^2 on the order of 0.25. This suggests that the MDS algorithm will somewhat overestimate matrix block variability, and underestimate the maximum block size. Cumulative probability plots for volume, surface area, sigma factor and Z-dimension are shown for both algorithms in Figures 7-15 through 7-22.

Table 7-4 Block Size Statistics from MDS Algorithm

	Volume	**Surface Area**	**Sigma Factor σ**	**Z-dimension**
Mean	1.32E+05	1.53E+04	0.67	21.52
Median	4.15E+03	2.23E+03	0.02	16.50
Standard Deviation	3.72E+05	3.40E+04	3.90	17.78
Minimum	1.60E+01	3.20E+01	0.0001	1.00
Maximum	2.07E+06	1.73E+05	25.00	58.00

Table 7-5 Block Size Statistics from Convex Hull (CH) Algorithm

	Volume	**Surface Area**	**Sigma Factor σ**	**Z-dimension**
Mean	4.14E+04	7.02E+03	8.95	16.25
Median	1.70E+02*	1.80E+02*	1.29*	3.76*
Standard Deviation	6.54E+04	3.53E+04	22.49	98.46
Minimum	<2.18E+02	<5.66E+02	<0.00016	<0.29
Maximum	1.69E+07	2.42E+06	160.46	661.61

*Estimated by extrapolating cumulative probability curve. Minimum values represent upper bounds.

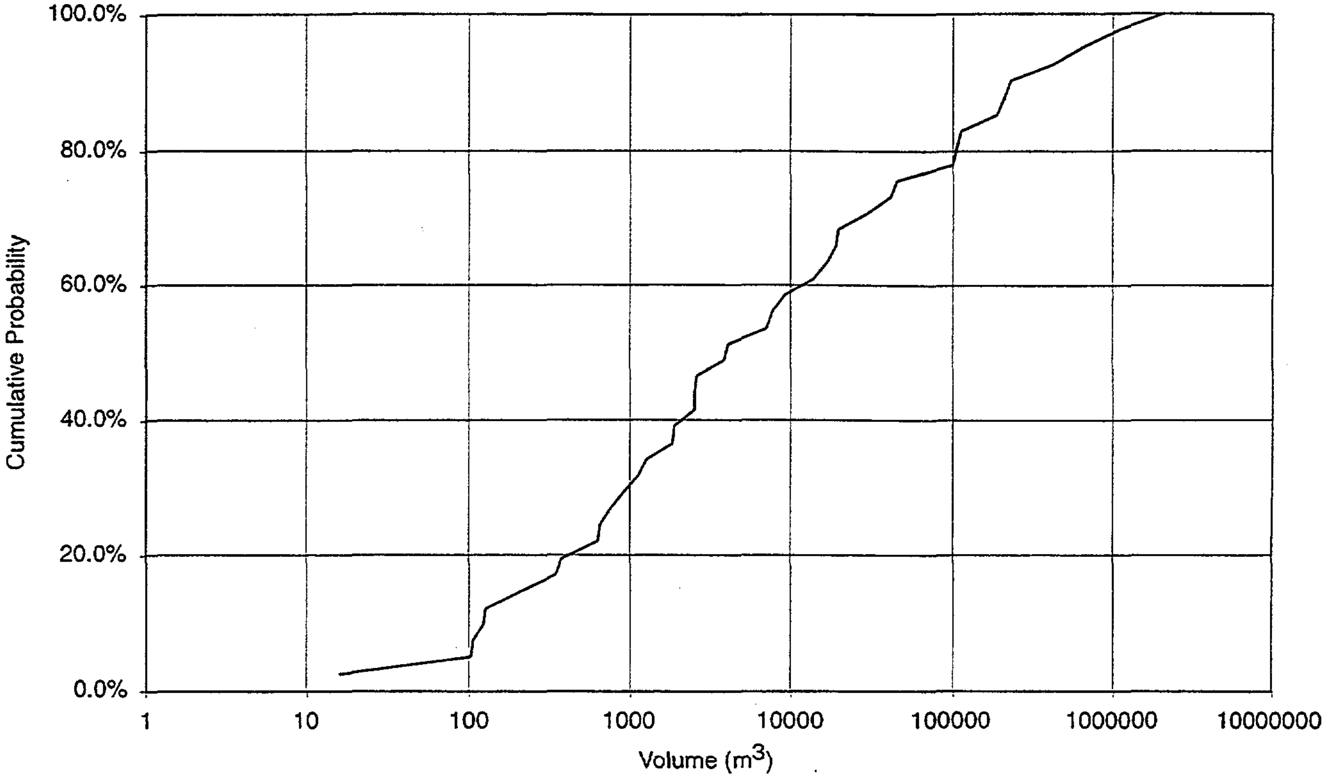

FIGURE **7-15**

DISTRIBUTION OF BLOCK VOLUME, MDS ALGORITHM

BDM-NIPER/FRACMAN

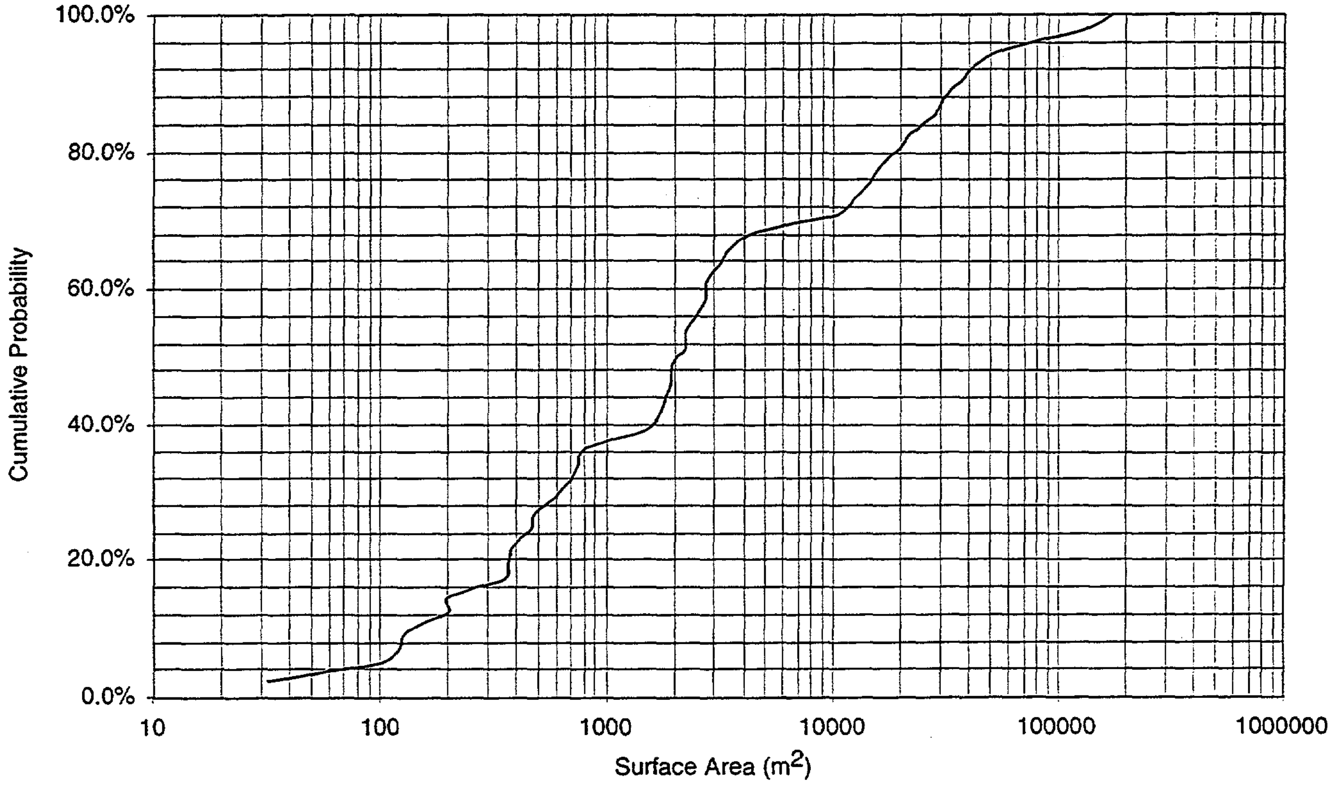

FIGURE **7-16**

DISTRIBUTION OF SURFACE AREA, MDS ALGORITHM

BDM-NIPER/FRACMAN

PROJECT NO. 963 1357.521 DRAWING NO. 72149 DATE 4/4/97 DRAWN BY CB

Golder Associates

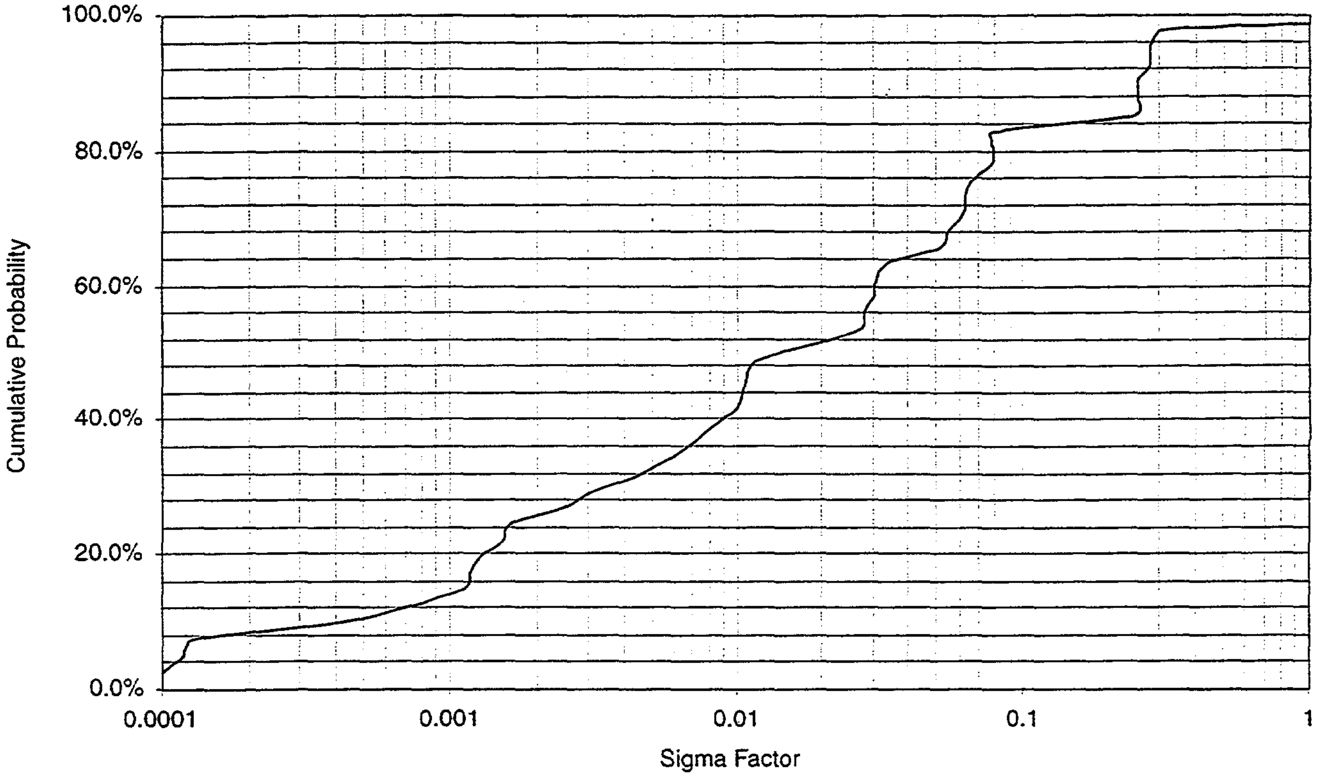

FIGURE 7-17
DISTRIBUTION OF SIGMA FACTOR, MDS ALGORITHM
BDM-NIPER/FRACMAN

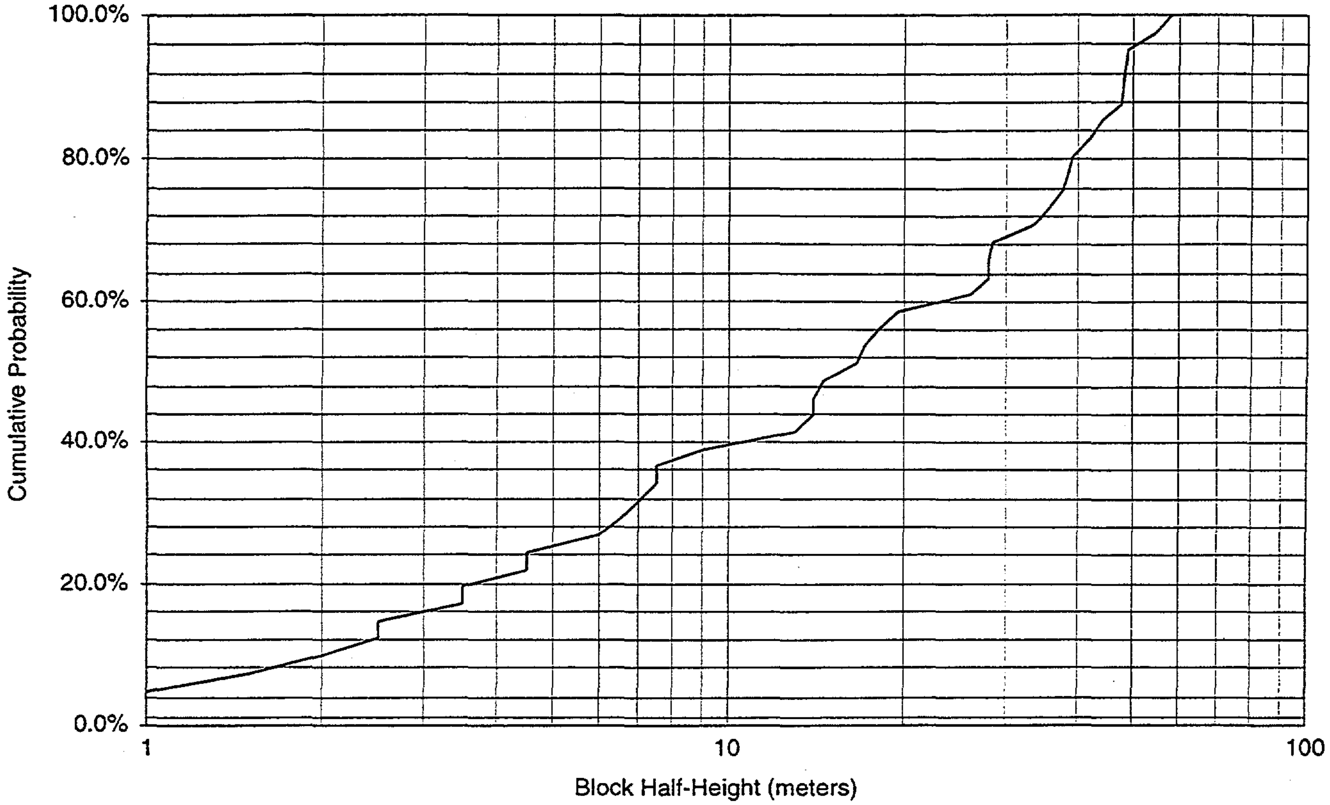

FIGURE **7-18**

DISTRIBUTION OF Z-DIMENSION, MDS ALGORITHM

BDM-NIPER/FRACMAN

PROJECT NO. 963 1357.521 DRAWING NO. 72151 DATE 4/4/97 DRAWN BY CB

Golder Associates

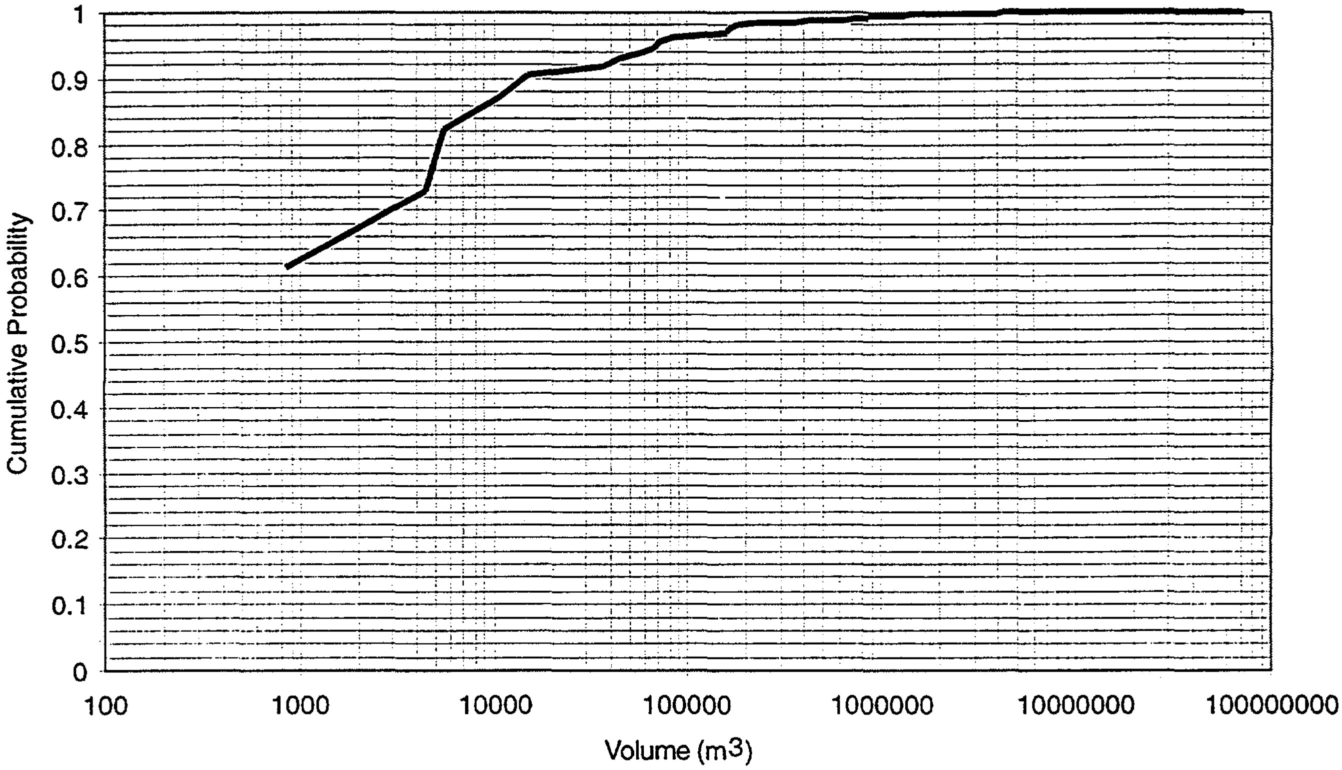

FIGURE **7-19**

**DISTRIBUTION OF BLOCK VOLUME-
CONVEX HULL ALGORITHM**

BDM-NIPER/FRACMAN

PROJECT NO. 963 1357.521 DRAWING NO. 72152 DATE 4/4/97 DRAWN BY EA

Golder Associates

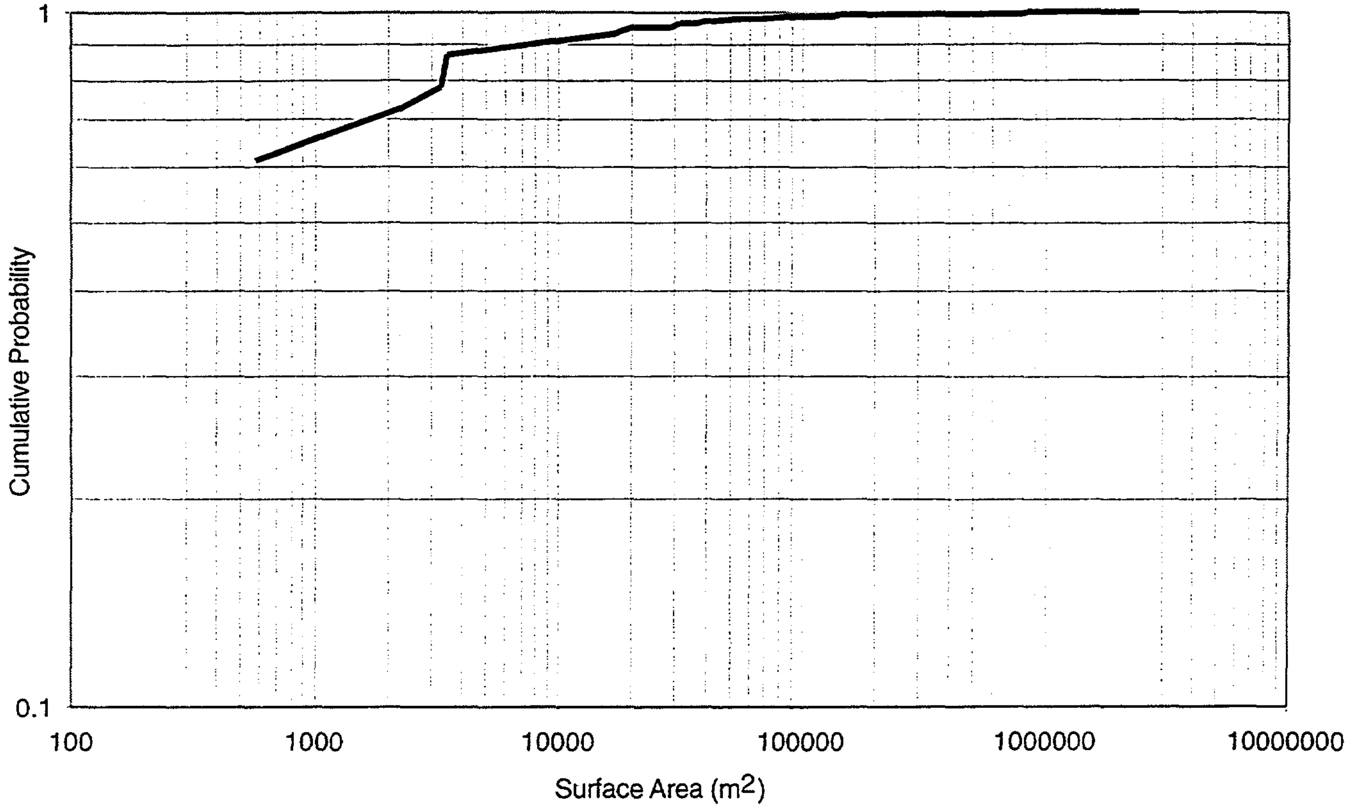

FIGURE **7-20**

**DISTRIBUTION OF SURFACE AREA-
CONVEX HULL ALGORITHM**
BDM-NIPER/FRACMAN

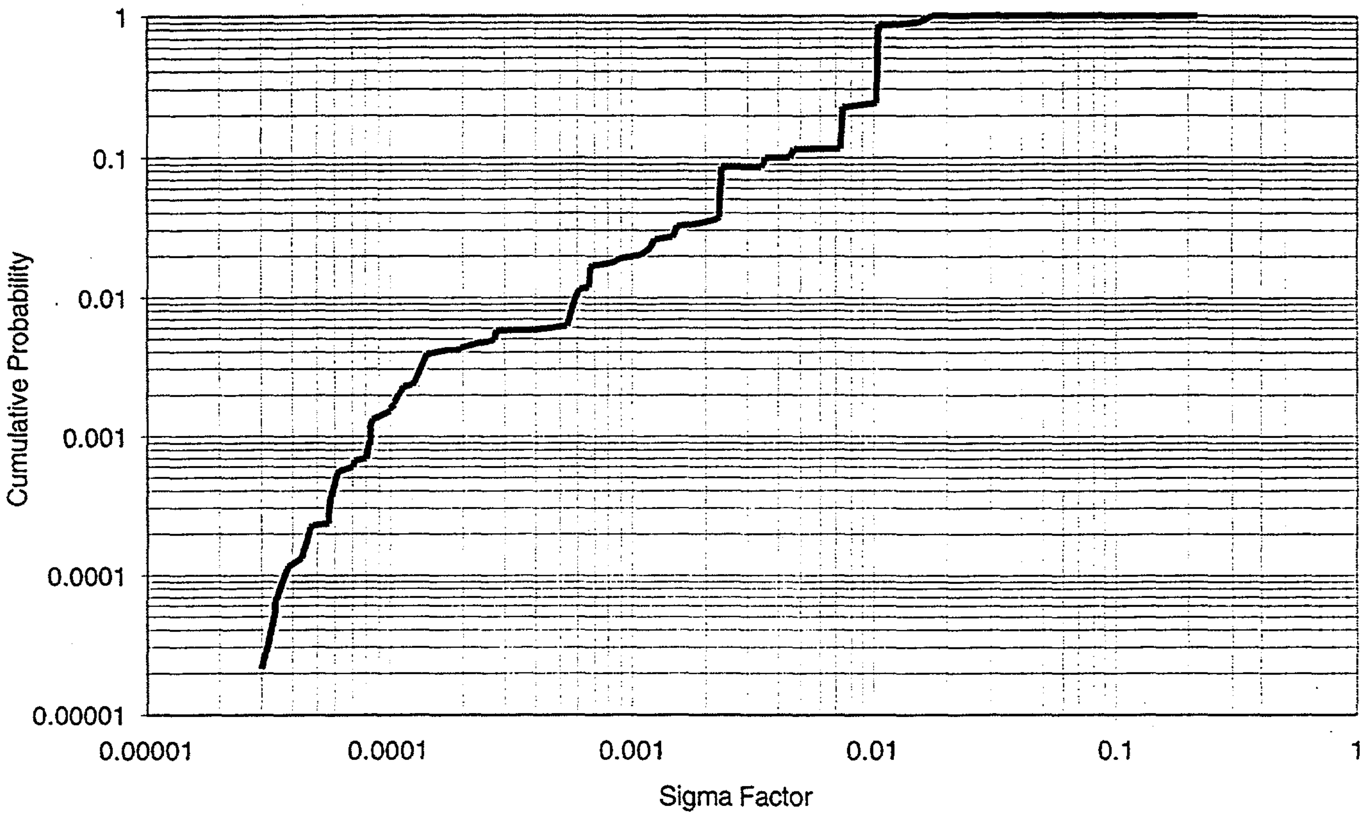

FIGURE **7-21**

**DISTRIBUTION OF SIGMA FACTOR-
CONVEX HULL ALGORITHM**

BDM-NIPER/FRACMAN

PROJECT NO. 963 1357.521 DRAWING NO. 72154 DATE 4/4/97 DRAWN BY EA

Golder Associates

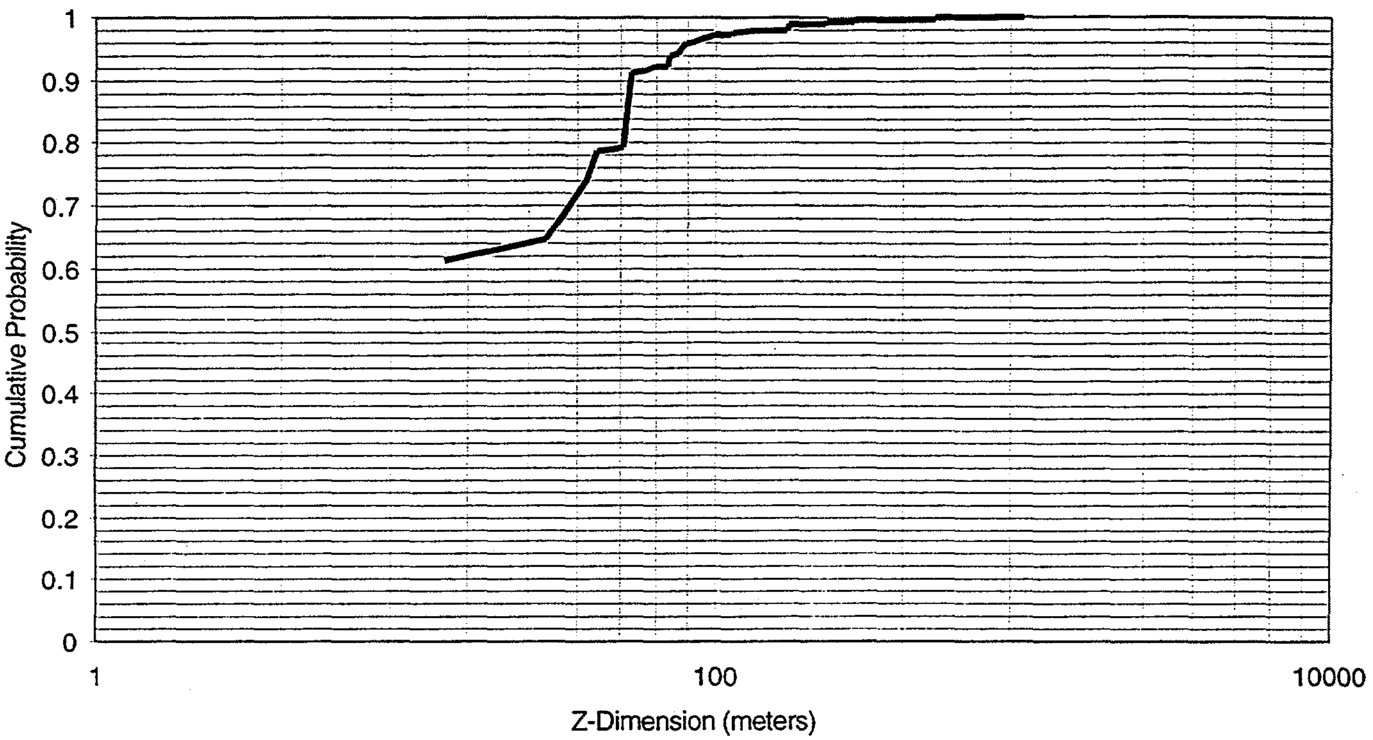

FIGURE **7-22**

DISTRIBUTION OF VERTICAL BLOCK DIMENSIONS-CONVEX HULL ALGORITHM

BDM-NIPER/FRACMAN

PROJECT NO. 963 1357.521 DRAWING NO. 72155 DATE 4/4/97 DRAWN BY EA

Golder Associates

7.3 Task 3.2.3 Software Linking

Software linking between DFN models and reservoir simulators such as ECLIPSE and THERM-DK requires that DFN models be adapted to provide the parameters needed for reservoir simulation, on a cell by cell basis. Table 7-6 illustrates the approach being developed to map between ECLIPSE parameters and DFN models.

Note that Table 7-6 assumes that the DFN approach is being used primarily as an upscaling tool, to facilitate continuum modeling with ECLIPSE or THERM/DK. For many reservoirs, continuum modeling will not be practical at reservoir scales due to heterogeneous connectivity and compartmentalization effects. In addition, for sub REV scales (such as a single well) , it is frequently preferable to directly model the reservoir using DFN methods such as MAFIC, PAWorks, and FraCluster.

Table 7-6 Approaches for Linking DFN and ECLIPSE Models

ECLIPSE MODEL PARAMETER	DFN APPROACH	Comments
cell size	FraCluster: Compute block size distribution from DFN model	Determines the probability for a given cell (size) to contain insufficient fractures to be modeled as a continuum → change cell size or use DFN
active cell	FraCluster: Compute block size distribution from DFN model	Determines the probability for a given cell (size) to contain no fractures (inactive cell) → spatial distribution of inactive cell
fracture porosities	FracWorks: Compute fracture volume in DFN model	Based on fracture aperture distribution
directional absolute permeabilities	PAWorks: Calculate percolation probabilities and effective permeabilities from DFN model MAFIC: Simulate DFN flow in rock blocks and fracture networks connected to wells	Steady state flow through two sides of a cube initiated by constant head boundaries, other four sides are no flow boundaries, k_a is calculated from the resulting flow rate
directional relative permeabilities	PAWorks: Calculate percolation probabilities and effective permeabilities from DFN model including multi-phase effects MAFIC: Simulate multiphase DFN flow in rock blocks and fracture networks connected to wells	Steady state flow through two sides of a cube initiated by constant head boundaries, other four sides are no flow boundaries, function of k_r vs. saturation is calculated from the resulting flow rates for different saturations
matrix-fracture coupling	FraCluster: Compute typical x,y,z dimension of a matrix block, calculate S in DFN model	Based on Kazemi et al., (SPEJ(Dec 1976) 317-326)
well kh	run Oxfilet	Based on fracture intensity distribution and transmissivity distribution
well productivity/ injectivity index	FraCluster: Calculate tributary drainage volumes and compartmentalization in DFN model PAWorks: Calculate effective permeabilities from DFN model including multi-phase effects MAFIC: Simulate DFN flow in rock blocks and fracture networks connected to wells	Based on connected fracture network distribution (tributary drainage volume)

8. TASK 4.1: RESERVOIR PERFORMANCE DATA COLLECTION

8.1 Task 4.1.1 Fracture Image Data Acquisition

Throughout the year, Marathon collected and processed fracture image data, and provided the data for posting on the WWW server. Over 30 Megabytes of fracture image data are now available through the project web server. Example fracture image data is illustrated in Figures 8-1 and 8-2.

8.2 Task 4.1.2 Well Testing Data Acquisition

Throughout the year, Marathon collected and processed well test and hydraulic response data, and provided the data for posting on the WWW server. The well test and hydraulic responses provided by Marathon during the year are summarized in Figures 8-3 and 8-4.

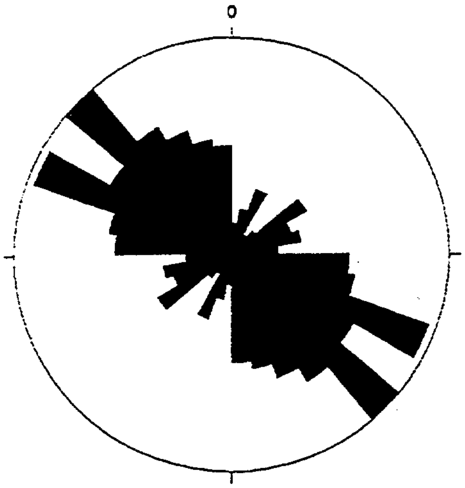

YU1711: 222 log fractures

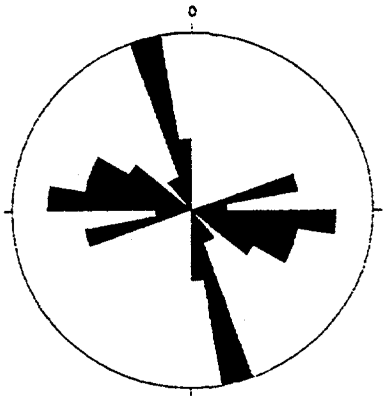

YU1711: Fracture set F
25 fractures; dips=27-47

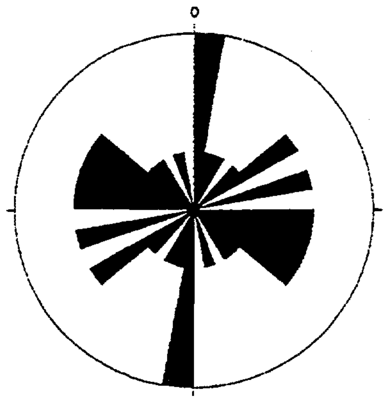

YU1711: Fracture set S
21 fractures; dips>75

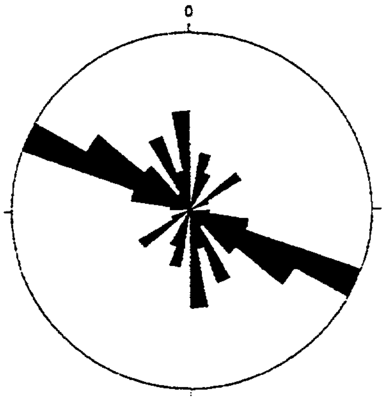

YU1711: Fracture set D1
43 open fractures; dips=62-74

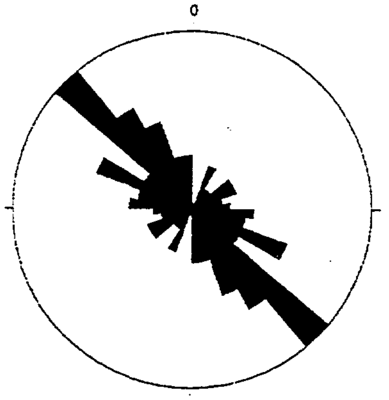

YU1711: Fracture set D2
133 fractures; dips=47-72
39 open; 67 partially filled; 27 healed

FIGURE **8-1**
FRACTURE ORIENTATIONS
FROM WELL YU1711
BDM-NIPER/FRACMAN

TRACT 17: Cored Well YU1776

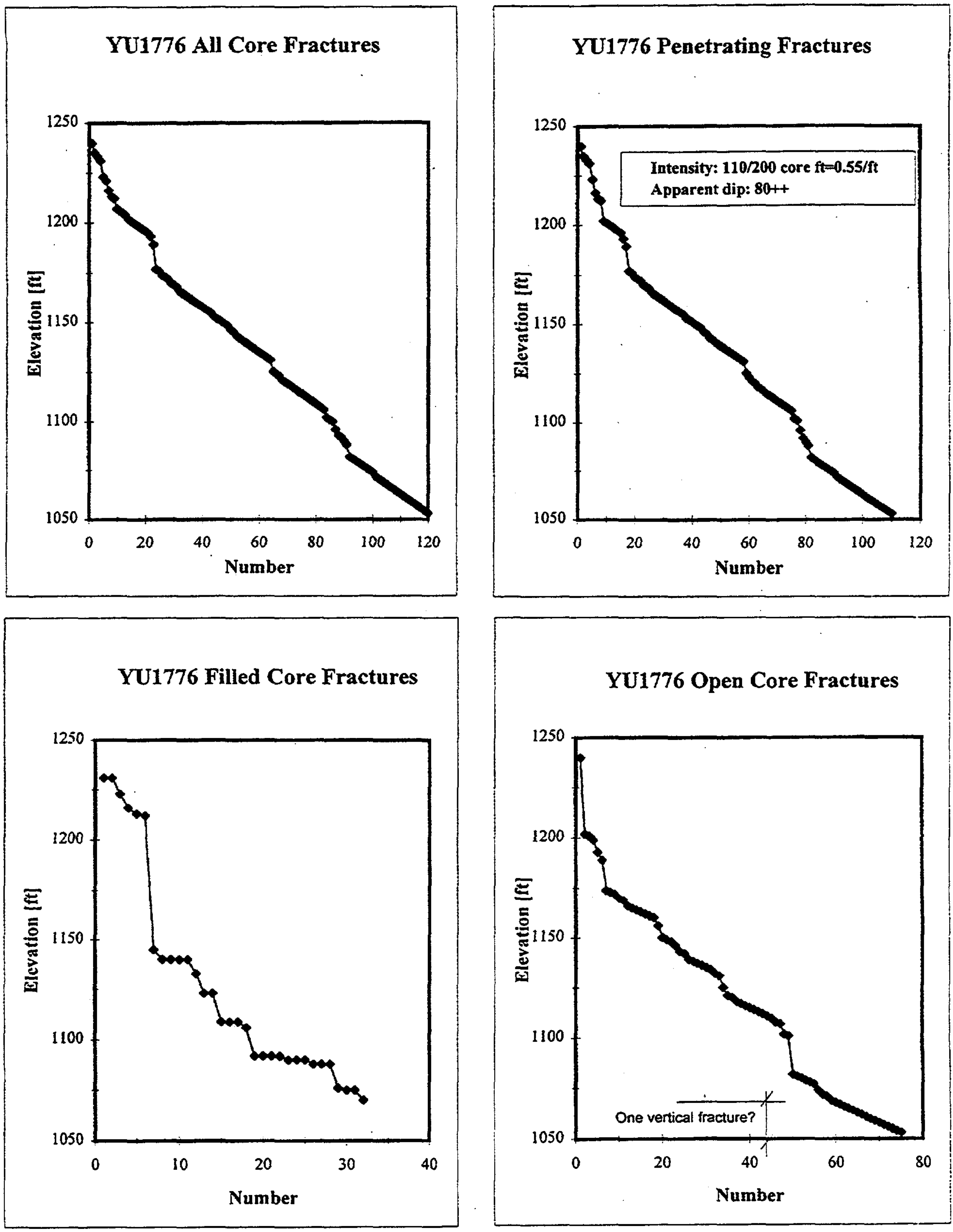

FIGURE **8-2**
FRACTURE INTENSITIES FROM WELL YU1776
BDM-NIPER/FRACMAN

PROJECT NO. 963 1357.521 DRAWING NO. 69443 DATE 4/8/97 DRAWN BY EA

Golder Associates

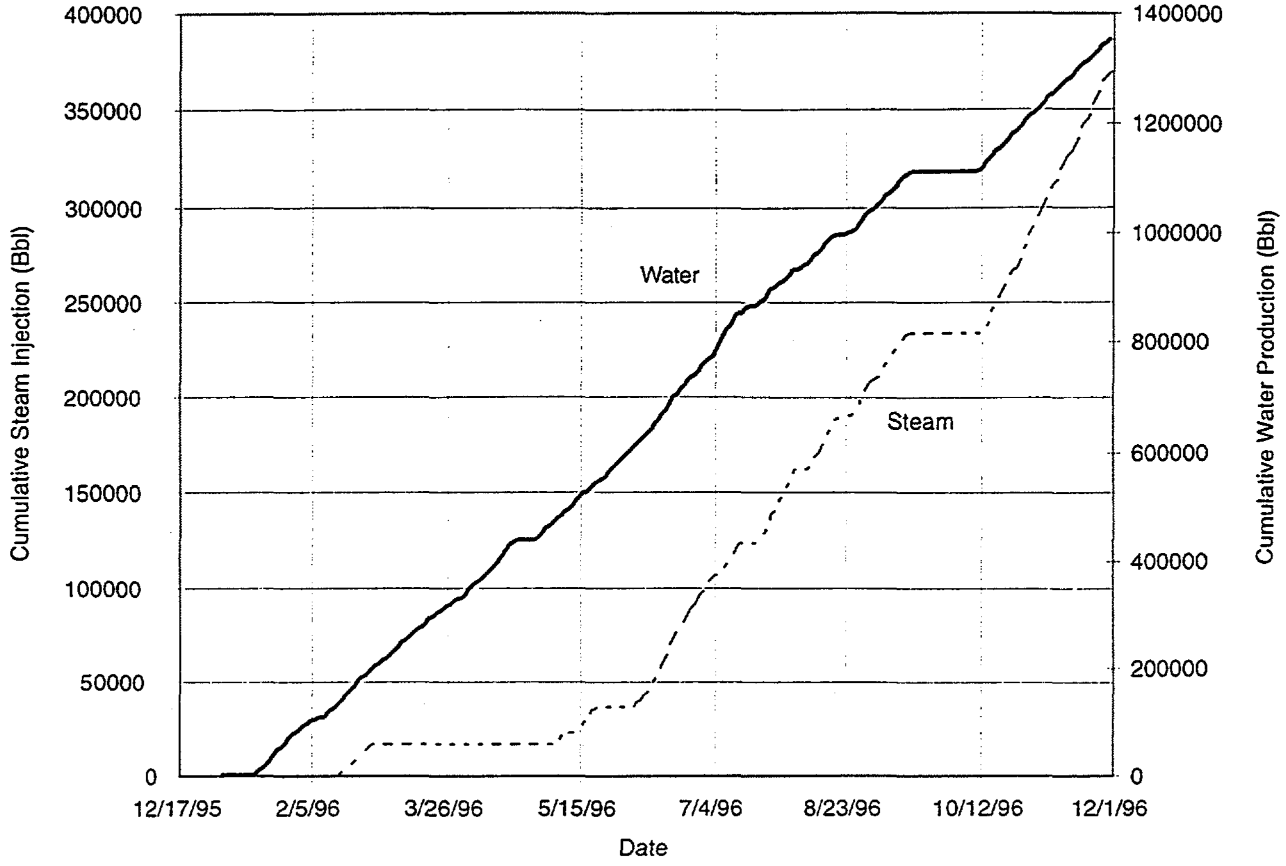

FIGURE **8-3**

STREAM INJECTION DATA

BDM-NIPER/FRACMAN

PROJECT NO. 963 1357.521 DRAWING NO. 69433 DATE 4/7/97 DRAWN BY CB

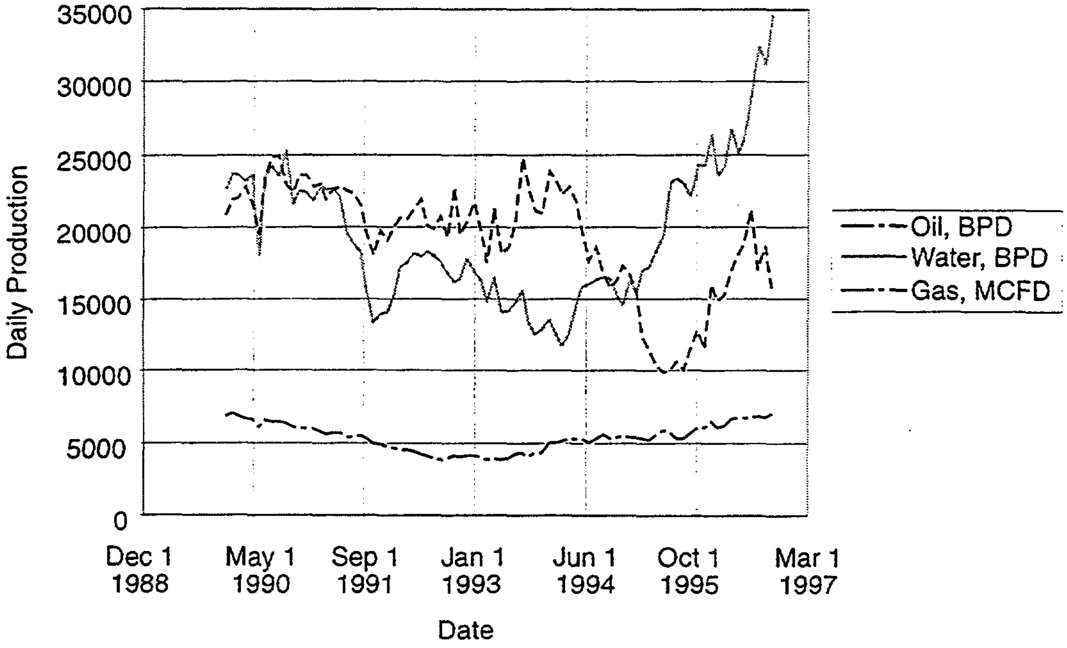

(a) Production History, Tract 17

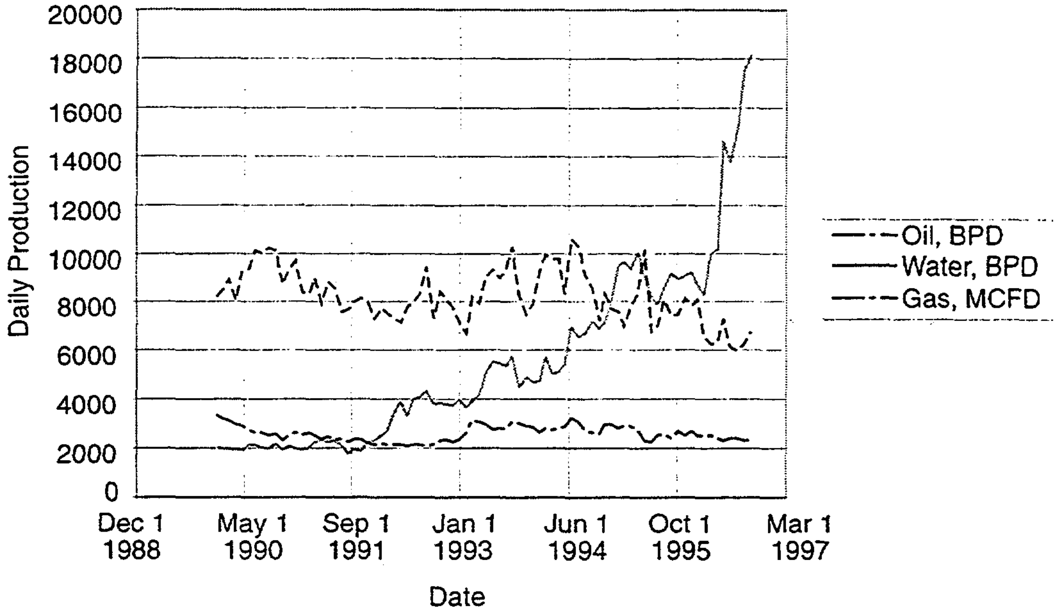

(b) Production History, Tract 49

FIGURE **8-4**

PRODUCTION HISTORY DATA

BDM-NIPER/FRACMAN

9. CONCLUSION

The first year of the research project, Fractured Reservoir Discrete Fracture Network Technologies has been very productive in development and implementation of new and innovative technologies. In particular, compartmentalization analysis technologies hold substantial promise to improve reservoir production. We look forward to a continued program during the next two project years.

10. NOTATION

b	extent of flow region, L
Dr	ratio of inner-zone to outer-zone diffusivities
h	hydraulic head, L
h_D	dimensionless head
h_w	constant head at source, L
H	head in source, L
H_D	dimensionless head in source
$I_v(z)$	Modified Bessel function
K	hydraulic conductivity, LT^{-1}
$K_v(z)$	modified Bessel function
n	flow dimension
p	Laplace transform variable
q	transient flux rate for constant-head conditions, L^3T^{-1}
q_D	dimensionless flux rate for constant-head condition
Q	constant injection (or withdrawal) rate for constant-rate condition, L^3T^{-1}
Q_D	dimensionless cumulative injection (or withdrawal) for constant-head condition
r	radial distance from source, L
r_D	dimensionless radial distance from source
r_{D1}	dimensionless radius of the inner region
r_1	radius of the inner region, L
r_w	radius of the source, L
S_s	specific storage, L^{-1}
S_w	storage capacity of the source, L^2
S_{wD}	dimensionless storage capacity of the source
t	time, T
t_D	dimensionless time
v	parameter defined in (A20)
a_n	area of a unit sphere in n dimensions
D_1	dimensionless group defined by (A16)
D_2	dimensionless group defined by (A17)
l_1	dimensionless group defined by (A18)
l_2	dimensionless group defined by (A19)
s	dimensionless parameter defined by (A10)

<u>Subscripts</u>

D	dimensionless
i	= 1 (for inner region), or 2 (for outer region)
w	source
1	inner region
2	outer region

11. REFERENCES

Barber, C. B., D.P. Dobkin, and H.T. Huhdanpaa, 1993. The Quickhull Algorithm for Convex Hull, Technical Report GCG53, available as ftp://geom.umn.edu/pub/ documents/ preprints/GCG53. The Geometry Center, Minneapolis, MN., 1993.

Barber, C. B., D.P. Dobkin, and H.T. Huhdanpaa, 1995. The Quickhull Algorithm for Convex Hulls, ACM Transactions on Mathematical Software.

Barker, J.A., 1988. A Generalized Radial Flow Model for Pumping Tests in Fractured Rock. Water Resources Research, Vol. 24, p 1796-1804.

Caine, J.S., J.P. Evans, and C.B. Forster, 1996. Fault Zone Architecture and Permeability Structure. Geology, v. 24, no. 11, p. 1025-1028.

Choquette, P.W., and L.C. Pray, 1970. Geologic nomenclature and classification of porosity in sedimentary carbonates. American Association of Petroleum Geologists Bulletin, v. 54, p. 207-250.

Craig, D.H. 1958. Regional Geologic Setting of the Yates Field. Technical Memorandum No. 63-30C, Denver Research Center, Marathon Oil Company.

Craig, D.H. 1988. Caves and other features of Permian karst in San Andres dolomite, Yates Field reservoir, west Texas, in James, N.P., and Choquette, P.W. eds., Paleokarst: Springer, New York, p. 342-363.

Craig, D.H. 1990. Yates and other Guadalupian (Kazanian) oil fields, U.S. Permian Basin, *in* Brooks, J., ed., Classic Petroleum Provinces: Geologic Society of London Special Publication No. 50, p. 259-263.

Dershowitz, W. and P. La Pointe, 1985. Discrete Fracture Approaches for Oil and Gas Applications. Proceedings, NARMS '94, North American Rock Mechanics Symposium, Austin, TX. Balkema, Rotterdam.

Dershowitz, W. and T. Doe, 1997. Analysis of Heterogeneously Connected Rock Masses by Forward Modeling of Fractional Dimensional Flow Behavior. International Journal of Rock Mechanics, Mining Sciences, and Geomechanics Abstracts, Vol. 34, No. 3.

Dershowitz, W., G. Lee, J. Geier, T. Foxford, P. La Pointe, and A. Thomas, 1996. FracMan Interactive Discrete Feature Data Analysis, Geometric Modeling, and Exploration Simulation - User Documentation, Version 2.5. Golder Associates Inc., Seattle.

Dershowitz, W., N. Hurley, and K. Been, 1992. Stochastic Discrete Fracture Modeling of Heterogeneous and Fractured Reservoirs. Proceedings, 3rd International Conference on the Mathematics of Oil Recovery. Delft, Holland, June 1992.

Dershowitz, W., P. La Pointe, H. Einstein, and V. Ivanova, 1996. Fractured Reservoir Discrete Feature Modeling Technologies. Second Quarterly Progress Report, June 7, 1996 to August 31, 1996. Prepared for Contract G4S51728, BDM-Oklahoma, US Department of Energy National Oil and Related Programs. Golder Associates Inc., Seattle (September).

Dershowitz, W., P. La Pointe, and T. Foxford, 1997. Generating Fractal Reservoirs through Neural Network Analyses of Geological Data. Submitted to AAPG Bulletin.

Dershowitz, W., R. Busse, J. Geier, and M. Uchida, 1996. A Stochastic Approach to Fracture Set Definition. Proceedings, NARMS '96, North American Rock Mechanics Symposium, Montreal, Quebec. Balkema, Rotterdam.

Doe, T., 1991. Fractional Dimension Analysis of Constant-Pressure Well Tests. SPE paper 22702, presented at the 66th Annual SPE Technical Conference & Exhibition. SPE, Dallas.

Doe, T. and C. Chakrabarty, 1996. Analysis of Well Tests in Two-Zone Composite Systems with Different Spatial Dimensions. Water Resources Research (in press).

Doe, T. and J. Geier, 1991. Interpretation of Fracture System Geometry Using Well Test Data. OECD/NEA Stripa Project Technical Report TR-91-03. SKB, Stockholm.

Dunham, R.J., 1962. A classification of carbonate rock types according to depositional texture, in Ham, W.E. ed., Classification of Carbonate Rocks: American Association of Petroleum Geologists Memoir 1, p. 108-122.

Eberhart, R.C. and R.W. Dobbins, 1990. Neural Network PC Tools. Academic Press, London, 414p.

Ellis, G.W., C. Yao, R. Zhao, and D. Penumadu, 1995. Stress-strain modeling of sands using artificial neural networks, Journal of Geotechnical Engineering, v. 121, n. 5, p. 429-435.

Feng, Xiating, 1995. Neural network approach to comprehensive classification of rock stability, blastability and drillability, International Journal of Surface Mining, Reclamation and Environment v. 9, n. 2, p. 57-62.

Galley, J.E., 1958. Oil and Geology in the Permian Basin of Texas and New Mexico. Symposium. Habitat of Oil (ed. L.G. Weeks), American Association of Petroleum Geologists, p.395-446.

Geier, J., W. Dershowitz, P. Wallmann, and T. Doe, 1995. Discrete Fracture Modeling of In-Situ Hydrologic and Tracer Experiments, *in* Myer, L.R., N.G.W. Cook, R.E. Goodman, and C.-F. Tsang, eds, Fractured and Jointed Rock Masses. Balkema, Rotterdam.

Goh, T.C., 1994. Seismic liquefaction potential assessed by neural networks, Journal of Geotechnical Engineering, v. 120, n. 9, p. 1467-1480.

Hills, J.M., 1970. Late Paleozoic structural directions in Southern Permian basin, West Texas and Southeastern New Mexico. American Association of Petroleum Geologists Bulletin, v. 54, p. 1809-1827.

Intera, 1994. ECLIPSE Reservoir Simulator. Intera-ECC, Henley, U.K.

Isaaks, E.H. and R.M. Srivastava, 1985. An Introduction to Applied Geostatistics. Oxford University Press, Oxford.

Ivanova, V., 1995. Three-Dimensional Stochastic Modeling of Rock Fracture Systems. M. Sc. thesis, Massachusetts Institute of Technology, Cambridge, MA, 200 p.

Ivanova, V., X. Yu, D. Veneziano, and H. Einstein, 1995. Development of stochastic models for fracture systems, in Proceedings: 35th U.S. Rock Mechanics Symposium, University of Nevada, Reno, June 5-7, 1995, p. 725-730.

Kazemi, H., L.S. Merrill, Jr., K.L. Porterfield, and P.R. Zeman, 1976. Numerical Simulation of Water-Oil Flow in Naturally Fractured Reservoirs, Society of Petroleum Engineers of AIME Journal, v. 16, n. 6, p. 317-326.

Kenyon, J., 1996. TAGS Heated Volume Analysis. Personal Communication. Marathon Oil, Midland, TX.

La Pointe, P.R. and C.C. Barton, 1995. Creating Reservoir Simulations with Fractal Characteristics, *In* Barton, C.C. and P.R. La Pointe, eds., Fractals in Petroleum Geology and Earth Processes. Plenum Press, New York.

La Pointe, P.R. and J. Hudson, 1985. Characterization and Interpretation of Rock Joint Patterns. GSA Special Paper 199. GSA, Denver.

La Pointe, P.R., P.C. Wallmann, and S. Follin, 1995. Estimation of effective block conductivites based on discrete network analyses using data from the Äspö site, SKB Technical Report 95-15, Swedish Nuclear Fuel and Waste Management Co., Stockholm.

La Pointe, P., T. Foxford, and W. Dershowitz, 1996. Research Report Reservoir Compartmentalization. Prepared for Contract G4S51728, BDM-Oklahoma, U.S. Department of Energy National Oil and Related Programs. Golder Associates Inc., Seattle (December).

Lee, C., and R. Sterling, 1992. Identifying probable failure modes for underground openings using a neural network, International Journal of Rock Mechanics, Mining Sciences, and Geomechanics Abstracts, v. 29, n. 1, p. 49-67.

Masters, T., 1993. Practical Neural Network recipes in CH. Academic Press, New York.

Maqurek, M., P. Bossart, and T. Eliasson, 1995. Classification and Characterization of Water Conducting Fractures at Äspö. SKB Äspö Program Report PR-25-95-03. SKB, Stockholm.

Merkel, R.H., 1992. FMS Interpretation of YFU-17D5. Marathon Oil Company, Intracompany correspondence.

Miller, I., G. Lee, W. Dershowitz, and G. Sharp, 1995. MAFIC Matrix/Fracture Interaction Code with Solute Transport - User Documentation, Version B1.5. Golder Associates Inc., Seattle.

Ortoleva, P.J. ed, 1994. Basin Compartments and Seals. AAPG Memoir 61, American Association of Petroleum Geologists, Tulsa.

Parzan, E., 1962. On Estimation of a Probability Density Function and Mode. Annals of Mathematical Statistics, v. 33, p. 1065-1076.

Pusch, R., 1995. Categorization of Discontinuities in Rock. Clay Technology AB, Lund.

Sedgewick, R., 1990. Algorithms in C. Addison-Wesley Pub. Co., Reading, MA.

Specht, D., 1990. Probabilistic Neural Networks. Neural Networks, v. 3, p. 109-118.

Stearns, D.W. and M. Friedman, 1972. Reservoirs in fractured rock, in King, R.E., ed., Stratigraphic Oil and Gas Fields - Classification, Exploration Methods and Case Histories: American Association of Petroleum Geologists Memoir 16, p. 82-106.

Thomas, A.L. and P.R. La Pointe, 1995. Conductive fracture identification using neural networks. Proceedings: 35th U.S. Rock Mechanics Symposium, University of Nevada, Reno, June 5-7, 1995, p. 627-632.

Tinker, S.W., 1996. Building the 3-D Jigsaw Puzzle: applications of sequence stratigraphy to 3-D reservoir characterization, Permian Basin. American Association of Petroleum Geologists Bulletin, v.80, n. 4, p.460-485.

Tinker, S.W., J.R. Ehrets, and M.D. Brondos, 1995. Multiple karst events related to stratigraphic cyclicity: San Andres formation, Yates field, west Texas, in Budd, D.A., Saller A. H., and Harris, P.M., eds., Unconformities and Porosity in Carbonate Strata: American Association of Petroleum Geologists Memoir 63, p.213-237.

Tinker, S.W., and D.H. Mruk, 1995. Reservoir characterization of a Permian giant: Yates field, west Texas, in E. Stoudt and P.M. Harris, eds., Hydrocarbon reservoir characterization, geologic framework and flow-unit modeling: SEPM Short Course 34, p.51-128.

Tung, A.T., F.S. Wong, and W. Dong, 1994. Prediction of the spatial distribution of the modified Mercalli intensity using neural networks, Earthquake Engineering and Structural Dynamics, v. 23, n. 49, p 62.

Xu, Q., and R.Q. Huang, 1994. Artificial neural network methods for spatial prediction of slope stability. Oliveira, R., L.F. Rodrigues, A.G. Coelho, and A.P. Cunha, eds, Proceedings; Seventh in International Congress; International Association of Engineering Geology, v. 7, p. 4725-4728.

Winberg, A., ed., 1996. First TRUE State - Tracer Retention Understanding Experiments. Descriptive Structural-Hydraulic Models on Block and Detailed Scales of the TRUE-1 Site. SKB Äspö International Cooperative Report ICR 96-04. SKB, Stockholm.

ATTACHMENT C

REFEREED PUBLICATION

Chakrabarty, C. and T. Doe (1997)
Analysis of Well Tests in Two Zone Composite Systems
with Different Spatial Dimensions
Submitted to Water Resources Research (in review)

Analysis of well tests in two-zone composite systems with different spatial dimensions

CHAYAN CHAKRABARTY
Golder Associates (UK) Ltd.
Landmere Lane, Edwalton, Nottingham, UK

THOMAS. W. DOE
Golder Associates Inc.
4044 - 148th Avenue N.E., Redmond, Washington

Single continuum models for hydraulic tests in fractured and unfractured rocks do not treat the flow geometry in the immediate vicinity of the source explicitly. If the geometric and flow properties of the medium in a region close to the source well are significantly different from those in a region farther away from the well, then a single continuum model will not be able to provide an accurate overall representation of flow in such a system.

This study presents a new analytical model for analysis of well tests in a flow system that may be viewed as a two-zone composite medium. The two regions of the composite medium describe flow regimes that are characterised by arbitrarily assigned flow dimensions, transmissivities and storativities, which may be different for the two regions. The source well is considered to have a finite radius; both constant-rate (with wellbore storage) and constant-head conditions at source are considered.

Solutions to the flow equations are obtained analytically and sensitivity runs are conducted to find the effect of the various model parameters on the pumping-induced responses in such systems.

Key words: composite system, GRF, fractional dimension, flow dimension, hydraulic test, well test analysis.

1. INTRODUCTION

1.1 *Nature of Dimension in Well Tests*

This paper presents a mathematical description of a two-zone composite model of flow to a well where the two zones may have an arbitrarily assigned dimension. The model is an extension of the generalized radial flow (GRF) approach of *Barker* [1988] to the case of flow geometries where there may be changes in flow dimension with distance from the well.

For a rock with homogeneous hydraulic properties, the flow dimension of a well test geometry describes the change in the cross-sectional area through which flow occurs with distance from a pumping well. For the familiar radial-cylindrical geometry [e.g., *Theis*, 1935], this area changes with the first power of distance from the well. Flow areas for spherical geometries change by a power of two, and linear flow geometries (such as vertical fractures or flow channels) do not change with distance. Fractional dimensions arise when the area of the flow system varies by some non-integer power with radial distance. *Barker* [1988] envisioned such behaviour as a distinctive characteristic of fracture systems, but the concept applies to any heterogeneous medium, porous or fractured, where the conducting portion of the rock incompletely fills the available space.

In Barker's model [1988], radial flow is considered to take place through a porous conduit whose cross-sectional flow area (A) is proportional to a power of distance from the source and is expressed as $A \propto r^{(n-1)}$, where n is the flow dimension. The value of this dimension, *n*, need not be an integer. The concept of flow dimension and certain aspects of its use to interpret hydraulic test data have been examined in recent studies [*Doe and Geier,* 1991; *Black*, 1994; *Wei and Chakrabarty*, 1996]. *Wei and Chakrabarty* [1996] demonstrated, using fracture network simulations, that hydraulic test responses exhibiting non-integral flow dimensions were commonplace. *Doe and Geier* [1991] discussed the geometric interpretation of the flow dimension and extended the GRF model to constant-head tests. *Bangoy et al.* [1992] and *Chakrabarty* [1994] provided simple straight-line plot techniques for generalized dimensional analysis of constant-rate interference tests. *Doe and Wallmann* [1995] showed that the flow dimension may reflect the space-filling properties of the fracture network as determined by the density of fractures per unit volume of rock.

Fractal patterns are an important example of a geometry which partially fills space and has power-law variation of transmissive and storage properties with distance [*Chang and Yortsos*, 1990; *Acuna and Yortsos*, 1995]. Fractional dimensions may also reflect variability in hydraulic properties. For example, a medium with a linear flow geometry and hydraulic properties that vary as a particular power of distance will produce the same well test behaviour as a medium with homogeneous properties and a cross-sectional area which varies as the same power of distance [*Doe and Geier*, 1991; *Chakrabarty*, 1993]. In this paper, we will restrict the discussion to the case of invariant flow properties within each zone of the composite model.

1.2 *Origins of Composite Dimension Behaviour*

The flow solutions in the Generalized Radial Flow (GRF) Model of *Barker* [1988] only considered a flow system with a single homogeneous dimension. Realistic well tests, however, may behave as two-zone composites with distinct dimensions in each zone if either of the two following conditions exist:

a) if the source well dimension differs from the dimension of the conducting medium, or

b) if the medium is a network of conductors where the inner zone has the dimension of an individual conductor directly connected to the source well and the outer zone has the dimension of the network as a whole.

Consider first the well geometry itself. Barker's GRF Model viewed the source well as a "sphere" (of n dimensions, projected through three-dimensional space) having the same dimension as that of the surrounding medium. Hence, the GRF Model represents cylindrical flow with cylindrical sources (n = 2), spherical flow with spherical sources (n = 3), and a specific partial dimensional flow with a surface consistent with that partial dimension.

Composite flow may arise where the geometry of the source well has a different dimension from that of the surrounding medium. The well test literature contains a number of examples of composite dimension behaviour where the inner zone dimension is imposed by the geometry of the well itself. For example, the corrections to the Theis solution for the effects of a finite source radius produce a composite dimensionality where the inner dimension is one (as typified by a characteristic logarithmic half slope) and the outer dimension is two [*Mueller and Witherspoon*, 1965]. The solution for partial penetration of a tabular aquifer is also a composite dimension system of at least two zones. In this case, the inner zone may behave in a spherical manner (if the well penetration is short compared with the aquifer thickness) and the outer zone behaves cylindrically [*Hantush*, 1964]. Similarly, solutions for spherical flow which consider the cylindrical geometry of the source well produce a composite behaviour with an inner-zone dimension of two and an outer-zone dimension of three [*Hantush*, 1961].

The geometry of fluid conductors can create composite systems particularly where the medium consists of a network of fractures or channels. If the network is sparse relative to the size of the source interval, the connection between the network and the source well may be a few or even a single fracture or channel. In this event, the dimension of the individual conductor influences the dimensional behaviour of the inner zone, while the dimensional characteristics of the network as a whole control the behaviour of the outer shell. Figure 1 shows some of the possibilities. Given a three dimensional network of fractures or linear channels, the dimension of the network should approach a spherical flow. The connection of this network to the well, however, may consist of a single conduit. If this conduit is a channel, the inner zone dimension should be very low, even one. Or if it is a homogeneous fracture, the dimension may approach two. Should the channels or fractures be heterogeneous internally or leaky, the dimensions may be lowered or raised to a fractional value.

This effect was demonstrated by the numerical modelling of well tests in fractal networks [*Acuna and Yortsos*, 1995]. The late-time pressure transients of the simulated well tests behaved according to the fractional dimension of the network. The early time behaviour, on the other hand, was strongly influenced by the local geometry of the connection of the well to the network.

Karasaki et al. [1988] presented a two-zone composite model that could be used to represent some fracture systems. The model viewed the fractured aquifer as a lattice of interconnected, one-dimensional conductors. The intersection of a borehole with the lattice would produce a one dimensional geometry, hence the near field flow geometry is one-dimensional or linear. At greater distances the flow geometry would become two-dimensional as the lattice segments intersect one another to form a space-filling network. Karasaki's analytical model presented the case for a constant-rate condition with no wellbore storage or skin. The model also was restricted effectively to representing a two-dimensional space.

Novakowski [1989] presented a two-zone composite model to represent hydraulic parameters in the immediate vicinity of the pumping well that were different from those for the aquifer as a whole. While his solutions included wellbore storage at the pumping well, they were derived for two-dimensional flow geometry throughout the aquifer.

Three dimensional fracture networks may have a wider range of dimensional responses. A vertical well in a three dimensional network should dominantly intersect horizontal fractures. The horizontal fractures, when space-filling within their planes, should impose an early time two-dimensional response, followed by spherical behaviour from the fracture network. Partial penetration of two dimensional features can produce early time spherical flow and late time cylindrical flow. If the feature being partially-penetrated is a linear feature, such as a sand channel, the later time response may even be one dimensional.

The analytical model we present in this paper is completely generalized with respect to the dimensions of the composite regions. A single set of equations can express the hydraulic behaviour of the system for any combination of dimensions. In addition, the transmissivities and storativities of the regions are allowed to be different.

Before discussing composite systems, it is valuable to review the characteristic behaviours of transient curves in homogeneous media. The *Barker* [1988] type curves for constant rate flow in a single dimension system show that fractional dimensions less than two are readily recognised in logarithmic plots by their straight line behaviour. The slope of these lines is equal to $slope_{n<2} = 1 - \frac{n}{2}$. Transient rate data from constant pressure tests exhibit a similar behaviour, but with slopes of opposite sign to the constant-rate case (*Doe, 1991*). Derivative curves, such as those developed for cylindrical flow by *Bourdet et al.* [1983], are very effective for recognising dimensions. Log plots of the pressure derivative for constant rate tests, $\frac{dP}{dln(t)}$, also tend to straight lines with slopes of ($1-n/2$) regardless of dimension. The same slopes appear for constant pressure curves where the derivative is taken using the inverse flow rate rather than the pressure [*Doe*, 1991]. The use of derivative plots greatly enhances the recognition of the test dimension, particularly for dimensions greater than 2.

2. MATHEMATICAL MODEL FOR A COMPOSITE SYSTEM

2.1 Assumptions.

The main assumptions made in the course of developing the models for transient rate and pressure behaviour in a two-zone composite system are as follows:

i) transient radial Darcian flow takes place in the system;

ii) the i^{th} zone is characterised by flow dimension n_i ($i = 1$ for the inner zone and $i = 2$ for the outer zone), where n_i is not necessarily an integer; the source well is an n_1-dimensional "sphere" projected through three-dimensional space;

iii) the i^{th} zone is characterised by hydraulic conductivity and specific storage K_i and S_{si}, respectively ($i = 1$ for the inner zone and $i = 2$ for the outer zone);

iv) the system is infinite, and either a constant-rate or a constant-pressure condition is imposed at the source well;

v) wellbore/source storage capacity is non-negligible.

2.2 Constant-Rate Case.

Formulation of Flow Equations:

The radial flow behaviour of water in a two-zone composite system is governed by the following equations (the form of the equations is the same as in *Barker*, 1988):

$$\frac{K_1}{r^{n_1-1}}\frac{\partial}{\partial r}\left(r^{n_1-1}\frac{\partial h_1}{\partial r}\right)=S_{s1}\frac{\partial h_1}{\partial t},\ r_w \le r \le r_1 \qquad (1)$$

$$\frac{K_2}{r^{n_2-1}}\frac{\partial}{\partial r}\left(r^{n_2-1}\frac{\partial h_2}{\partial r}\right)=S_{s2}\frac{\partial h_2}{\partial t},\ r_1 \le r < \infty \qquad (2)$$

where $h_1(r,t)$ and $h_2(r,t)$ are the heads in the inner and outer zones, respectively, and r_1 is the radius of the inner zone. The objective is to solve the system of partial differential equations shown above, with the following conditions:

<u>initial condition</u>

$$h_1(r,t=0) = h_2(r,t=0) = H(t=0) = 0 \qquad (3)$$

where H(t) is the head in the source well and is given by

$$H(t) = h_1(r_{w+0}, t) \qquad (4)$$

inner boundary condition

$$S_w \frac{dH(t)}{dt} = Q + K_1\, b^{3-n_1}\, \alpha_{n_1}\, r_w^{n_1-1}\, \frac{\partial h_1}{\partial r}\Big|_{r=r_w} \tag{5a}$$

where S_w is the storage capacity of the source well ($S_W = \pi r_w^2$ for open pumping wells), b is the extent of the inner and outer flow regions (e.g., for 2-D flow in a confined homogeneous aquifer, b equals the aquifer thickness), and

$$\alpha_n = \frac{2\pi^{n/2}}{\Gamma(n/2)} \tag{5b}$$

outer boundary condition

$$h_2(r \rightarrow \infty, t) = 0 \tag{6}$$

rate continuity at the boundary of the inner and outer regions

$$\left(\frac{K_1\, b^{n_2-n_1}}{K_2} \frac{\alpha_{n_1}}{\alpha_{n_2}} r_1^{n_1-n_2} \right) \frac{\partial h_1}{\partial r}\Big|_{r=r_1} = \frac{\partial h_2}{\partial r}\Big|_{r=r_1} \tag{7}$$

head continuity at the boundary of the inner and outer regions

$$h_1(r = r_1, t) = h_2(r = r_1, t) \tag{8}$$

Dimensionless variables are defined in this study as follows

$$h_{Di}(r_D, t_D) = \frac{K_1\, b^{3-n_1}\, \alpha_{n_1}\, r_w^{n_1-2}}{Q} h_i(r,t), \; i = 1,\ 2 \tag{9}$$

$$t_D = \frac{K_1\, t}{S_{s1}\, r_w^2} \tag{10}$$

$$r_D = r / r_w \tag{11}$$

Substituting (9) through (11) into (1) and (2), we can rewrite the governing equations in terms of the dimensionless variables (see (A1) and (A2), respectively, of Appendix A). The linear parabolic partial differential equations given by (A1) and (A2) are solved using the Laplace transformation and modified Bessel functions. The mathematical development of the analytical solution is similar to that for other composite models of this type (e.g., *Karasaki et al.*, 1988; *Novakowski*, 1989) except that this model includes not only a step variation in transmissivity and storativity but also in generalized spatial dimension. The details of the transform-space solution of this system of equations, for the constant-rate inner boundary condition, are presented in Appendix A.

Analytical Solution of the Flow Equations

As shown in Appendix A, the solution for the dimensionless head in the inner zone of an infinite two-zone composite system is given by (A14). The solution for transient head in the source well is given by (A21). This solution is a more generalized form of composite medium solutions provided in similar studies [e.g., *Novakowski*, 1989; *Karasaki et al.*, 1988]; for example, by setting $n_1 = n_2 = 2$, and defining the dimensionless variables in terms of the outer zone properties (i.e., in terms of K_2 and S_{s2}), (A21) will reduce to (14) of *Novakowski* [1989].

Also, it can be demonstrated that for $n_1 = n_2 = n$, σ (the interzone coefficient, defined by (A10)) = 1, and D_r (the diffusivity ratio, defined by (A3)) = 1, (A14) reduces to

$$\bar{h}_D(r_D, p) = \frac{K_v(r_D\sqrt{p})}{p\left\{p\, S_{wD}\, K_v(\sqrt{p}) + \sqrt{p}\, K_{v-1}(\sqrt{p})\right\}} r_D^v, \quad 1 \le r_D < \infty \qquad (12)$$

where parameter v is defined with respect to n. Equation (12) is the dimensionless variable equivalent to the solution of *Barker* [1988] for transient head during a constant-rate test with wellbore storage (S_{wD}) and a skin factor equal to zero in an infinite medium characterised by a single flow dimension.

2.3 Constant-Head Case

Formulation of Flow Equations

A constant-head inner boundary condition may be expressed as

$$h_1(r_w, t) = H_w \tag{13}$$

where H_w is the constant head maintained at the source over the duration of the test. For the constant-head case, the dimensionless head, flux rate, and cumulative injection may be defined, respectively, as

$$h_{Di}(r_D, t_D) = \frac{h_i(r,t)}{h_w}, \; i = 1,\ 2 \tag{14}$$

$$q_D(t_D) = \frac{q(t)}{K\, h_w\, b^{3-n_1}\, \alpha_{n_1}\, r_w^{n_1-2}} \tag{15}$$

and

$$Q_D(t_D) = \int_0^{t_D} q_D(t_D)\, dt_D \tag{16}$$

The dimensionless time and radius are defined by (10) and (11), respectively. Substituting (10), (11) and (14) into (1) and (2), the governing equations are expressed, in terms of the dimensionless variables, by (A1) and (A2). The details of the solution of this system of equations, for the constant-head condition at source, are provided in Appendix B.

3. RESULTS AND DISCUSSION

3.1. *Single Well Situation*

This section graphically presents transient solutions for constant rate and constant head tests in a two-zone composite system. The solutions are presented using both source head (for a constant rate situation) and rate (for a constant head condition) as well as their derivatives. The solutions presented graphically are obtained from numerical inversion of the Laplace transformed solutions using the algorithm of *Stehfest* [1970].

Figures 2 and 3 show log-log plots of the constant rate solution for a composite system with the inner and outer zones represented by flow dimensions of 2 and 1.5, respectively. In a fracture-dominated formation, this situation may describe an areal flow network where the source well meets a sufficiently large number of interconnected fractures so that the flow dimension near the pumping well is larger than that for the formation as a whole. The composite solution also includes the following dimensionless parameters: radius of the inner region (r_{D1}) = 100, $S_{wD} = 0.1$, $\sigma = 1$, and $D_r = 1$. The composite solution is compared with single-zone solutions for flow dimensions of 2 and 1.5.

As Figures 2 and 3 show, the composite solution is identical to the single-zone solution (n = 2) up to a dimensionless time of approximately 3000. This is demonstrated quite clearly by the derivative plot. For fully developed generalized radial flow (flow dimension = n), the log-log derivative plot has a large-time slope of (1-n/2); note that, as expected [*Bourdet et al.*, 1983], the large-time derivative is independent of time for n = 2. Figures 2 and 3 also show that the early-time behaviour is followed by a transition period, after which the composite solution mimics the single-zone solution for n = 1.5.

Figures 4 and 5 present log-log plots of the constant head solution and demonstrate the temporal variation of the dimensionless rate and the magnitude of the rate derivative, respectively, for a composite medium with $n_1 = 2.5$ and $n_2 = 1.5$. These figures show that up to a dimensionless time of about 700, the composite solution overlies the solution for the single zone with flow dimension of 2.5. And, as in the constant-rate case, at late time the composite solution is parallel to that for the single zone represented by $n = n_2$.

Thus, the early time flow regime for a composite medium is dominated by inner-zone characteristics, provided the wellbore storage effects (for a constant-rate test) are small and the extent of the inner zone is large enough. Large S_{wD} values act to mask the influence of the inner zone for small inner zone extents and therefore can have a significant impact on our capability of recognising the behaviour of the inner zone; a similar observation was made by *Novakowski* [1989] for cylindrical symmetry flow in his two-zone composite model. With increasing times, a transition region appears after the inner-zone dominated flow and is followed by a flow regime controlled by the outer-zone response.

Figure 6 demonstrates the effect of outer zone flow dimension (n_2) on constant rate solution for composite systems. At late time, the head response is controlled by the value of n_2; for a smaller value of n_2, the late time head solution has a steeper slope. As shown in Figure 6, the effect of n_2 on the late time derivative is much more dramatic; thus, use of both head and derivative plots is recommended for recognising dimensional variations. The heads and derivatives in Figure 6 indicate that the onset of late-time linear behaviour (on the log-log plot) occurs later for values of n_2 smaller than the inner zone dimension. For example, for $n_2 = 1.5$ the outer zone controlled linear behaviour in derivative starts at more than one-half log cycle in time later than that for $n_2 = 2.5$.

Note that the value of D_r in Figure 6 is 10. Thus, for $n_2 = 2$, the type curves represent a situation where $n_1 = n_2$ and $K_1 = K_2$ (as $\sigma = 1$), but $S_{s1} = 0.1\ S_{s2}$. The change in diffusivity at the interface of the two zones forces the rate of drawdown to change to a different slope, as the $n_2 = 2$ type curves show. Clearly, this change in the rate of drawdown (caused by an increase in storage coefficient in the outer zone) could be easily misinterpreted to be a lateral reduction in hydraulic conductivity. Further discussion related to the effect of D_r on the composite model will be presented later in this section.

The theoretical head and derivative responses presented so far dealt with a fixed value of the interzone coefficient (σ) of 1. The interzone coefficient, given by (A10), quantifies the hydraulic nature of the "interface" between the inner and outer zones in terms of their flow dimension and hydraulic conductivity. To better understand the meaning of σ, let us consider a composite medium with $n_1 = n_2$. Then, from (A10), σ is a function of K_1/K_2, and increases with increasing K_1/K_2; for $K_1 > K_2$, σ (> 1) reflects the permeability reduction away from the source well (akin to the "higher permeability in the skin region" scenario of *Novakowski*, 1989). On the other hand, for $K_1 = K_2$ and $b = r_1$, σ is a function of n_1 and n_2, and increases with increasing n_1/n_2; in this case, for $n_1 > n_2$, σ (> 1) reflects the flow "restriction" away from the source well at the interface. Conversely, for $n_1 < n_2$, σ (< 1) reflects the flow "expansion" away from the source well at the interface because of improved hydraulic connection to a more expansive flow volume in the outer zone.

Figures 7a and 7b demonstrate the effects of σ and D_r on source zone head. Figure 7a considers a case of different flow dimensions in the inner and outer zones, with three sets of values of σ and D_r. Figure 7a shows that variation in σ for the same value of D_r is much more distinguishable from the head and derivative plots than variation in D_r for the same value of σ. Also, fully developed outer zone dominated flow (shown by the derivatives) occurs at different times for different values of σ. While it appears that for $\sigma < 1$ (not shown here) the time to outer zone "stabilisation" (i.e. linear behaviour on the log-log plot) is not strongly dependent on the value of σ, it certainly seems to increase with increasing σ when $\sigma > 1$. That is, fully developed outer zone dominated flow occurs later for larger values of σ for the same D_r. The situation considered in Figure 7b is that of two concentric 2-D cylindrical flow media with different hydraulic conductivity and specific storage, with σ being the ratio of the inner-zone to the outer-zone hydraulic conductivity. The derivative segments are flat during both inner- and outer-zone dominated flow, as expected from fully developed cylindrical symmetry flow in the two zones. However, the outer-zone derivative stabilisations occur at different times and at different stabilised values with respect to the inner zone stabilisation for different values of σ and D_r. In Figure 7b, the lowest derivative curve is a single zone 2-D response curve; the next (upper) curve has $K_1 = K_2$ and $S_{s1} = 0.1\ S_{s2}$, while the uppermost curve has $K_1 = 10\ K_2$ and $S_{s1} = 10\ S_{s2}$.

Figures 7a and 7b indicate that it may not be possible to obtain unique values of both K- and S_s-ratios (in addition to the flow dimensions) from late time head and derivative data because of non-uniqueness in the effect of their variations on the shape of well test data. However, because of the large impact of σ on the shape of the derivatives, it is recommended that this model be used to derive a value of σ from the well test data by assuming a value of D_r.

Figure 8 demonstrates the effect of inner zone flow dimension on the constant rate solution for different wellbore storage values. The head curves are presented for $n_2 = 2$, $r_{D1} = 50$, S_{wD} of 100 and 0.1, and $\sigma = D_r = 1$. Inner zone flow dimensions of 1.5 and 2.5 have been considered. At early times, the head curves show wellbore storage effects followed by the inner-zone flow dimension behaviour. As discussed earlier, relatively large wellbore storage values may completely mask characteristics of the inner zone flow dimension, especially if it is smaller than the outer zone dimension. However, for relatively small magnitudes of wellbore storage and/or large extents of inner zone, the identification of n_2 can be made quite simply with this model.

3.2. *Constant Rate Interference Test*

The effects of location of the observation well and inner-zone flow dimension on a constant-rate interference test are shown in Figures 9 and 19. Figure 9 exhibits the interference response for different values of inner-zone flow dimension with $S_{wD} = 0.1$. The dimensionless radius of the inner-zone is 50; the observation well is located within the outer zone at a distance of $r_D = 100$ from the source. As Figure 9 demonstrates, for $n_2 = 2$ the observation zone response is not likely to distinguish between these values of n_1.

Figure 10 exhibits the interference response for different values of inner-zone flow dimension with the observation well is located within the inner zone at a distance of $r_D = 10$ from the source, with the composite radius being 200. The shapes of observation well head and derivative curves are quite significantly influenced by the value of n_1 when r_{D1} is larger than

r_D. However, if the observation well is located near the interface between the two zones, then the effects of the interface between the two zones may mask those of n_1 and it may be difficult to obtain a unique value of n_1.

Thus, for a composite system with an observation well located well within the outer zone, the observation well response may not be useful from a type-curve matching standpoint for estimation of n_1. However, if the observation well is located in the inner zone such that the inner zone effects are fully seen in the observation well prior to the interface effects, the observation well response may be used to derive n_1, especially with the use of derivative type curves.

4. DISCUSSION

The interface conditions given by (7) and (8) describe the continuity at the boundary of the inner and outer regions. Equation (7) describes the continuity of volumetric rate by assuming that b remains invariant and flow dimension undergoes a step change across the boundary. Equation (8) defines the head continuity by assuming that there is an infinitesimally thin ring of infinite conductivity between the inner and outer regions. An identical assumption was also incorporated into the model of *Karasaki et al.* [1988]. Note that the assumption made in (8) is equivalent to a negligible head loss between the inner and outer regions so that the model essentially predicts an instantaneous "dimensionality adjustment" of the head transients at the boundary. However, this assumption does not preclude the development of a transition regime between fully developed inner and outer region flow (as shown in Section 3.1).

As in other two-zone composite models (e.g., *Karasaki et al.*, 1988; *Novakowski*, 1989), this model characterises the "interface" between the two regions by three parameters. These dimensionless parameters in this model are r_{D1}, σ and D_r. The parameter r_{D1} defines the dimensionless radius required before the system response adjusts to the outer zone dimensionality. The interzone coefficient (σ) can be seen as an indicator of the ease or difficulty with which flow transition occurs from the inner zone to the outer zone. Increasing flow restriction away from the source well at the interface (e.g., for $n_1 > n_2$ or $K_1 > K_2$) increases the magnitude of σ. The diffusivity ratio (D_r) describes the contrast in the speed of propagation of hydraulic disturbances in the two regions. This parameter describes not only the difference in permeability across the boundary, but also that in parameters such as formation compressibility, fracture stiffness, etc.

5. CONCLUSIONS

The two-zone composite analytical solution for well test analysis presented in this paper will be widely applicable to both fractured and heterogeneous flow systems. It is particularly useful for compartmentalised systems and for systems in which the flow behaviour in the vicinity of the well are not representative of larger scale behaviour of interest. Possible applications include analysis of drill-stem tests in fractured and compartmentalised oil and gas reservoirs, analysis of heterogeneous and compartmentalised rock masses for underground storage or disposal facilities, and water supply well analysis.

The two-zone approach described in this paper has been applied successfully to analysis of well tests in Canada, Sweden, the United Kingdom, and Japan. These applications are described in a companion paper.

Future developments of the fractional dimension approach will include extension to three-zone and four-zone systems, and the use of alternative boundary conditions.

APPENDIX A

SOLUTION SCHEME FOR THE CONSTANT RATE CASE

The governing equations in the inner and outer regions, expressed in terms of the dimensionless variables defined in (9) through (11), are:

$$\frac{\partial^2 h_{D1}}{\partial r_D^2}+\frac{n_1-1}{r_D}\frac{\partial h_{D1}}{\partial r_D}=\frac{\partial h_{D1}}{\partial t_D},\ 1 \le r_D \le r_{D1} \tag{A1}$$

and

$$\frac{\partial^2 h_{D2}}{\partial r_D^2}+\frac{n_2-1}{r_D}\frac{\partial h_{D2}}{\partial r_D}= D_r \frac{\partial h_{D2}}{\partial t_D},\ r_{D1} \le r_D < \infty \tag{A2}$$

respectively, where

$$D_r = \frac{K_1/S_{s1}}{K_2/S_{s2}} \tag{A3}$$

In terms of the dimensionless variables, the initial and boundary conditions become

$$h_{D1}(r_D,0) = h_{D2}(r_D,0) = H_D(0) = 0 \tag{A4}$$

$$S_{wD}\frac{d H_D}{d t_D} = 1+\frac{\partial h_{D1}}{\partial r_D}\bigg|_{r_D = 1} \tag{A5}$$

$$h_{D2}(r_D \to \infty, t_D) = 0 \tag{A6}$$

$$h_{D1}(r_{D1}, t_D) = h_{D2}(r_{D1}, t_D) \tag{A7}$$

and

$$\sigma \frac{\partial h_{D1}}{\partial r_D}\bigg|_{r_{D1}} = \frac{\partial h_{D2}}{\partial r_D}\bigg|_{r_{D1}} \tag{A8}$$

where

$$S_{wD} = \frac{S_w}{S_{s1}\, b^{3-n_1}\, \alpha_{n_1}\, r_w^{n_1}} \tag{A9}$$

$$\sigma = \frac{K_1\, (b / r_1)^{n_2 - n_1}}{K_2} \frac{\alpha_{n_1}}{\alpha_{n_2}} \tag{A10}$$

and

$$r_{D1} = r_1 / r_w \tag{A11}$$

Laplace transforms can be used to solve the system of partial differential equations. The subsidiary equations are

$$\frac{d^2 \bar{h}_{D1}}{d r_D^2} + \frac{n_1 - 1}{r_D} \frac{d \bar{h}_{D1}}{d r_D} = p\, \bar{h}_{D1},\ 1 \le r_D \le r_{D1} \tag{A12}$$

and

$$\frac{d^2 \bar{h}_{D2}}{d r_D^2} + \frac{n_2 - 1}{r_D} \frac{d \bar{h}_{D2}}{d r_D} = p\, D_r\, \bar{h}_{D2},\ r_{D1} \le r_D < \infty \tag{A13}$$

After transforming the boundary conditions, (A12) and (A13) are solved simultaneously. The solutions in Laplace space are

$$\bar{h}_{D1}(r_D, p) = \frac{\Delta_2\, K_{v_1}(r_D \sqrt{p}) + \Delta_1\, I_{v_1}(r_D \sqrt{p})}{p\, (\Delta_1 \lambda_2 + \Delta_2 \lambda_1)}\, r_D^{v_1},\ 1 \le r_D \le r_{D1} \tag{A14}$$

and

$$\bar{h}_{D2}(r_D, p) = \frac{\left[\Delta_2 K_{v_1}(r_{D1} \sqrt{p}) + \Delta_1 I_{v_1}(r_{D1} \sqrt{p})\right] K_{v_2}(r_D \sqrt{D_r\, p})\, r_{D1}^{v_1 - v_2}\, r_D^{v2}}{p\, K_{v_2}(r_{D1} \sqrt{D_r\, p})\, (\Delta_1 \lambda_2 + \Delta_2 \lambda_1)},$$

$$r_{D1} \le r_D < \infty \qquad \text{(A15)}$$

where

$$\Delta_1 = \frac{\sigma}{\sqrt{D_r}} K_{v_1-1}(r_{D1}\sqrt{p})\, K_{v_2}(r_{D1}\sqrt{D_r\, p}) - K_{v_2-1}(r_{D1}\sqrt{D_r\, p})\, K_{v_1}(r_{D1}\sqrt{p}) \qquad \text{(A16)}$$

$$\Delta_2 = \frac{\sigma}{\sqrt{D_r}} I_{v_1-1}(r_{D1}\sqrt{p})\, K_{v_2}(r_{D1}\sqrt{D_r\, p}) + K_{v_2-1}(r_{D1}\sqrt{D_r\, p})\, I_{v_1}(r_{D1}\sqrt{p}) \qquad \text{(A17)}$$

$$\lambda_1 = p\, S_{wD}\, K_{v_1}(\sqrt{p}) + \sqrt{p}\, K_{v_1-1}(\sqrt{p}) \qquad \text{(A18)}$$

$$\lambda_2 = p\, S_{wD}\, I_{v_1}(\sqrt{p}) - \sqrt{p}\, I_{v_1-1}(\sqrt{p}) \qquad \text{(A19)}$$

$$v_i = 1 - \frac{n_i}{2},\ i = 1,\ 2 \qquad \text{(A20)}$$

From (A14), the solution for transient head at source may be expressed as

$$\overline{H}_D(p) = \frac{\Delta_2\, K_{v_1}(\sqrt{p}) + \Delta_1\, I_{v_1}(\sqrt{p})}{p\,(\Delta_1 \lambda_2 + \Delta_2 \lambda_1)} \qquad \text{(A21)}$$

APPENDIX B

SOLUTION SCHEME FOR THE CONSTANT-HEAD CASE

The governing equations for transient flow in the two zone composite medium are given, in terms of dimensionless variables defined by (10, (11) and (14), by (A1) and (A2). The initial condition for the constant-head flow situation is

$$h_{D1}(r_D = 1,\ t_D) = 1 \qquad \text{(B1)}$$

The outer and interface boundary conditions are described by (A6) through (A8).

Laplace transforms are again applied to solve the system of partial differential equations. Defining the equations in Laplace space for the two regions by (A13) and (A14) and transforming boundary conditions in Laplace space, the solution for dimensionless head in the inner region is derived to be

$$\bar{h}_{D1}(r_D, p) = \frac{\Delta_2 K_{v_1}(r_D\sqrt{p}) + \Delta_1 I_{v_1}(r_D\sqrt{p})}{p\left[\Delta_1 I_{v_1}(\sqrt{p}) + \Delta_2 K_{v_1}(\sqrt{p})\right]} \tag{B2}$$

where Δ_1 and Δ_2 are given by (A16) and (A17), respectively,

Darcy's law for volumetric rate at the source can be written as

$$q(t) = -K_1 b^{3-n_1} \alpha_{n_1} r_w^{n_1-1} \frac{\partial h_1}{\partial r}\bigg|_{r=r_w} \tag{B3}$$

which, on substituting from (19) and (20), becomes, in Laplace space

$$\bar{q}_D(p) = -\frac{d\bar{h}_{D1}}{d r_D}\bigg|_{r_D=1} \tag{B4}$$

From (B2) and (B4), the solution for dimensionless rate in Laplace space may be expressed as

$$\bar{q}_D(p) = \frac{\Delta_2 K_{v_1-1}(\sqrt{p}) - \Delta_1 I_{v_1-1}(\sqrt{p})}{\sqrt{p}\left[\Delta_1 I_{v_1}(\sqrt{p}) + \Delta_2 K_{v_1}(\sqrt{p})\right]} \tag{B5}$$

For $n_1 = n_2$ and $\sigma = 1$, (B5) reduces to the solution for dimensionless rate during a constant-head test with zero skin in an infinite flow medium characterised by a single value of the flow dimension [*Doe*, 1991].

Comparing (B5) with the constant-rate solution, (A21), for $S_{wD} = 0$, gives

$$\bar{q}_D(p).\bar{H}_D(p) = \frac{1}{p^2} \tag{B6}$$

Finally, the dimensionless cumulative injection, defined by (16) and related to the dimensionless rate by

$$\bar{Q}_D(p) = \frac{\bar{q}_D(p)}{p} \tag{B7}$$

can be expressed in Laplace space as

$$\bar{Q}_D(p) = \frac{\Delta_2\, K_{v_1-1}(\sqrt{p}) - \Delta_1\, I_{v_1-1}(\sqrt{p})}{p\sqrt{p}\left[\Delta_1\, I_{v_1}(\sqrt{p}) + \Delta_2\, K_{v_1}(\sqrt{p})\right]} \tag{B8}$$

so that

$$\bar{Q}_D(p).\bar{H}_D(p) = \frac{1}{p^3} \tag{B9}$$

NOTATION

b	extent of flow region, L
Dr	ratio of inner-zone to outer-zone diffusivities
h	hydraulic head, L
h_D	dimensionless head
h_w	constant head at source, L
H	head in source, L
H_D	dimensionless head in source
$I_v(z)$	Modified Bessel function
K	hydraulic conductivity, LT^{-1}
$K_v(z)$	modified Bessel function
n	flow dimension
p	Laplace transform variable
q	transient flux rate for constant-head conditions, L^3T^{-1}
q_D	dimensionless flux rate for constant-head condition
Q	constant injection (or withdrawal) rate for constant-rate condition, L^3T^{-1}
Q_D	dimensionless cumulative injection (or withdrawal) for constant-head condition
r	radial distance from source, L
r_D	dimensionless radial distance from source
r_{DI}	dimensionless radius of the inner region
r_I	radius of the inner region, L
r_w	radius of the source, L
S_s	specific storage, L^{-1}
S_w	storage capacity of the source, L^2
S_{wD}	dimensionless storage capacity of the source
t	time, T
t_D	dimensionless time
v	dimensionless parameter defined in (A20)
α_n	area of a unit sphere in n dimensions
Δ_1	dimensionless group defined by (A16)
Δ_2	dimensionless group defined by (A17)
λ_1	dimensionless group defined by (A18)
λ_2	dimensionless group defined by (A19)
σ	dimensionless parameter defined by (A10)

Subscripts

D	dimensionless
i	= 1 (for inner region), or 2 (for outer region)
w	source
1	inner region
2	outer region

REFERENCES

Acuña, J. A., and Y. C. Yortsos, Application of fractal geometry to the study of networks of fractures and their pressure transient, *Water Resour. Res.*, 31(3), 527-540, 1995.

Bangoy, L. M., P. Bidaux, C. Drogue, R. Plegat, and S. Pistre, A new method for characterizing fissured media by pumping tests with observation wells, *Jour. Hydrol.*, 138, 77-88, 1992.

Barker, J. A., A generalized radial flow model for hydraulic tests in fractured rock, *Water Resour. Res.*, 24(10), 1796-1804, 1988.

Black, J. H., Hydrogeology of fractured rocks - a question of uncertainty about geometry, *Appl. Hydrogeol.*, 2(3), 56-70, 1994.

Bourdet, D., Whittle, T.M., Douglas, A.A. and Pirard, Y.M., A new set of type-curves simplifies well test analysis, *World Oil*, 95-106, May 1983.

Chakrabarty, C., Pressure-transient analysis of non-Newtonian power-law fluid flow in fractal reservoirs, Ph.D. dissertation, University of Alberta, Edmonton, Canada, 1993.

Chakrabarty, C., A note on fractional dimension analysis of constant rate interference tests, *Water Resour. Res*, 30(7), 2339-2341, 1994.

Chang, J., and Yortsos, Y. C., Pressure-transient analysis of fractal reservoirs, *SPE Formation Evaluation*, 5, 31-38, March 1990.

Doe, T. W., Fractional dimension analysis of contact-pressure well tests, paper SPE 22702 presented at the 66th Annual Technical Conference & Exhibition of the SPE, Dallas, TX, Oct. 6-9, 1991.

Doe, T. W. and J. E. Geier, Interpretation of fracture system geometry using well test data, *Stripa Proj., Tech. Rep. 91-03*, Swed. Nucl. Fuel and Waste Manage. Co., Stockholm, 1991.

Doe, T. W. and Wallmann, P. C., 1995. Hydraulic characterization of fracture geometry for discrete fracture modeling. Proceedings of International Congress on Rock Mechanics, Tokyo, 767-773.

Karasaki, K., J. C. S. Long, and P. A. Witherspoon, A new analytic model for fracture dominated reservoirs, *SPE Formation Evaluation*, 3 (1), 241-250, 1988.

Novakowski, K. S., A composite analytical model for analysis of pumping tests affected by well bore storage and finite thickness skin, *Water Resour. Res*, 25(9), 1937-1946, 1989.

Stehfest, H., Algorithm 368 - Numerical inversion of Laplace transforms [D5], *Communications of the ACM*, 13(1), 47-49, January 1970.

Theis, C. V., The relation between the lowering of the piezometric surface and the rate and duration of discharge of a well using groundwater storage, *Trans. Amer. Geophys. Union*, 16, 519-524, 1935.

Wei, L. and C. Chakrabarty, Evaluation of a self-consistent approach to fractured crystalline rock characterization, Final Report EUR 16926 EN, 4th CEC Research and Development Programme on Management and Storage of Radioactive Waste (1990 - 1994), Comm. of Eur. Communities, Brussels, Belgium, 1996.

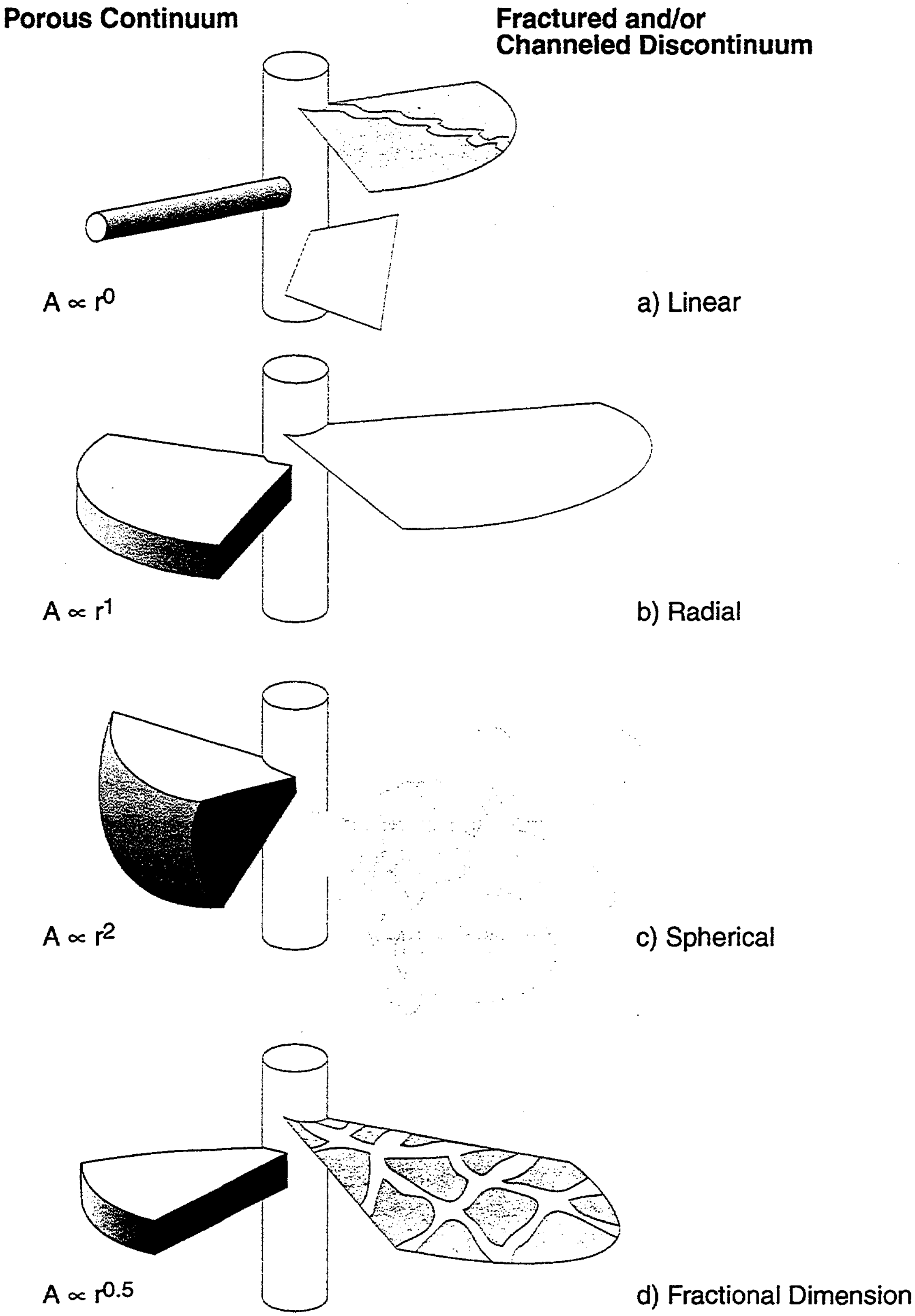

Figure 1. Integer and Fractional Flow Dimension

PROJECT NO. 963 1357.521 DRAWING NO. 72641 DATE 4/18/97 DRAWN BY CB

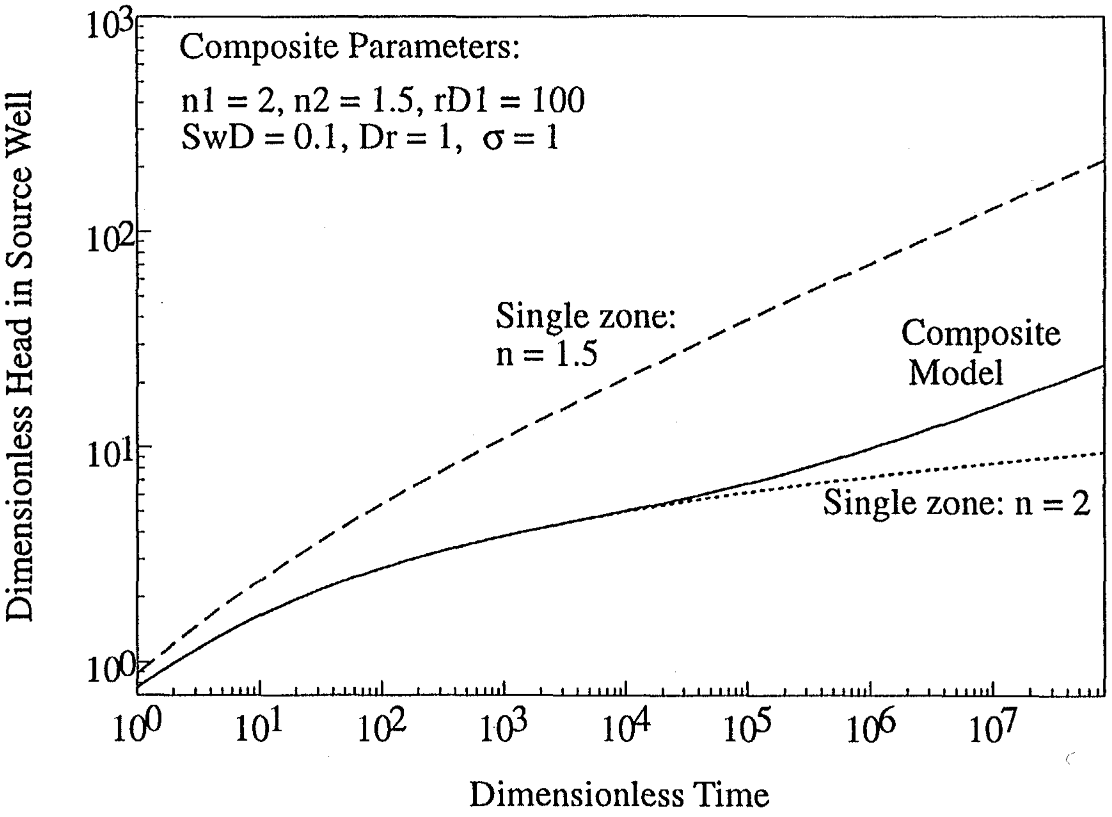

Figure 2: Dimensionless plot of head in source well vs. time for composite model (single-zone models shown for comparative purposes)

PROJECT NO. 953 1357.521 DRAWING NO. 72642 DATE 4/18/97 DRAWN BY CB

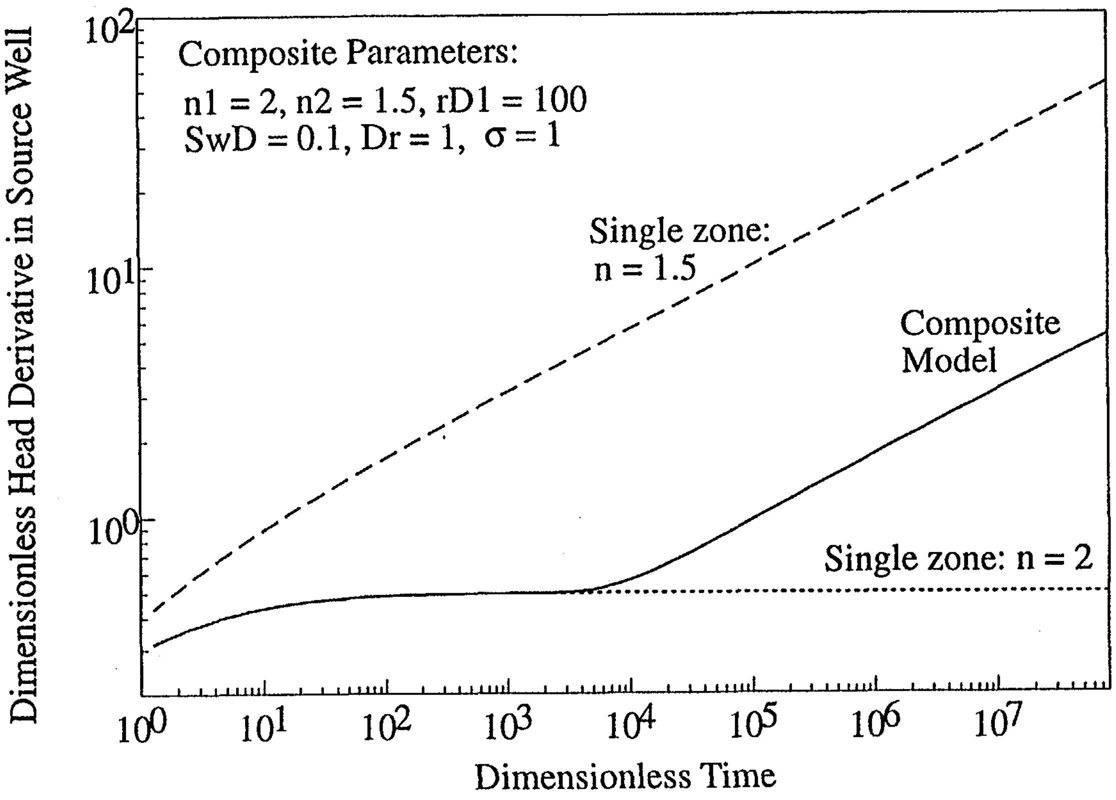

Figure 3: Dimensionless plot of derivative of head in source well vs. time for composite model (single-zone models shown for comparative purposes)

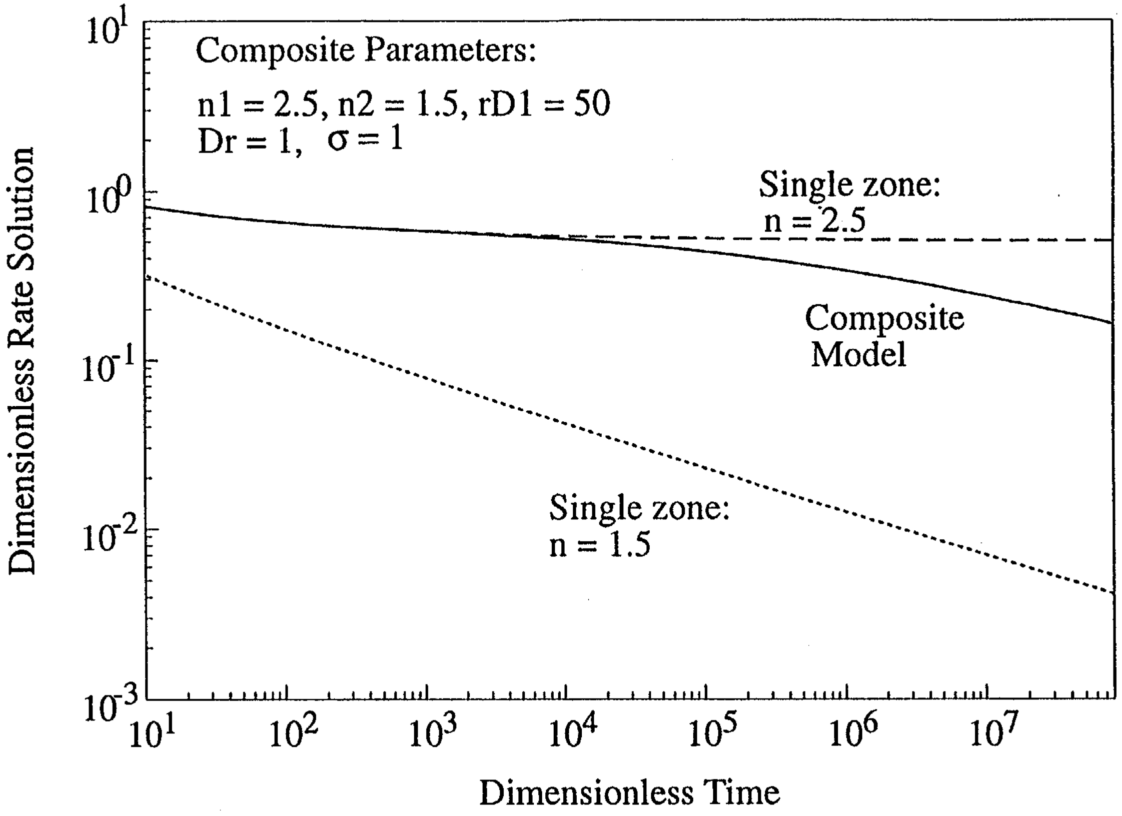

Figure 4: Dimensionless rate solution vs. time for composite model (single-zone models shown for comparative purposes)

PROJECT NO. 953 1357.521 DRAWING NO. 72844 DATE 4/18/97 DRAWN BY CB

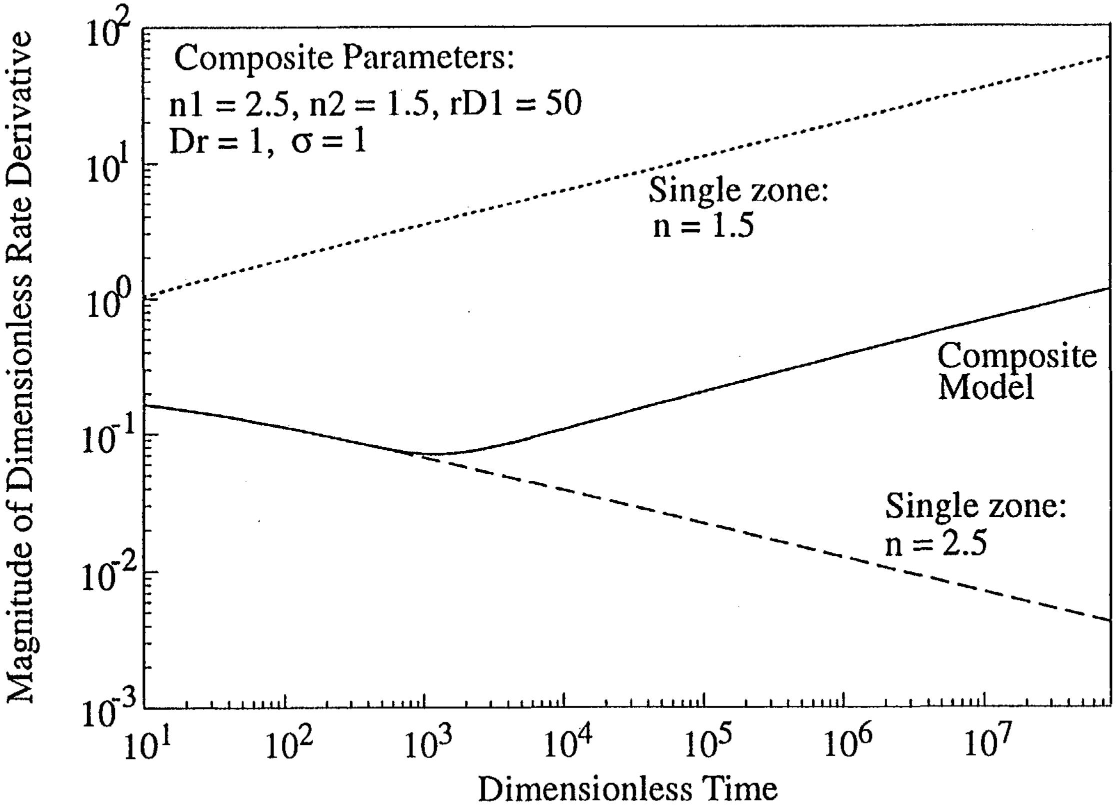

Figure 5: Magnitude of dimensionless derivative vs. time for composite model (single-zone models shown for comparative purposes)

PROJECT NO. 953 1357.521 DRAWING NO. 72645 DATE 4/18/97 DRAWN BY CB

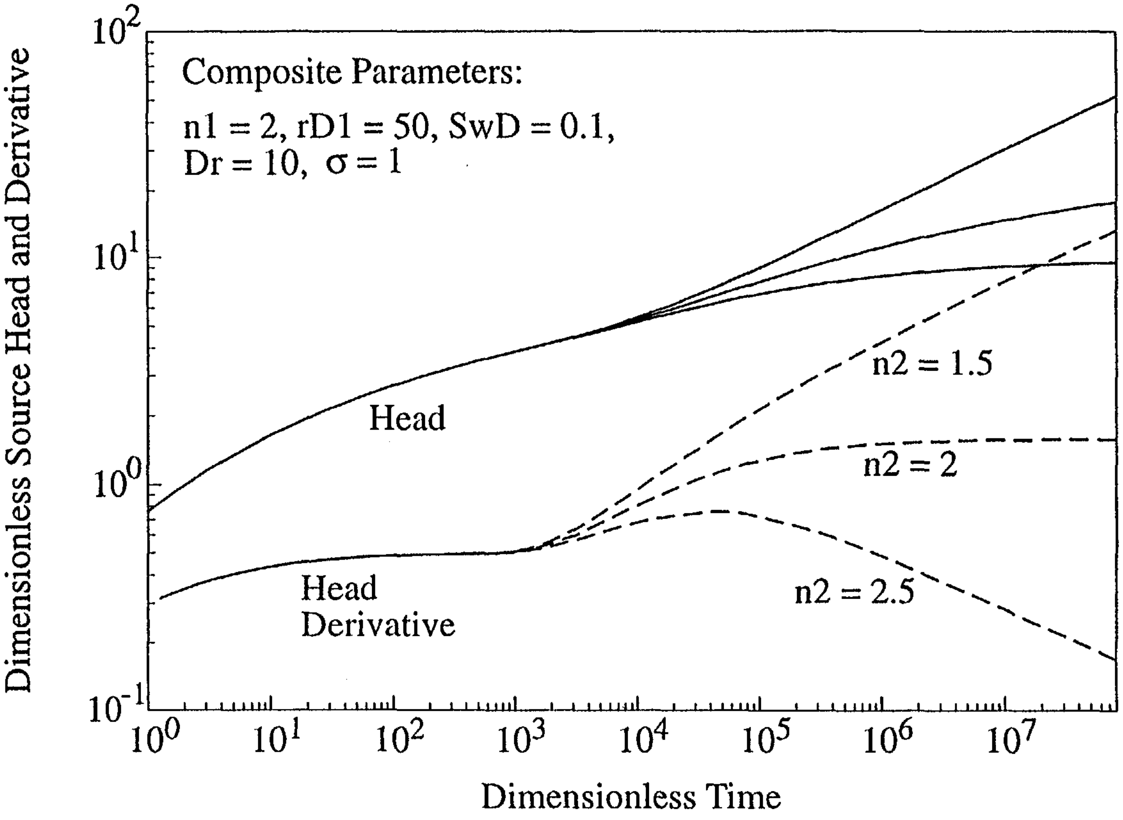

Figure 6: Dimensionless head and head derivative in source well vs. time with different outer zone flow dimensions

PROJECT NO. 953 1357.521 DRAWING NO. 72646 DATE 4/18/97 DRAWN BY CB

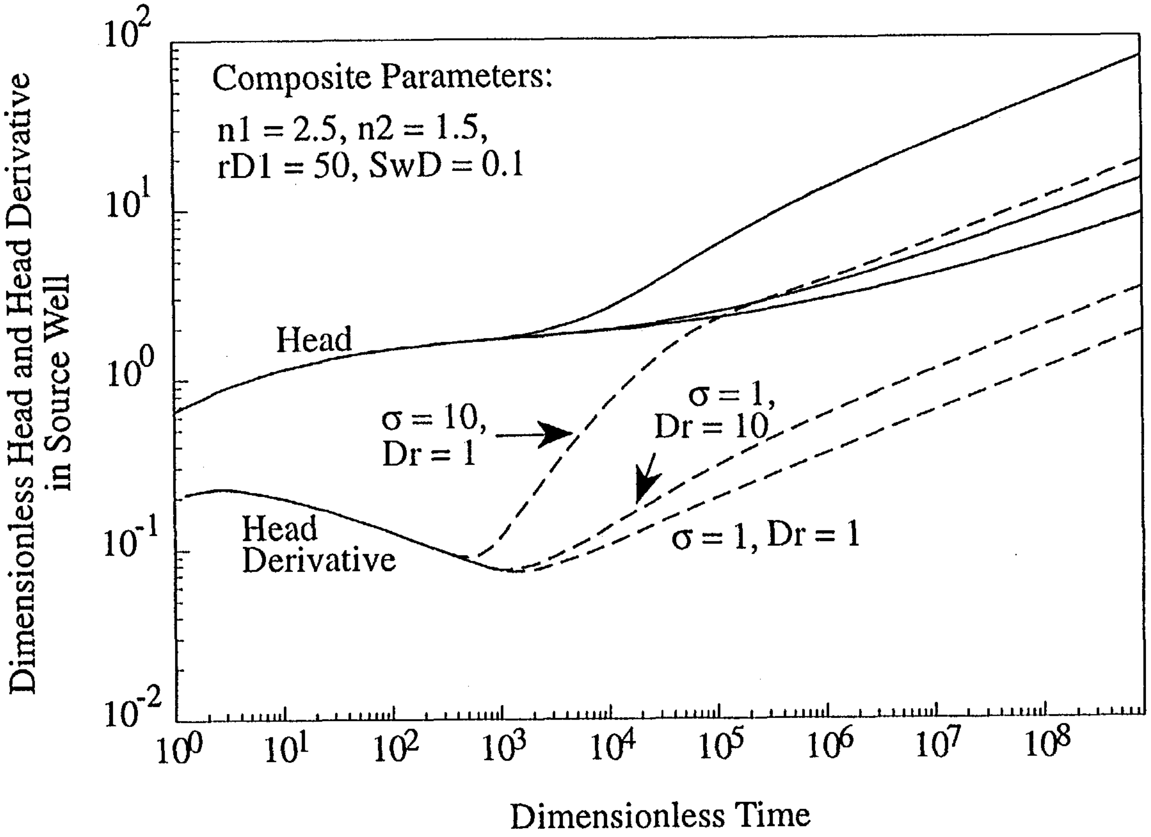

Figure 7a: Dimensionless plot of head and head derivative in source well vs. time for different values of σ and Dr

PROJECT NO. 953 1357.521 DRAWING NO. 72647 DATE 4/18/97 DRAWN BY CB

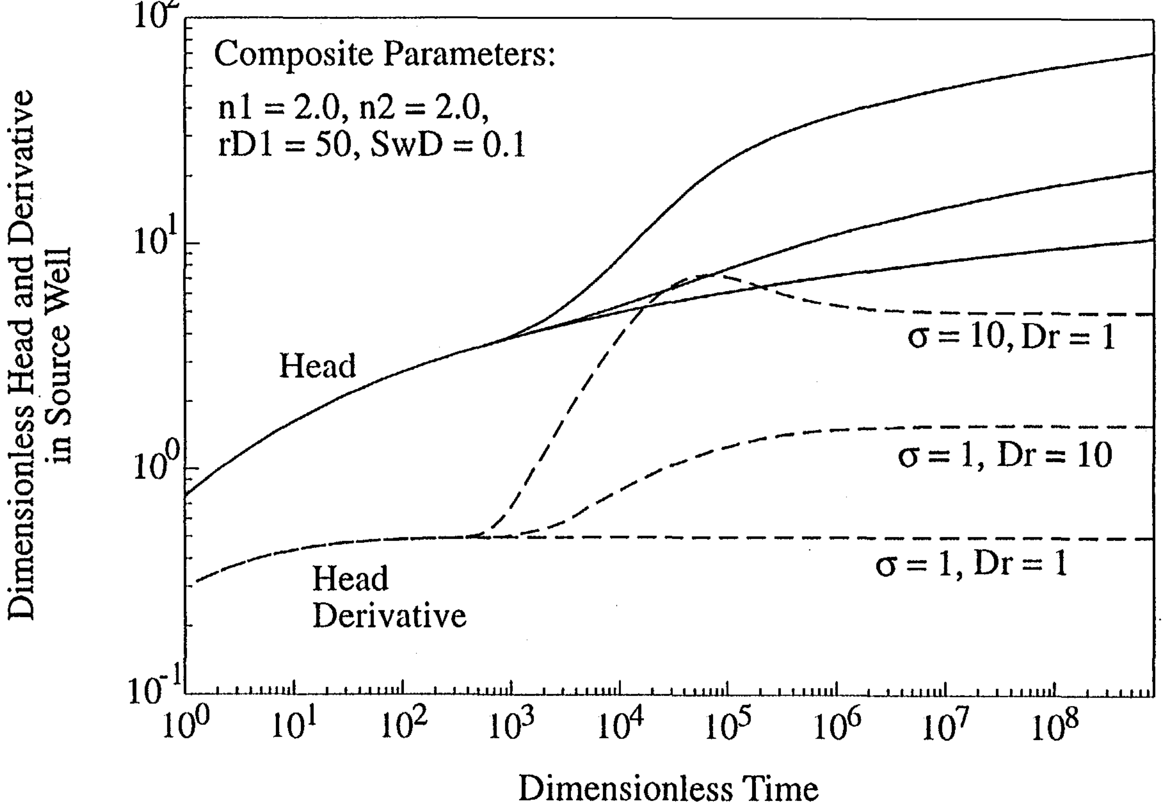

Figure 7b: Dimensionless plot of head and head derivative in source well vs. time for different values of σ and Dr: n1 = n2 = 2

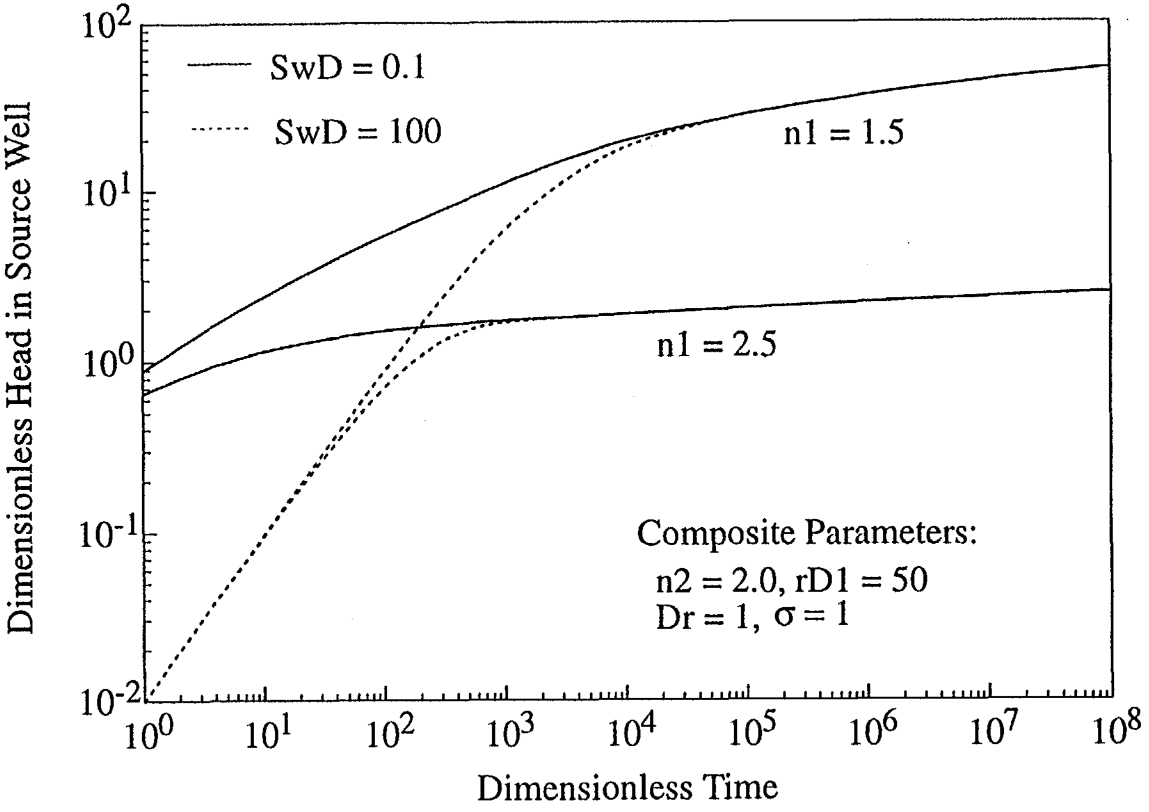

Figure 8: Effect of wellbore storage on dimensionless head in source well

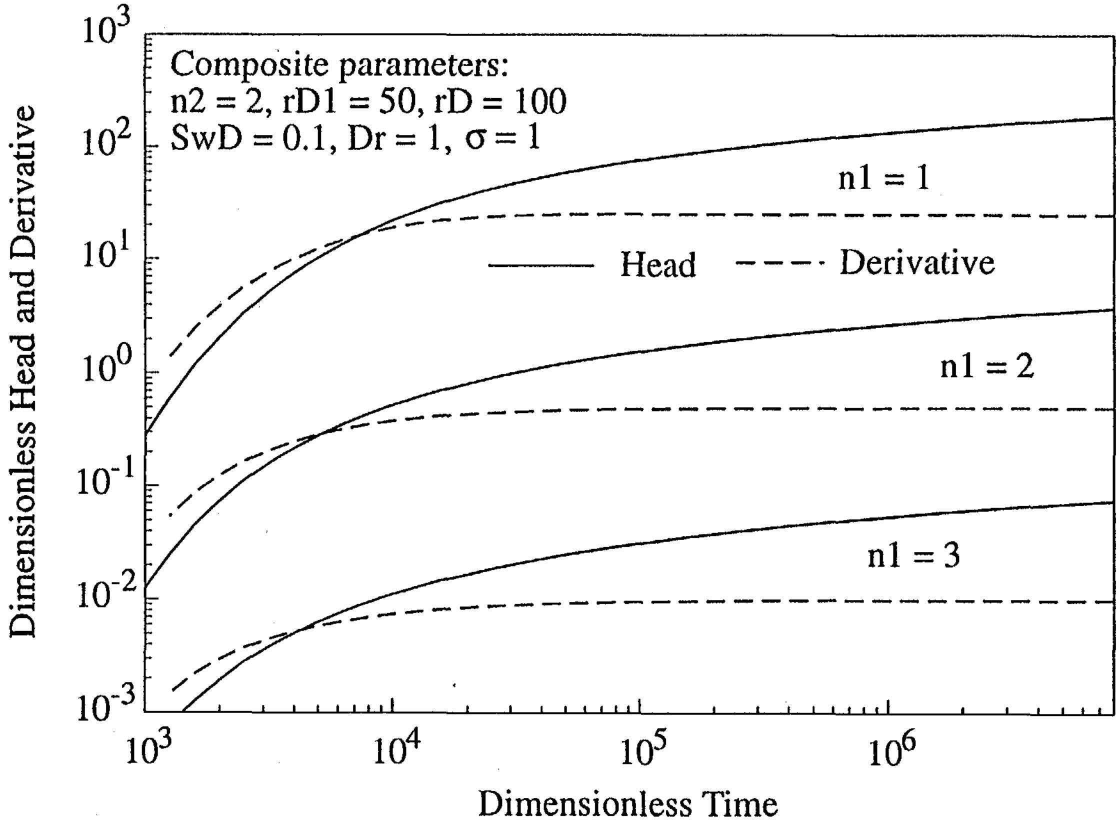

Figure 9: Constant rate interference test solution with varying inner zone flow dimension: observation well in outer zone

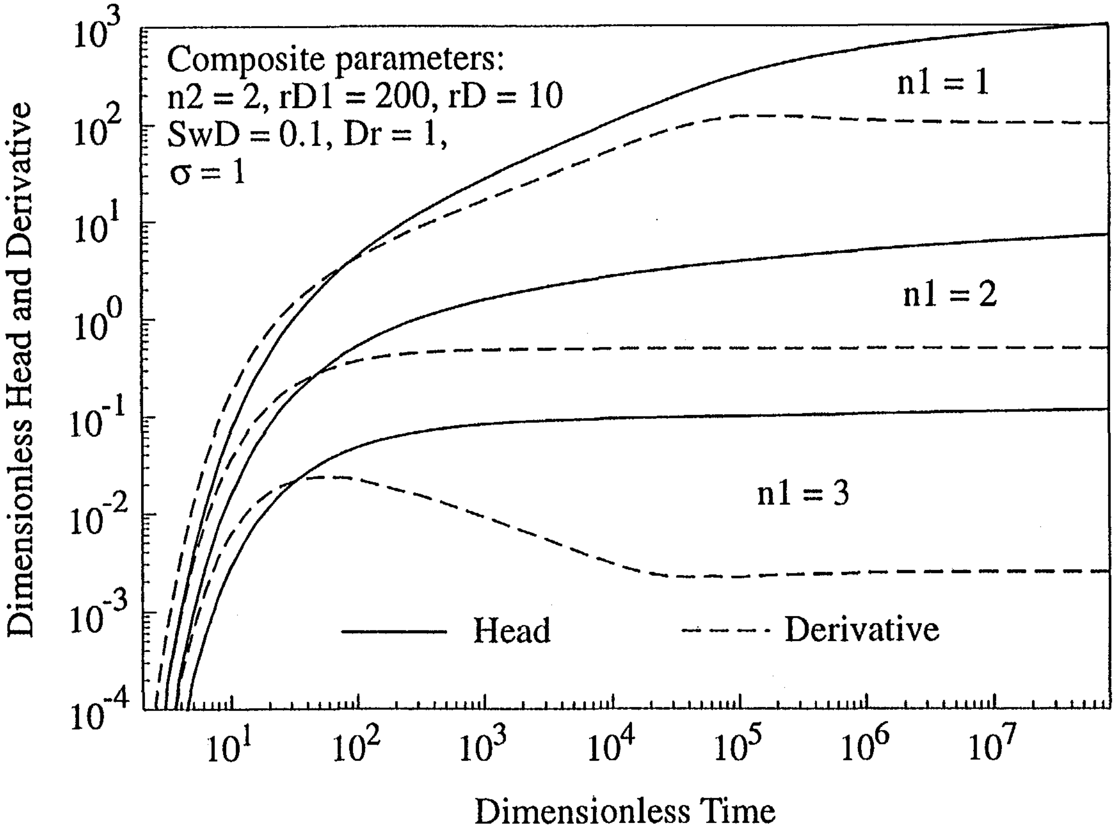

Figure 10: Constant rate interference test solution with varying inner zone flow dimension: observation well in inner zone

ATTACHMENT D

REFEREED PUBLICATION

Dershowitz, W., P. La Pointe and T. Foxford
Improved Fractured Reservoir Characterization Through Neural
Net Analyses of Geological Data
Submitted to American Association of Petroleum Geologists Bulletin (in review)

IMPROVED FRACTURED RESERVOIR CHARACTERIZATION THROUGH NEURAL NET ANALYSES OF GEOLOGICAL DATA

W. Dershowitz[1], P. La Pointe[1], T. Foxford[1]

[1]Golder Associates Inc. 4104 148th Avenue NE, Redmond, Washington 98052

ABSTRACT

Geologists often need to characterize the geology or resource potential of a basin, play or reservoir from sparse information obtained from core or well logs. Extrapolation of well data to a much larger volume of rock is guided by geological concepts and the spatial pattern of data or observations. Over the past decade, pattern recognition tools, such as sequence stratigraphy, remote sensing and neural nets, have been applied to improve geological characterization for purposes of exploration or reservoir engineering.

Fractured reservoirs present many challenges to geologists. Natural fractures are among the most inhomogeneous of geological features, so their extrapolation to portions of a basin or reservoir not penetrated by wells contains much uncertainty. However, successful exploration and profitable development of fractured reservoirs require an accurate understanding of the fracture geometry. Reservoir permeability, compartmentalization and ultimate recovery often depend significantly upon the connectivity of the natural fracture system. Connectivity, in turn, is a function of fracture size, orientation, intensity and fluid-flow properties. The building block for understanding connectivity is the ability to identify fracture sets based on several characteristics, including but not limited to fracture orientations. Thus, any tools or concepts which help the geologist to better characterize the fracture system reduces the risk of unprofitable exploration and improves the ultimate recovery from a reservoir.

This paper presents a new method for improving fractured reservoir characterization based upon the geology and geometry of fractures detected in core or through well logs. The method exploits a specialized type of pattern recognition tool known as a probabilistic neural net (PNN), which has been little used in the earth sciences, and which differs from the back-propagation nets used in the petroleum industry. Probabilistic neural networks provide the flexibility to assign sets combining a wide variety of geological information. Fractures are grouped into sets based not only on orientations, as would traditionally be done, but also by comparing all known characteristics of each fracture to the characteristics of the other fractures in the set. The PNN methodology minimizes the "cost" of fracture misclassification, a strategy known as "Bayes Optimal." The algorithm is verified through a synthetic test case and then an example application to the Yates Field in West Texas is provided.

INTRODUCTION

Fractured reservoirs often surprise engineers and geologists. High initial production rates can give way to unexpectedly low production after a short period of time. Wells separated by kilometers may exhibit near-instantaneous communication, while intervening wells are unaffected. One well may be a prolific producer, while a nearby well, ostensibly in the same geological environment, is not economic.

Whether evaluating a frontier basin, high-grading an existing play, or evaluating a lease, an exploration geologist must identify profitable opportunities by extending sparse well data to a much larger volume of rock. Likewise, the reservoir geologist undertakes studies to help assess the economics of infill drilling, well orientation, or to advise engineers on the geological factors that govern the efficiency of a tertiary flooding process. Uncertainty exists in the simplest of conventional reservoirs, and only increases for fractured reservoirs due to their complex spatial inhomogeneity.

Several technological advances over the past decade have fostered increased interest in fractured reservoirs, most notably, horizontal drilling. This advance in production technology has been accompanied by the development of logging tools that provide geologists with better subsurface information on fractures intersected by a well. Another major advance in this effort has been the development and refinement of discrete fracture network models (Dershowitz et al., 1992; Swaby and Rawnsley, 1996; La Pointe et al., 1997), both for building more geologically realistic reservoir models and for calculating more accurate reservoir simulator parameters.

Discrete fracture network approaches for fractured reservoir exploration or engineering translate the detailed geological information collected by geologists into a form easily input into reservoir simulators or exploration analysis tools. Figure 1 shows a simple DFN model of a fractured carbonate play. In this play, several fractured limestone and dolomite horizons are charged with oil. The reservoir rock was deposited as a series of flat-lying alternating units of fractured carbonate and relatively unfractured shales. Subsequent to deposition, EW shortening caused regional tilting, development of horst structures, and, eventually, uplift and erosion of the upper units. After subsidence, additional sedimentary units were deposited, creating an angular unconformity. Some of these younger strata were also fractured due to a combination of regional stresses and diagenetic processes.

The DFN model shown in Figure 1 represents the conductive fractures by polygons at the scale of interest. These polygons have their intensities, orientations, sizes and fluid flow properties conditioned to the geologically relevant fold geometry, faulting or regional stress field. Additional information on DFN models can be found in Dershowitz et al. (1994) and Bear et al. (1993).

Development of DFN models requires robust field characterization of the geometry and geology of the fracturing. The geologist must separate the fractures into *sets*, and then analyze each set to estimate its characteristic size, orientation, fluid flow properties and other salient properties. Consider the construction of a reservoir model as an example of this process. A geologist has several wells for which core is available, some FMI logs, and a conventional suite of wireline logs. A much larger number of wells only have logs. In order to provide input to a reservoir simulator, the geologist needs to estimate values of fracture spacings in three orthogonal directions and then compute a sigma factor (Kazemi et al. 1976) or similar measure of the coupling between matrix and fractures.

Often a reservoir geologist will infer fracture intensity throughout the reservoir based upon curvature maps. This is often not successful, because some of the fracture sets may not have formed due to folding, and thus are not correlated to curvature. By first separating out the sets that do correlate to curvature from those that do not, the analysis of fracture size, transmissivity and intensity for each set will be more accurate. Inadvertent mixing of fractures from different populations obscures set-specific properties. Yet it is often difficult to confidently assign fractures to the correct sets based upon well logs alone.

The assignment of an individual fracture, inferred from log responses, to a particular fracture is a type of classification problem. Based on a certain set of parameters, it is necessary to develop a technique to classify unknown observations with as much accuracy as possible into their proper classes or sets. While classification inaccuracy might seem inconsequential, in fact, incorrect estimation of fracture set characteristics can have significant consequences. Studies have shown that estimated reservoir compartmentalization, tributary drainage volume, and fluid exchange between matrix and the fracture system is sensitive to fracture intensity (La Pointe, 1997). Thus it is important to first accurately separate fractures into meaningful groups before analyzing each group for its salient reservoir characteristics.

Unfortunately, the most common technique for fracture set definition, stereonet contouring (e.g., Shanley and Mahtab, 1974), relies exclusively on fracture orientations (see e.g., Fisher et al., 1987). In this method, fracture sets are defined by contours that define fracture "preferred" fracture orientations. A fracture is assigned to a set if its orientation lies within the "significant" contour levels of that set. Classifying fractures based upon orientation introduces several problems. First, it ignores fracture characteristics that may provide information on reservoir permeability and recovery, such as the geological factors that affect fracture transmissivity like planarity, roughness, mineral fillings and termination style. In addition, contouring-based algorithms encounter severe problems when the orientations of fractures belonging to distinct fracture sets overlap. For example, the fracture orientations formed by shear due to folding might overlap with the orientations of a fracture set formed by pure extension. In this case, assigning fracture sets based on orientation alone may obscure the fluid flow and geometrical properties belonging to each set.

Recent work on fracture set definition has greatly improved upon the simplistic definition of sets based upon nearest-neighbor orientation analysis. For example, Dershowitz et al. (1996) developed a probabilistic algorithm for fracture set definition based upon multiple geologic properties. In their approach, sets are defined by a number of parameters, including orientation, termination modes, striation, planarity, roughness, mineral infillings, lithology and aperture. One set might be defined by the tendency for the fractures to be smooth, planar, unfilled and subvertical in orientation. Another set might be defined as rough, unfilled or sometimes filled with calcite, often terminating against other fractures in a high-angle intersection, and subvertical in orientation. A third set might be defined as a subhorizontal set. This algorithm makes probabilistic assignments of each fracture to a fracture data set based upon the *a priori* probability distribution of the parameters used in defining the sets. Once all of the fractures have been assigned to a set, the probability distributions for the parameters in each set are recalculated, and used as new *a priori* probabilities. This procedure iterates until the probability distributions for the set parameters change little for each successive iteration. A weakness in this algorithm is that it can misclassify fracture data when the set definition parameters, such as orientation, overlap.

This paper presents an extension of the probabilistic algorithm which overcomes its limitations by using the technique of probabilistic neural networks (PNN). The new algorithm has been successfully verified for fractures sets with significant overlaps in orientation, and has been applied to data from the Yates Field in West Texas.

Both the present neural network method, and the method of Dershowitz et al. (1996) recognize that every fracture identified in the field has a finite probability of membership in any given fracture set. Thus, the boundaries between fracture sets are probabilistic rather than definite. This is a powerful departure from the assignment of a fracture to a set if its orientation falls within the orientation contours for a set. The difference between the present algorithm and other algorithms is that this approach can more accurately classify data under far more statistically pathologic situations, which, unfortunately dominate typical petroleum systems. Although developed and illustrated for fractured reservoir problems, the method is widely applicable to any geological classification problem to which conventional back-propagation neural nets or other pattern recognition tools have been applied.

NEURAL NETWORKS

Neural networks are a sophisticated form of non-linear pattern recognition that are used in such diverse areas as stock market analysis, loan application screening, voice recognition, disease diagnosis, and medical expert systems (Eberhart and Dobbins, 1990). They are particularly well-suited for problems in which the input and output variables are of different mathematical types (e.g. class, ordinal, and continuous variables) and are potentially correlated. Neural network have found geologic application in a variety of areas including slope stability analysis (Xu and Huang, 1994), rock and soil mechanics (Ellis et al., 1995; Feng, 1995; Lee et al., 1992), fracture network hydrology (La Pointe et al., 1995; Thomas and La Pointe, 1995), prediction of earthquake intensity and liquefaction (Goh, 1994; Tung et al. 1994), and petroleum geology

(Baldwin et al., 1989, 1990; Raiche, 1991; Weiner et al., 1991; Osborne, 1992; Rogers et al., 1992, 1995). The most common type of neural network used in published geological applications is the *Back-Propagation* network (e.g., Rogers et al., 1992). This type of net has proven useful for classifying data, for example, looking at the parameter values of a series of wireline logs for each 1-foot interval and classifying the interval as sandstone, shale, etc. It is similar in function to classical *discriminant analysis* (Davis, 1973).

There are many types of neural networks, but all share a common architecture consisting of *neurons* and *synapses* (Figure 2). A neuron is simply a node in the network which uses a non-linear transfer function to convert an input signal (value) to an output signal. Neurons are connected by synapses. A synapse takes the output signal from one neuron, multiplies it by a *synaptic weight*, and passes the modified signal to an adjacent neuron as input. Depending on the number of incoming and outgoing synapses connected to it, a neuron can be classified into one of three categories:

1. *Input neurons* have zero incoming synapses and one or more outgoing synapses. They represent input variables, and take the variable value as their output.
2. *Output neurons* have one or more incoming synapses and zero outgoing synapses. They represent output variables, and produce an output signal which equals the predicted variable value.
3. *Hidden neurons* have one or more incoming synapses and one or more outgoing synapses. They sit between the input and output neurons and pass signals through the network.

A distinct advantage of neural networks over other classification methods is their ability to learn the relative importance and complex interrelations among input and output variables. By changing the neuron transfer functions, the synaptic weights, or the network connectivity, a neural network can be conditioned to provide the expected response for a given input pattern. Once trained, a neural network can then be used to make predictions for input patterns whose correct classification is unknown.

The probabilistic neural network (Specht, 1990) is a combination of probability theory and Bayesian statistics, and was developed primarily for solving multivariate classification problems (Masters, 1993, 1995). The probabilistic neural network algorithm is designed to provide a classification which minimizes misclassification of fractures to the wrong set. The classification system which has the minimum "cost" of misclassification is termed "Bayes Optimal" (Parzan, 1962). For treatment of fracture data, it is assumed that the cost of misclassification is equal for all fractures. This means that it is no worse to misclassify any particular fracture in the fracture population; all misclassifications are equally bad. The major advantages of using a PNN is that it can account for data "shape", overlap, outliers, and multiple modes with a high degree of classification accuracy (Figure 3). For example, the U.S. National Institute of Standards & Technology carried out two studies comparing several popular traditional and neural network classification techniques. The Probabilistic Neural Network (PNN) gave the lowest error rate on very complicated databases (Candela and Chellappa, 1993; Grother and Candela, 1993). In addition, the ability of a PNN to minimize the cost of misclassification and provide mathematically rigorous confidence levels for decision analysis make PNN's the preferred neural net algorithm for a variety of military applications (Masters, 1995). The major drawback of PNN's are that they require very large amounts of memory and computational speed, which were not widely and cheaply available for realistically-sized problems until the 1990's.

The basic architecture of a PNN is illustrated in Figure 2. It consists of four layers: an Input layer, a Pattern layer, a Summation layer, and the Output layer. The Input layer has the same number of neurons as there are input parameters. The number of neurons in the Pattern layer is equal to the number of training cases used for each class. In the figure, there are two classes and two training sets for each class, producing a total of 4 neurons in the Pattern layer. There is one Summation layer neuron for each class. The Output layer consists of a very simple single neuron which determines which Summation layer neuron is producing the maximum signal.

There are several ways in which a PNN could be implemented for fracture set classification. One way would be to first train the neural net on existing data. The existing data is separated randomly into two portions: a *training set* and a *test set*. The training set is used to calibrate or train the network which is then used to predict the test set data. The parameters that give the best prediction of the test set data are those that are retained for classification of new data. While it might seem more appropriate to retain the parameters that allow the net to classify the training set most accurately, this often reduces the ability of the net to correctly classify new data. There are many degrees of freedom in any neural net, so that maximizing classification accuracy for the training set amounts to finding parameter values that are specific to the training set, with a consequent loss in generality. Once the network has been trained, it can then be used to process new data. This type of implementation is straightforward and useful, but it allows for little incorporation of qualitative geological ideas other than deciding what the input and output geological variables should be.

Another strategy for implementing the PNN is to provide the geologist with more opportunity to include qualitative geological insight into the fracture classification process. In order to achieve this, it is possible to embed a PNN within a more flexible probabilistic classification scheme. This allows the geologist to postulate that certain parameters are important for classifying fractures, construct a PNN based on these assumptions, and apply it to new data. The embedded neural network algorithm for fracture set definition is summarized below.

The geologist first analyzes fracture data to decide what variables might be important for classification. It does not matter whether these variables are redundant or ultimately have little impact on classification. Variable selection might be based upon geological insight, or various forms of statistical cluster analysis (Davis, 1973), including neural nets which perform unsupervised learning such as Kohonen Nets. For example, Set A might be defined by a near horizontal orientation, with 0% termination at intersections, while Set B might be defined by fractures with 100% termination at intersections. The next step is to stochastically generate a set of fractures according to this classification. Once the network has been trained on the synthetic data, it is then used to classify the fracture data into sets. This approach is very flexible because it allows the geologist to rapidly and interactively evaluate different fracture set definitions.

The probabilistic neural network algorithm implementation is illustrated in Figure 4. The algorithm proceeds as follows:

1. The user evaluates the data to define the variables to be considered in set classification.
2. The user evaluates the data to define prior probability distributions for each of the sets. Fractures with these distributions of properties are generated to constitute the "training set".

3. The user specifies weightings W_i for each of the classification variables, for use in the utility function for evaluation of set classification.

$$V(c) = \sum_i W_i \sum_j D_j(j|c)$$

   where $V(c)$ is the utility for classification c, W_i is the weighting for variable i, and $D_i(j|c)$ is the Euclidean distance from the data point j for its classification c.

4. The neural network algorithm uses the utility $V(c)$ for each data point to determine which set it should be assigned to. Each fracture is evaluated for its probability of membership in each of the defined sets, and is assigned to those sets.

5. The statistics for each set are reported based on the fractures assigned to each set.

6. Set statistics and graphical displays are provided.

The classes of fracture properties which can be used in this algorithm are provided in Table 1.

TEST CASES & APPLICATIONS

A simple simulation illustrates how a PNN can accurately classify fracture data. In this simulation (Fig. 5), four fracture sets related to fold geometry were created. These sets consist of a transverse (T) set, a longitudinal (L) set, and two shear sets (D1 and D2), as shown in the figure. There are 2000 fractures in the model, with each set having exactly 500 fractures. Each set was created with orientation dispersion conforming to a Fisher distribution (Fisher et al., 1987) with $\kappa = 15$. As a result, there is substantial overlap in the orientations among the sets, which can be seen in Figure 5. In a reservoir, it is quite likely that each of these sets would have their own fluid flow properties. For example, the transverse and longitudinal sets are formed in pure extension, while the shear fractures are formed in shear. Moreover, the fractures in the longitudinal set will have very different orientations than the transverse set with respect to the *in situ* stress field in the reservoir. Thus, the correct classification of fractures into these four sets could be important for accurately estimating reservoir parameters such as the sigma factor.

In order to evaluate the PNN, the 2000 fractures are randomly separated into three categories. The *training set* (N=668) is used to calibrate the PNN. The *test set* (N=666), composed of fractures not used for calibration, is used to evaluate how well the trained net performs. The *production set* (N=666) is used for neither training nor testing. Statistics concerning the results of the training or calibration phase of the PNN are shown in Table 2.

The PNN achieved about a 70% correct classification of the new data, which is promising, considering the substantial overlap in orientations among the four sets, and the absence of any other information. This simple, yet challenging example, illustrates how PNN's can potentially aid the geologist in exploiting sparse well data on fracturing.

Another test case was carried out for sets in which the distinction between fracture populations was based on geological properties in addition to orientation. This second test case had three sets, some of which were defined by multiple parameters with multiple values. It represents the most general type of classification available. The prescribed set definitions are given in Table 4. For these definitions, the expected set classifications were derived by statistical methods given in Table 5.

The information in the table demonstrates that the algorithm identified three sets with properties very similar to those expected based on the parameters used to generate the synthetic data sets.

YATES FIELD, WEST TEXAS

Finally, we present an application of the neural network algorithm for assignment of natural fractures to sets for the Yates Field, West Texas (Figure 6). The Yates Field is a study site for development of technologies for enhanced oil recovery by Thermally-Assisted Gravity Separation (TAGS) (Wadleigh, 1996). The method relies heavily on an understanding of the fracture network which defines rock blocks for thermal conduction and compartments for oil production (La Pointe et al, 1997).

Figure 7 presents the fracture orientation data from outcrop mapping and FMS/FMI logging in the project study areas. Although this data can be visually discriminated into two sets, there is significant overlap and scatter. Statistical analysis of these two sets yields orientation parameters summarized in Table 6. Preliminary analysis of the fracture geology also suggests that one of the sets may have preferential solution features and cave development along it, although this will require additional analysis.

To date, the algorithm described above has been applied for discrimination of sets based on orientation alone, since more complete geological information has not yet been assembled on a field-wide basis. However, the results summarized in Table 6 and illustrated in Figure 8 show that the PNN approach performs well in separating data into sets based upon well log data. The correct classification of 668 new fractures not used in the calibration of PNN achieved about an 82% success rate, and the error was relatively unbiased. Future analyses will be carried out including geological and oil production data.

CONCLUSIONS

The approach for defining fracture sets developed in this paper has significant advantages for applications in fractured reservoirs. Most importantly, fracture sets can be defined even when fracture set orientations overlap, and when characteristics other than fracture orientation need to be considered. The method has been applied successfully for fracture data from the Yates Field, West Texas, based on fracture information obtained using FMS/FMI imaging technologies. The fracture set definitions will be useful in discrete feature modeling of the site for analysis of enhanced oil recovery technologies.

ACKNOWLEDGMENTS

The work described in this paper was supported by the US Department of Energy as part of the Fundamental Geoscience Research and Development program, administered by BDM-OK/NIPER. Project support is gratefully acknowledged. For further information, please access the web site http://www.golder.com/niper/niprhome.htm

REFERENCES

Baldwin, J. L., A. R. M. Bateman, and C. L. Wheatley, 1990, Application of neural network to the problem of mineral identification from well logs: The Log Analyst, v. 3, p. 279-293.

Baldwin, J. L., D. N. Otte, and C. L. Wheatley, 1989, Computer emulation of human mental process: application of neural network simulation to problems in well log interpretation: Society of Petroleum Engineers SPE Paper 19619, p. 481-493.

Bear, J., C. F. Tsang, G. de Marsily, 1993, Flow and contaminant transport in fractured rock: Academic Press, San Diego, CA.

Candela, G. T. and R. Chellappa, 1993, Comparative perofrmance of classification methods for fingerprints. National Inst. of Standards & Tech, NISTIR-5163.

Davis, J. C., 1973, Statistics and Data Analysis in Geology, John Wiley and Sons, Inc., New York.

Dershowitz, W.S. and P. La Pointe, 1994, Discrete fracture approaches for oil and gas applications." Keynote paper. Proceedings, 1st North American Rock Mechanics Symposium, Austin. AA Bakema, Rotterdam.

Dershowitz, W. J., N. Hurley and K. Been, 1992, Stochastic discrete fracture modeling of heterogeneous and fractured reservoirs. Proc. 3rd Int. Conf. On Mathematics of Oil Recovery. Delft, Holland, June 1992.

Dershowitz, W., J. Geier, M. Uchida, and R. Busse, 1996, A stochastic approach for fracture set definition: Proceedings, NARMS'96, North American Rock Mechanics Symposium, Montreal, PQ. A.A. Balkema, Rotterdam.

Eberhart, R.C. and Dobbins, R.W., 1990. Neural Network PC Tools. Academic Press, London, 414p.

Ellis, G.W. 1995, Stress-strain modeling of sands using artificial neural networks: Journal of Geotechnical Engineering, v 121. p 429-435.

Feng, X., 1995. Neural network approach to comprehensive classification of rock stability, blastability and drillability: International Journal of Surface Mining, Reclamation and Environment, v. 9, no. 2, p 57-62.

Fisher, N, T. Lewis, and B. Embleton, 1987, Statistical analysis of spherical data: Cambridge University Press, Cambridge, England.

Goh, A.T.C.,1994, Seismic liquefaction potential assessed by neural networks: Journal of Geotechnical Engineering, v. 120, no. 9, p. 1467-1480.

Grother, P. J., and G. T. Candela, 1993, Comparison of handprinted digit classifiers. National Inst. of Standards & Tech., NISTIR-5209.

La Pointe, P. R., 1997. Flow compartmentalization and effective permeability in 3D fractal fracture networks. Int. J. Rock Mech. & Min Sci. Vol. 34, No.3-4.

La Pointe, P. R., Wallmann, P.C., and Follin, S, 1995, Estimation of effective block conductivities based on discrete network analyses using data from the Aspo site: SKB Technical Report 95-15, Swedish Nuclear Fuel and Waste Management Co., Stockholm.

LaPointe, P., W. Dershowitz, A. Thomas, and T. Eiben, 1997, Compartmentalization analysis using discrete fracture network models: Proceedings, 4th International Reservoir Characterization Technical Conference, Houston. DOE/NIPER, Bartlesville, OK.

Lee, C., January 1992, Identifying probable failure modes for underground openings using a neural network: International Journal of Rock Mechanics, Mining Sciences, and Geomechanics Abstracts, v. 29, no. 1, p 49-67.

Masters, T., 1993, Practical neural network recipes in C++: Academic Press, New York.

Masters, T., 1995, Advanced Algorithms for Neural Networks, A C++ Sourcebook: John Wiley & Sons, Inc., New York.

Osborne, D. A., 1992, Neural networks provide more accurate reservoir permeability: Oil & Gas Journal, (Sept. 28), p. 80-87.

Rogers, S. J., H. C. Chen, D. C. Kopaska-Merkel, and J. H. Fang, 1995, Predicting permeability from porosity using artificial neural networks: AAPG Bulletin, v. 79, p. 1786-1797.

Rogers, S. J., J. H. Fang, C. L. Karr, and D. A Stanley, 1992, Determination of lithology from well logsusing a neural network: AAPG Bulletin, v. 76, p. 731-739.

Parzan, E., 1962, On estimation of a probability density function and mode: Annals of Mathematical Statistics, v. 33, p. 1065-1076.

Raiche, A., 1991, A pattern recognition approach to geophysical inversion using neural nets: Geophysical Journal International, v. 105, p. 629-648.

Shanley, R. and M. Mahtab, 1974, Delineation and analysis of clusters in orientation data: Mathematical Geology, v. 8, no. 1, p. 9-23.

Specht, D., 1990, Probabilistic neural networks: Neural Networks, v. 3, p. 109-118.

Swaby, P. A. and K. D. Rawnsley, 1996, An interactive 3D fracture modelling environment. Soc. Petroleum Engineers, Petroleum Computer Conference, Dallas, TX, 2-5 June 1996. SPE 36004.

Thomas, A.L. and La Pointe, P.R., 1995. Conductive fracture identification using neural networks: Proceedings: 35th U.S. Rock Mechanics Symposium, University of Nevada, Reno, June 5-7, 1995, p. 627-632.

Tung, A.T., Wong, F.S., and Dong, W., 1994. Prediction of the spatial distribution of the modified Mercalli intensity using neural networks: Earthquake Engineering and Structural Dynamics, v. 23, n. 49, p. 62.

Wadleigh, G., 1996. Thermally assisted gravity separation: Marathon Oil Technical Note, Marathon Oil, Midland TX.

Weiner, J. M., J. A. Rogers, J. R. Rogers, and R. F. Moll, 1991, Predicting carbonate permeabilities from wireline logs using a back-propagation neural network, CM1.1: Society of Exploration Geophysicists, Expanded Abstracts with Biographies, Technical Program, v. 1, p. 285-289.

Xu, Q., and R. Q. Huang, 1994, Artificial neural network methods for spatial prediction of slope stability: *in* Oliveira, R., L. F. Rodrigues, A. G. Coelho, and A. P. Cunha, (eds.), Seventh International Congress; International Association of Engineering Geology, v. 7, p. 4725-4728.

LIST OF FIGURES

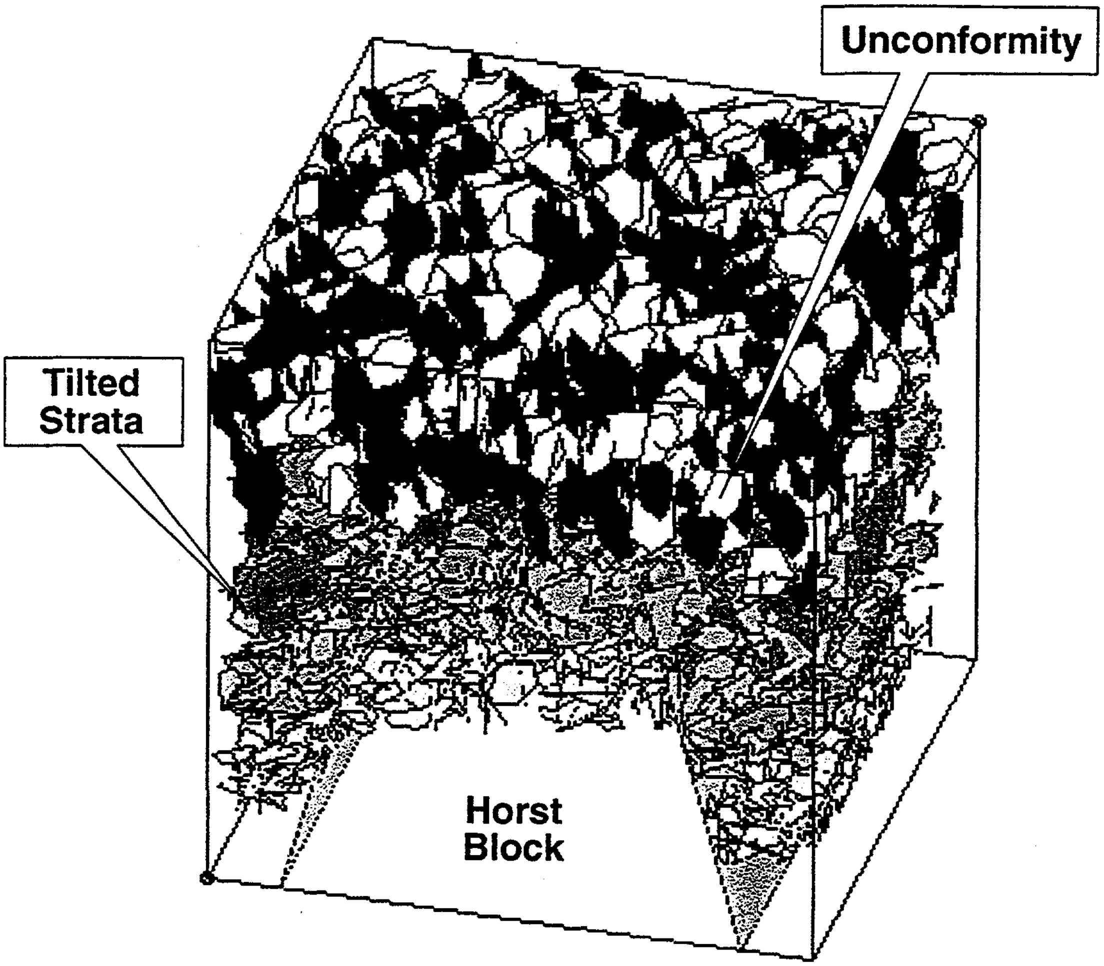

Figure 1. DFN Model of Fractured Carbonate Play

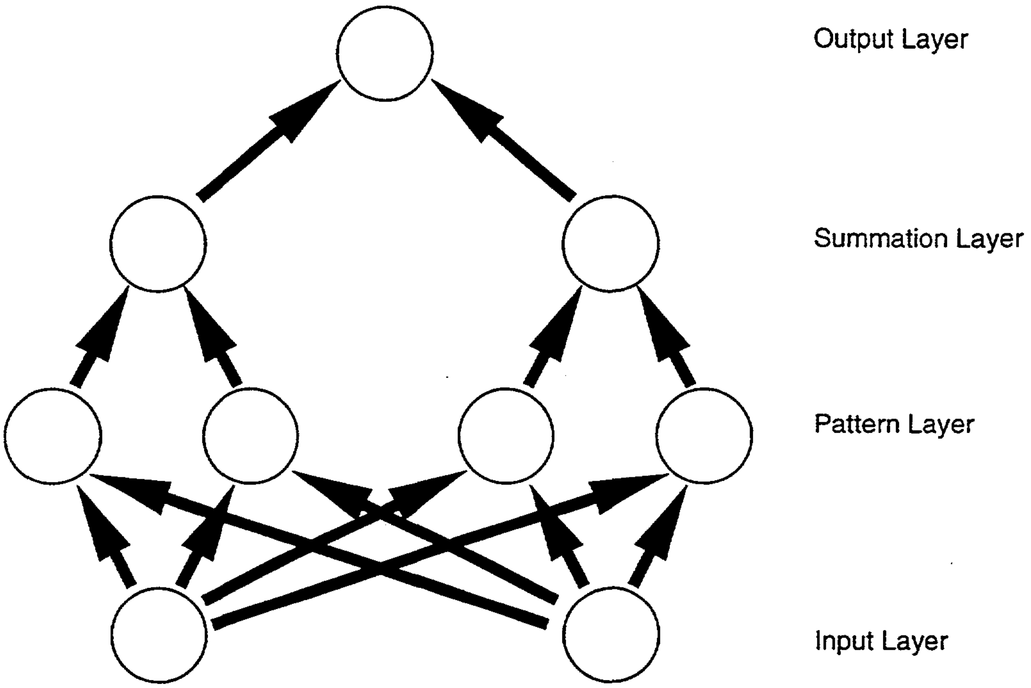

Figure 2. Specht's PNN Architecture

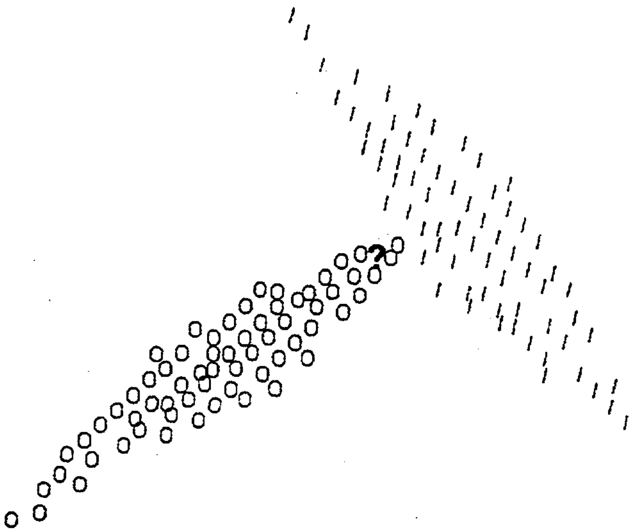

(a) Classification must use overall shape.

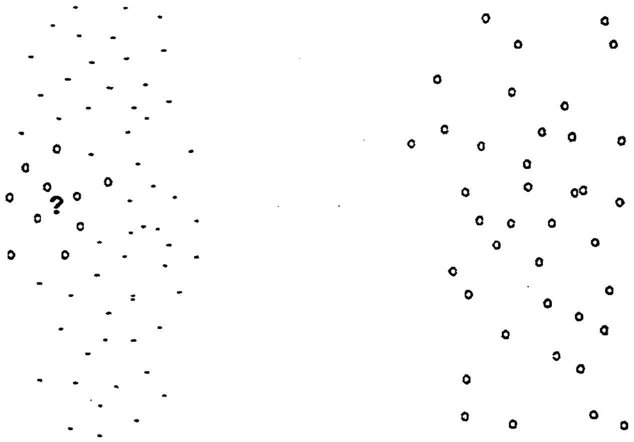

(b) Classes may have multiple nodes.

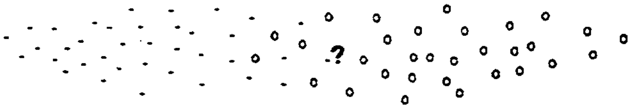

(c) Nearest-neighbor methods can fail.

After Masters 1995

Figure 3. PNN Algorithm for Classification

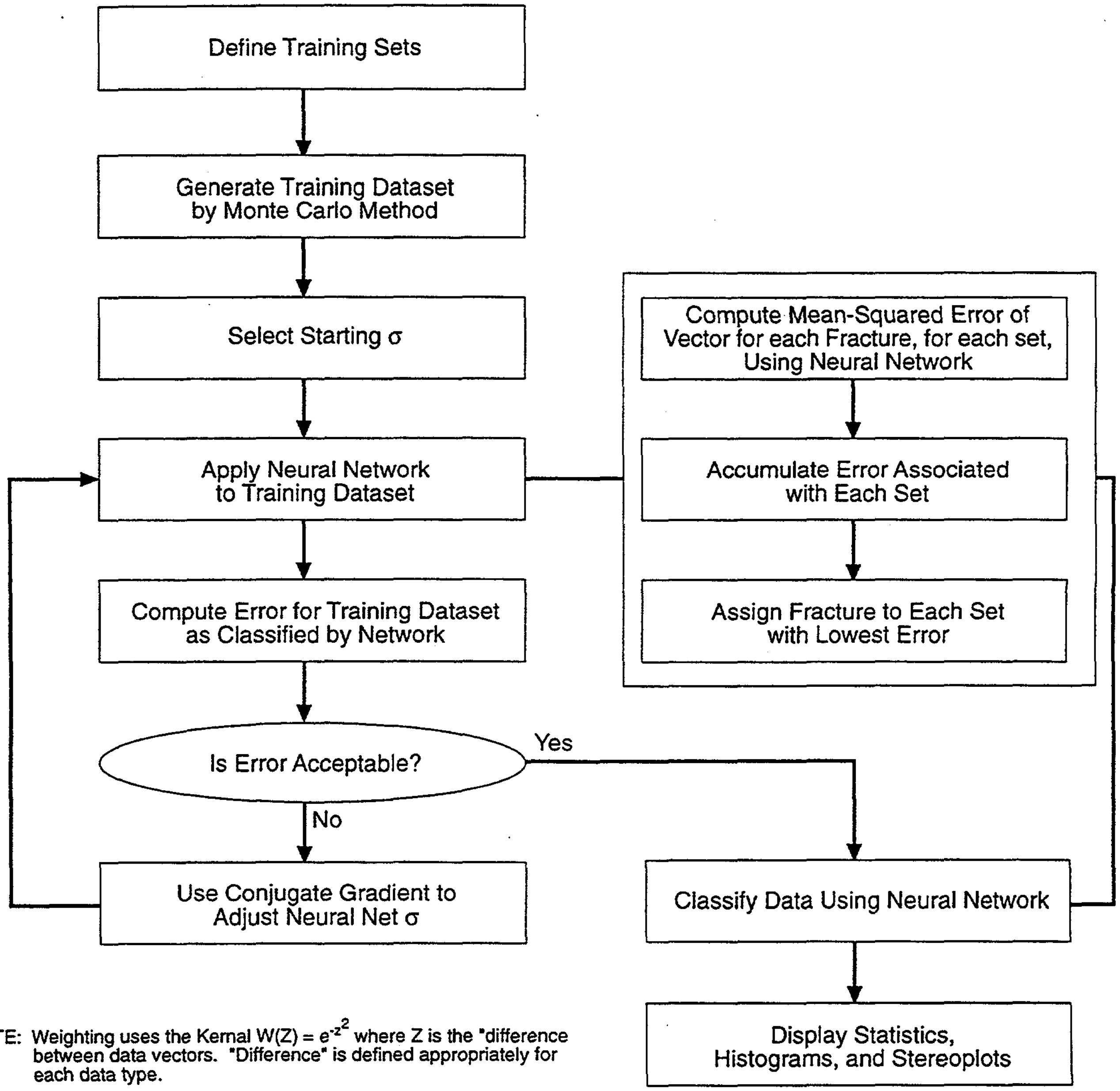

NOTE: Weighting uses the Kernal $W(Z) = e^{-z^2}$ where Z is the "difference between data vectors. "Difference" is defined appropriately for each data type.

Figure 4. Probabilistic Neural Network Algorithm

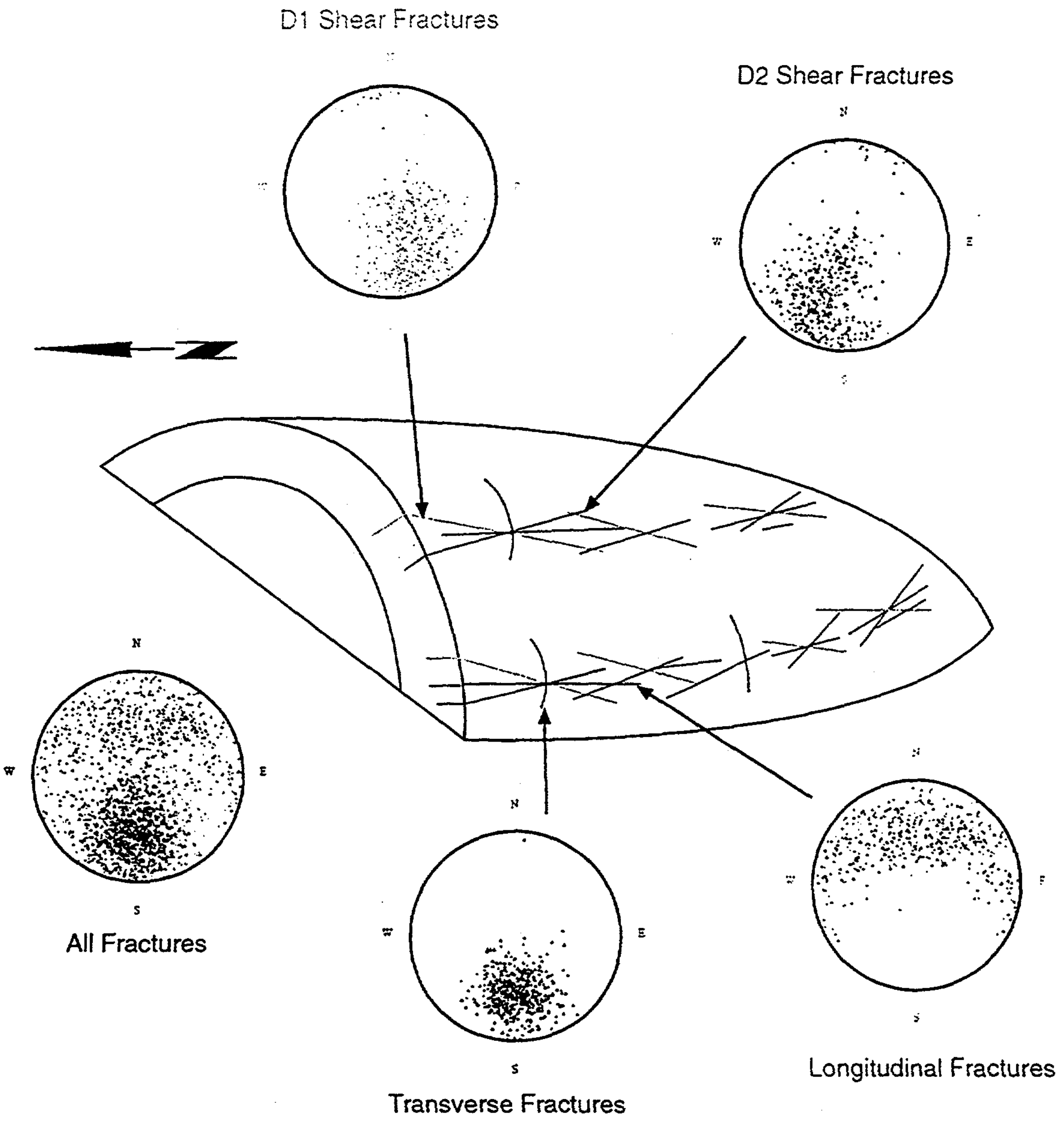

Figure 5. Fractures in a Plunging Anticline

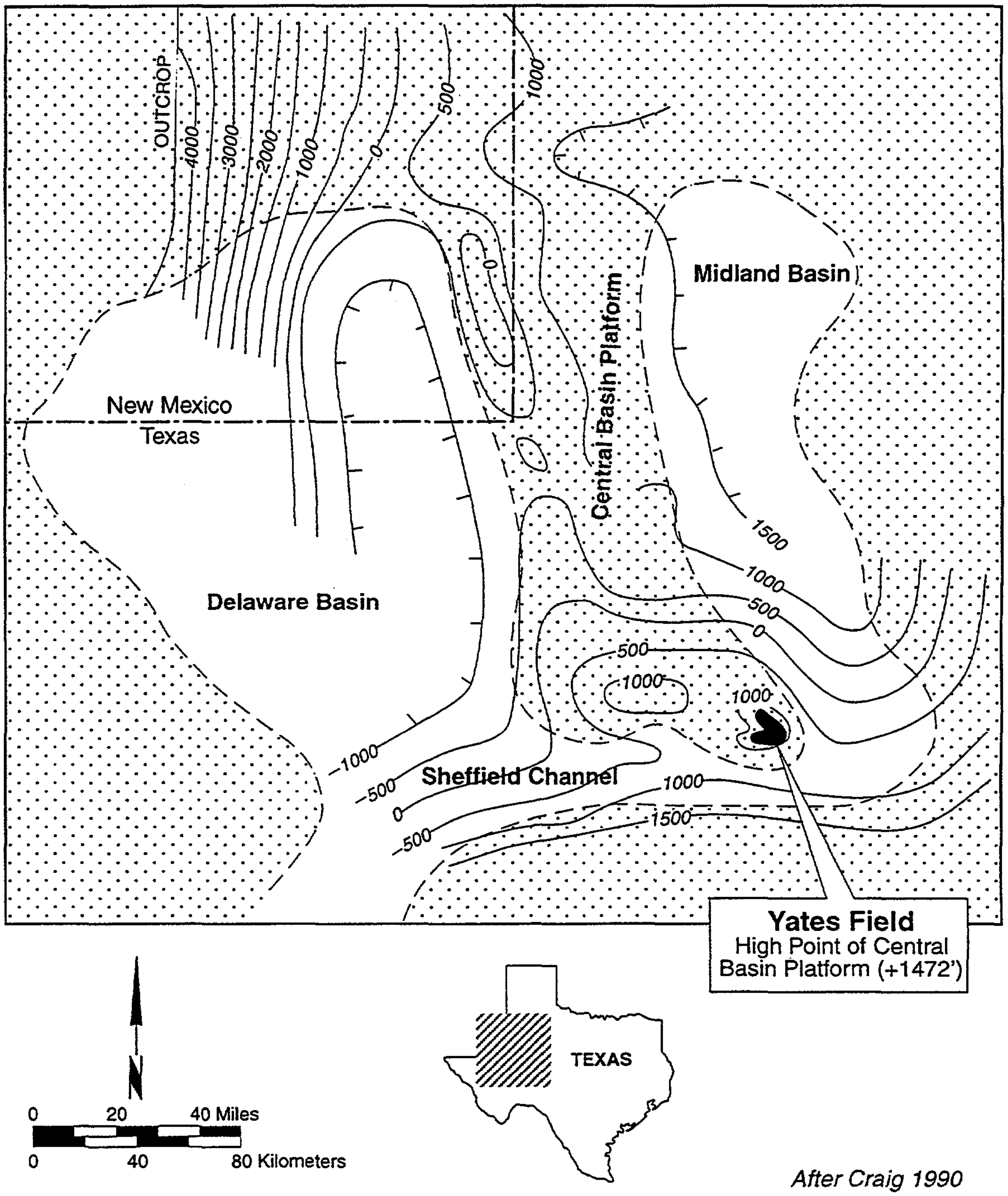

After Craig 1990

Figure 6. Location of the Yates Field

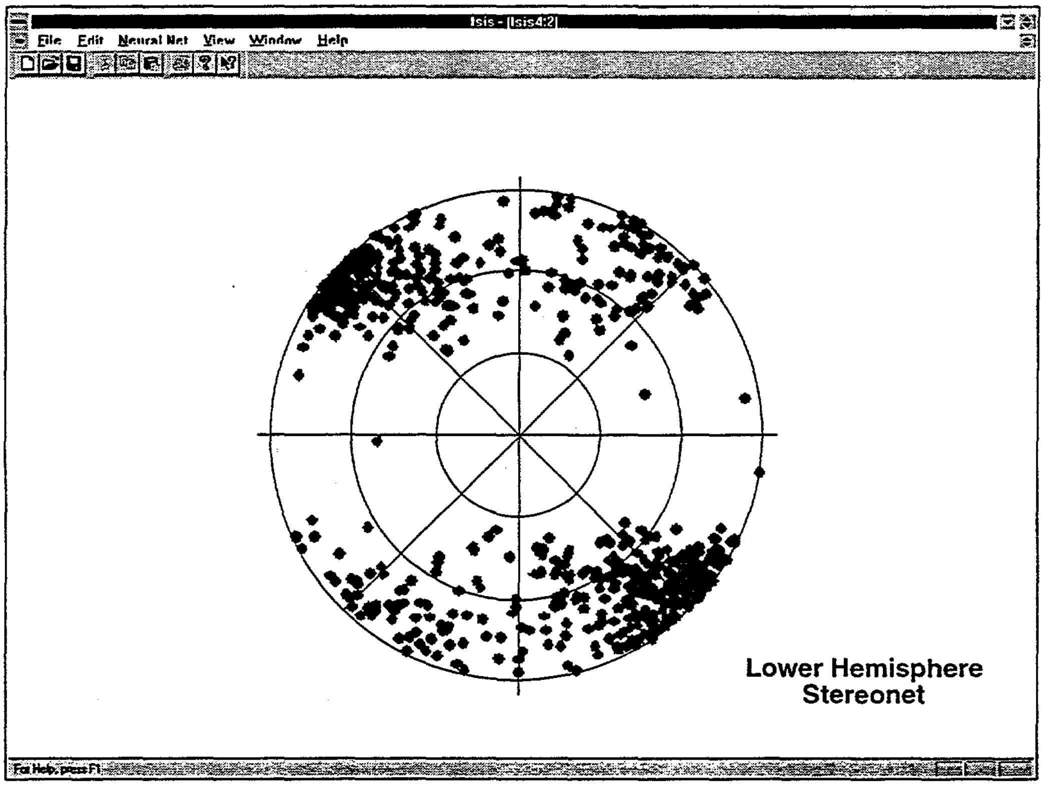

Figure 7. Yates Field FMI Data

963 1357.521/72232.fh7

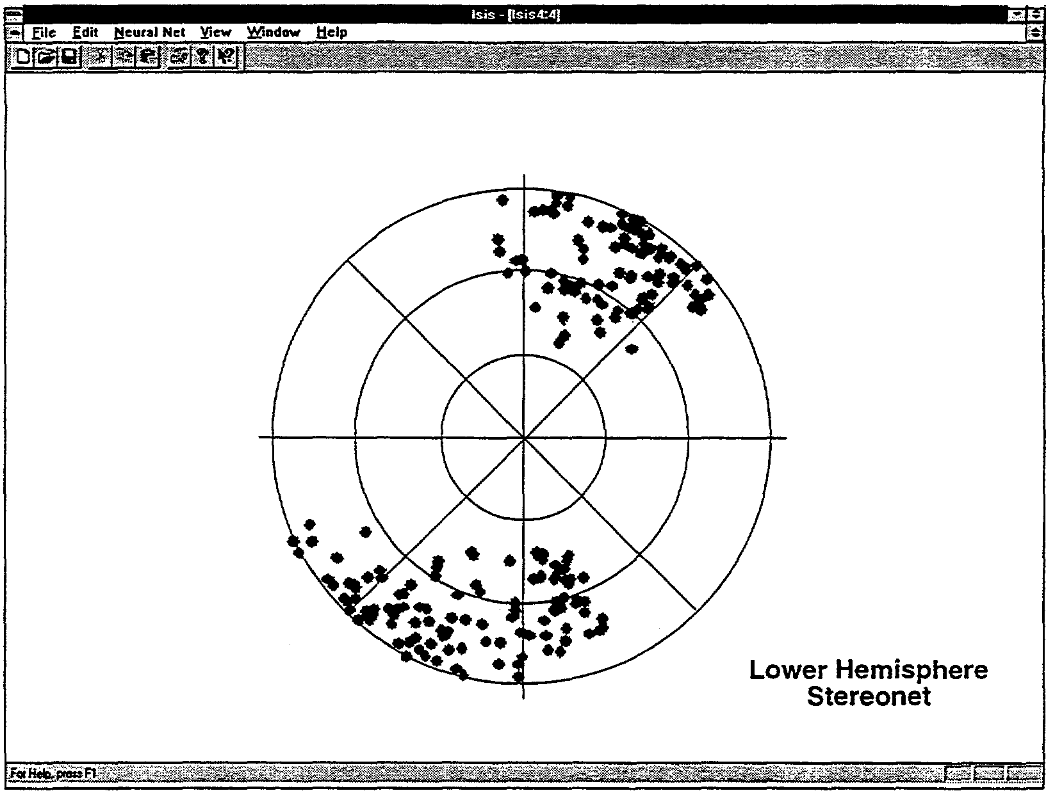

(a) Set 1

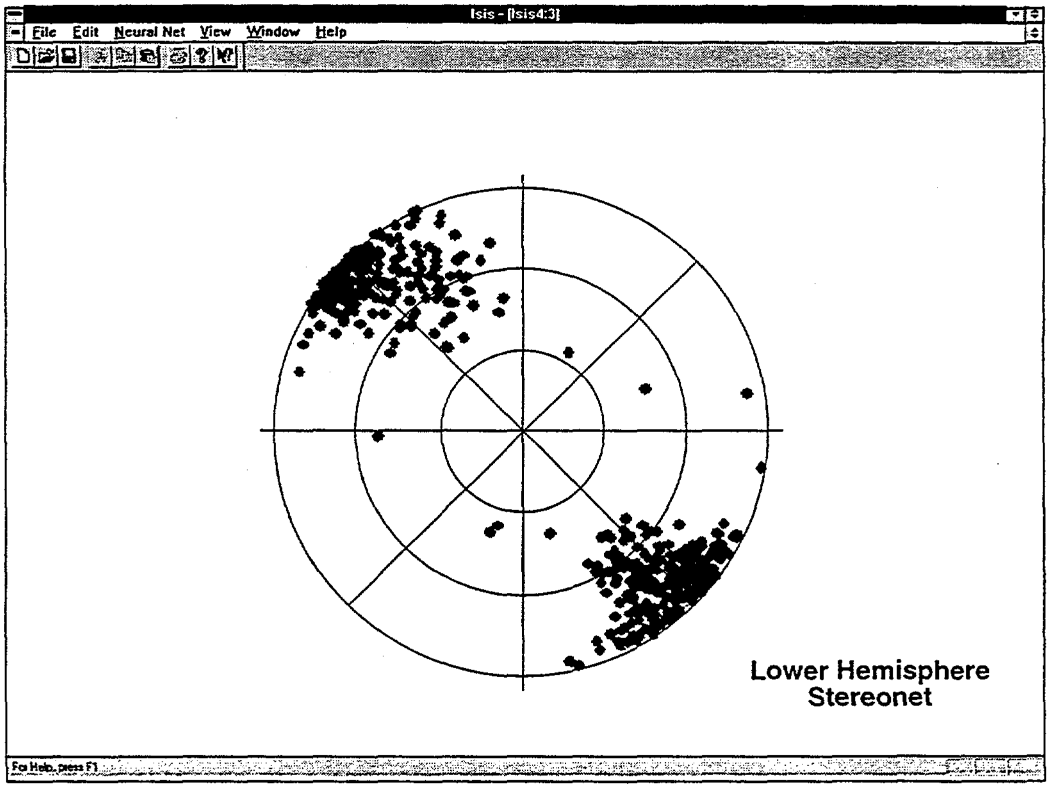

(b) Set 2

Figure 8. Set Definitions for Yates Field Data

Table 1: Fracture Property Classes

Property Class	Description	Example
Real	Real valued number	Trace length, aperture
Integer	Integer valued number	JRC, RQD
Orientation	Trend θ on [0,360] and dip ϕ on [0,90] for the dip vector (D) or pole vector (P). For calculation of spherical angles, the minimum angle of either the upper or lower hemisphere orientation vector is used. The default is lower hemisphere	Fracture orientation, striation orientation, foliation orientation.
Vector	Similar to orientation, but uses only lower hemisphere values	
Class	Membership in a group, as a logical (0,1) cvalue	Rock type, fracture termination mode
Ordinal	Positive, integer value	Fracture set number

Table 2: Fracture Set Training

	Actual Percentage				
	D1 Shear	D2 Shear	Longitudinal	Transverse	# fractures in set
D1 Shear	62.7	0.0	17.5	19.9	166
D2 Shear	0.0	97.6	6	1.8	167
Longitudinal	21.8	1.1	67.2	9.8	174
Transverse	29.6	1.9	15.1	53.5	159

Table 3: Three Set Verification Case

Fracture Set	Weight to Property	Parameter
1	50% Orientation 40% Planarity 10% Weathering	Mean Pole Trend = 35°, Plunge=75° Planar=70%, Curved=30% Weathered=0%, Unweathered=100%
2	10%Orientation 90%Weathering	Mean Pole Trend = 40°, Plunge=65° Weathered=100%, Unweathered/0%
3	90%Orientation 10% Weathering	Mean Pole = 240°, Plunge=10° Weathered=50%, Unweathered=50%

Table 4: Expected and Algorithm Results for Multiset Verification Case

Parameter	Set 1		Set 2		Set 3	
	Algorithm	Expected	Algorithm	Expected	Algorithm	Expected
Number of Fractures	25	33	32	27	24	23
Planarity						
Planar	20%	24%	9%	7%	4%	3%
Curved	12%	22%	19%	10%	46%	45%
Other	62%	53%	72%	83%	50%	54%
Weathering						
Weathered	4%	6%	62%	72%	8%	6%
Unweathered	56%	47%	0%	0%	29%	34%
Other	40%	47%	38%	28%	63%	60%

Table 5: Fracture Set Statistics

Set	Distribution	Mean Pole (Trend, Plunge)	Dispersion κ_1,κ_2
Set 1	Fisher	133.9, 62.1	21.8
Set 2	Fisher	61.6, 96.03	9.9

Table 6: Fracture Set Statistics

	Classified As Set 1	Classified As Set 2
Actual Set 1	86.3	13.7
Actual Set 2	22.0	78.0